

DYNAMIC ENHANCED RECOVERY TECHNOLOGIES
CLASS I

Final Report
Part I
July 1994 - October 1995

By
Roger N. Anderson

Performed Under Contract No. DE-FC22-93BC14961

Columbia University
New York, New York



National Petroleum Technology Office
U. S. DEPARTMENT OF ENERGY
Tulsa, Oklahoma

DISCLAIMER

This report was prepared as an account of work sponsored by an agency of the United States Government. Neither the United States Government nor any agency thereof, nor any of their employees, makes any warranty, expressed or implied, or assumes any legal liability or responsibility for the accuracy, completeness, or usefulness of any information, apparatus, product, or process disclosed, or represents that its use would not infringe privately owned rights. Reference herein to any specific commercial product, process, or service by trade name, trademark, manufacturer, or otherwise does not necessarily constitute or imply its endorsement, recommendation, or favoring by the United States Government or any agency thereof. The views and opinions of authors expressed herein do not necessarily state or reflect those of the United States Government.

This report has been reproduced directly from the best available copy.

Available to DOE and DOE contractors from the Office of Scientific and Technical Information, P.O. Box 62, Oak Ridge, TN 37831; prices available from (615) 576-8401.

Available to the public from the National Technical Information Service, U.S. Department of Commerce, 5285 Port Royal Rd., Springfield VA 22161

Dynamic Enhanced Recovery Technologies
Class I
Part I

By
Roger N. Anderson

Work Performed Under Contract No. DE-FC22-93BC14961

Prepared for
U.S. Department of Energy
Assistant Secretary for Fossil Energy

Chandra Nautiyal, Technology Manager
National Petroleum Technology Office
P.O. Box 3628
Tulsa, OK 74101

Prepared by:
Columbia University
New York, NY 10021

Executive Summary

Task One - Management Start-Up Roger N. Anderson - Task Manager

OBJECTIVE:

The purpose of this task was to equip the project with staff and resources (computer and otherwise) to accomplish the other 6 tasks of this project; to negotiate contracts with several industry and university subcontractors to achieve the task objectives; and to initiate the technology transfer to industry and the public from the very beginning of this project.

SUMMARY:

This task was completed in Phase I of our project. Technology Transfer will be discussed in the Task 7 report.

Task Two - Database Management Roger N. Anderson - Task Manager

OBJECTIVE:

The objectives of this task were to accumulate, archive, and disseminate the geological information available within the area of research of this project; networked database creation, generation of new seismic interpretation with high-tech software, and real-time visualization of the on-line database.

SUMMARY:

2.1 Fluid-Flow Monitoring Using Industry Multiple 3-D Seismic Data Sets: This has been one of the outstanding new discoveries of the project. We have developed and submitted a patent for 4D seismic processing software that can recognize amplitude and impedance changes caused by the addition and subtraction of oil and gas from reservoirs over time intervals as short as a few years. The technique has been developed using the 1992 Shell/Exxon data set (received December 1994) with the two previously acquired 3-D seismic surveys, the Texaco/Chevron data set (acquired in 1988) and the Pennzoil et al data set (acquired in 1985). This DOE project is one of the first Case Histories of 4D seismic reservoir monitoring in the oil industry, and as such, has received industry-wide interest.

Liqing Xu developed the LDEO 4D Software as a set of AVS modules that are networked to form a 4-D package library. He has written, modified, debugged and mounted more than 100,000 lines of C code that form the AVS modules making up the code. Liqing also worked out the 4-D imaging and visualization requirements, and has completed a new 4-D software homepage that was demonstrated at the SEG convention in Houston in October, 1995. ~~The description of the 13 major "chapters" that makes up the code follows.~~

LDEO 4D Software is copyrighted by Columbia University in the City of New York(CU), and ownership remains with CU, for whom a United States Letters Patent is pending.

Task Three - Field Demonstration Experiment

Roger N. Anderson - Task Manager

OBJECTIVE:

The objective of task three was to drill one well extension to test the Dynamic Enhanced Recovery Technologies objectives of this project. In November and December, 1993, we drilled into the fault zone in Eugene Island Block 330 (A20-ST) and performed the following experiments: whole coring, wireline logging, sidewall coring, formation pressure tests, stress tests, completion with frac-pack, flow test, and pressure transient test.

SUMMARY:

3.1 Environmental Assessment: Sub-task 3.1 is completed and was discussed in 10/15/93 technical quarterly report.

3.2 Field Demonstration Well: Sub-task 3.2 is completed and was discussed in 1/15/94 technical quarterly report. Technology transfer of the field demonstration experiment data and results are discussed in Task 7 of this report. The declination of the Columbia funding supplement request by the Pittsburg office has caused Pennzoil and partners to absorb the added expenses of the Pathfinder well tests, because the contract was represented as a "Cost-Reimbursement" contract by DOE, and because the actual costs of the Field Demonstration Experiment were within 3 % of the budgeted estimate, the oil companies were expecting DOE to pay the overage. The declination has resulted in Pennzoil writing explicitly in the contract for continued support of the 4-D seismic monitoring Joint Industry Consortium that no Federal funds will be sought in the future by the consortium.

3.3 Interpretation of Results of Well Experiments: The A-20ST "Pathfinder" well was drilled by Pennzoil Exploration and Production Co., on behalf of partners Exxon, Mobil and Cockrell, into the OI-4 reservoir just above the "Red" growth fault zone that forms the northern boundary of the Eugene Island 330 minibasin. The well was then extended across the fault zone and into the footwall with DOE funding. The GBRN Field Demonstration Project consisted of three phases: whole coring, extensive logging, and stress and production testing in the Pathfinder extension. Measurements were made to determine in-situ conditions within and surrounding the fault zone and to test the hypothesis that hydrocarbons could be produced from a fault zone.

We found and sampled oil and gas from silty shales within the fault zone and discovered that the oils have similar chemistry to those being produced from the reservoirs directly above the fault zone. Whole coring revealed that faulting and fracturing extended at least 350 feet into the shales of the upthrown block. Many of the faults and fractures contained oil. Hydrocarbons would not flow at economically viable rates during drill-stem tests. The larger the drawdown pressure applied across the perforations, the lower the permeability of the fault zone became.

Where the A-20ST crossed the fault zone, the horizontal closure stress was found to be 500 psi greater than the fluid pressure. An increase in the pore pressure of 500 psi was then found to induce significant permeability within the fault zone.

A related well, the A-10ST, was drilled into the fault zone in EI 330 in October, 1993, in anticipation of the Pathfinder well, completely with industry funds. In contrast to the "tight" fault encountered in the Pathfinder well, fluids flowed strongly when the fault zone was penetrated by the shallower A-10ST well. Fluid flow within the high-pressured fault zone was sufficient to cause differential sticking and the loss of two bottom-hole assemblies in the well. A pulsed-neutron, Thermal Decay Time log run through the stuck drillpipe recorded increased gamma ray radiation from oxygen activation indicating that water was flowing at rates of up to 700 barrels/day within the fault zone.

Task Four - Reservoir Characterization **Peter Flemings - Task Manager**

OBJECTIVE:

The purpose of this task was to integrate the geological and geophysical data to construct the minibasin and reservoir models in the SEI 330 Area in order to understand the hydrodynamics of the minibasins. The minibasins are analyzed through stratigraphic interpretation, salt analysis, pressure and temperature mapping. Temporal seismic amplitude analysis is to monitor the dynamic changes occurred in the reservoir.

SUMMARY:

This is the second and final annual report summarizing the completed research in the Reservoir Characterization Task. Detailed results are presented in Attachments 1 through 3. ~~A summary of accomplishments is discussed below.~~

~~An outline of the individual tasks are provided below.~~ Primary responsibility for tasks are shown in parentheses: PSU = Penn State University, CU = University of Colorado- Boulder, LDEO = Lamont-Doherty Earth Observatory. Completed tasks are indicated by a pound sign (#).

<u>Task #</u>	<u>Name</u>	<u>Start</u>	<u>Finish</u>	<u>Status</u>
Task 4:	Reservoir Characterization	10/92	10/95	#
4.1:	Stratigraphic Interpretation			
4.1.1:	16 Block 2-D Analysis (PSU)	10/92	4/94	#
4.1.2:	4 Block 3-D Analysis (PSU)	10/92	11/94	#
4.1.3:	North-South Transects (CU)	10/92	5/94	#
4.2:	Salt Analysis and Paleogeographic Reconstruction			
4.2.1:	North-South Transects (CU & PSU)	10/92	3/94	#
4.2.2:	16 Block 3-D Restoration (CU)	10/92	12/95	
4.3:	Fluid Potential Analysis			
4.3.1:	Fault Plane Mapping (PSU)	10/92	1/95	#
4.3.2:	Structure Maps (PSU)	10/92	10/94	#
4.3.3:	3-D Permeability Pathways (PSU)	8/94	10/95	#
4.3.4:	Pressure Mapping (PSU)	10/92	6/94	#
4.3.5:	Temperature Mapping (G. Guerin, LDEO)			#
4.4:	Amplitude Mapping Analysis (R. Anderson, LDEO)			#

Through the final year of the project we continued to acquire important data for the 330 field. These included: 1) complete wire- line data for Blocks 338 and 339 (donated by Texaco), 2) fracture completion data, and leak off data for Blocks 330, 338, and 339, and 3) the entire 316 A-12 core (now housed in the Penn State Core Repository) which was

recently drilled by Pennzoil. Throughout the year, Beth Bishop and Amanda Shaw have continually updated the Landmark Openworks project and distributed data to all of our colleagues in this DOE-funded project.

Task Five - Modeling **Larry Cathles - Task Manager**

OBJECTIVE:

The objectives of the modeling task as set forth in the DOE proposal funded 3 years ago were to address:

- the cause of pressure, temperature, fluid chemical, and porosity anomalies near the Red Fault,
- the possible sources of oil and gas moving up the fault, and
- the causes of organic and inorganic chemical alteration near the fault.

This was to be done realistically and with the aim of facilitating the interpretation of data collected in the study area. Particular attention was to be focused on: (1) porosity and excess pressure development in the RVE, (2) hydrocarbon maturation in the RVE, (3) detailed fluid flow near the fault focusing on the detailed distribution of high permeability sands, (4) the effects of salt diapirism on subsurface temperatures, (5) the effects of fault movement on fault permeability and fluid venting out of the fault, (6) the effects of gas venting on oil migration, (7) the transport of oil as a separate phase up the fault, and (8) the effects of fluid flow (water, gas, and oil) on rock chemistry and mineralogy. The modeling was to be carried out in 3D as well as 2D.

No computer software existed that was adequate to these tasks. To even attempt to interpret specific geologic data, the models needed to couple disparate phenomena such as faulting, salt diapirism, sealing and overpressure development, temperature and fluid flow, and needed to do so realistically- specifically for the configuration of faults and salt domes in the South Eugene Island Block 330 area and in three dimensions. To fill these needs we have, in collaboration with a finite element modeling company, the Computational Mechanics Corp. of Knoxville, Tennessee, developed a basin modeling system capable of investigating the highly coupled phenomena associated with hydrocarbon migration up the Red Fault of the South Eugene Island Minibasin, and applied that modeling system to the geologic data collected under other tasks of the DOE project.

The AKCESS.BASIN Modeling System we developed and applied to the SEI Block 330 region is described in full in this final report. Because there is a great deal of material to report, the report is organized hierarchically: Section II gives an executive summary of the principle accomplishments of Modeling Task 5. Section III reviews the plans and performance in each sub-task. References are given there to the detailed reports given in the various subsections of Sections IV. In this way it is hoped that an interested reader can both rapidly obtain an overview of what has been done and also rapidly find parts of the work of specific interest.

It is probably natural that not all of the work proposed has been accomplished in exactly the fashion proposed three years ago. Preparation of the geologic data in a fashion that takes account of diapirism, overpressuring, and faulting in three dimensions, proved far more difficult and time consuming than we had anticipated. Substantial effort was also devoted

to developing algorithms that accurately describe critical parameters such as thermal conductivity and permeability in the data cube. However some areas proceeded far better than originally envisioned, and many new results have been obtained. All the important principal subtasks will be fully accomplished by the time the students involved in this project complete their Ph.D. theses. Furthermore, a powerful modeling capability has been created that is supported by a private company and a growing group of academics spread over five separate institutions. This is certain to impact basin studies for years to come.

SUMMARY:

The principal accomplishments to date under this proposal and the matching projects it encompasses are:

1. Development of a 3D finite element basin modeling system with sound and fully articulated fundamentals (Section I) and accurate algorithms for thermal conductivity and sand permeability, that provides for easy input of highly detailed three dimensional geologic data with options to infer salt diapirism from the surface pattern of sedimentation and sea level (Section II), takes into account all major physical and chemical phenomena (e.g., isostasy, salt diapirism, faulting, overpressuring, seals, hydrocarbon maturation, fluid flow driven by haline or thermal convection, water table topography, or overpressuring, salt dissolution and transport, etc.), solves the coupled equations with an easy to use but versatile and controllable finite element solver which can execute rapidly on parallel machines (Section III), and has convenient and easy to use visualization tools at all stages (Section II, III, V).
2. Distribution of that modeling system across 5 institutions (Cornell, LSU, Michigan Tech., and Bowling Green) with appropriate training of professionals and students at each.
3. Extensive benchmarking demonstrate the validity of various aspects of the modeling system (Section IV).
4. Application of the Modeling System to eight ~100 km long 2D seismic lines centered on the South Eugene Island Block 330 area of the Gulf of Mexico and one 1200 km interpreted N-S section. The modeling shows that the flexural rigidity of the Gulf lithosphere is less than about 10^{23} M-m. The history of salt movement over the last 20 Ma inferred directly from sedimentation shows evolution from a salt sheet to multiple minibasins and domes. The domes have a major impact on subsurface temperature ($\pm 70^\circ\text{C}$ temperature anomalies above and below the salt domes). (Section II and V.)
5. Construction of highly detailed 3D data cube in the SEI 330 area resolving all principal sands and their displacement across four NE-SW faults over the last 3.4 Ma. The salt movement inferred from the pattern of sedimentation shows the burial of a local salt sill and its remobilization into the South Eugene Island Block 330 Minibasin with the Red Fault at its northern margin.
6. Detailed analysis of bottom hole temperature data shows a positive temperature anomaly of about 5°C below the Pennzoil oil and gas fields roughly along the Red Fault and a negative (-5°C) temperature anomaly above the oil reservoirs. Modeling shows that temperature anomalies of this magnitude or greater will be produced by the insulating hydrocarbon-filled sand reservoirs. Fluid flow could produce the positive anomaly below the reservoirs along the Red Fault, but not the negative anomaly above the reservoirs. This suggests that the present day temperature field in the South Eugene Island Block 330 minibasin is due to thermal conductivity anomalies associated with hydrocarbon reservoirs and not rapid fluid flow (Section V).

migration, such as evaporative fractionation and biodegradation. Gas is characterized via higher thermal maturity than oil, suggesting that the oil is "swept up" by vertically migrating gas. Brine composition, specifically ^{129}I and $^{87}\text{Sr}/^{86}\text{Sr}$, supports the interpretation of large-scale vertical migration of fluid into the reservoirs. Systematic variations in major elements, specifically chlorine, (composition of brine between reservoirs) indicate that brine entered the reservoirs at different times and/or from different directions.

⊖ A variety of data support ongoing filling of the GA sand via rapid injection, and high fluid flux in the fault zone in the past. Repeated sampling of wells over a period of 10 years has led to the finding that unbiodegraded oils are injected into the GA sand on the time scale of years or less. Biodegradation occurs rapidly there, and the presence of unaltered oil is interpreted to reflect rapid influx from depths at which biodegradation does not take place. A variety of other organic geochemical data corroborate this conclusion. In the A6ST well, which penetrates the main growth fault a point 1000 feet from the fault intercept in the Pathfinder well, sediments from within the growth fault are characterized by anomalously high vitrinite reflectances relative to sediments outside the fault, indicating that the fault is locally a paleothermal anomaly. Combined with stable isotopic composition of minerals from the fault in that well, these data support the conclusion that the fault, at least at some locations, acted as a conduit of relatively high-temperature fluids.

✓ The Pathfinder core contains three structurally - distinct fault domains, only the deepest of which contains oil. Based on structural and geologic data, this deepest domain is concluded to have been most recently active. Structural and geochemical data indicate the other two fault domains were active prior to oil migration. The oil-barren domains contain fractures that are favorably oriented to transmit oil, and oil is furthermore present in sands in these domains; it is evident that fault zone oil migration took place only within that part of the fault that was active during the time migratable oil was available to the fault. Despite the variability of hydrogeologic characteristics of faults as evident in the core, the geochemical data indicate that none of these cored faults transmitted significant amounts of fluid in the Pathfinder well, indicating the operation of a higher-order control on fluid flow in the growth fault. The same fault in the A6ST well has apparently acted as a fluid conduit, indicating relatively short-range lateral variability in fluid flow behavior in the fault.

Task Seven - Technology Transfer

Roger N. Anderson - Task Manager

OBJECTIVE:

The purpose of this task was to integrate all results into one comprehensive perspective of the project's objectives and to transfer the results to industry. This will involve the interactions between the various project task outputs and the transfer and dissemination of the major conclusions of the study. There were two main efforts related to technology transfer in the field demonstration project. First, we made special efforts to patent and license technology developed as part of this project so that it would become commercially available to the oil industry. Second, we commissioned a study using the United States Geological Survey's fractal oil and gas reserves techniques to identify whether we were dealing with an additional source of oil and gas in the Eugene Island 330 field's recharge-along-faults.

SUMMARY:

The DOE field Demonstration Project "Dynamic Enhanced Recovery technologies" has been a resounding success by any gauge. It has spawned important new technologies such as 4D Seismic Monitoring, resulted in the placement of successful new wells to drain new and bypassed oil and gas in one of the most prolific oil fields in the U.S. Offshore, grown into industry-only funding consortia for all its major tasks, and promoted Internet collaboration across institutional boundaries at a time before Internet was such a household word. In addition, there is every prospect that the U.S. Treasury will be repaid many times over for the direct investment of funds into the future of the oil industry in America.

Task One - Management Start-Up

Roger N. Anderson - Task Manager

OBJECTIVE:

The purpose of this task was to equip the project with staff and resources (computer and otherwise) to accomplish the other 6 tasks of this project; to negotiate contracts with several industry and university subcontractors to achieve the task objectives; and to initiate the technology transfer to industry and the public from the very beginning of this project.

SUMMARY:

This task was completed in Phase I of our project. Technology Transfer will be discussed in the Task 7 report.

Task Two - Database Management

Roger N. Anderson - Task Manager

OBJECTIVE:

The objectives of this task were to accumulate, archive, and disseminate the geological information available within the area of research of this project; networked database creation, generation of new seismic interpretation with high-tech software, and real-time visualization of the on-line database.

SUMMARY:

2.1 Fluid-Flow Monitoring Using Industry Multiple 3-D Seismic Data Sets: This has been one of the outstanding new discoveries of the project. We have developed and submitted a patent for 4D seismic processing software that can recognize amplitude and impedance changes caused by the addition and subtraction of oil and gas from reservoirs over time intervals as short as a few years. The technique has been developed using the 1992 Shell/Exxon data set (received December 1994) with the two previously acquired 3-D seismic surveys, the Texaco/Chevron data set (acquired in 1988) and the Pennzoil et al data set (acquired in 1985). This DOE project is one of the first Case Histories of 4D seismic reservoir monitoring in the oil industry, and as such, has received industry-wide interest.

Liqing Xu developed the LDEO 4D Software as a set of AVS modules that are networked to form a 4-D package library. He has written, modified, debugged and mounted more than 100,000 lines of C code that form the AVS modules making up the code. Liqing also worked out the 4-D imaging and visualization requirements, and has completed a new 4-D software homepage that was demonstrated at the SEG convention in Houston in October, 1995. The description of the 13 major "chapters" that makes up the code follows.

LDEO 4D Software is copyrighted by Columbia University in the City of New York(CU), and ownership remains with CU, for whom a United States Letters Patent is pending.

Introduction

LDEO 4D Software was developed at Lamont-Doherty Earth Observatory of Columbia University in the City of New York. Software implementation started in 1994. It was initiated within the DOE Class I Oils Field Demonstration Project "Enhanced Dynamic Recovery Technologies" of the Global Basin Research Network(GBRN) which is headed by Dr. Roger N Anderson. LDEO 4D software was written by

HREF="mailto:liqing.ldeo.columbia.edu">Liqing Xu with design input from Wei He and Albert Boulanger.

LDEO 4D Software has applications to the interpretation of time-dependent changes in multiple 3D seismic surveys acquired over the same subsurface volume at

different times to monitor the changes in impedance caused by drainage and migration of hydrocarbons and other subsurface fluids, for which a United States Letters Patent is pending. LDEO 4D Software also has modules for seismic data processing, image processing, data interpretation and data visualization in 2D and 3D. It is built on top of [Advanced Visual Systems](http://www.avis.com) (AVS), which provides the modular programming environment and basic modules for image display and 3D rendering. The LDEO 4D software currently contains more than 100,000 lines of C code in the form of 110 AVS modules which cover seismic data input, well log analysis, and horizon data input into AVS. Modules are provided for 4D seismic data interpretation, horizon extraction and interpretation, volume processing and imaging which form the backbone of the LDEO 4D software. Because LDEO 4D Software is built on top of AVS, users can dynamically connect our software modules to create 4D seismic analysis networks. Each module is small and specifically designed to accomplish one task within the 4D analysis framework. The LDEO 4D Software divides major applications into groups of AVS modules which can be either independently executed in stages, or networked together to perform "batch" analyses of 4D Seismic datasets.

The major purpose of the LDEO 4D Software is to provide a "Quick Look" tool to track changes of seismic amplitude and impedance over the time as hydrocarbon pool drainage proceeds. The LDEO 4D software modules are designed to extract differences and similarities among multiple generations of 3D seismic surveys (4D seismic data). LDEO 4D Software provides a methodology whereby hydrocarbon migration and drainage pathways and reservoir fluid locations and volumes can be mapped over time.

The LDEO 4D Software provides all required data processing functions for 4D analysis, such as amplitude and frequency spectral normalization, seismic attribute computation, and a rich set of data filters. The processing flow of the LDEO 4D Software proceeds from the rebinning and pre-processing of multiple 3D seismic data, to procedures for amplitude and frequency normalization, cross-correlated to minimize spatial shift and navigation errors. Then each seismic dataset is converted to the seismic attribute domain, and reflection strength, or the amplitude envelope of the seismic signal, is computed for each waveform. The individual 3D seismic datasets are then region grown about seed points of the highest amplitudes within each seismic dataset to obtain volumetric representations of the hydrocarbon reservoirs. Then, differencing and similarity techniques are applied to the region-grown volumes. Another important part of the LDEO 4D Software is visualization capabilities to display and recognize the dim-outs, amplitude brightening and sustained amplitude regions that delineate drainage, water encroachment, gas cap formation, and most importantly, locations of bypassed pay. LDEO 4D software provides a rich set of visualization modules such as slicing (orthogonal and arbitrary slicing), volumetric rendering of reservoirs, seismic and well log visualization along wellpaths (regardless of deviation), multiple horizon slicing, amplitude extraction, horizon visualization, skeleton building, migration pathway manifold and 2D particle flow simulation. All visualization is implemented in real 3D space, but since we image only within grown regions, the datasets have been intelligently downsized for rapid manipulation with standard workstation graphics capabilities. Also, LDEO 4D Software provides an added set of utility modules to generate print-ready and Internet mountable html output easily.

LDEO 4D Software contains five basic operations: data loading, data pre-processing, data interpretation, 4D differencing, and visualization. In this instructional Home Page, we explain these 5 operations within 12 chapters, which provide the complete procedures to fully analyse multiple 3D seismic datasets for 4D drainage and fluid migration changes.

Chapter 1: Data Loading

Before going into the details of data loading, we introduce our project description file format, which is an ASCII file that contains the details of each 3D seismic dataset.

#The following is the project description file

#for the project "Shell" for the 4D school, 1/10/1996">

#created Tue Dec 12 16:18:21 1995

#by Liqing Xu

Project "Shell"

line 4200 to 5200 interval 5

trace 680 to 280 interval -3

time 1700.000000 to 2300.000000 interval 4.000000

nlines 201

ntraces 134

nsamples 151

crop information

xoffset 0

yoffset 0

zoffset 0

survey border corner coordinates

LL 1874329.3750000 -162082.8906250

LR 1884310.6250000 -162082.7656250

UR 1884309.8750000 -152076.7968750

UL 1874329.3750000 -152077.0312500

rotation 0.000718

dx 75.042290

dy 50.029842

dz 4.000000

matrix to transfer real world to index

0.0133258 0.0000002 0.0000000 -24976.9492188

-0.0000003 0.0199881 0.0000000 3240.1931152

0.0000000 0.0000000 0.2500000 0.0000000

0.0000000 0.0000000 0.0000000 1.0000000

matrix to transfer index to real world

75.0422897 -0.0006265 0.0000000 1874329.3750000

0.0009398 50.0298424 0.0000000 -162082.8906250

0.0000000 0.0000000 4.0000000 0.0000000

0.0000000 0.0000000 0.0000000 1.0000000

north arrow start and end (x, y) in index coordinate system

start 107.1999969 160.8000031 end 107.2002487 180.8999939

north arrow start and end (x, y) in real coordinate system

start 1882313.7500000 -154078.0156250 end 1882313.7500000 -
153077.4218750

Such a project description file is created for each 3D seismic dataset to be analysed.

The LDEO 4D Software uses multiple time-lapsed 3D seismic surveys to track changes of seismic amplitude and impedance over time with as pool drainage proceeds. Before comparing different 3D seismic datasets, however, we must make sure all 3D surveys are rebinned into the same grid. This is done by geometrically transforming the grids of older surveys to the common grid of the newest survey, because it generally is the finest mesh with the best navigational accuracy. Details on how we do this will be discussed in next chapter -- Data Orientation.

An additional note before we begin with the procedures for loading SEG-Y 3D seismic datasets. We visualize seismic data and well log data together, and well path geometry is usually defined in real world coordinate system (UTM), but seismic data is defined in an indexed coordinate system. In order to visualize well data with the seismic data, we convert UTM to index coordinates, (i, j, k) to (x, y, z). These operations require information about the transformation matrix, which can be computed from the survey grid information. Here we assume each 3D survey covers a rectangular area which is easily defined by 4 corners (lower left, lower right, upper left and upper right), also line numbers are assumed to increase or decrease along the Y direction and trace numbers are assumed to increase or decrease along the X direction. This definitely will introduce some confusion when lines are actually along the X direction (we are going to change this soon).

For the LDEO 4D Software, each dataset should have a unique project description file in which dimensions must be consistent with the total number of lines, traces and samples. The Project Description File contains several parts, beginning with comments, which describe when and who constructed the file. Next are line, trace and time specifications, line number ranges (in the example, from 4200 to 5200) with line number interval (5), trace number ranges (from 680 to 280), the trace number interval (-3), and time range (1700 to 2300 ms) at what sampling interval (4 ms). Total number of lines (201), total number of traces (134) and total number of samples (151) are next. Next is "cropping information" to specify if this is a cropped volume from a bigger seismic volume, and if it is, what are the offset dimensions. Then we see (x, y) coordinates of the 4 corners of the cropped survey grid starting from the lower left corner and ending at the upper right corner. After survey corner coordinates comes the rotation angle, which is the angle between the East and the bottom of the grid in the X direction -- positive indicates the grid rotates to the North and negative indicates rotation to the South, dx, dy and dz are trace intervals, line intervals and time sampling intervals after rotation of the bottom of the survey grid.

The most important information in the file are two matrices, one is the matrix to transform from real world (x, y) to the index coordinates (i, j) of the seismic survey, and the other is the matrix to transform the index (i, j) to the real world coordinates (x, y). <P>The last part of this file is the vector of the NORTH arrow for index coordinate and real world coordinate systems, which will be placed within all volume visualizations to orient the viewer.

The project description file is used heavily by many of the LDEO 4D Software modules, such as seismic orientation, real world to index, . There are several ways to construct the project description file, LDEO 4D Software provides 3 separate modules to do this depending upon the form of the 3D seismic survey being entered.

First, there is the project description which provides a fill-in-the-blanks template; second, is the subproject desc create which provides a convenient way to construct the project file for cropped volumes of bigger datasets; and third, is the data loader module described in the next section. For all of these modules, survey corner coordinates (x, y) are the most important information that must be correctly entered. Also, line, trace, and time parameters must be entered correctly.

LDEO 4D Software is built to deal with any of the various forms of SEG-Y or SEG-D 3D seismic data, as well as well log and horizon data imported from Landmark Graphics systems. LDEO 4D Software provides a module called "data loader" which will load SEG-Y data, AVS formatted data, SpreadSheet (data stream: no header, just seismic traces), LDEO 4D formatted data (which is an AVS field format but some information about data is encoded in the header comment of the field).

The "data loader" is a module which will construct an AVS network automatically, so the module only needs to be dragged from the module library to the working space. Figure 1 shows the network after loading the "data loader" module.<P ALIGN=

<H3 ALIGN="CENTER">Fig. 1 AVS network of data loader and interface</H3><P>

From Figure 1, we can see the "data loader" constructs an AVS network which has attached modules "generate colormap", "data loader", "graph viewer" and image viewer". Most of the parameters are controlled by the pull down menu. From the panel "AVS Data Loader", we can see seven menu items: "File" provides functions such as "open a file", "save a file", "save data" to the a new file, and "Save Desc" which saves the project description to a file. From "Format", we can see 5 data formats are supported. They are SEG-Y, SEG-D (not yet implemented, 1/96), SpreadSheet, AVS field and LDEO 4D format.

<P>"Input Type" specifies the data type of the input data, but this selection is only for SpreadSheet formatted file input. "Output Type" specifies which data type is for the output, usually this is left to the module to decide. Also "data loader" module provides a set of mathematical operations that can be applied to the input data, such as adding/subtracting a constant, multiplying/dividing the input data by a constant, obtaining the absolute value of each input data value, square rooting each input data value, flipping data sign, clipping data to a specified dynamic range, thresholding the input data, normalizaing the input data, cropping the data, and downsizing the data volume.

<P> Input data can be viewed in several forms to varify a good load: in orthogonal slices inline, crossline or as timeslices, in single trace display, and as a histogram display of the input data. The "Input setup" button will popup a panel of parameters which are ensential for the project description file. The "data loader" module has parameter blanks such as "Lower Left XY", "Lower Right XY", "Upper Left XY" and "Upper Right XY" specifying (x, y) coordinates of the 4 corners of the survey grid. </P>

<P>

When the input data is in SEG-Y format, LDEO 4D format or AVS field format, you usually don't have to worry about the parameters dim1, dim2, dim3, time, trace or line, except you may want to change the line, trace and time setup. dim1 is desingated as the dimension of the input dataset which is changing fastest, dim2 is the second dimension of the input data set which is changing second fastest, and the dim3 is the third dimension of the input dataset which is changing slowest. When dim1, dim2 or dim3 are pushed, you have select corresponding line, trace or time for this dimension. Line indicates this dimension is the line direction, trace indicates trace direction of the input and time is the time direction the input. For example, with the input data for SpreadSheet (which is a data stream), a sequence of traces are contained in this file, so time is changing fastest, it is dim1. Then you specify the time parameter, say 0, 3000, 4, which are specifying

minimum time (0), maximum time (3000), and the time interval (4) in milliseconds. "dim2" will be the trace, so you specify trace parameters, say (1000, 3000, 5) and dim3 is line, which is changing slowest, so you specify line parameters (say 15000, 10000, -5).

</P>

<P>

For SEG-Y formatted data, if you don't specify line, trace and time parameters, then the program will scan the input file and find how many traces exist for each line, and how many samples are present for each trace. You then have to tell the program those bytes in the trace header used for the trace number. Also, you can read only part of the data by specifying the line, trace and time parameters. For SEG-Y data, these parameters are quartile numbers, for example line (1000 2000 3000 10), says read lines from 2000 to 3000 at a line number interval of 10, but ignore lines from 1000 to 2000. For trace and time you can define partial data in this way too.</P>

<P>

For SpreadSheet format, dim1 is again the dimension 1 of the input data which is changing fastest, dim2 is the dimension 2 of the input data which is changing second fastest, dim3 is the dimension 3 of the input data is changing slowest. Time, trace or line are typed in a string of triple or quartile numbers separated by spaces. Say time (0.0 3000.0 4.0) which indicates the input dataset starts from 0 sec and ends at 3 sec with sampling interval 4 ms. </P>

<P>

For AVS formatted data, all dimension information is already encoded in the header of the input (field description part), so line, trace and time parameter specification are only for the project description file.</P>

<P>

For LDEO 4D formatted data, the project description is already encoded in the comment part of the header, and you don't have to provide any information for reading, except if you want to change the line, trace and time setup.</P>

<P>SEG-Y formatted data can be from disk file or tape, but other formatted inputs must be disk files.</P>

<P>Here, we give an example of data loading. In this example, we read an AVS 3D uniform byte field. All input setups for the survey grid, the histogram of the input, and one of the time slices of the input data are shown.</P>

<P ALIGN=CENTER></P>

<H3 ALIGN="CENTER">Fig. 2 Result of an example data loading and parameter setup</H3><p></P>

Chapter 2: Data Orientation</H1>

<P>Chapter 1 covered the loading of multiple 3D surveys successfully into AVS, i.e. converting whatever input format into the AVS field formatted files. Right now most of the LDEO 4D Software modules only accept AVS field formatted data, so all input 3D seismic datasets must be converted to the AVS field file. In addition, project description files must be generated for each 3D surveys.

<P>Before doing any further intercomparisons, we must now rebin all 3D surveys to the same grid, i.e. all must have the same line and trace configuration. One survey is chosen to be the target grid (usually the most modern), and all other grids are converted to this grid orientation and spacing. Seismic rebinning (orientation) involves two steps: first, there is a geometric transformation, then an interpolation to calculate new traces at the grid locations. LDEO 4D Software provides one module to accomplish these two operation: "seismic orientation". The module requires two 3D surveys with project description files for each survey. Figure 3 illustrates the network to do the seismic orientation.</P>

<P ALIGN=CENTER></P>

<H3 ALIGN="CENTER">Figure 3 AVS network for 3D seismic orientation</H3><p></P>

From Figure 3, we can see two file browsers for project description selection. The top one is the parameter "source project desc file" which is the project description file for the field to be converted. The bottom one is the "destination project desc file" which defines the destination grid. The rightmost port on the "seismic orientation" module icon is the destination seismic (first input) --which is not going to be changed. The leftmost port is the seismic data (second input) which is going to be reorientated to the destination survey grid. The "seismic orientation" module outputs two AVS fields: the rightmost output port is the output of overlapped regions of the two surveys, it may be the same as the first input or not depending upon the geographic coverage of the two surveys. The leftmost output is the orientated version of the second input which now has the same dimensions in X and Y as the first input.

<P>But the third dimension (time) could be different between the two surveys (e.g. minimum phase versus zero phase). We will discuss corrections to time in the next chapter.

<P>Also, you can see that there are another 4 parameters in the network, called "mirror src X", "mirror src Y", "mirror dst X", "mirror dst Y". These parameters are used when the index coordinate direction is opposite to the real world coordinate. For example, assume index i of the destination field is increasing from right to left. Then you must "turn on" "mirror dst X" in order to insure consistency of the orientation. For the real world coordinate system, X is always increasing from left to right, and Y is always increasing from south to north.

<P>All geometric transformation is based on an index of (0, 0, 0), which is the lower left corner of the survey grid. (dim0-1, 0, 0) is the lower right corner of the survey, (dim0-1, dim1-1, 0) is the upper left corner and (0, dim1-1, 0) is the upper right corner of the survey grid. Here "dim0" is the field dim0 in the input AVS field file, "dim1" is the field dim1 in the input AVS field file. </P>

<P>Interpolation is implemented by an "area weighting" algorithm. This is illustrated in Figure 4. </P>

<P ALIGN="CENTER"></P>

<H3 ALIGN="CENTER">Figure 4 Seismic interpolation method in orientation</H3><p></P>

<P>In Figure 4, four green spheres represent 4 grid points in the source grid, the red sphere is the destination grid point position. The 4 grid points construct a rectangular cell which is already geometrically rotated and transformed, two red lines through the red sphere divide the cell into 4 subareas, each of them has an area, named A1, A2, A3, A4. These are computed directly from the real world coordinates of the 4 grid points and (x, y, z) of the red sphere. The interpolated data value at the red sphere position will be $A4 * val(i, j, k) + A1 * val(i+1, j+1, k) + A3 * val(i+1, j, k) + A2 * val(i, j+1, k)$. </P>

<P>In Figure 4, there are three time slices shown: the leftmost one is the original destination field, the second one is the oriented data, and the third one is the original unorientated data. You can see that after orientation, features corresponds very well now. </P>

Chapter 3: Data View</H1>

<P>Data visualization is a very important part of being able to interpret changes in seismic attributes over time, and so the LDEO 4D Software contains many critical visualization components. AVS provides many modules with which we visualize seismic data. 3D seismic data can be visualized in orthogonal slices, arbitrary slices, multiple slices. Horizons can be displayed along with "zapping" of amplitudes along any of those surfaces

<P>Volumetric visualizations include traditional isosurfacing, volumetric rendering of region-grown reservoirs, migration pathway, skeletons, or "manifolds" of 2D or 3D

data, wiggle plots of seismic traces, well path displays in 3D, well log data displays in 3D, etc.

LDEO 4D Software also provides a rich set of utility modules to draw bounding boxes of geometric objects, draw 3D axes, annotate, 3D vector label, add general labeling, line drawing, position marking, north arrow, etc. In the following, we present a set of networks to do various kinds of visualization.




Figure 5: AVS network to visualize seismic data in orthogonal slices

In Figure 5, we read in two 3D seismic datasets, output them to the AVS "orthogonal slicer" module, and use the module "integer" to control which slice to select. Then output from the "orthogonal slicer" passes to the "seismic viewer" module which convert each data value into an AVS color representation (A, R, G, B). This is then fed into "image viewer" to visualize the product. You can easily change "orthogonal slicer" into "arbitrary slicer" to do slicing in an arbitrary direction. However, "integer" must be replaced by the module "float".

Figure 6 gives an example network to do volumetric visualization of the region-grown dataset. The module "res builder" which constructs outermost surfaces of reservoirs. We can see that surfaces constructed by the module "res builder" are different from the AVS module "isosurface", which creates polygonal models of constant value surfaces from 3D data. For region-grown data, values on the surface are not constant, and the surface reflects this fact when each vertex is colorized. The modules "mirror" and "crop" are optional here. The module "res builder" can be replaced by the AVS "isosurface" module.



Figure 6: AVS network to visualize seismic data in volumetric surfaces

Another way to visualize the seismic data is arbitrary slicing into the volume. The slice plane can be either an interpreted horizon or an arbitrary planar slice. We present a way to map data onto an arbitrary plane. Figure 7 is an example network and Figure 8 is the resulting image. Horizon files usually are multiple column ASCII files such as

X	Y	Z1	Z2	Z3
1876540.0	-157634.56	1200.0	1400.0	1800.0

.....

here X and Y are real world coordinates of a picked point. Z1, Z2, Z3 ... are two way travel times in ms. The horizon file will include all trace positions, but when no valid value is picked for a position, then Z will be a default value like -999, specifying this point is not an valid point. The horizon file can be easily read into AVS by "read field" module. After reading the horizon file in, the module "extract horizon" will pick any horizon in the input horizon file and feed this horizon as a sequence of (x, y, t) to the "real world to index" module to do the conversion from the real world (x, y, t) to the index (i, j, k) coordinate system. Then, the converted horizon feeds to "curver slicer" which will extract data from the volume along the horizon points, then output from the "curve slicer" will feed to the "point 2 surface" module for surface rendering.



Figure 7: AVS network to visualize horizon mapping



Figure 8: Result from example network of Figure 7

<P>Also, LDEO 4D Software provides several modules to do multiple orthogonal, arbitrary slicing. Also, well log data and well path geometry can be easily integrated into the seismic volume and we can visualize them together. Refer Chapter 12 for details. </P>

Chapter 4: Cross Correlation</H1>

<P>After rebinning all 3D surveys into the same survey grid, the next thing to do is to remove any shifts in time (depth) and space (navigational error) among the surveys. The time differences can have been introduced by static shifts, different depths of receiving cables in the water, different waveform phases used in the processing, etc. Spatial shifts can have been introduced by inaccurate navigation,. If we assume the shifting in time and space is neither locally distributed nor associated with each other, then we can use cross-correlation to minimize the shift between two surveys independently for time and space. </P>

<P>LDEO 4D Software provides one module to remove either shift between two surveys. Correction or shifting is performed on any dimension (i, j or k) of the input dataset. For two 3D seismic surveys, i and j are usually trace and line direction, k is the time direction. Usually, the time shift is corrected first. The "cross correlation" module requires two inputs: the rightmost input is the 3D survey which is not going to be changed, it is used as reference for the second survey which entered through the left-most port of the module icon. Cross-correlation is implemented through a fast Fourier transform, so this module provides several parameters to control the correlation window length and window starting sample point. The default window length is dimensions of either i, j or k depending upon which shifting direction is selected. For example, if the current correction direction is k, then the default correlation window length will be the field "dim2" in the input field description file. The window starting sample point is the first sample in the default selection. Also, the maximum shift can be controlled. For example, if the maximum shift between two surveys in time should be less than 20 ms, then the maximum shift will be 5 samples.</P>

<P>The module provides another parameter "run" which is used to invoke the module execution when you finally have it set exactly as required, because cross-correlation of 3D seismic dataset can be very slow, (depending upon the speed of the cycles available to you). Also, the AVS kernel will invoke the module when any parameter or input to the module is changed, you can get around this by using "Disable Flow Executive" too. Only when "run" is finally turned on, the module will start executing. Also this module has a message window to display the stage of execution of the module. </P>

<P>The second correction is then applied to the output from the first correction. When the shifting direction is k, then the input 2 will be either shifted up or down depending upon the cross-correlation coefficient. When the volume is shifted down 5 samples, then the first 5 samples of the each trace will be replaced by zeros. If the volume is shifted up, the last five samples of each trace will be replaced by repeating the end to the trace.</P>

Chapter 5: Data Interpretation</H1>

<P>Seismic interpretation is an important part of any seismic data processing and analysis package, and so we have constructed these capabilities into the LDEO 4D Software. They provide very useful tools to help users manipulate the very complicated, diversified 4D datasets. Operations available are such standards as horizon autopicking, horizon mapping, fault interpretation, amplitude extraction along a horizon (zapping), well log interpretation, etc. </P>

<P>LDEO 4D Software currently provides all this in one, very sophisticated module "Horizon Dumper" which will provide all the functions an interpreter is familiar with (such as horizon autopicking, mapping, zapping, contouring, contouring on a time

slice, slicing data in line, trace, or time, displaying data in the user picked window in ASCII text, displaying data between any two picked points in graphic form, etc. </P>
<P>The module "Horizon Dumper" is stand-alone module, like the previous "Data Loader" module. It constructs an AVS network inside the graeter program. The user drags needed modules from the library to the workspace, and the correct network will be automatically constructed. Figure 9 is a network constructed by the "Horizon Dumper" module.</P>

<P ALIGN=CENTER></P>

<H3 ALIGN="CENTER">Figure 9: An exemplary network of the module "Horizon Dumper"</H3><p></P>

<P>The "Horizon Dumper" module is menu-driven, and most of operations are in the pull-down menu. From Figure 9, we can see that major menu items are: File, Operations, Select, Display Options, Track Mode, Output Type, Misc Paras.

File item has 6 operations: Open Seismic will load a 3D seismic dataset. Open Horizon will load back the user-interpreted horizon files. Save will save picked horizons to an existing file. Save As will save picked horizons to a new file. New Horizon is for entering a horizon name for the horizon to be picked. Before picking a new horizon, the name must be provided. When the Dump Now is turned on, then a file browser is popped up automatically for you to specify a file to save this horizon to. All horizons picked after the first one will be saved to this file. The Dump Now option will also invoke an autotracking process based on user picked seed points. Only when this option is activated will the horizon will be dumped to the initial file. Otherwise, no saving action will be taken. . When New Horizon is pushed, the module will do a reinitialization, so the previously picked horizons will be lost. However, this module also provides an auto-saving function, so that when a new horizon is picked and dumped, it will save the old horizon as well to the file you specified for the very first horizon picked (a lesson learned the hard way).</P>

<P>The Operations module provides options for major opertaions to be performed on the input seismic data. Horizon Pick indicates the operation performed next will be horizon interpretation. The program will do the iniatialization, memory allocation, etc. , automatically. The Display Data option lets the user pick two points on the image. These two points will construct a rectangular window, and all data inside this window will be displayed into a text browser window. Information such as the dynamic range of the whole dataset, the dynamic range of only that data inside this window, and a list of data in the form (i, j, k, value) will be displayed within this window. The Track option lets the user pick any two points on the image, and all points falls on the straight line connecting the two picked points will be displayed in the form of graph. The Contour option will do contouring of the currently picked horizon or time slice. When it is selected, a geometry viewer window will pop up with some parameters for the user to specify, such as range for contouring, contouring interval, annotation interval, etc. Please refer to the "horizon_dumper.txt" provided for the details. The Zap option will map the data to the picked horizon.</P>

<P>The item Select provides an option for the user to select slicing direction, which can be i, which is dimension 1 of the input data, j, dimension 2 of the input data, or k, dimension 3 of the input data. For horizon interpretation, either i or j must be used -- not the time slice k.</P>

<P>The item Display Options specifies how the input data is to be displayed. It can be Image, Wiggle (not fully developed yet), Color for colorized images, "gray scale" for gray-scale images. Polarity will display images in pure black and white, with all positive data values in black, and all negative data value in white.</P>

<P>The item Track Mode specifies how autotracking is to proceed. Autotracking can track either the zero crossing, the peak or the trough of the wiggle. Either peak or trough will give the best tracking. Usually seed points are planted along continuous seismic events in order to obtain ideal tracking. The default option is autotrack mode. However, the interpreted horizon can be interpolated from seed point to seed point, if necessary. This option is designed for very bad quality data such as where the signal/noise ratio is very low</P>

<P>The item Output Type specifies how the picked horizon is to be dumped.

<P>The item Misc Paras provides miscellaneous parameters. For example, the option Wiggle Paras will pop up another window for you to specify parameters for wiggle plotting, such as every N traces to plot, only one trace, etc. Weight specifies the weight coefficient for smoothing of the picked horizon. The default value is 0, and the range is 0-1. For heavy smoothing, weight must be low (such as 0.25).

Min, Max options are user-defined dynamic ranges for colorizing data. When min is larger than the minimum value of the input data, then all data values lower than "min" will be colorized by the selected color. The same principle is applied to the cases where "max" is less than maximum value of the input data. Combination of the options "Red", "Green" and "Blue" will give color to the tracking line when performing horizon autopicking. The option Window specifies the window length for the autotracking horizon. The Ratio sets up the threshold for the cross-correlation coefficient when performing horizon autotracking. When any cross-correlation coefficient is less than this chosen value, it will result no picking point for that trace. Cross-correlation is performed between the current trace and its immediate adjacent traces. The Width specifies the width of the drawn horizon picking line. </P>

<P>At the bottom of Figure 9, you can see several parameters. Which asks you to specify exactly which slice to display. Forward will simply display the next slice forward. Backward displays the next slice backward. Pick will invoke AVS's image picking routine. Clear Picks will clear all picks on the screen. Show Horizon will tell the program if the loaded horizon is to be displayed with the image or not. Annotation will pop up a window for the user to specify parameters for annotation of the display--Annotation is not implemented yet.</P>

<P>When the horizon is saved to a file, two files will be created. One is called Horizon Index, and the other is the pure horizon file, which contains all picked times (depths) for each trace. The index file will look like


```
#This is a horizon file generated by <horizon dump> <BR>
```

```
#file name is /data/dragon/liqing/temp/test_horizon<BR>
```

```
#horizon <test horizon> created at Wed Aug 16 20:59:23 1995<BR>
```

```
#by liqing<BR>
```

```
-----don't modify after this line-----<BR>
```

```
name=test horizon<BR>
```

```
dim0=181<BR>
```

```
dim1=31<BR>
```

```
invalid pick = -999<BR>
```

```
#The file is the generated horizon file by <horizon dump><BR>
```

```
#file name is /data/dragon/liqing/temp/test_horizon<BR>
```

```
#horizon <test 1> created at Wed Aug 23 15:40:34 1995<BR>
```

```
#by liqing<BR>
```

```
-----don't modify after this line-----<BR>
```

```
name=test 1<BR>
```

```
dim0=181<BR>
```

```
dim1=31<BR>
```

```
invalid pick = -999<BR>
```

```
#The file is the generated horizon file by <horizon dump><BR>
#file name is /data/dragon/liqing/temp/test_horizon<BR>
#horizon <test 3> created at Wed Aug 23 21:51:54 1995<BR>
#by liqing<BR>
```

```
-----don't modify after this line-----<BR>
```

```
name=test 3<BR>
```

```
dim0=181<BR>
```

```
dim1=31<BR>
```

```
invalid pick = -999<BR>
```

```
<BR>
```

From this file, we can see that 3 horizons have been saved in this file, they are named "test horizon", "test 1", and "test 3", dimensions are: dimension 1 is 181, 31 for dimension 2, and an invalid picking point for dimension 3 has the value -999. All lines starting with "#" will be comment lines, don't modify any line without "#" as the first character.

</P>

<P>When saved horizons are loaded back, two windows are popped up for the user to select and deselect horizons for display. The left window contains the horizon names not selected. The right window contains the horizons selected. Selection and deselection is based on horizon names.</P>

<P>This module is still in the experimental stage of development. It is going to be modified and improved continuously, with well log interpretation incorporated into this module next.</P>

<P>For details about all parameters, please refer to the provided manual help page which is in the file "horizon_dumper.txt"

</P>

Chapter 6: Seismic Attribute Analysis</H1>

<P>

LDEO 4D difference and similarity technologies are first applied to the amplitude envelope of the 3D seismic data, called Reflection Strength. The first reflection strength can be further filtered to obtain Second Reflection Strength if the frequency differences of the surveys to be compared are large. The advantage of reflection strength is that it is the absolute reflection energy of the seismic reflections themselves. It also remedies problems such as phase differences between different 3D seismic datasets. When seismic reflection data is converted into reflection strength data, seismic wavelets are converted into only positive major peaks. That means that the high frequency interleaving of peaks and troughs in the original seismic reflection traces is removed. Reflection strengths of each reservoir are characterized by a major peak near the top. Very small changes in the original reflection data are smoothed prior to differencing, but further differencing of reflection strengths within a thick reservoir (thicker than the tuning frequency of the seismic source) will reintroduce high frequency data into the interpretation.

</P>

<P>

The LDEO 4D Software inter-comparisons are accomplished in attribute-derivative space because we have found that only the lowest frequency amplitude spectra preserve commonality among different vintages of 3D seismic surveys with very different power spectra. Another reason is the region growing techniques we use (see below). Region growing is used to segment the whole 3D volume into much smaller volumes of similar high amplitude regions. Our region growing algorithm requires input data that must be all positive values. Thus original seismic reflection data is not appropriate for region growing.

</P>

<P>

LDEO 4D Software provides one module to convert reflection seismic data into attribute-derivate data. The module is called Seismic Attributes , and it takes in AVS field data, which can be 1D, 2D or 3D. It will create 3 AVS output fields which have the same dimensions as the input field. The right most output port is Amplitude Envelop, the second port to the left is the Instantaneous Frequency, and the left most port is the Instantaneous Phase. The only parameter required for this module is Sampling Interval which is specified because a FFT algorithm is used to compute the attributes (the default is 4 ms).

</P>

<P>

Before converting reflection seismic data to attribute-derivative data, the seismic volume usually needs to be band-passed to remove very high frequency noise. When S/N ratio is very high, this step can be bypassed. Several filter modules are provided.

</P>

<P>

Figure 10 is an exemplary AVS network to derive seismic attributes. The input is AVS field formatted seismic reflection data, which can be in any dimension (subset or whole volume). The output from the Read Field module feeds the Seismic Attributes module, which computes instantaneous amplitude, frequency and phase. Orthogonal Slicer and Image Viewer are used to display derived attribute data. Also, two Extract Trace modules are used to extract seismic traces and derived attributes and display them together in the AVS Graph Viewer for verification sake.

</P>

<P ALIGN=CENTER></P>

<H3 ALIGN="CENTER">Figure 10: An exemplary network to compute seismic attributes.</H3><p></P>

<P>

To calculate second reflection strength, simply drag another Seismic Attributes module and send the right-most output from the previous Seismic Attributes module into the new one. Then, the right-most output port of the second Seismic Attributes module will be the computed second reflection strength. For differencing, either first or second reflection strength can be the appropriate choice, depending upon the power spectra of the 3D seismic surveys to be differenced (see below).

</P>

Chapter 7: Data Normalization</H1>

<P>

Two or more 3-D seismic surveys can not be immediately differenced in LDEO 4D seismic applications because acquisition and processing parameters applied to them by different geophysical service and oil companies over differing times often varies markedly. Consequently, the seismic attributes, such as amplitude, phase and the frequency bandwidth of the different surveys, may not be similar enough to each other even though the surveys were acquired over the same geographic location. As part of LDEO 4D Software, we apply several normalization techniques to extract similar power spectra from multiple surveys. The result can only be as good as the worst (often the oldest) dataset, however. First, we use spectral matching, then amplitude normalization, and finally phase correction to minimize the differences between seismic volumes so that the procesed volumes can be then input in our region growing and differencing analyses.

</P>

<P>

Currently, LDEO 4D Software provides one module to solve both frequency and amplitude matching problems. The frequency matching problem is attacked through band-

pass filtering. Again, when one of the dataset has broad bandwidth, but another has very narrow bandwidth, we can not add unacquired frequency content to the narrow one. We can only cut off those frequencies from the one having broad bandwidth, and band-pass filtering is effective for doing this. Amplitude normalization is a more difficult, with the normalization begun by observing how close of histograms of the two 3-D surveys are to each other after band-pass filtering. The normalization is implemented by shifting and scaling. The assumption here is each 3-D survey has been acquired and processed consistently. We are not dealing with local normalization (which contains the very signal we are trying to extract), but rather the normalization is based upon the statistic distribution of the major population of the whole the volume. Very wild low or high amplitude values are not included. Right now, amplitude normalization is done interactively by the user. The user first observes the histogram distribution of the two datasets to decide how much to scale and shift which volume to match the other. For post-filtered seismic data, shifting is usually not necessary.

</P>

<P><P ALIGN="CENTER"></P>

<H3 ALIGN="CENTER">Fig. 11 An exemplary network to accomplish amplitude and frequency normalization</H3><p></P>

<P>Figure 11 is an AVS exemplary network to do the amplitude and frequency normalization steps, together. The two Read Field modules are required to load in two 3-D surveys for normalization. The Amplitude Matcher module will perform both frequency and amplitude normalizations. From the interface of the Amplitude Normalizer, we can see parameters required for this module. Choices are: Field 1 and Field 2 for user to specify which fields are selected to be processed. Scale Factor specifies how much each field should be scaled. Shift either adds a constant to the selected field when you enter a positive number, or subtracts a constant from the volume when it is negative. Low Cut and High Cut together specify the band-pass filter bandwidth. The default is no filtering. Delta is the sampling interval for each 3D survey. The two surveys must have the same sampling interval. If they are not, the Digital Filter must be used to band-pass each volume separately before feeding them to the amplitude normalizer. Min Value and Max Value together will specify the data range for the histogram analysis. Bin Size specifies the bin size for the histogram calculation, with the default bin size set at 1. The toggle Clip Output will clip the normalized data according to Min Value and Max Value. When the toggle Make Output is turned-on, the normalized input 3-D surveys will be written out to two new files which are AVS field formatted. Two file browsers are provided for selecting file names for the output. If the file previously existed, a confirmation for overwriting is requested.

</P>

<P>

There is a graphic monitoring window to guide the user through the selection of band-pass, scaling and shifting parameters. The top curves are the frequency spectra of arbitrary selected traces of the two volumes. The input 1 which is the right most port of the Amplitude Normalizer module is always in red, the input 2 which is the left most port of the Amplitude Normalizer is always in blue. The bottom figure contains histograms and cumulative histograms of the inputs 1 and 2. This figure is always updated when parameters are changed. Scaling and shifting operations must be applied to the input 1 and 2 datasets to force the two histogram to closely resemble each other. An exact match is not required.

</P>

<P>Both the scaling and shifting operations are cumulative, which means that if you applied scaling of first 1.3, then 1.7 to the input dataset, these two operations would be equivalent of applying one scaling factor of 2.21. Put another way, all operations are

applied to the latest copy of the input data--not the input data itself, because we don't ever change the original input datasets. HOWEVER, band-pass filtering is not cumulative (see below).

Chapter 8: Filter Techniques

As we all know, filtering is an important part of any seismic data processing. LDEO 4D Software provides various kinds of filters. Here we describe several modules widely used in the LDEO 4D seismic analysis.

When the input dataset is too large for workstation computers to handle, you naturally think about how to reduce the size of the dataset. One way to do it is downsizing the input by a factor of 2, 4, etc. In the AVS module **Downsize**, the data is resampled, which naturally reduces the resolution of the data. LDEO 4D Software provides a module to downsize through neighbor-averaging, instead of the AVS method. Our technique will smooth the data and also keep as much information as possible. This module is called **Neighbor Average**, and in fact, this module provides both low pass filtering and resampling.

LDEO 4D Software provides another module called **Digital Filter** to accomplish many filtering operations. Using this module, you can apply low-pass, high-pass, band-pass and notch-filtering to any input dataset. Filtering can be applied in any of the I, j, or k directions of the input field.

For surface data such as horizons, smoothing of zapped data is often required. LDEO 4D Software provides a module called **Surface Smooth** to accomplish this task. Please refer the help manual page **"surface_smooth.txt"** for details.

Another important filter used in the LDEO 4D Software is a median filter, which is used to remove sparsely distributed, noisy data from the volume. When the data has very high S/N ratio, this step can be neglected. The median filter is a widely used technique for noise removal in image processing, but is usually applied only in 2-D. Because of limits of seismic reflection resolution, bright spots are actually identified as 3D "packages" of high amplitudes, and so we have constructed a 3D median filter module. If a dataset is contaminated by noise, a high seismic amplitude region will not be grown as it should into a single whole region as expected, but instead will grow into several segmented regions. Statistically, noise is usually very low or high values, whereas high seismic amplitude signal will be distributed into a much very narrower range. When the median filter is applied to such noise-contaminated data, the filter will replace wild and very low or high values by the median value. Therefore, it will reconnect segmented regions but, the risk is that it makes a region usually somewhat smaller than without filtering. When region-growing the data later on (see below), you have to loosen the thresholds for searching and growing a little bit in order compensate for this effect.

The LDEO 4D Software network to do median filtering is very simple. Figure 12 is an exemplary AVS network to accomplish this task.

ALIGN=CENTER**>****IMG SRC=**"medium_filter_net.gif"**>**

H3 ALIGN="CENTER"**>**Figure 12: An exemplary network to do median filtering.

In Figure 12, there are two images: at left, is a time slice after median filtering, and at right is the original unfiltered image. It is clear that the region is very clean after vs before, and well separated, but the high seismic amplitude region has shrunk a little bit.

Also, the fault is very clearly shown after median filtering because seismic amplitude is disturbed around the fault zone.

</P>

<P>

Other filters are provided for pure data manipulation. Both AVS and standard UNIX utility programs use everyday filters. LDEO 4D Software provides many of these filter modules too. For example, we have included modules from AVS for Crop, Downsize. Please refer to the Appendix for a listing of LDEO 4D Software modules, as of 1/96.

</P>

Chapter 9: Region Growing</H1>

<P>

So far, we have a) rebinned multiple 3D seismic surveys, b) amplitude, frequency, and phase normalized them, and c) spatially corrected them. We have computed either d) first or second reflection strength datasets, and optionally e) median filtered them. Now it is time to do the primary task of the LDEO 4D Software prior to differencing: f) region growing to find high seismic amplitude packages within the volumes.

<P>Region growing is a technique used to find coherent, locally connected, high seismic amplitude regions by growing from "seed points of the highest amplitudes. The software looks outward in 3D, always testing for AMPLITUDE GRADIENT thresholds. There are two kinds of thresholds for 4D Region Grow module: a searching threshold and a growing threshold. The Searching Threshold determines the amplitude threshold for the beginning seed points for region growing, and is usually a very high value selected from the highest tail of the amplitude histogram. Growing will start from these seed points and growing outward based on the change in amplitudes at surrounding voxels to these seed points. The Growing Threshold has wider range, which usually includes the searching range so that if connectivity is present between seed points, they are Manifolded together. When a region is growing outward, voxels must be inside the growing threshold in order to be selected for the region. Region growing is a searching algorithm, and it efficiently constructs a Data Tree which will ultimately form the regions of interest for the differencing algorithm.</P>

<P>

4D software provides one module called Grow Region to accomplish this. It has six parameters: box size, search low, search high, grow low, grow high, erosion. The box size is a 3D cubic box which will limit the growing range, when the box size is large, the search will be slower, but very closely spaced regions will be connected. The default box size is 3, which means a 3x3x3 cubic box is selected around each seed point, which is always sitting at the center of this box. Searching is constrained to be within this box, but when new points are found, these new points become part of an enlarged region of seed points and growing continues from this bigger volume until all points along the outside perimeter of the seed volume have found no further voxels outside them that are within the growth threshold. Search low will determine the lower threshold for starting seed points, and search high will determine the high threshold for starting seed points. Grow low will determine the lower threshold for future searching for new seed points, grow higher will determine the high threshold for future search for new seed points to include in the growing region. These thresholds must be manually set-up from a histogram of the amplitude content of each dataset. However, region growing is relatively robust, and it is not very sensitive to these threshold parameters. Default parameters can be used immediately to start the region growing process. The erosion parameter is used to control the size of very small regions, which we want to exclude. Also this parameter will smooth the outside boundary of the region. Maximum erosion size is the total number of points included in

the search box, when the number of new searched points falls below this parameter, all seed points for this search box will be discarded.

</P>

<P>

Figure 13 is an AVS network to do region growing and display the results from the region growing. Also shown is a comparison of the differences between region growing and pure thresholding of the dataset.

</P>

<P ALIGN=CENTER></P>

<H3 ALIGN="CENTER">Figure 13: An exemplary network to do region growing</H3><p></P>

<P>

The example network is simple because it only needs, in addition to the region grow module, read field, orthogonal slicer, integer, generate colormap, and image viewer module. In Figure 13, there are displayed 3 time slices of (left) a grown region, (center) the original volume and (right) a pure thresholded volume. From the left image, we can see some of the regions are interconnected, whereas they are not in the thresholding (isosurface) volume. This is one powerful feature of region growing: manifold construction.

</P>

Chapter 10: Volumetric Rendering of Reservoirs</H1>

<P>

After region growing, the volume now is represented by segmented, high seismic amplitude packages. Regions now define volumetric boundaries we are interested in differencing to determine seismic changes that have occurred over time. The amplitude values within voxels defining the outside boundaries of these regions are different from isosurfaces, which construct surfaces bounded by equal data values. But our region grown data can be colorized to display the varying amplitude values on the outer surface of the grown regions. A comparison can be computed using the AVS module isosurface to prepare an isosurface volume for the same dataset run through the LDEO 4D Software module res builder, which is used to construct the surfaces of each high seismic amplitude region within the same dataset. The surface constructed by the res builder can be colorized by connecting the generate colormap module. The colormap can be constructed by combination of parameters R, G, B. The parameter smooth window length is used to smooth the outer surface. Figure 6 is such a result, after rendering with this module. You can see the surface constructed is colorized by the real amplitude value which is not constant across the body.

</P>

Chapter 11: Differencing and Similarity Analysis</H1>

<P>

After completing the above described processes for all involved 3-D surveys, we are finally ready to perform the most critical activity of the LDOE 4d Software, the computation of similarities and differences among datasets. The differencing process is only applied to the region grown datasets, not the original seismic volumes, because we are only interested in differences among segmented, high seismic amplitude region. We usually subtract the new survey from the older survey.

<P>The final differenced volume contains 3 different parts: high negative differences which are caused by brighter amplitudes on the new survey versus the old survey (we color these red to denote the most likely cause of the brightening--increased gas content of the pore fluids. This anomaly can be introduced by gas cap formation, residual gas being left behind during oil production, or by non-fluid events such as diagenetic precipitation of hard, fast pre filling minerals.

High positive difference indicate dimming of the seismic amplitudes with time, which can be caused by the replacement of oil and gas with higher velocity water. we color these intervals blue because of the possible link of dimouts and watering-out.

Another critical result is the identification of the parts of the high amplitude regions where only very small differences are seen over time. This reflects no radical seismic reflection change over time, which can be caused by bypassed oil or gas, or by hard reflectors that do not change with time such as those from salt boundaries. we color these green to indicate possible bypassed pay. Within the green interval of similarity, we color yellow those amplitudes that changed less than 5%, indicating especially persistent amplitude intervals. These are the areas for concentrated geological, stratigraphic and petrophysical study to further determine if bypassed pay is present.

LDEO 4D Software provides one module **field math op** which performs the necessary mathematical operations on the input field. The output from this module can be normalized to [0, 255] dynamic range. This module supports operations such as **addition** which adds one dataset to another dataset or adds a constant to the input dataset, **surtraction** which subtracts a second field from the first input field or subtracts a constant from the single input field. The option **by intersect** will perform subtraction between two input fields, but only at those voxels that are a union of the two fields, that is, only where grown regions exist in both datasets. The union field is created by checking if two datasets have nonzero data values at the same position (i, j, k) in each. If they are then subtraction is performed. Otherwise, output at this position (i, j, k) is set to zero. The option ***** does multiplication of two input fields or multiplies the single field by a constant. The option **/** does a similar division operation. The option **intersection** creates output based on a mask. You might want to mask salt from the calculation so that you only see similarities and differences around the salt volume. In this case, the first port of the module must be the dataset and second port of the module is the masking field (the polygonal description of the salt region. Antithetically, the option **union_mask** will generate a union of the two input fields. For other options please refer to the help page for this module.

Figure 14 is an example AVS network to do differencing and visualize the results.

ALIGN=CENTER**>**

H3 ALIGN="CENTER">Figure 14: An example network to do differencing**</H3><p>**

From figure 14, we first see the resulting histogram of the differenced volume. The histogram has 3 peaks: a big negative peak represent ing dramatic diming-out sincethe last survey, a very small positive peak indicating that in this example, insignificant gas cap formation has occurred because little brightening has occurred, and a region of similarity, which is pretty small too. A standard color bar is applied to the differenced volume using this histogram.

The interpretation of the volumetric changes that have occurred within the grown regions can be discovered in a variety of ways. We have found that either orthogonal slices or horizon slices made through the volume provide the best images to quantify the locations of bypassed pay for further analysis (see below). Drainage has been found to be decidedly non-linear, with water encroachment occurring from all sides. Often, drainage volumes can be defined around specific wells, with water coning from below often evident. Gravitationally-driven oil/water contact movement is a simplification of what the 4D similarities and differences often point to as the hydrodynamic regime controlling drainage.

</P>If more than one time-lapse image is present, changes must be examined from snapshot to snapshot. If, for example, first a gas cap is formed, then drained, time lapse one may show a brightening updip, but then time lapse two will show a dimming.

</P>Residual gas can be identified much more readily because through the 4D analysis than in individual 3D surveys because, while it may remain bright, residual gas will indeed have a lower overall amplitude than fully saturated gas. It will thus appear as a dimout in the 4D difference analysis.

</P>

Chapter 12: Integration of Seismic Differences with Well Log Data</H1>

<P>

Well log data is an important calibrator of seismic changes over time. Particularly, pulsed neutron logs run through casing during workovers provides direct calibration evidence for changes in water, oil and gas saturation with time. Other logs are critical for interpretation as well as calibration. LDEO 4D Software contains modules to display well log data within both the original seismic data and the difference volumes, as well as the unique capability of displaying a seismic extractio along the wellpath, even if highly deviated or horizontal.</P>

<P>

Before we introduce log analysis modules, we must first describe how we handle the format of well log data. For any well log data, 3 parts must be described. First, we must define the well path geometry (x, y, z), where z can be two-way travel time, vertical depth, or measured depth. Next, an accurate time-depth conversion table must be entered for each well. Then, all well log values must be entered, such as resistivity, gamma ray. Currently these 3 parts are each in their own format. The following is the description of the well path geometry file format.

PATH 330_PZ_A-12 17710401150

1883042.00 -155571.00

330_PZ_A-12	0.00	0.00	0.00
330_PZ_A-12	-4.27	-6.40	2400.01
330_PZ_A-12	-6.42	-9.91	2500.10
330_PZ_A-12	-8.77	-13.20	2600.18
330_PZ_A-12	-10.72	-16.27	2700.24
330_PZ_A-12	-12.35	-19.46	2800.31
330_PZ_A-12	-14.46	-23.44	2900.41
330_PZ_A-12	-17.24	-28.55	3000.58

.

.

.

.

PATH 330_PZ_A-6 17710400810

1883029.00 -155569.00

330_PZ_A-6	0.00	0.00	0.00
330_PZ_A-6	-22.00	-25.00	1198.46
330_PZ_A-6	-32.96	-36.75	1298.45
330_PZ_A-6	-46.80	-49.88	1398.45
330_PZ_A-6	-62.47	-64.50	1498.45
330_PZ_A-6	-79.54	-80.42	1598.44

.

.

.

.

This file can contains multiple wells, with each well starting with the line

 PATH WELL_NAME WELL_ID

 x0 y0. This line contains the first pair (x, y) of the well path, which is usually coordinates of the platform or surface location of the well. This is followed by a sequence (dx, dy, time). Each point begins with the well name.

Another file is called the time-depth coversion table, which has formatted as below:

```
<BR><BR>
TDCN      330_PZ_A-12  17710401150      <BR>
1883042.00 -155571.00      <BR>
330_PZ_A-12      0.00      0.00 <BR>
330_PZ_A-12      1119.00      400.00 <BR>
.      .      .      <BR>
.      .      .      <BR>
.      .      .      <BR>
.      .      .      <BR>
```


Each well starts with the line:

TDCN 330_PZ_A-12 17710401150
. Here ,TDCN stands for time depth conversion. This line is followed by the (x, y) pair of the first point, then sequences of (time, depth) pairs, each beginning withthe well name.

The following section shows the format of the well log data files themselves.


```
HH 330_PZ_A-12 17710401150 1883042.00 -155571.00 <BR>
MD ASN BLSP CALI GR ILD RHOB<BR>
3639.00 -999.000 -999.000 -999.000 -999.000 -999.000 -999.000<BR>
3640.00 0.666 -23.239 -999.000 -999.000 0.504 -999.000<BR>
3641.00 0.927 -21.487 -999.000 -999.000 0.727 -999.000<BR>
3642.00 1.015 -21.277 -999.000 -999.000 0.872 -999.000<BR>
3643.00 1.069 -21.323 -999.000 -999.000 0.875 -999.000<BR>
3644.00 1.111 -22.231 -999.000 -999.000 0.815 -999.000<BR>
.      .      .      <BR>
.      .      .      <BR>
.      .      .      <BR>
.      .      .      <BR>
```


The well log file always starts with:

HH 330_PZ_A-12 17710401150 1883042.00 -155571.00

Here HH is a magic string like the magic number in most image formats. HH is followed by the well name, then the well id, then the first pair of (x, y) coordinates of the well path. The second line contains log names in this file. This file contains measured depth (MD) which must be first column, always:ASN, BLISP, CALI, GR, ILD, RHOB. After this line is a sequences of actual values for each log. This file can contain multiple well logs. All modules for well log data are selected based upon the well name.

</P>

<P>LDEO 4D Software provides a module create tdc well data which combines the well path file and time depth file into one file. The combined file will look like this:


```
AA: 17710401150 330_PZ_A-12<BR>
BB: 1883042.000000 -155571.000000 0.000000 0.000000 0.000000<BR>
BB: 1883037.750000 -155577.406250 793.002991 2400.010010 2400.022217<BR>
BB: 1883035.625000 -155580.906250 823.028687 2500.100098 2500.196045<BR>
BB: 1883033.250000 -155584.203125 851.718262 2600.179932 2600.358398<BR>
BB: 1883031.250000 -155587.265625 880.402100 2700.239990 2700.485352<BR>
BB: 1883029.625000 -155590.453125 909.087830 2800.310059 2800.619385<BR>
```

```

BB: 1883027.500000 -155594.437500 937.449463 2900.409912 2900.821045<BR>
BB: 1883024.750000 -155599.546875 965.830994 3000.580078 3001.159180<BR>
BB: 1883021.250000 -155605.343750 994.232239 3100.810059 3101.617676<BR>
BB: 1883016.750000 -155611.984375 1022.990540 3201.129883 3202.257812<BR>
BB: 1883011.750000 -155619.437500 1051.771973 3301.530029 3303.058350<BR>
BB: 1883006.125000 -155627.203125 1080.563843 3401.989990 3403.974854<BR>
. . . .<BR>
. . . .<BR>
. . . .<BR>
. . . .<BR>

```

Here each well starts with the line:


```
<B>AA: 17710401150 330_PZ_A-12</B><BR>
```

AA: is a magic string, followed by the well id and well name. This line is then followed by a series of five number strings (x, y, time, vertical depth, measured depth). Each line starts with the string BB:. This file is accepted by most of modules in the LDEO 4D Software. Create tdc well data is a stand alone module which reads in well path geometry, the time depth conversion file, then outputs a tdc formatted file.

</P>

<P>The module read tdc well is used to read in tdc formatted files. It has 3 browsers: first, is a well name browser; second, is a browser to select which column, either time, vertical depth, or measured depth to use; and third, is a browser for the input well log selection. This module only extracts one well log each time, thus the output is an AVS 1-D, 3-space, irregular field</P>

<P>

The module read all well paths reads all wells in the file at once. This module has two browsers: first, is a browser for selecting time, vertical depth or measured depth; the second is a browser for log selection. This module has two outputs: the left most port is the 1-D, 3-space, irregular field which contains all (x, y, z)s of the all well path; and the right most port is the 1-D, integer, uniform field, which contains the number of points for each well in the input file. The output from this module is input to the module

```
<B>draw all well paths</B></P>
```

<P>

The module draw all well paths is used to draw all well paths at once. If the well path is displayed with seismic together, you have to convert all real world coordinate pairs (x, y) of well path to the index world of the seismic volume. This can be easily done by connecting the left most port of the read all well paths module to the module real world to index. The well path is draw by connecting all points together, thus it forms a line. This line can be any color, which is controlled by the usual AVS parameters red, green, blue. All wells can be labelled at the top or bottom of the well path.</P>

<P>

Single well paths can be drawn by the module well path draw which is object oriented. Each well path geometry object will be the well name, with a suffix string

```
<B>"_path"</B>.</P>
```

<P>Well path can be rendered into a very thick cylinder if necessary, which is implemented by the module well extrude. This module generates a cylinder representation of the input well path. The thickness of the cylinder is controlled by the radius parameter, and smoothness of the cylinder is controlled by the parameter cylinder division. The out from this module is a 2-D, 3-space, irregular field which is usually input into the module point 2 surface.</P>

<P>

You can extract seismic or any other data (reflection strength, similarities and differences) along the well path whatever its angle and deviation. The module

extract data along well will accomplish this. It requires two field inputs: the right most port is the volumetric data; and the left most port is the well path geometry data which comes from the module **read tdc well**. Also this module requires the project description file for this volume to do the correct coordinate conversion of the well path geometry. The output is data extracted along the well path which is in the form of a 1-D, 3-space, irregular float that can be drawn by the module **log draw**.

<P>

Log draw is the module to draw well log data in 3-D space, you can label the log curves next to the well name at either the top or bottom of the well path. The log curve to be drawn is colorized by the single color which is determined by the combination of the usual parameters **red, green, blue**. The log "wiggles" curves can be shifted along x, y and along the well path.**</P>**

<P>

Well logs are read in by the module **read well log**. This module has three browsers: the first is the log file browser; the second is the well name browser for well selection; and the third is for log selection. When the file is read in, the second and third browsers will be filled in according to the input file.**</P>**

<P>Also you can extract sectional data along i or j directions of a seismic volume according to the well path geometry and attach well log data to the extracted section. This extraction is implemented exactly along the well path. Thus, when the well path is not vertical, then the extracted section will follow the curvature of the well path exactly. This module allows for an accurate comparison between well log data and the seismic data.**</P>**

<P>

Figure 15 is an example network to display well log data and seismic data together.**</P>**

<P ALIGN="CENTER"></P>

<H3 ALIGN="CENTER">Figure 15: An example network to integrate well and seismic data</H3><p></P>

<P>Figure 15 shows how to use **read tdc well, well extrude, label well** modules to render a well path into a cylinder.**</P>**

<P>Figure 16 is an example network to draw all well paths, and extract a seismic section along one well path.**</P>**

<P ALIGN="CENTER"></P>

<H3 ALIGN="CENTER">Figure 16: An example network to draw all well paths and extract a seismic section along one well path</H3><p></P>

<P>From Figure 16, after reading **tdc well path**, the well path is input to the **read well log** module, which does not have well path geometry in the file. So the well path geometry must be provided. The **read well log** module will construct the well path with (x, y, measured depth, log data). Measured depth must be converted into time before coordinates conversion. Thus, the output from the **read well log** will be input to the module **tvd to time** which converts measured depth to time according to the time-depth table. The output will be sent to the module **real world to index** to convert coordinates, then the result is sent to the module **log on seismic** for seismic section extraction.**</P>**

<P>

To draw all well path is very simple. You read all well paths, then convert all of them, then send all to the **draw all well paths** module for drawing. The resulting image is also shown in Figure 16, where we can see that the extracted seismic section is not vertical.**</P>**

Chapter 13: Output</H1>

<P>

After the above processing, it is time to reward yourself by generating beautiful images which are ready for printing or electronic linkages to homepages, reports, documents, etc.

To make an understandable image in 3-D space is much more difficult than the plain paper 2-D pictures of the past. The labeling of 3-D geometry objects, annotating of those objects, drawing of bounding boxes, etc. are required..</P>

<P>

LDEO 4D Software provides a set of utility module to accomplish these imaging tasks. The most widely used modules may be modules of the entire collection may well be:draw bound, north arrow, 3d axis, anot axis, make label, and line maker. The draw bound module is a object-oriented module, within which you pick object s on the screen, then the program will compute the appropriate bounding box for that object. It then draws a box around that object. Also, the bounding range can be manually set up by selecting the minimum and maximum (x, y and z) coordinates. You can optionally draw the whole box, or only sides of the box (such as the minimum x side). You can mesh the bound box, display the origin of the box, and select the color for the box -- which can be multi-color ed, as well. Mesh color can be user selectable too.</P>

<P>

3d axiswill draw a 3D axis which is rendered as a cylinder along x, y and z. This is an object-oriented module, too. When an object is selected, the 3D axis will be drawn according to the bounding box range of that object.</P>

<P>The module anot axis is like draw bound, but it is used to draw and label ticks and marks. Please refer manual help page for details.</P>

<P>

To display seismic data, a north arrow direction is absolutely necessary to identify orientation. The module north arrow is used to do this. You provide two points which form a vector of the north direction. Then the module will add an arrow with the charatcter N on the position specified.</P>

<P>

Also, offshore block lines and property boundaries will be required to identify geographic location. The module draw block line will do this. This module will read the block line and block number file, and then put a line and number at the position. Please refer to the manual help page for details.</P>

<P>

LDEO 4D Software also provides another module vector label which will create a 3D label for real 3D geometry objects. The label will follow that object on the screen when rotating, transforming, etc. It is not like an AVS label, which always stays upright on the screen .</P>

<P>

You can output images by using the module write tif image or write gif image which are standard IAC modules. Also AVS provides modules to write images in AVS image format or output to a postscript file.</P>

2.2 Geological Analyses of Industry 3-D Seismic Surveys: Landmark has completed its task of comparing the traditional interpretation of the horizons and faults and the reinterpreted reflector horizons and faults in Phase I of this project. The reinterpreted geologic data was converted and exported to other databases as per previous reports. Integration of several data sets aided in the reassessment of the drilling location and the field demonstration experiment.

Lincoln Pratson has completed phase three of the development of an algorithm for well log/time series correlation. Development of a robust, non-parametric correlation statistic for testing and ranking the similarity of any two, related time series, specifically the well logs from the Eugene Island 330 field, continues. At the same time, a second study of the morphology of the sea floor in the Gulf of Mexico has been completed and published in *Geology*. In this study, the intraslope basin morphology of the Louisiana slope, which is the evolutionary precursor of the Eugene Island 330 basin, is compared to the morphology of other US continental slopes. The study shows that the Louisiana Slope morphology, though rugged, is flatter and more random at both regional ($>1,500 \text{ km}^2$) and local ($<0.1 \text{ km}^2$) measurement scales than any of the other US continental slopes, which span a range of sedimentary and tectonic settings. The low grade of the Louisiana slope is undoubtedly tied to the allochthonous salt that underlies the region. It is suggested that the salt may not be competent enough to support steep seafloor slopes, and/or, in moving, it may frequently trigger slope re-adjustment through failure. Evidence for the latter are the numerous debris aprons that emanate from the base of the Sigsbee Escarpment where allochthonous salt has been thrusting seaward.

2.3 Real-Time Visualization of Database:

Wei He completed a chapter of his Ph.D. thesis on hierarchical database classification techniques that allowed him to characterize the LF reservoirs in EI 330 necessary for the 4D seismic analysis (The quantitative LF reservoir model is being simulated now).

2.3.1 Reservoir characterization of the LF reservoir in the Eugene Island Block 330 Field of offshore Louisiana, Gulf of Mexico

The dynamic changes we have observed in the LF reservoir during hydrocarbon production suggest that this reservoir is very complex and internally heterogeneous. We characterize this complexity with a fine-scale reservoir characterization model that describes petrophysical properties such as lithology, porosity, and effective oil saturation.

For many years, reservoir characterization has played an essential role in oil field management. Reservoir simulations are used by geologists and reservoir engineers to optimize and maximize recovery efficiency. Traditionally, only wireline logging data and well production histories have been used in these characterizations. Consequently, the characterizations are often too smooth due to the lack of lateral resolution. As 3D seismic imaging has improved, its usefulness in reservoir characterization has increased (Doyen et al., 1992; Martinez et al., 1992 and He et al., 1994). Reservoir characterization has become increasingly accurate and reliable. However, the static reservoir descriptions cannot predict dynamic behavior of hydrocarbon reservoirs under production.

The combination of static reservoir characterization and 4D seismic monitoring techniques can be used to achieve much more accurate oil field management and higher economic returns (Anderson et al., 1995a and 1995b). We foresee that such a combination involving multiple 3D seismic datasets will play a more and more important role in future reservoir management and surveillance, and become the industry norm in the near future.

Reservoir characterization can be performed in micro-, meso-, macro-, and mega-scales depending on data availability. Well logs and surface reflection seismic data are useful for mesoscopic and macroscopic scales (i.e., reservoirs are characterized in terms of bed boundaries, stratification types, lithology and porosity).

The lack of a unified theory that can account for all geophysical and geological observations at different scales severely affects the development of reservoir characterization techniques. Numerous empirical relationships between reservoir petrophysical and acoustic properties have been developed (Archie, 1942; Gardner et al., 1974; Brock, 1984 and Han et al., 1986). These relationships are of limited effectiveness because the correlation between petrophysical properties are imprecise. These *in situ* relationships based on high frequency data (e.g., 10 KHz sonic log and 1 MHz ultrasonic core analysis frequency) are often very inaccurate when applied to lower frequency seismic surveys.

The imprecise relationship between rock lithology and acoustic properties is often a problem when multiple lithologies are present. However, stochastic simulations can be used to assess this ambiguity and to determine the spatial distribution of reservoir properties. The physics behind the use of stochastic simulation is that the petrophysical and acoustic properties (e.g., impedance) made over the same reservoir are closely associated even though they have different frequency bandwidth. These associations can be imaged through cross-correlations between the properties and between the impedance data measured in space.

In this chapter, we present a systematic technique for determining reservoir lithology, porosity, and oil saturation distributions and applied it to the LF reservoir. Our method consists of a combination of well data analysis for lithology determination, spatial cross-correlation computations between lithology and acoustic impedance, and a robust stochastic simulation technique (Deutsch et al., 1992).

We first investigate the lithology distribution within the LF reservoir because lithology is the dominant factor affecting the acoustic impedances. Reservoir lithology interpreted from well log data analysis is assumed to be the most reliable (hard data), while lithology derived from estimated acoustic impedances is assumed to be imprecise (soft data). We use the Markov-Bayes conditional sequential indicator simulation technique to simulate the most probable lithology distribution of the LF reservoir. This simulation technique integrates the shale volume fractions derived from the 1992 acoustic impedance volume (see Chapter 3) with shale volume fractions derived from the wireline logging data. The porosity and effective oil saturation distributions are then inferred using a time-average equation along with the 3D lithology model. The likelihood of the lithology model of the LF reservoir determines other properties, such as porosity and oil saturation.

2.3.2 Conditional soft indicator simulations

The conditional soft indicator simulation is a stochastic optimization technique, which integrates data from different sources with various probability and confidence levels assigned to produce multiple images of the spatial distribution of an attribute related to these data. The simulated images provide a rich family of characterized attribute distribution with equal probability. When this technique is used to simulate spatial distributions of lithology using well and seismic data, the estimated lithology images preserve the spatial statistic of the original well data. In addition, the lithology images also possess the higher lateral resolution of seismic data.

Uncertainties in an attribute, such as lithology, can be estimated by examining the statistics of an ensemble of estimated images to create probability maps. The simulated stochastic images are globally conditioned to all available information, and also locally conditioned by hard data. The sparse hard data is honored exactly while the soft data has influence in proportion to its degree of uncertainty.

2.3.2.1 The concept of indicator variables

Many geological properties, such lithology, permeability and pore fluid pressure, can be simulated as indicator variables because the classification of these parameters tends to be categorical. For instance, the continuous variables, shale volume fraction, can be categorized into sandy and silty regions. The indicator is represented by a binary numbers that takes the value 0 or 1. The indicator is assigned to be either 0 or 1 depending on value of the underlying continuous variable. The indicator categorize the value of the continuous variable. Thus indicator variables have the characteristics of both continuous and categorical variables. Indicator variables are useful when the number of hard data points is too few to produce reasonable statistical simulations of a continuous variable.

The concept of indicator variables is introduced, developed and applied to spatial statistics by Switzer (1977), Journel (1982, 1983, 1984 and 1986). Suppose, $Y(\mathbf{x})$, is a continuous random variable defined at position \mathbf{x} . The range of $Y(\mathbf{x})$ is divided into two intervals by the cutoff value y_c . Then the indicator, $I(\mathbf{x}, y_c)$, is defined by:

$$I(\mathbf{x}, y_c) = \begin{cases} 0, & \text{when } Y(\mathbf{x}) > y_c \\ 1, & \text{when } Y(\mathbf{x}) \leq y_c \end{cases} \quad (4.1)$$

The indicators can also be considered *a posteriori* conditional cumulative probability on $Y(\mathbf{x})$ given the realization $y(\mathbf{x})$:

$$I(\mathbf{x}, y_c) = P[Y(\mathbf{x}) \leq y_c | y(\mathbf{x})] = \begin{cases} 0, & \text{when } y_c < Y(\mathbf{x}) \\ 1, & \text{when } y_c \geq Y(\mathbf{x}) \end{cases} \quad (4.2)$$

For example, suppose $Y(\mathbf{x})$ corresponds to shale volume fraction, a lithology parameter. Then $y_c = 0.75$ divides all lithologies into shales ($I(\mathbf{x}, y_c) = 0$) and sands ($I(\mathbf{x}, y_c) = 1$).

Indicator coding can also be implemented with more than two classifications. The range of $y(\mathbf{x})$ is discretized into $N_c + 1$ classes defined by N_c cutoffs or thresholds, y_1, y_2, \dots, y_{N_c} . For instance, in our study, the shale volume fraction, f , is classified by three indicators, which divide shale volume fraction into four categories: sand, shaly sand, sandy shale, and shale (corresponding to $f \leq 0.25$, $0.25 < f \leq 0.5$, $0.5 < f \leq 0.75$, and $f \geq 0.75$, respectively). Such a classification is applied to both hard (well log shale volume fraction) and soft (impedance) data.

2.3.2.2 The relationship between the hard and soft indicators

The association between hard and soft data is established from the indicator properties. The random variables, $Y(\mathbf{x})$ and $I(\mathbf{x}, y_c)$, are assumed to be second order.

The expectation of $I(\mathbf{x}, y_c)$ is then:

$$E[I(\mathbf{x}, y_c)] = P[Y(\mathbf{x}) \leq y_c] = F(y_c) \quad (4.3)$$

Here $P[Y(\mathbf{x}) \leq y_c]$ is the probability of $Y(\mathbf{x}) \leq y_c$, and $F(y_c)$ is the cumulative distribution function (cdf) of $Y(\mathbf{x})$. The covariance that associates indicators at two different locations, say \mathbf{x}_1 and \mathbf{x}_2 , is given by:

$$E[I(\mathbf{x}_1, y_c), I(\mathbf{x}_2, y_c)] = P[I(\mathbf{x}_1, y_c) = 1, I(\mathbf{x}_2, y_c) = 1], \quad (4.4)$$

which is also equal to the probability $P[Y(\mathbf{x}_1) \leq y_c, Y(\mathbf{x}_2) \leq y_c]$. This is the joint bivariate cumulative distribution function of $Y(\mathbf{x}_1)$ and $Y(\mathbf{x}_2)$. The covariance defined

in this way only depends on the spatial distance $(x_2 - x_1)$ under the assumption of second order stationary. Using $\gamma(h)$ denotes the spatial distance $(x_2 - x_1)$, Eq. 4.1 can be rewritten as:

$$E[I(x_1, y_c), I(x_1 + h, y_c)] = \gamma(h) \quad (4.6)$$

The covariance is then:

$$C_I(h, y_c) = K_I(h, y_c) - \bar{I}^2$$

Several types of $\gamma(h)$ are usually involved in a soft indicator simulation. Each of these data types has both a cumulative distribution function and spatial covariance function. The estimation of the confidence level of hard data and to increase the confidence level of soft data (Journel, 1984 and Journel, 1986). Consequently, it is essential to estimate the $\gamma(h)$ conditional distributions under the same set of tiles.

We use the Markov-Bayes approach to establish the relationship between lithology indicators derived from well logs and the estimated acoustic impedances at well locations. The hard and soft data are first divided into several classes using cutoffs, and a one-to-one correlation developed between the hard and soft classes. Within each class, an *a priori* probability cumulative distribution function can be modeled from the cumulative histogram of hard data values such that the collocated secondary (soft) data values fall into the same class. The calibrated data distributions of both the hard and soft data values are then used for the conditional sequential indicator simulation under the Markov-Bayes.

2.3.2.3 The conditional indicator simulation algorithm

The key component of conditional indicator simulation algorithm is the indicator kriging. Since the *a priori* probability of the real lithology is hard to obtain, the *a posteriori* probability is used. Since there are four basic lithology types, we use three hard lithology indicators and three soft lithology indicators in simulating the lithology of the LF reservoir. Then, the *a posteriori* probability of simulated lithology can be computed as:

$$P_{cond}(x, r_c) = P[R(x) \leq r_c | I_1(x, r_c), \dots, I_n(x, r_c), \beta = \omega] \quad (4.7)$$

where r_c is the cutoff, $I_1(x, r_c)$ is the hard indicator, and $I_n(x, r_c)$ is the soft indicator.

Since the best estimate of the probability is the linear combination of the indicator data which minimizes the estimation variance (Journel, 1988), the *a posteriori* probability for lithology can be estimated as a linear combination of hard and soft indicators:

$$I^*(x, r_c) = \omega_0 + \sum_{\alpha=1}^n \omega_{\alpha} (x | I_{\alpha}(x, r_c)) + \sum_{\beta=1}^m \omega_{\beta} (x | I_{\beta}(x, r_c)) \quad (4.8)$$

where $I^*(x, r_c)$ is the conditional indicator, ω_0 , ω_{α} , and ω_{β} are weights of each indicator type at position x . ω_0 is given by the unbiased condition, and $\omega_1, \omega_2, \omega_3$ are determined from the following equations:

$$\sum_{\alpha=1}^n \omega_{\alpha}(x) C_I(x_1 - x_{\alpha}, r_c) + \sum_{\beta=1}^m \omega_{\beta}(x) C_{II}(x_1 - x_{\beta}, r_c) = C_I(x_1 - x_1, r_c), i = 1, n$$

$$\sum_{\alpha=1}^n \omega_{\alpha}(x) C_{II}(x_1 - x_{\alpha}, r_c) + \sum_{\beta=1}^m \omega_{\beta}(x) C_I(x_1 - x_{\beta}, r_c) = C_{II}(x_1 - x_1, r_c), j = 1, m$$

Eqs. 4.8 and 4.9 indicate that the quantity ω_{α} links the hard and soft data together. These equations are based on the fact that ω_{α} is the posterior probability of lithology.

conditional probability estimated in the simulation is equal to the probability of the hard indicator within each class.

2.3.2.4 The sequential, conditional, soft indicator simulation

The sequential, conditional indicator simulation is aggressive in practice. Once the lithology indicator at a location is simulated, this location is recategorized into the hard indicator and joins the stochastic simulation for the next location. Eq. 4.8 can take many forms, depending upon the physical and statistical analysis of the soft data. In our case, we simulate reservoir lithology using shale volume fraction from wells as hard data and those from impedance as soft data:

$$I^*(\mathbf{x}, r_c) = \omega_0 + \sum_{\alpha=1}^n \omega(\mathbf{x}_\alpha) I_w(\mathbf{x}_\alpha, r_c) + \omega(\mathbf{x}_\beta) \cdot I_z(\mathbf{x}_\beta, r_c), \quad (4.10)$$

where $I_w(\mathbf{x}_\alpha, r_c)$ and $I_z(\mathbf{x}_\beta, r_c)$ are the hard and soft indicators at cutoff, r_c . The weighting parameters are determined in the simulation process by minimizing the conditional variances (Eq. 4.9). This minimization only requires knowledge of the spatial autocovariance and cross-covariance of hard and soft indicators.

The simulations reproduce the indicator means, autocovariances, and cross-covariances. The simulated spatial distribution of an indicator variable honors both hard data (directly, as constraint) and soft data (indirectly, through its indicator).

2.3 Geological and geophysical logging data analysis in the LF reservoir

We perform our reservoir characterizations in the same area where we have performed the 4D analysis (Figure 4.1).

2.3.3.1 Well log analysis for lithology of the LF reservoir

The lithology of the LF reservoir is first studied using twenty logged wells in the study area (Figure 4.2). In sand and shale sequences, gamma ray (GR) and spontaneous potential (SP) logs are used to calculate the fractional shale volume by using empirical relationships described in Chapter 2 (Eqs. 2.5-2.8).

The well log analysis is then used to derive the hard lithology data of the LF reservoir and its surroundings (Figure 4.3). Because the spatial cross-correlation plays a very important role in the conditional sequential indicator simulation algorithm, these 20 wells have been chosen very carefully to have a good spatial coverage.

2.3.3.2 Qualitative description of the LF reservoir

The LF reservoir belongs to a vertically-stacked, deltaic sand package (JD-KE-LF sands) deposited during the proximal deltaic phase in the lowstand prograding wedge system tract in the EI-330 minibasin (Alexander et al., 1995). Holland et al (1990) used well logs and production data to analyze the overall reservoir properties.

The LF sand is a distributary-mouth bar deposit. The sand progressively thins updip and is shaled-out on the crest of the anticline. It is very fine-grained and clean, with a high irreducible water saturation. Unusually low resistivity is observed on resistivity logs. It consists of predominantly quartz with various, but minor amounts of detrital shale. Feldspars and other minerals may constitute as much as 30% of the total rock volume. Hard, uniformly cemented "streaks" of calcite precipitates, along with authigenic clay, silica, dolomite, and pyrite, are found toward the top of the sand in two cores (Flemings et al., 1996 and Hoover, 1996, personal communication).

As is typical with deltaic sand deposits, the sand bodies of the LF reservoir contain variable shale and other distributed fine-grained compositions that vary spatially. Using well data alone in traditional reservoir characterization, one must interpolate reservoir properties within each reservoir in order to estimate the spatial distributions of these properties. Simple contouring and kriging techniques are used to make the image

of the characterized LF reservoir (Figure 4.4). The LF reservoir is the most prolific oil-producing reservoir in the field. It has excellent water drive support, and a gas-cap exists near the structural crest of the EI-330 roll-over anticline (Figure 4.4). The average porosity is about 30%, and the net pay thickness averages about 17 m.

The characterizations of the LF reservoir from well data alone are qualitative. Only ranges of porosity and permeability have been estimated (Holland et al., 1990). These characterizations do not describe spatial variabilities, and cannot satisfy our needs for quantifying the 4D analysis, because the image is too smooth to capture the true heterogeneity of the reservoir. The addition of 3D seismic data enables a much more realistic reservoir characterization.

2.3.4 The geometry of the LF reservoir

The estimated 1992 acoustic impedance volume derived in Chapter 3 contains the JD, KE and LF reservoirs (Figure 4.5). This impedance volume is used along with the reservoir lithology derived from well logs within it to characterize the lithology and porosity distributions of the LF reservoir.

The estimated acoustic impedance volume is converted from two-way traveltimes to depth using conversion table created by averaging fourteen sonic logs. The converted acoustic impedance volume is then resampled every 1.5 m. The top and bottom of the LF reservoir in this impedance volume are consistent with the well tops, indicating that the conversion from two-way traveltimes to depth has been successful (Figure 4.6).

The interpreted top, bottom, and thickness of the LF reservoir are shown in Figures 4.7, 4.8, and 4.9, respectively. The thickest part of the LF reservoir is in the center of the study area (Figure 4.9). There appears to be a thick sand trend running along the north-east to south-west direction, consistent with the interpretation that the LF sand is in a deltaic mouth bar deposit. The map of depth to the top of the LF reservoir based on both seismic and log data (Figure 4.7) has much greater spatial resolution than the map based on log data alone (Figure 4.4). Dramatic stratigraphic thinning of the JD, KE, and LF sands onto the crest of anticline in the study area is also seen in the east-west cross-section (Figure 4.10).

2.3.5 The relationship between acoustic impedances and lithology in the LF reservoir

Correlations between lithology, porosity and acoustic impedance are often ambiguous. The classified reservoir lithologies do not always correspond to a particular impedance interval, and impedance ranges of different lithologies often overlap one another. The more the overlap, the greater the ambiguity of direct classification.

We first extract a calibration dataset from the impedance volume at the locations of logged wells. The statistical distribution of the extracted acoustic impedance data and the shale volume fraction data differ. Shale volume fraction data has strong bi-modal statistics, while acoustic impedance has is a single-modal statistics (but a long-tailed distribution) (Figure 4.11). Empirical relationships between volume fraction and impedance are difficult to justify, given such large difference in their statistics. Even within the narrow specified depth interval (91 m), the relation between the shale volume fraction and acoustic impedance is very poor (Figure 4.12).

Since the conditional stochastic simulation method requires the accurate hard data (log data) and inaccurate soft data (seismic) to have the same data type, we convert the estimated acoustic impedance to shale volume fraction using the empirical relationship (modified from the porosity-sonic relationship given by Schlumberger's Log Interpretation Principles/Applications):

$$f^* = \frac{Z - Z_{\text{sand}}}{Z_{\text{shale}} - Z_{\text{sand}}}, \quad (4.11)$$

where, f^* is the converted seismic shale volume fraction, Z is the estimated acoustic impedance value, Z_{sand} and Z_{shale} are the pure sand and pure shale impedances (see Chapter 3) (Figure 4.13).

2.3.6 The variogram models estimated from hard and soft data

Variogram is the variance of a random variable with respect to discretized distance increments. The shale volume fractions in the hard data clearly exhibit sand and shale categories, centered approximately at $f = 0.1$ and $f = 0.9$, respectively, whereas those of the soft data do not. However, the distribution of the soft data does have a long tail at the lower impedance end, which probably corresponds to clean sand saturated with either oil or gas.

The spatial correlation between the hard (shale volume fraction measured by logs) and the derived secondary data (shale volume fractions derived from the estimated acoustic impedance) is quantified using directional semivariograms. We choose these directions to be inclined from vertical, to match the measured dip of the LF reservoir.

Experimental semivariograms of both hard and soft shale volume fractions in the east-west, north-south, and depth directions are computed and correspond to one another (Figure 4.14). The hard shale volume fractions have much greater spatial variability than the soft data in all three directions. Introduction of the soft data will significantly improve estimates of the spatial distributions of reservoir properties.

We computed semivariograms of the three indicators using both hard and soft data (Figures 4.15-4.17). The observed semivariograms are then approximated by a simple, "spherical" semivariogram model (Deutsch et al., 1992). The hard and soft indicators have similar semivariograms. The maximum correlation length is larger in down-dip and along-strike directions, than in the depth direction (152 m corresponds to 15 m). Sand has the least spatial variability with a maximum correlation length (183 m) in the across-strike (down-dip) direction. The variability of shaly sand and sandy shale is twice that of the sand in lateral directions.

Our stochastic simulation is carried out in a finite difference 3D grid (it is also the 3D seismic grid) with dimensions of 134 node points in the down-dip direction, 125 node points in the across-strike direction, and 61 node points in the depth direction. The spacing in the down-dip, across-strike, and depth directions are 23 m, 15 m, and 1.5 m, respectively.

2.3.7 The Markov-Bayes calibration of the hard and soft indicators

The Markov-Bayes calibration is performed using the calibration dataset, which contains 1235 collocated hard and soft data pairs. The scattergram (Figure 4.13) is used to infer the soft *a priori* probabilities. These collocated data pairs give the prior conditioned cumulative frequency (local prior cdf) table for each class. The table then gives the linear scaling factors that ensure that the probability of random drawing of the realization at each data point is constrained to the collocated hard and soft data calibrations (Kulkarni, 1984). At this time, the shale volume fractions, which are not directly analyzed through the variogram studies, are incorporated implicitly into the simulation.

2.3.8 The simulated lithology distributions of the LF reservoir

Twenty simulations, using four different random seed points, are computed using the conditioned Markov-Bayes calibration table and the spatial semivariogram models. The starting points of the simulations are different, but the simulation paths used in the simulations are the same. A total of nine internal structures are applied to derive volumetric distribution of three cutoffs (four classes).

The simulated shale volume fraction realizations are compared with the estimated acoustic impedance distributions in the top, middle, and bottom of the LF reservoir (Figures 4.18-4.21). Remarkable lateral continuity of the simulated sand distributions are observed, even though such lateral continuity is not in either the estimated acoustic impedance or the well data (Figure 4.22). Similar sand and shale distribution patterns are observed in all twenty simulated images.

Because all the simulated lithologic images exactly honor the hard data, it is difficult to determine which image is the best description of the LF reservoir. We arithmetically average the twenty simulated shale volume fraction distributions to obtain a final estimate of the lithology (Figures 4.23 and 4.24). We then computed a probability volume that describe the probability that the lithology is sand, shaly sand, silty shale, or shale at each point within the lithology volume.

The LF sand gradually shales out towards the east, as expected. The shale line shown in the middle slice runs nearly north-south even though the structural contours wrap around the anticline (Figure 4.7). The thickening of the LF sand reservoir in the center just north of the F fault defines the depocenter. The clean sand distribution shows the greatest discontinuity on the upper slice and the greatest continuity along the middle slice. On the lower slice, clean sands are primarily located in the depocenter. The probability maps of sand corresponding to these three extracted slices are shown in Figure 4.25.

2.3.9 The porosity model of the LF reservoir

We use the final lithology volume, and an empirical time-average relationship relating lithology and porosity (modified from the Dresser Atlas Log interpretation charts) to infer a porosity volume (Figures 4.26 and 4.27). The relationship is:

$$\phi = \left(\frac{Z - Z_{\text{sand}}}{Z_{\text{fluid}} - Z_{\text{sand}}} \right) - f \left(\frac{Z_{\text{sand}} - Z_{\text{shale}}}{Z_{\text{fluid}} - Z_{\text{shale}}} \right), \quad (4.12)$$

where ϕ is the computed porosity, Z is the estimated acoustic impedance, Z_{sand} is the impedance of the sand matrix, Z_{fluid} is the impedance of water, f is the shale volume fraction derived from the stochastic simulation, and Z_{shale} is the impedance of shale. This relationship has been applied for many years to both sonic and density logs to compute porosities. Our modification is to use the impedance in place of the sonic velocity or density. The second term of the equation is a correction which eliminates the effect of the shale volume fractions in the sand body. Our use of the impedance of brine as the only fluid term will become important below when we then derive "effective oil saturation". The inferred porosity distributions are rather more continuous than the lithology, as is expected since the former is continuous while the latter is categorical (Figures 4.27 and 4.24).

2.3.10 Analysis of the estimated LF reservoir properties

The net sand thickness of the LF reservoir is computed by multiplying the reservoir thickness by the average sand volume fractions within LF sand interval (Figure 4.28). The thinning of the LF sand toward the east is clearly seen. A sharp decrease in sand thickness is found in the eastern part of the reservoir along the structural highs. The boundary between significant and insignificant net sand thickness runs north-south, and does not follow the structural contours. By the time the LF sand was deposited, the minibasin had significant relief, and fresh sediments were transported to the depocenter. Modification to the LF sand thickness by the ocean waves was apparently not significant. The cleaner sands are found in the depocenter, which is in the structural lows (Figure 4.28).

We assess the accuracy of the simulated lithology and porosity distributions by extracting four cross-sections of simulated shale volume fractions and estimated porosities along four well paths (Figures 4.29-4.32). Excellent correlation between the estimated and between resistivity and the estimated porosity are observed. The spatial consistency between the well logs and the simulated lithology and estimated porosity distributions is thus established. In this sense, we have obtained accurate lithology and porosity volumes that both honor the well logs and estimated acoustic impedances.

Calcite precipitation near the top of the LF reservoir sand in the down-dip direction has been observed both in cores and sonic log measurements (Flemings et al., 1996). The thickness of the cemented sand is less than 5 m. Acoustic velocity and density of this interval tends to be greater than that of the sands without such precipitation, but less than that of surrounding shales. Thus seismic amplitudes observed near the top of the LF reservoir are primarily caused by two interfaces. The interfaces are located between the shale and cemented sand and between the cemented sand and uncemented sand. The calcite precipitation causes velocity of cemented sands to increase. The magnitude of such an increase is about one third to one half of the velocity difference between shale and uncemented sand. The increase of velocity in this zone is also observed in the estimated porosity distribution (low porosity zone), which is consistent with the well log data. The characterized main body of the LF reservoir is not significantly affected by the occurrence of calcite precipitation.

In deriving the porosity, the fluid acoustic impedance used in Eq. 4.12 was set to saline acoustic impedance. The estimated porosities may thus be considered "effective hydrocarbon saturation" indicators, because the porosities in the areas saturated with oil or gas are overestimated. Thus, the areas of higher porosities in the LF sand are, in fact, areas of high hydrocarbon saturations, enable us to derive a map of effective oil saturation from the estimated porosity volume (Figure 4.33). Remarkable similarities between the bypassed hydrocarbon map (Figure 4.34) from our 4D acoustic impedance analysis (see Chapter 3) and the derived effective oil saturation map are observed. This observation substantiates the effectiveness of using acoustic impedance to estimate oil saturation. The net oil thickness computed using the effective oil saturations and the reservoir thickness is shown in Figure 4.35. While the distinct oil and water boundaries have been smeared by the thickness of the LF sand, the map indicates that the thickest oil-saturated sand can be found in the depocenter of the LF reservoir.

In the future, we can use the effective oil saturations computed in this way as the soft data and the oil saturations derived from well log and production data as hard data to further simulate the hydrocarbon saturations. These saturations will substantially improve the accuracy of oil field management.

2.3.11 Conclusion

We have presented an integrated method to quantitatively characterize the LF reservoir in the EI-330 Field in terms of lithology, porosity, and effective hydrocarbon saturation. The results show great consistency throughout the LF reservoir and the surrounding shale formations. The constructed lithology models exactly honor the well log data. The porosity model is less accurate than the lithology model because no porosity measurements are available in the study area. Inaccuracy of the estimated porosities is caused primarily by the hydrocarbon saturation in pore spaces. We developed a new concept, that uses the discrepancy to locate hydrocarbons.

In practice, we have found the Markov-Bayes sequential indicator simulation technique to be powerful and robust. The technique systematically integrates the hard and soft data into a statistically optimized 3D model.

Reservoir characterization based on the stochastic simulations is of great importance, especially in the integration of legacy 4D seismic datasets. Multi-disciplinary data, including geological, geophysical, and production data, can all be

AVS analyzed system, and we difference that data set with the Pennzoil and Texaco/Chevron 3-D surveys. An AAPG 3-D Atlas manuscript based upon these interpretations has been accepted for publication in 1996. (we have completed the inversion of the seismic volumes from Shell and Pennzoil and have performed the 4D analysis of them.

2.4.1 Nonlinear inversion of 4D seismic datasets in the Eugene Island Block 330 Field of offshore Louisiana, Gulf of Mexico

2.4.1.1 Introduction

Parameters derived from seismic reflection data have been used to identify hydrocarbon reservoirs for decades. Variations of seismic amplitude, such as bright-spots and flat spots, are associated with oil- or gas-bearing strata. As 3D seismic technologies merge with the reservoir characterization, acoustic impedances estimated from seismic waveforms are becoming more and more important. Unlike seismic amplitudes, which measure the acoustic impedance variations, the acoustic impedance itself is directly associated with petrophysical properties of sedimentary rocks and the fluids that fill pore spaces. The techniques by which the acoustic impedance are obtained are the bridge connecting reflection seismic data and rock petrophysical properties.

Acoustic impedance volumes estimated from 3D seismic surveys have only recently begun to be used in reservoir characterization. The nonlinear seismic inversion technique described in Chapter 1 is a robust method of estimating acoustic impedance. It contains features particularly useful for analyzing 4D (time-lapse 3D) seismic datasets. The time-variant, dynamic wavelet extraction eliminates the differences caused by most of the post-stack seismic processes applied to the various 3D seismic datasets used in the 4D analysis. The low-frequency constraints imposed on the estimated impedance functions can preserve the unchanging nature of the overall regional geological settings. As a result, dynamic changes of reservoir fluids can be imaged.

In this chapter, we have applied our nonlinear seismic inversion technique (see Chapter 1) to two time-lapse 3D seismic datasets to estimate acoustic impedance volumes in the EI-330 minibasin. The same geological and geophysical constraints derived from well log analysis are incorporated into the nonlinear seismic inversion of both seismic datasets. Both the technique and procedure used to construct the acoustic impedance constraints are presented in detail. Independent estimations of the accuracy and reliability of the estimated acoustic impedance are performed using acoustic well logging data. Our seismic inversion technique is found to be stable and consistent throughout the computation.

2.4.1.2 Geological background

The Eugene Island (EI) 330 minibasin is located approximately 270 Km southwest of New Orleans (Figure 2.1), which is one of the most prolific minibasins in the offshore Gulf of Mexico region. The EI-330 minibasin is oblong, approximately 19 Km by 15 Km (11.9 miles by 9.4 miles), and fault-bounded. It sits on a major shelf margin deltaic depocenter of Plio-Pleistocene age. Hydrocarbons of the EI-330 Field are produced from over twenty-five different Plio-Pleistocene sand reservoirs that are segmented into at least a hundred structural and stratigraphic traps (Holland et al., 1990).

Alexander et al. (1995) suggest that the minibasin evolved in three phases: prodelta, proximal deltaic, and fluvial. In the prodelta phase, bathymal and outer neritic shales and turbidites loaded and mobilized an underlying salt sheet. During the proximal deltaic phase, salt continued to withdraw from beneath the minibasin and lowstand shelf margin deltas deposited large volumes of sediment. Regional growth faults bound the northern margin of the minibasin. Sediment accumulation and fault slip rates were high as thick sequences of deltaic sands were deposited adjacent to the fault system. During the final fluvial phase, salt withdrawal waned, and the creation of accommodation space within the minibasin ceased. The minibasin was filled and lowstands deltaic systems prograded southward (Alexander et al., 1995). Most of the hydrocarbon reservoirs discovered in the EI-330 Field were formed during the second and third phases. The seismic data input to the nonlinear inversion has a time window large enough to include all major sand reservoirs in the study area (0-3 seconds).

2.4.1.3 4D seismic datasets: registration and wireline logging database

Since the discovery of the EI-330 Field, more than five hundred wells were drilled to explore and produce this most prolific oil field in offshore US. Gulf of Mexico. Well data collected in this area from several oil companies provide substantial control to the inversion and subsequent analyses. In addition to extensive 2D seismic surveys, three partially-overlapping 3D seismic surveys have been acquired since 1985. Two of the 3D seismic surveys, acquired in 1985 and 1992 (Figure 2.1), were selected for 4D analysis. The overlapping area is centered at the Block 330/331 boundary and covers approximately equal amounts of each block (Figure 2.1). Structurally, this area is situated on the western flank of the Block 330 roll-over anticline, which forms the closure trapping hydrocarbons against the northern growth fault system.

2.4.1.4 Registration of 4D seismic datasets

To date, no 4D seismic dataset has been acquired for the expressed purpose of fluid monitoring in the offshore Gulf of Mexico. The 3D seismic surveys were acquired with different orientations and spacings, and processed with different parameters by different geophysical service companies. Despite these disadvantages, we found that these "legacy" 4D seismic datasets are sufficiently similar to be used for fluid monitoring purposes.

Legacy 4D seismic datasets must be properly registered in space and time. Differences between the results of two surveys can be caused by differences in seismic data acquisition and processing as well as by dynamic changes that occur in the reservoirs. Changes caused by data acquisition and processing must be eliminated before hydrodynamic changes can be identified. Difference caused by acquisition in different directions, at different spacing or different cable length, cannot be corrected after stacking and migration have been performed. Fortunately, modern seismic imaging technologies are much better than a decade ago. Difference due to different directions are often small in areas of low subsurface relief such as the Eugene Island Area. Especially helpful: the 1985 3D survey was re-processed in 1992 using new processing techniques.

The general geology (locations of faults geometry, lithology and porosity) should be in the same location between the surveys. Indeed, the two 3D seismic datasets are remarkably similar, at least in regions where no steeply dipping geological structures (salt and large faults) occur. Salt withdrawal structures do occur in our study area, but do not distort the seismic images of the hydrocarbon reservoirs because they are usually deeper. We assume that the differences observed in the stacked and migrated datasets are dominantly affected by hydrocarbon drainage caused by production and different post-stack processing parameters, and not by different acquisition geometry.

The 1985 seismic survey was acquired in the northwest-southeast oriented lines, while the 1992 survey was acquired in north-south lines (Figure 2.1). The "bin" spacing of the two surveys is also different. A re-gridding process is applied to relocate the two surveys into a common grid before any further seismic analysis is performed. We use an algorithm that interpolates one three-dimensional mesh into another three dimensional mesh slice-by-slice in travelttime and orient the 1985 seismic survey onto the 1992 grid. The algorithm computes the areal weights in a moving window in depth, and interpolates new data values into the destination survey coordinates. After the re-gridding process, only data points common to both surveys are preserved, the rest being assigned null values (Figures 2.2 and 2.3). Seismic sections extracted from these two volumes at the same location from the two volumes are generally similar, although some differences are evident (Figure 2.4) The loss of high frequency content in seismic data becomes significant in the deeper portion of seismic volumes.

Spectral matching between the two seismic datasets is not necessary in the seismic inversion approach to the analysis of 4D seismic datasets, unlike 4D seismic amplitude differencing technologies (Anderson et al., 1995). But phase matching is performed in order to compare the inversion results. Our nonlinear inversion technique (Chapter 1) is capable of eliminating other post-stack processing artifacts using dynamically extracted seismic source functions. However, since the true amplitudes of seismic datasets are unknown, amplitude renormalization must be performed. We first normalize each seismic volume by mapping the histogram of amplitudes onto one another. The normalized seismic traces are rescaled to the proper amplitude by comparing them to synthetic seismograms computed from impedance measurements (i.e., sonic and density logs) from wells in the area. Scaling factors of 0.15 and 0.25 are used for the 1985 and 1992 seismic surveys, respectively. The extracted seismic source functions are normalized to unity so that the reflectivity functions derived from the estimated acoustic impedances are realistic (i.e., within the range of ± 0.15). Normally, Tertiary sedimentary basins filled with sand and shale sequences have true seismic amplitudes less than ± 0.3 .

2.4.1.5 Digital wireline logging database

The nonlinear inversion of seismic data requires a good *a priori* reference model. There are more than seventy wells in our study area overlapped by the two seismic datasets (Figures 2.2 and 2.3). However, sonic and bulk density logs which are needed to compute impedance are only available in fourteen of these wells. The limited sonic data availability may be overcome by using the correlation between sonic and other logs to empirically calculate a "pseudo" sonic log (a common technique in petrophysical analysis). In wells without density logs, we use the inverse Gardner relationship to calculate density logs from measured or estimated sonic logs (Gardner et al., 1976).

2.4.1.6 Well log analysis for the impedance inversion

The band-limited nature of observed seismic datasets requires that the estimated acoustic impedance functions, i.e., the short-wave length model parameter (Tarantola, 1982 and 1984), should also be within a confined frequency bandwidth in order to have physical meanings. Detailed trend analysis for predicting long-wavelength constraints on impedance is essential. Such constraints derived independently from acoustic measurements in wells, not only increase accuracy of the estimated impedance, but also stabilize the iterative seismic inversion (He et al., 1995). The low-frequency impedance constraints derived from well logs are sufficient to allow our nonlinear seismic inversion to converge on true acoustic impedance solutions.

2.4.1.7 The principles of wireline logging and data interpretation

Geophysical log data are recorded using probes which are lowered on the end of a wireline through the drillpipe and into the previously drilled borehole. The depth at which the measurements are made is determined by measuring the length of cable run into the hole. Modern logging technologies can measure many different physical properties. Three major types of log data are in general available for well data analysis: electrical, radioactive, and sonic logs. The well log database in our study area includes natural gamma ray (GR), spontaneous potential (SP), resistivity (RES), induction (ILD), bulk density (RHOB), sonic (DT), and caliper (CALI) measurements. Some wells also contain porosity measurements made on side-wall cores.

The natural gamma ray log utilizes a scintillation detector to measure the natural radiation emitted by the rocks surrounding the borehole. The response of the tool is a simple function of the concentration by weight of radioactive materials and the rock density. The average investigation depth into sedimentary formations is about 0.3 m, and

actual resolution is 0.15 m. GR is used principally as a sand/shale discriminator since shales contain abundant radioactive minerals such as clays, whereas sandstones do not.

Density is measured by the lithodensity logging tool. A radioactive source is mounted in the tool body, and a bow-spring forces it and a pair of detectors against the borehole wall. The two detectors measure the returned flux of scattered gamma rays in a series of energy bands, which is used to determine formation density (RHOB) and photo-electric factor (PEF). A measure of tool performance based on the energy distribution at the near and far receivers (DRHO) is also provided. The interaction between the gamma ray and electrons in the formation causes Compton scattering. The density logging tool measures electron density directly, and formation density is determined using the fact that in most rock-forming elements atomic weight is roughly twice atomic number. This measurement is almost independent of porosity and can be used as a matrix lithology indicator. The depth of investigation of the lithodensity tool depends on the density of the rock: the higher the density, the lower the penetration. In porous and permeable formations, the density tool does not read deeper than 0.15 m. The vertical resolution is about 0.3 m.

The array induction tool string indirectly measures electrical resistivity and gamma ray "shaliness", which are related to porosity and hydrocarbon content. The array induction tool is a resistivity logging device that provides measurements of spontaneous potential (SP) and resistivity. Resistivity is reported for three different depths (deep, medium, and shallow).

Differences between shallow and deep resistivity measurements can be related to the invasion of drilling fluids into permeable horizons. Resistivity is controlled mainly by the amount and connectivity of the porosity and the conductivity of the pore fluids, since the solid constituents are orders of magnitude more resistive than pore fluids in most rocks.

Sonic tools are designed to measure the compressional wave velocity of the rock surrounding the borehole. The sonic tool can be thought of as a miniature seismic refraction experiment carried out within the cylindrical borehole. The tool is centered in the hole by means of bowsprings, and contains one or more acoustic sources and receivers. A source emits acoustic waves that are transmitted into the borehole fluid. A refracted compressional wave is generated when the wavefront impinges on the borehole wall. Waves arrive at the receivers at a time which is linearly proportional to their offset from the source. Compressional wave velocities can be determined by differencing the arrival times at multiple receivers a known distance apart.

The Caliper log measures wellbore diameter, and is run at the top of both array induction and sonic combinations. It is primarily used to indicate "washouts", where other logs may read inaccurately, and to correct logs whose response is sensitive to hole diameter. However, caliper response can also be indicative of lithology. For instance, in zones with swelling clays, hole constrictions are observed where the caliper reads less than the bit size. Variations in hole diameter may correlate with lithologic changes, since hole conditions are in general a consequence of rock properties.

Lithology can be obtained from GR and SP logs. Resistivity and induction logs are used to identify pore fluid composition. Formation porosity is one of the primary physical property measurements made in a wellbore, and direct measurements are made by neutron logging tools. The difference between thermal and epithermal neutron porosity is a measure of the amount of bound water in clay minerals. Since neutron logging tools were not run in most of production wells drilled in the study area, porosities in our wellbores are indirectly derived from sonic, density, and resistivity logs. The relationship between resistivity and porosity has been quantified by "Archie's Law" (Archie, 1942), which relates the resistivity to an inverse power of the porosity. This empirical relationship works reasonably well in the sands found in hydrocarbon reservoirs.

2.4.1.8 Well log interpretation for nonlinear seismic inversion

The estimated acoustic impedance functions are sampled in traveltime whereas well logs are sampled in depth. We converted logs from depth to two-way traveltime using sonic logs and velocity measured by "checkshot" vertical seismic profiles (VSP). Synthetic seismograms, generated from the sonic logs, are compared with seismic data to verify the depth-time conversion.

2.4.1.9 Acoustic velocity and density logs estimated from other logs

Empirical relationships between well logs have been widely used in the oil industry for many years. In wells that have only density logs, the pseudo-sonic velocity can be estimated using the Gardner's relationship (Gardner et al., 1974):

$$V = \left(\frac{\rho}{2.1} \right)^4, \quad (2.1)$$

where V is the sonic velocity and ρ is the bulk density. In wells with neither sonic nor density logs, the pseudo-sonic log can be computed from porosity, ϕ , shale volume fraction, f , using the time-average equation:

$$\frac{1}{V} = \frac{\phi}{V_f} + (1 - \phi) \left[\frac{f}{V_{shale}} + \frac{(1 - f)}{V_{sand}} \right]. \quad (2.2)$$

Here V_f is the acoustic velocity of pore fluids, V_{shale} is the acoustic velocity of pure shale and V_{sand} is the acoustic velocity of pure sand. Using the gamma ray logs, sand and shale compaction curves can be regressed from the extracted pure sand and shale reciprocal velocity in depth (Figure 2.6). The sand and shale compaction curves in the study area are given by:

$$\begin{cases} V_{sand}^{-1} = 199.47 - 2.6 \times 10^{-2} \cdot z + 3.01 \times 10^{-6} \cdot z^2 - 1.16 \times 10^{-10} \cdot z^3 \\ V_{shale}^{-1} = 213.84 - 3.0 \times 10^{-2} \cdot z + 2.96 \times 10^{-6} \cdot z^2 - 9.73 \times 10^{-11} \cdot z^3 \end{cases} \quad (2.3)$$

respectively, where V_{sand} and V_{shale} are velocities of sand and shale in m/s, and z is the depth in meter. The sand and shale compaction curves intersect each other at about 1,067 m, indicating that the acoustic velocity of shale sequences exceeds that of sand sequences at greater depth.

The fractional porosity, ϕ , in Eq. 2.2 can be computed from resistivity logs using Archie's Law (Archie, 1942):

$$\phi = \frac{\alpha}{R^n}, \quad (2.4)$$

where α and n are constants empirically determined and R is resistivity in $\Omega - m$. $\alpha = 0.125$ for sand and 0.08 for shale, and $n = 0.5$ in our study. Fractional shale volumes, f , can be computed by (Brock, 1984):

$$f = \beta_1 (2^{2.9 \cdot GR_{indx}} - 1) \quad (2.5)$$

or

$$f = \beta_2 (2^{2.9 \cdot SP_{indx}} - 1). \quad (2.6)$$

Here f is the shale volume fraction, β_1 and β_2 are empirical constants (we use 0.21), GR_{indx} and SP_{indx} are gamma ray and spontaneous potential indices, respectively. GR_{indx} and SP_{indx} are computed from the equations (Schlumberger Log interpretation Principles/Application, 1989):

$$GR_{indx} = \frac{GR - GR_{sand}}{GR_{shale} - GR_{sand}} \quad (2.7)$$

and

$$SP_{\text{indx}} = \frac{SP - SP_{\text{sand}}}{SP_{\text{shale}} - SP_{\text{sand}}} \quad (2.8)$$

Here GR and SP are the measured gamma ray intensities in API and spontaneous potential in mV respectively. The subscripted quantities represent the sand and shale baseline values read from the corresponding logs.

Velocity-depth profile varies laterally due to formation structure and stratigraphy. We compensate by adjusting the regressed sand and shale compaction curves according to stratigraphic horizons in our study area. For example, the structure maps of two sand tops (the tops of JD and LF reservoirs) indicate that the sands dip about 20 degrees westwards along the west flank of the EI-330 roll-over anticline (Figure 2.7). The regressed sand and shale compaction curves are adjusted for the amount of structural uplift at each well location by an amount determined from wells with sonic measurements. The low-frequency trends are consistent with both geological structure, and direct measurements made in neighboring wells. Both the measured and estimated pseudo-sonic logs were then used to compute acoustic impedance logs and to convert logs in depth to logs in two-way traveltime.

When no density log is available for a well, the pseudo-density log can be computed from the sonic log by using the inverse Gardner relationship:

$$\rho = 2.1 \cdot V^4 \quad (2.9)$$

Here ρ is density and V is the acoustic velocity.

Calibrations are performed on wells with full suites of log measurements to determine the constants in the above empirical relationships. Figure 2.8 shows the comparison between the measured and computed sonic and density logs in well 331_SH_A-1. Due to the crossover of the sand and shale compaction curves, the sand sections are high-velocity anomalies in the shallow portion of the well (above 1067 m) and are low-velocity anomalies at depth. We can see that the estimated velocity and density logs are very similar to the measured logs. The low-frequency trend in the estimated pseudo-velocity log agrees with the measured trend as well. The relative error between the estimated and measured velocity logs is 6% and that of density logs is 6.7%. The comparison between the estimated acoustic impedance logs is shown in Figure 2.9. The average relative error between the estimated and measured impedance logs is 5.5%. The velocity, density, and acoustic impedance logs are in agreement throughout the depth range, justifying the use of the empirical relationships. These results also indicate that superimposing the regressed low-frequency trend of velocity to the high-frequency velocity variations derived from resistivity and lithology logs is viable. We will also use only the low-frequency impedance functions to constrain the estimation of high-frequency impedance functions.

The seismic section in Figure 2.9 is an arbitrary seismic line extracted from the 1985 seismic survey. Several sand tops identified in well logs show good ties with the corresponding seismic reflectors in traveltime (Figure 2.10).

2.4.1.10 *A priori* acoustic impedance model construction

The nonlinear inversion employs a one-dimensional inversion algorithm. An *a priori* impedance model has to be constructed for each trace of both 3D seismic surveys. We use impedance logs from twelve wells with sonic and density measurements in the study area to construct the reference impedance model. The acoustic impedance logs from these twelve wells are first analyzed to extract compaction trends at each location. Depth is then converted to two-way traveltime using the velocity logs at each well (Figure 2.11). We then construct a 3D impedance model by linearly interpolating these impedance trend curves into the common seismic grid. The interpolated 3D impedance model contains only the low-frequency trend of the acoustic impedance function. Each

vertical trace of this model is then treated as the *a priori* impedance model and the initial model for the corresponding seismic trace.

Data and model space covariance functions are also needed to constrain the inversion process, in addition to an *a priori* impedance model. These covariance functions represent uncertainties associated with data and model parameter optimizations. Details are addressed in the next section.

2.4.1.11 Nonlinear inversion of 4D seismic datasets

The two seismic datasets are independently inverted with the same *a priori* low-frequency impedance and initial impedance models. The covariance functions that describe uncertainties in estimated impedance functions and the observed seismic traces are treated in the same manner for each seismic trace of both seismic surveys, so the inversion of the two seismic datasets is under a uniform constraints and uncertainties.

2.4.1.12 Dynamic extraction of seismic source functions

The first step of the full-scale nonlinear seismic inversion is to extract seismic source functions from the observed seismic trace. We dynamically extract a time-variant source function from each seismic trace in the dataset. The time-variant source function actually contains three source functions that are applied to different time windows within the seismic trace. These source functions are determined from a moving-window autocorrelation function computed for each seismic trace, along with assumption that they are zero-phase. These dynamic source functions eliminate data processing artifacts that were introduced by using different processing parameters after the stacking and migration processes. Using the method, the spatial variation of frequency bandwidth of the impedance function in the estimated acoustic impedance volumes are made internally consistent.

Two seismic traces extracted from the same location of the 1985 and 1992 3D seismic surveys are shown in Figure 2.12. The corresponding time-varying autocorrelation functions are shown in Figures 2.13 and Figure 2.14. The two traces have significant differences in frequency content and shape. The trace from the 1992 survey has the higher data quality, but its frequency content is lower than that of its 1985 counterpart. Frequency segmentation observed in both traces suggests that three seismic source functions are necessary to properly retain the frequency bandwidth of the estimated impedance functions, acting in three distinct time windows (0-1 seconds, 1-2 seconds and 2-3 seconds) (Figures 2.13 and 2.14). Similar behavior is observed in other traces within the surveys, leading us to use three seismic source functions in three time windows for the inversion.

2.4.1.13 Estimation of impedance volumes from 4D seismic dataset

We focus on seismic data from 0.9 to 2.8 seconds two-way traveltimes. Each seismic trace in these surveys is sampled at 4 ms interval and contains 476 samples. The full-scale nonlinear seismic inversion is applied to each seismic trace of both surveys independently. The similarity in the estimated acoustic impedance volumes is an independent check of the success of the inversion.

The seismic data contain multiple reflections, side reflections, and noise which affect the quality of the inversion. This contamination is modeled as random noise described by a Gaussian data covariance functions. Uncertainty in the model parameters are also modeled by a Gaussian distribution law. The *a priori* acoustic impedance at each sample location is expressed in terms of a mean and a covariance. The covariance expresses our degree of certainty that the true impedance is close to the *a priori* impedance. We use the low-frequency impedance model derived from well logs in section 2.4.4 as the *a priori* impedance. The variance of the impedance is taken to be about 20% of its mean.

The computational steps taken in the inversion of 1985 and 1992 seismic volumes are summarized as follows:

Step 1: Extract the time-varying seismic source functions, W_i ($i = 1, 2, 3$), from the seismic trace, d^{obs} . Seismic source functions for each seismic trace are extracted independently throughout the seismic volume.

Step 2: Construct the a priori reference model of the impedance function Z^{ref} using log data in the entire seismic volume (we used only twelve wells with impedance measurements, other wells are used to examine the inversion results). Its covariance function C_m is given by:

$$[C_m]_{ik} = (\sigma_i^m)^2 \exp \left\{ -0.5 \left[\frac{(t_i - t_k)^2}{L_v^2} \right] \right\}, i = 0, 475. \quad (2.10)$$

Here σ_i^m is a variance of the i -th sample of the impedance function (20% of the *a priori* impedance), and L_v is the time window over which one expects the estimated impedance to be smooth, $L_v = 28$ ms (7 samples at the 4 ms sample rate).

Step 3: Construct the covariance function of the seismic data, C_d , using:

$$[C_d]_{ik} = (\sigma_i^d)^2 \exp \left\{ -0.5 \left[\frac{(t_i - t_k)^2}{L_v^2} \right] \right\}, i = 0, 475. \quad (2.11)$$

Here σ_i^d is the variance of seismic amplitude at the i -th sample (taken as 10% of the absolute maximum seismic amplitude of the entire seismic volume). The correlation length, L_v , is also set to 28 ms (7 samples at the 4 ms sample rate).

Step 4: Compute the objective function, $F(\mathbf{m}^{(0)})$, starting from an initial impedance function, $Z^{(0)}$. We set the initial model equal to the *a priori* impedance, Z^{ref} . The modeled seismic trace $d_m^{(0)}$ is generated by convolving W_i ($i = 1, 2, 3$) with the reflectivity function derived from $\mathbf{m}^{(0)}$ in the three different time windows. The objective function, $F(\mathbf{m}^{(0)})$, at $\mathbf{m}^{(0)}$ is then computed as:

$$F(\mathbf{m}^{(0)}) = (d^{obs} - d^{(0)})^T [C_d]^{-1} (d^{obs} - d^{(0)}) + (\mathbf{m}^{ref} - \mathbf{m}^{(0)})^T [C_m]^{-1} (\mathbf{m}^{ref} - \mathbf{m}^{(0)}). \quad (2.12)$$

Step 5: Compute the gradient matrix of the objective function with respect to each model parameter by using the forward difference algorithm:

$$\frac{\partial F(\mathbf{m}^{(0)})}{\partial m_j} = \frac{F(\mathbf{m}^{(0)} + \delta m_j) - F(\mathbf{m}^{(0)})}{\delta m_j}. \quad (2.13)$$

Step 6: Reduce the objective function $F(\mathbf{m}^{(0)})$ by searching for a perturbation, $\Delta \mathbf{m}$, which updates the current model, $\mathbf{m}^{(0)}$. This step is accomplished in the modified Levenberg-Marquardt algorithm. The new model $\mathbf{m}^{(1)} = \mathbf{m}^{(0)} + \Delta \mathbf{m}$ becomes the current model.

Step 7: Test for convergence. Terminate the iteration when the relative reduction of the objective function in two consecutive iterations is less than 1.0×10^{-8} or if the objective function is less than 1.0×10^{-6} . Otherwise, the inversion process reverts to Step 4.

Estimated impedance volumes, and corresponding wavelet (source function) volumes have been derived for the 1985 and 1992 datasets (Figures 2.15-2.18). The seismic source function volumes differ in both frequency content and smoothness, with the 1992 source functions being smoother.

2.4.1.14 Discussion and conclusion

Like the seismic volumes, the estimated 1985 and 1992 acoustic impedance volumes are in general similar to one another. However, significant small-scale differences, occur. These changes are possibly caused by hydrocarbon production drainage in reservoirs.

Vertical wells drilled in offshore oil fields are rare, most of the wells were drilled with deviations. Thus the best way to compare the estimated impedance functions with the measurements from logs is to use arbitrary impedance cross-sections that follow the deviation pattern of the wells. Figure 2.19 (a) is the G-G' cross-section extracted from the 1985 impedance volume that passes platform A in Block 331 and platform B in Block 330. Figure 2.19 (b) is the same cross-section extracted from the 1992 impedance volume. For clarity, only two wells, 331_SH_A-23 and 330_PZ_B-9, drilled exactly along this section (Figure 2.19 (a) and (b)) are displayed along with the seismic data. The sonic and GR logs are displayed along well path. Sonic logs are displayed to the left of the well path, and GR logs to the right. Excellent match can be seen between the sonic logs and estimated impedance section along the well paths on both sections. The low impedance anomalies are often correlated to the hydrocarbon reservoirs.

There is significant evidence for hydrocarbon drainage from areas of low impedance observed in 1985. In 1992, these regions have patched of both increased impedances and decreased impedances. The increase in acoustic impedance often indicates that reservoir voids which were occupied by hydrocarbons in 1985, have been replaced by formation brine by 1992 (Anderson et al., 1995).

2.4.1.14.1 Accuracy and reliability of estimated impedance volumes

Evaluation of the estimated acoustic impedance volumes is usually difficult to implement because we do not have exact knowledge of the acoustic properties in the entire sediment volume. We analyze the accuracy and reliability of our inversion results by examining the estimated impedances by using sonic, density, GR, and resistivity logs. These well logs are well-correlated to the acoustic impedance, in general. Because the initial and *a priori* impedance models are based on only the low-frequency part of impedance logs, the high-frequency data from those wells constitute independent data.

We compare the estimated acoustic impedance volume of the 1992 survey to these independent well log data. Figure 2.20 shows the structure map of the top of LF sand, one which, we have annotated the locations of cross-sections, C-C', D-D', E-E', F-F', and H-H'. These acoustic impedance cross-sections along with the well logs which intersect the cross-sections are illustrated in Figures 2.21-2.25. Good agreement between the location of hydrocarbon reservoirs and low acoustic impedance anomalies is observed on all of these cross-sections.

We plotted the measured impedance log in a vertical well, 331_SH_1, against the estimated acoustic impedance function in Figure 2.26. The estimated impedance function has the same low-frequency trend as the impedance log. The high-frequency content in the estimated impedance is not as high as that of the impedance log. However, the relative error between the impedance log and the estimated impedance function in well 331_SH_1 is small, only 8.0%. A good linear correlation is observed between the impedance log and the estimated acoustic impedance (Figure 2.27). Similar results were also obtained from several other logs.

These tests demonstrate that the estimated acoustic impedance volumes are acceptable for use in 4D and other geological analyses. Although the estimated impedance function has less resolution than the sparsely-distributed well logs, the lateral continuity makes the impedance results much more useful.

2.4.1.14.2 Conclusion

We have developed a full-scale, nonlinear 4D seismic inversion technique to invert two time-lapse, 4D seismic volumes under low-frequency acoustic impedance constraints. Prior to the inversion process, *a priori* information about the acoustic impedance model is constructed from a limited number of wells that have sonic and density logs. We do not use all available wells to construct the reference impedance model, so that control wells can be used after the inversion to analyze the reliability and accuracy of the computed impedance volumes. Independent examinations of the estimated acoustic impedance volumes using these control well logs indicate that the inversion is able to recover accurate acoustic impedance functions to less than $\pm 10\%$. The consistency observed between impedance volumes suggests that our nonlinear inversion avoids serious artifacts.

The geological features observed in the two impedance volumes are remarkably similar. Good agreements between the estimated impedance functions and well logs are observed, suggesting that the nonuniqueness of the estimated impedance volumes is not significant. The impedance volumes are now ready for 4D seismic monitoring analysis (Task 2.5) and reservoir characterization (Task 2.3).

Time-varying seismic source functions are also obtained for all seismic traces in the two inverted seismic data volumes. These wavelets may be of some usefulness in estimating spatial frequency variations caused by both acquisition and processing variability. We have not implemented phase adjustment into source extraction process. In the future, such refinements may further improve the inversion process.

Our estimated impedance volumes are well-behaved and laterally continuous. We believe that the integration of high lateral resolution from the estimated acoustic impedance volumes and high vertical resolution from sparsely-distributed well logs can be used to achieve a much better characterization of changes in oil and gas reservoirs over time than today's standard analysis techniques.

References

- Alexander, L., and P.B. Flemings, 1995, Geologic evolution of a Plio-Pleistocene salt-withdrawal minibasin: Eugene Island Block 330, Offshore Louisiana: American Association of Petroleum Geologists Bulletin, v. 79, p. 1737-1756.
- Anderson, R.N., A. Boulanger, W. He, Y.F. Sun, L. Xu, and B. Hart, 1995, 4-D seismic monitoring of drainage in the Eugene Island 330 Field in the offshore Gulf of Mexico: American Association of Petroleum Geologist special publication, in press.
- Archie, G.E., 1942, The electrical resistivity log as an aid in determining some reservoir characteristics: Transactions AIME 146, p. 54-62.
- Brock, J., 1984, Analyzing Your Logs, Vol. II-Advanced Open Hole Log Interpretation: Petromedia, Tyler, 173 p.
- Gardner, G.H.F., L.W. Gardner and A.R. Gregory, 1974, Formation Velocity and Density-The Diagnostic Basics for Stratigraphic Traps: Geophysics, V. 39, No. 6, p. 770-780.
- He, W., R.N. Anderson, and Y.-C. Teng, 1995, Application of seismic inversion to quantitative mapping geopressure transition zones in the Pleistocene, offshore Louisiana, Gulf of Mexico: The 2nd International Conference on Theoretical and Computational Acoustics, Honolulu, Hawaii.
- Tarantola, A., and B. Valette, 1982, Inversion = Quest for information: Geophysics, v. 50, p. 159-170.
- Tarantola, A., 1984, Inversion of seismic reflection data in the acoustic approximation: Geophysics, v. 49, p. 1259-1266.

2.5.1 4D seismic monitoring of subsurface fluids in the EI-330 Field of offshore Louisiana, Gulf of Mexico

3D seismic images have improved to the point that they are being applied to reservoir production and engineering problems. 4D (time-lapse 3D) seismic imaging may soon be applied to oil field monitoring. However, this technology will require a better understanding of the link between stratigraphy, fluid content and changes in seismic response.

Time-dependence of individual reservoirs have long been observed in production wells. The use of 4D seismic datasets to monitor fluid movements dates back to more than a decade when thermal and CO₂ injection enhanced oil recovery projects were carried out (Nur, 1982; Dunlop et al., 1988 and Breitenbach et al., 1989). Petrophysical studies indicate that seismic datasets may be used to monitor subsurface fluid movement in sandstone reservoirs saturated with medium-to-light weight hydrocarbons (Wang et al., 1992). The acoustic contrasts caused by lightweight, gas saturated hydrocarbons (oils with high gas:oil ratio, GOR) can produce even greater seismic amplitude changes.

Changes in seismic amplitude within a given reservoir can be caused by changes in gas:oil:water ratios, fluid pressures and/or fluid contact levels. Time-lapse 3D seismic surveys acquired can quantify these changes. These seismic datasets can be used to decipher both temporal and spatial distributions of oil, gas and water in reservoirs under production. We believe that such 4D seismic technologies, integrated with petrophysics and other related multi-disciplinary principles, will become the industry standard in hydrocarbon exploitation.

4D seismic technology is still in its infancy. New techniques are being developed yearly, as the great potential of using such datasets in reservoir surveillance and management is recognized (Nur, 1989; Lumbly, 1995; Anderson, et al., 1995a, 1995b and 1995c).

In order to extract 4D seismic changes, we examine successive 3D seismic surveys and examine their similarities and differences. The temporal changes allow us to predict the locations and compositions of bypassed hydrocarbons. We also use wireline logs (sonic, density, porosity, oil saturation variations over time) and production data (pressure, water cut, GOR variations over time) to calibrate our models of acoustic impedance changes. The model results will allow us to predict the quantitative changes in seismic response.

Because the time-lapse 3D seismic datasets used in this study were acquired for other purposes, we must pay special attention to their registration in space and time. The acquisition and processing parameters of different surveys were not the same, and thus we must correctly register the seismic datasets to preserve the maximum amount of common information of these surveys.

Despite these disadvantages, the results obtained from analyzing these "legacy" datasets are rather encouraging. Elimination of artifacts caused by differences in data processing enables us to distinguish the actual acoustic changes in hydrocarbon reservoirs. Many such legacy 4D seismic datasets are available, especially for the producing oil fields in the offshore Gulf of Mexico. We expect that the application of 4D seismic techniques to these seismic datasets will result in the recovery of a large volume of bypassed oil. Nevertheless, much research will be needed to advance 4D seismic techniques so that they can be used to view of the true dynamic of the drainage of oil and gas from reservoirs.

In this chapter, we present a seismic amplitude analysis technique, applied to the LF reservoir in the Eugene Island 330 Field. A 4D seismic dataset consisting of two 3D seismic surveys (acquired in 1985 and 1992, respectively) is used to locate regions where seismic amplitudes have changed over time. These changes are qualitatively analyzed in term of brightening, dim-outs, and unchanged areas that might contain bypassed hydrocarbons (pay). We then examine the spatial and temporal changes in acoustic

impedance, as determined by the nonlinear 4D seismic inversion techniques described in Chapter 2. The changes in the estimated 4D acoustic impedances are better imaged than those changes observed in seismic amplitudes alone.

2.5.2 Seismic prediction of dynamic changes in hydrocarbon reservoirs

Laboratory experiments indicate that the acoustic reflection coefficients varies with oil, gas and water mix, effective pressure and temperature (Wyllie et al., 1958; King, 1965; Domenico, 1976; Gregory, 1976 and Wang et al., 1988). This behavior is also observed in the field in water and steam floods, which have produced noticeable acoustic differences over time (Nur, 1982 and 1989; Dunlop et al., 1988; Breitenbach et al., 1989 and Wang et al., 1992).

Changes in seismic data expected from the production of hydrocarbons in the LF hydrocarbon reservoir are summarized using a simple seismic modeling approach (Figure 3.1). Seismic amplitudes were modeled by varying the acoustic properties across a hypothetical, constant thickness sandstone reservoir undergoing pressure depletion and GOR changes. The 1985-1992 petrophysical changes match the production data for the LF reservoir. The acoustic property changes are computed using the experimental data from Ottawa sand (Domenico, 1976). The changing gas/water contact (G/W), gas/oil contact (G/O), and oil/water contact (O/W) also causes changes in seismic amplitudes across the reservoir boundaries. Effective pressure (overburden pressure minus pore fluid pressure) increases as hydrocarbons are drained from a reservoir, reducing seismic amplitudes in both oil and gas sands. If, however, a GOR increase occurs during production, as with the formation of a secondary gas cap, seismic amplitudes are predicted to increase (brighten) over time, because the acoustic affects of the fluid change dominate over the pressure depletion affects. Similarly, seismic amplitudes can dramatically decrease (dim-out), if, in addition to pressure depletion of a high GOR oil, the O/W contact migrates across a reservoir. The amplitude decrease caused by pressure depletion is further enhanced by the drop in the impedance contrast caused by the replacement of low velocity oil and/or gas by relatively high velocity water.

Our seismic modeling investigation suggests that bypassed hydrocarbons are associated with near-zero changes in regions of high seismic amplitude over time, if there has been little change in effective pressure (as within a water-drive reservoir). Areas of sustained high seismic amplitudes are either the highest permeability drainage pathways through which the hydrocarbons move, or isolated pressure compartments that are not connected to the wellbore drainage system. Bypassed hydrocarbon can be located on the basis of changes in seismic amplitudes only after the cause for impedance changes is understood.

2.5.3 4D seismic monitoring technology

Our 4D seismic analysis technology consists of imaging, feature extraction, and pattern recognition functions, coupled iteratively with high resolution, seismic forward and inverse modeling. Due to the practical limitations, systematic seismic forward modeling methods are only discussed briefly because they are still being developed. Pattern recognition, rather than interpolation and recomputation, is used to examine similarities and differences among the seismic amplitudes and acoustic impedances of the datasets in the hope that we can use large amount of legacy 3D seismic datasets to monitor hydrocarbon drainage and to locate bypassed pay in the mean time.

2.5.4 The Eugene Island Block 330 Field

The Eugene Island Block 330 (EI-330) Field is located approximately 270 Km south-west of New Orleans (Figure 3.2). This field has produced more than 7.9×10^7 m³ (equivalent to 5×10^8 barrels of oil) since 1972. The oil and gas are produced from more than twenty-five stacked sand reservoirs in roll-over anticlines abutting against the large

growth fault system (the Red fault) and associated smaller antithetic faults (e.g., the F fault in the study area).

The ongoing development of this field and the remarkable amount of seismic, production, geological and wireline data available from the field make it an ideal location to research the effects of production and fluid migration on changing acoustic (seismic) signals over time. Multiple vintages of 3D seismic data, large amounts of digital wireline logging data, and production histories from multiple wells enable us to study the reservoir fluid dynamics of the LF in great detail within the EI-330 Field.

The study area in this chapter is centered along the Block 330/331 boundary where two vintages of 3D seismic surveys overlap. The two 3D seismic surveys are the 1985 survey centered on Block 330 and the 1992 survey centered on Block 331 (Figure 3.2 (b)). Well logs and production data from nineteen wells are available in the overlap area (Figure 3.3). Combined stratigraphic, structural and seismic attribute analyses of the legacy 3D seismic datasets have shown how depositional features and faults compartmentalize reservoirs in this field. Geopressures in the study area are also predicted and characterized (He et al., 1995a and 1995b) as part of the larger study contained in Chapter 5. It is believed that hydrodynamic disequilibrium that has produced dramatic variations along the top-of-geopressure surface over short distances in the minibasin, coupled with periodic fluid release up the large regional growth fault system, is the primary cause for the active hydrodynamic fluid flow in this region. The well-connected aquifer supporting the water drive mechanism within the LF is one result from this dynamic system.

2.5.5 4D seismic data registration

Amplitude measurements from two 3D seismic surveys cannot be directly used because the data acquisition and processing parameters applied to them originally were very different. Seismic attributes, such as amplitude, phase, and frequency bandwidth, differ considerably. We use spectral matching, amplitude normalization, and phase corrections to correct the data.

The 1985 and the 1992 3D seismic surveys were first re-binned into the same common grid described in Chapter 2. When comparing the two 3D seismic volumes acquired seven years apart, navigation errors may have been introduced because the resolution of navigational systems at sea has been constantly improved. In our case, we found that there is a 62 m displacement in the east-west direction between the two seismic volumes. The offset was determined from a global cross-correlation between the two seismic volumes in both the north-south and the east-west directions. The global cross-correlations are computed from sequential time slices through the entire two volumes.

The frequency bandwidth of the 1985 volume differs from that of the 1992 seismic volume because seismic sources have been steadily improved over the years. To match the frequency bandwidth, we first computed the global frequency spectrum of each volume, determined the bandwidth that common to both, and used it to bandpass filter both datasets. A zero-phase filter is used (Figure 3.4).

Different static shifts were applied to seismic datasets in the original processing. We correct for this shift by cross-correlating corresponding traces to determine the relative offset. The offset is then averaged over all the seismic traces, and the average is applied to the 1985 seismic survey to correct it to that the 1992 survey (Figure 3.5).

Phase shifts between legacy seismic surveys are determined using a cross-correlation technique to determine the phase angle difference between the two volumes. We held the seismic traces from the 1985 survey fixed, while phase-shifting the traces of the 1992 survey with all possible angles (0-360 degree). The phase angle that maximizes the correlation between the two traces is applied to the 1992 survey to correct it (Figure 3.6). Numerical experiments carried out in our volume matching techniques indicate that

the matching of conventional post-stack seismic volumes can be best performed by applying time-variant filters to different time windows because the seismic waveform characteristics vary with traveltime (Figure 3.7 and Chapter 2).

Amplitudes of the two seismic volumes are normalized by requiring that the cumulative amplitude histograms of the two seismic volumes be similar. The two surveys have rather different amplitude distributions (compare Figure 3.8 (a) with 3.8 (b)). We choose the 1992 seismic volume as the amplitude reference, performed a global histogram renormalization of the 1985 survey (Figures 3.8 (c) and 3.8 (d)). The amplitudes are rescaled by a factor appropriate for real acoustic variations in the earth by comparison with synthetic traces computed from sonic and density logs.

The corrected 4D dataset are shown in Figure 3.9 and Figure 3.10, and two cross-sections are shown in Figure 3.11. Amplitude of the two surveys are generally similar, but significant differences occur within the producing reservoirs. We will next focus on the time window from 1.7 to 2.2 seconds, which includes the LF reservoir, to perform our 4D seismic analysis.

2.5.6 The LF reservoir in the study area

The LF reservoir is centered along the boundary of blocks EI-330/331 (Figure 3.12). It dips gently to the west from the crest of the roll-over anticline in the center of EI-330, and is bounded on the north by the south-dipping B fault and on the south by the north-dipping F antithetic fault. It is one in a stack of reservoirs (JD-KE-LF) that are main oil and gas producers in the field. Structural dips are of the order of 10-20 degrees, and the sand top deepens from about 2,012 m (6600 ft) to over 2,316 m (7,600 ft) in this fault block. Figure 3.16 also shows the locations of production wells, and the positions of estimated fluid contacts at the beginning of production in 1972 and those estimated at the beginning of our 4D study in 1992, indicating their movement with time as interpreted from the production data. The regions in red are the original gas cap. Regions in pink are areas that have had oil replaced by gas due to expansion of a secondary gas cap down-dip. Regions in green are predicted to be oil-filled and are thought to have undergone no change in fluid composition. Regions in dark blue are water. Regions in light blue in the west are water sweep occurred since 1972. This figure shows a large region to the west that has been water swept between 1972 and 1992, whereas between the wells 330_PZ_C-18 and 330_PZ_A-16ST to the east of the 330/331 block boundary, a secondary gas cap has grown between the time production started in 1972 and 1992. Low permeability gas is also detected from logs near the crest of the structure (regions in dark pink). The original oil-water contact in the LF reservoir is interpreted to be at the 2,307 m (7,568 ft) level from the production data. Uniform, gravity-driven, up-dip movement of the oil-water contact is predicted from production data. The oil-water contact as deduced from the sparse well data is not horizontal in 1992, but appears to cut across structural contours in the south of the F fault. The dip could indicate that the thick LF sand located in these zones is more permeable, and fluids are being preferentially drawn from these high quality sands.

2.5.7 4D Seismic amplitude analysis technique

2.5.7.1 The region-growing algorithms

In practice, the amplitude normalization, frequency and phase matching techniques cannot totally correct for differences in original seismic surveys, so the match is never perfect. The inter-comparisons are accomplished in attribute-derivative space since we have found that only the lowest frequency in amplitude spectra preserve the best commonality among the differently-processed seismic datasets. Comparison based on wavefield envelope are more robust than those based on the seismic trace itself. Therefore, we use the reflection strength, or instantaneous amplitude (Taner et al., 1979;

also see Appendix A) of the seismic amplitude in our analysis. These reflection strength volumes computed and divided into volumes of similar high amplitude regions (HARs) through the use of region-growing algorithms that we have developed. The conventional isosurfacing technique bounds regions by connecting data points with the same amplitude values on the surface (Figure 3.13 (a)). The usefulness of this technique applied to as noisy seismic data is very limited. Our region-growing technique is more robust. The technique employs nonlinear, 3D operators to isolate HARs within the seismic datasets. Beginning from a set of initial "seed" points (with large amplitude values), we track the magnitude of the change-in-amplitude in 3D. A threshold value of amplitude gradient is selected to bound the regions. The HARs are bounded by surfaces of high amplitudes that exceed the threshold in the gradient of amplitudes away from the seed points. Data points outside HARs are excluded from analysis, downsizing the overall amount of data (Figure 3.13 (b)). Rough-cut connectivity between HARs within each dataset are obtained by properly choosing threshold operator so that lowpass spatial filtering, dilation and erosion "grows" the connections between segmented HAR seed points. An example of applying our region-growing and differencing techniques to two traces (1D) extracted from the 1985 and 1992 seismic volumes is shown in Figure 3.14 (Anderson et al., 1995b).

We then difference the two 3D seismic datasets within each of the HARs. Corresponding HARs defined from the two separate surveys are merged into a single set of HARs by a volume union operation (Anderson et al., 1995b). Each HARs is characterized as having undergone near-zero change, brightening (red in the figure), or dim-out (color coded as green/yellow, red, and blue in Figure 3.15 (a)). Fine-scaled structure within a single HAR may be indicative of bypassed pay (green in Figure 3.15 (a)). Intervals of sustained high amplitudes that are within 10% of each other can be used to reveal inter-connectivity (Figure 3.15 (b)). The 3D pattern of bypassed hydrocarbons has a surprising inter-connectivity. The amplitude pattern is aligned 30 degrees to the major bounding faults in this portion of the LF reservoir. The apparent lineation may be due to small faults caused by westward shear in the vicinity of the LF reservoir. This pattern is not evident in either of the primary 3D seismic surveys.

Misregistration errors can cause edge effects on the differentiated seismic data, as can be created by velocity differences caused by the changing fluid composition. For example, the formation of a gas cap significantly lowers the velocities within the top of the reservoir, resulting in a mismatch between the two times. These edge effects must be removed from the final image of the reservoir (Figures 3.16-3.18).

2.5.7.2 Volumetric analysis of drainage of the LF reservoir

Regions of near-zero seismic amplitude differences may possibly contain bypassed hydrocarbons (green in Figure 3.18). Dim-outs could be caused by water encroachment or pressure depletion (blue in Figure 3.18) and brightened regions could be from GOR increases and secondary gas dissolution (red in Figure 3.18).

This detailed hydrocarbon distribution image can be combined with production data to further analyze the drainage patterns caused by production. More than 7.5×10^4 (470,000 barrels) of oil with low GOR has been produced from this part of the LF reservoir from 1985 to 1992, mostly from wells A-12A, A-6, A-8, and B-4. The other thirteen wells (Figure 3.32) in both Blocks 330 and 331 stopped producing due to water intrusion or mechanical failure early in the production history (before the 1985 3D survey was acquired).

The estimated initial (1972) and current (1992) oil/water and oil/gas contacts from the production data are shown in Figure 3.12. The oil/water contact has moved about 107 m (350 ft) in vertical distance up-dip and to the east, and the gas expansion should have deepened the gas/oil contact by about 15 m (50 ft) down-dip and to the west. From these

production history interpretations, new wells would have to be placed in a very narrow (< 610 m or 2,000 ft wide) band along the structure contours in the fault block B.

However, the 4D image of the LF reservoir predicts a significant different drainage pattern from the interpretation derived based on the gravitational assumptions of the production history (Figure 3.19). The drainage is much more heterogeneous than indicated by the production data. The drainage patterns of the LF reservoir do not follow structure contours. Instead, the bypassed hydrocarbons appear to be related to fingered sands trending in the north-west to south-east direction. Water intrusions appear to have fingered into the reservoir in the same direction. The isolated regions with water invasion appear to be caused by water-coning.

2.5.7.3 Horizon amplitude extraction of the LF reservoir

We sample the 3D amplitude along the 2D top horizon of the LF reservoir, which corresponds to a strong seismic reflector (Figures 3.20 (a) and (b)). The 1985 2D image clearly shows dim-outs that are approximately parallel to structural contours, especially in the west and near the bounding faults B and F in the north and south. These amplitude boundaries correspond to the 1985 oil/water contacts. The amplitude pattern is more continuous in the east. However, by 1992, the amplitudes have become discontinuous. The total area of high reflectivity has decreased with time, as expected for an actively-produced reservoir with decreasing fluid pressures and oil saturations.

Amplitude changes in the top of the LF reservoir also indicate brightened areas marking gas formation (red in Figure 3.21) and dim-out areas marking water invasion (blue in Figure 3.21). However, the boundaries are more complex and less clearly tied to structure than in the gravitational model derived from production data. Depletion of the gas cap from 1985 to 1992 is imaged as an amplitude dim-out in the eastern portion of the reservoir (up-dip in Figure 3.21), with brightening indicated within the newly depleted oil zone (down-dip to the west). Areas of near-zero amplitude change (green and yellow in Figure 3.21) are primarily located in regions where no active production wells were operated (e.g., Block 331). We predict that there are significant bypassed oil located in the LF reservoir of this fault block.

Significant edge effects are caused by traveltimes misalignment of the LF reservoir in the southwest and south of the fault block (just north of the F fault). This misalignment is probably caused by velocity changes from the significant drainage in the shallower JD reservoir, which is a large gas producer.

2.5.7.4 Volumetric variations of seismic amplitude differences

The HAR analysis measures the acoustic thickness of the LF reservoir, and allows variations within the volume to be examined. We difference HARs to create volumetric representations of the seismic amplitude changes between the 1985 and 1992 seismic surveys (Figure 3.22). Because 3D variations are difficult to convey on paper, we slice the difference volume through its top, middle and bottom along planes parallel to the LF structure surface (Figure 3.23). We present both a fluid contact interpretation of the differences (Figure 3.22), and the absolute difference images (Figure 3.23).

We then compared these HAR slices with a slice made along the top of the reservoir, as defined by the seismic reflector (Figure 3.21). Both show the gas formation, but the HAR slices demonstrate that the high amplitude anomalies have migrated much deeper into the reservoir and to the west by 1992 (Figure 3.22). However, in the eastern portion of the reservoir (up-dip), water sweep has changed the original gas distribution dramatically due to the active production in Block 330. For example, the A-6 well (in Block 330) produced oil since 1981. The A-6 well was shut-in in 1987 because of a sudden water intrusion, and it was producing hydrocarbon at a GOR of 3,000 before the shut-in (Figure 3.34). The case of amplitude increase (brightening) in Block 331 is unknown-it contains no active production wells. Perhaps pressure decreases within the

overall reservoir caused gas to come out of solution. However, the brightened amplitudes moved more than 305 m (1,000 feet) to the northwest from 1985 to 1992, so we believe the amplitude increases to be real.

2.5.8 4D acoustic impedance analysis technique

Volumetric reservoir descriptions based upon seismic amplitude data are less physical than those based upon acoustic impedance. Because acoustic impedance is more closely associated with the petrophysical and fluid properties of reservoirs than amplitudes. We apply the same region-growing technique to the estimated acoustic impedance volumes. We therefore inverted the amplitude-normalized, phase-matched seismic datasets to produce the estimated impedance volumes. The constrained, full-scale nonlinear seismic inversion technique discussed in Chapter 2 is applied. The estimated 4D acoustic impedance volumes from the 1985 and 1992 seismic volumes within the time window from 1.7 to 2.2 seconds are shown in Figures 3.24 (a) and (b). The hydrocarbon reservoirs correspond to low impedance regions within these two impedance volumes.

2.5.8.1 Differences in acoustic impedance between 1985 and 1992 in the LF reservoir

Using our region-growing algorithms, the 1985 and 1992 acoustic impedance volumes are then segmented into similar Low Impedance Regions (LIRs) and data from outside these LIRs are excluded from future analysis (Figure 3.25).

The shape of the LIRs (derived from acoustic impedance volumes) differs from that of the HARs (derived from seismic amplitude volumes). Because seismic amplitudes are sensitive to reservoir boundaries, to fluid contacts, and to impedance contrasts, while acoustic impedances are more sensitive to internal continuity and heterogeneity within the reservoir itself. Reservoir thicknesses derived from the estimated acoustic impedance volumes are much more accurate than those resolved from seismic amplitudes. As we will see later in this section, our region-growing techniques are more robust when applied to the estimated acoustic impedance data.

Reservoir drainage from the shallower JD reservoir causes vertical traveltime delays in the LF reflections. Up to 20 ms of delay in the 1992 survey versus the 1985 survey can be seen in Figure 3.26. We compensate the traveltime delays by applying a horizon-balancing technique. We interpreted the top of the LF reservoir sand on both estimated acoustic impedance volumes. The traveltime differences in the study area caused by production can be seen in Figure 3.27. We then corrected the traveltime differences between the 1985 and 1992 LF reservoir tops by shifting the 1985 data. The edge effects shown in Figure 3.18 are thus eliminated.

The differences within the LIRs of the LF reservoir between 1985 and 1992 were then computed (Figure 3.28). Changes in acoustic impedance over time are quantitatively related to the drainage of hydrocarbons. Near-zero impedance differences indicate locations where there was minimal change within the LIRs of the surveys, which we interpret to be possible bypassed hydrocarbons (green in Figure 3.28). Increases in impedance are likely caused by water encroachment or pressure depletion between the times of the two surveys (blue in Figure 3.28), and decreases from GOR increases and secondary gas dissolution (red in Figure 3.28). A visualization of the volumetric changes within the LF reservoir is created by slicing through the upper-, mid-, and lower-intervals of the LF LIR (Figure 3.29). Comparing this result to the similar figure made from seismic amplitude differences (Figure 3.19), more coherences are observed within the LIR than in the seismic amplitude HAR. In the upper-interval slice, green regions can be from either oil or gas, since the original reservoir in 1985 contained a gas cap in this fault block. In the mid-interval slice, red and green regions are the primary features, which indicate that both gas and oil are still present in 1992. In the lower-interval slice, blue

regions are predominant, indicating the water sweep started from the base of the reservoir, as expected. However, water appears to have encroached in what might be fingers through high permeability sand from several directions, not just from the deeper portion of the reservoir in the west.

2.5.8.2 Horizon acoustic impedance extraction of the LF reservoir

The acoustic impedances extracted from along the LF reservoir top structure from each impedance volume are shown in Figure 3.30. The extracted impedances can be directly used to delineate distributions of hydrocarbons remaining within the reservoir.

The reservoirs are outlined by the boundaries between high (blue) and low (red) impedances. The reservoir dim-outs and brightenings have higher coherence than in the corresponding analysis that used seismic amplitudes. The hydrocarbon contacts are clearly seen on both images. The similarities and differences between the 1985 and 1992 extractions (Figures 3.30 (a) and 3.30 (b)) show the quantitative hydrocarbon changes that have occurred within the LF reservoir. Such changes indicate reservoir dim-outs and brightening inside the reservoir from 1985 to 1992.

As with the qualitative results obtained from the amplitude analysis, the dim-outs (increased impedance) are approximately parallel to structural contours, particularly in the western part of reservoir (Figure 3.31). These impedance boundaries correspond to the oil/water contact. No obvious water intrusion is detected perpendicular to structural contours in the northwest. However, long-distance water encroachment perpendicular to the structural contours has occurred along the north of the F fault. In 1985, the region of low impedances show continuity to the eastern part of the reservoir. But by 1992, the continuity has markedly decreased. In general, the area of low impedances decreases with time, as might be expected for an actively-produced reservoir.

2.5.8.3 Volumetric variations of acoustic impedance differences in the LF reservoir

Impedance differences within the LIRs are related to hydrocarbon movement (Figure 3.32). Brightened volumes mark gas cap formation (red in Figure 3.32) and volumes with dim-outs mark water sweep (blue in Figure 3.32). But the boundaries are more complex and less tied to the reservoir structure than described by production data analysis. Low impedance regions above the initial gas/oil contact (red and pink regions in Figure 3.12) in fault block B are considered to be gas. Depletion of the gas cap from 1985 to 1992 is not obvious in these regions as shown in Figures 3.28-3.29. However, areas with decreasing impedances occur further down-dip to the west within the oil zone (Figure 3.12 and Figure 3.32), suggesting down-dip migration of the gas cap and gas dissolution from oil. The areas with near-zero impedance change (green regions in Figure 3.32 (b)) in Block 331 are greater than those in Block 330, indicating that there may be more bypassed hydrocarbon reserves in Block 331 of the fault block. However, as what we have noted previously, the cause of these regions with decreased impedance is unknown because there was no well producing from 1985 to 1992.

We present a fluid contact interpretation of the differences (Figure 3.33) based on the analysis of images shown in Figure 3.32. Both volumetric impedance extractions and planar extractions show the low impedance anomalies migrated much deeper down-dip. This information is not present in the 2D surface extraction analysis (Figure 3.31).

The total volume of decreased impedance (shown as red) and near-zero impedance change (green) is larger than those observed in the HAR analysis, and these volumes are more continuous as well. This improvement occurs because traveltime delays caused by production of shallower reservoirs have been eliminated.

The regions with near-zero impedance changes (green and yellow in Figure 3.33) within the original gas cap to the east should still be gas. However, significant water encroachment is detected, and the original gas distribution (gas/oil contact) has been changed dramatically by the production in Block 330.

Production data from the nineteen wells used in this study are shown in Figures 3.33. The well data in Block 330 are consistent with the predicted hydrocarbon drainage patterns from the 4D amplitude and impedance analyses. For example, in 1985, A-8 well produced oil, gas, and water (Figure 3.34) as the water front moves up-dip toward east and south, the well was shut-in in mid 1987 because of water encroachment. This well is located in the area of water sweep predicted by our 4D analysis (Figures 3.22 and 3.33). The nearby A-6 well (in the up-dip direction to the south of A-8) has a similar history, but it saw water about six months earlier (instead of later) than A-8, indicating that either the water intrusion in the LF reservoir is preferentially oriented in certain directions or it is caused by water-conning. Another example is the B-4 well (Figure 3.34), which came into production in 1984, it has produced oil steadily with low GOR into 1991. It is on the edge of the area of bypassed oil predicted by our 4D analysis (Figure 3.33).

The water-conning is observed much more clearly in the Block 331 (isolated blue areas in Figures 3.22 and 3.33). Although production from wells in Block 331 has stopped because of water encroachment or sand-flow induced mechanical failures before 1985, there are water encroachment "halos" detected from our 4D analysis existing around the watered-out wells (e.g., wells A-4, A-7 and A-5). Nevertheless, the predicted water encroachment are not radially isotropic, instead, the drainage appears to have been significantly affected by sand quality variations and other permeability heterogeneities.

2.5.9 Quantitative 4D seismic monitoring technique

In an effort to further quantify our 4D seismic monitoring techniques (He et al., 1994 and 1995b), we have used a multi-dimensional seismic forward model based on the finite element method (FEM) and fluid substitution technique (Sun, 1994) to verify whether the hydrocarbon drainage changes can produce the observable seismic amplitude changes. We constructed a velocity model of the LF reservoir as it appeared in 1985. The 1985 seismic response is shown in Figure 3.35 (a). To change the reservoir petrophysical properties, we use Gassman's equation combined with the dynamical theory of porous media (Sun, 1994) for estimating the acoustic velocity of rock containing a multi-phase pore fluid. We incorporate changes in gas cap development, water intrusion, GOR increase and unchanged oil saturation into the 1992 model. We then compare its FEM seismic response to the 1985 response.

The modeled seismic amplitudes of the LF reservoir in 1992 are shown in Figure 3.35 (b), and the differenced seismic model results in Figure 3.35 (c). Dim-outs (blue in Figure 3.35 (c)), brightening (red in Figure 3.35 (c)), and unchanged differences (<10% change, green in Figure 3.35 (c)) are all observed. The FEM model results indicate that surface seismic data can be used to monitor the hydrocarbon drainage process.

2.5.10 Conclusion

When applied to data from the LF reservoir in the EI-330 Field of offshore Louisiana, our 4D seismic monitoring techniques are effective in determining the locations and volumes of bypassed hydrocarbons. Corrections for spatial data registration and traveltimes from delays caused by drainage above the reservoir are very important. Without them, the resulting edge effects may cause the 4D analysis to fail.

The application of our 4D seismic monitoring techniques to seismic amplitude and estimated acoustic impedance data suggested that: a) the amplitude analysis is the better prediction of reservoir drainage patterns; and b) the impedance analysis is better prediction of reservoir petrophysical property changes. The integration of the two techniques produces a quantitative understanding of the drainage of hydrocarbon reservoirs over time.

Our analysis suggests that drainage patterns are very sensitive to heterogeneities in lithology, porosity, and permeability of the reservoir. Water intrusion and gas cap expansion are found to be almost independent of the LF reservoir structure. Instead, we

found that they are determined by potential fluid pathways provided by faults and fine-scale sediment fairways with high permeability.

Production wells within the LF reservoir in fault block B were found to have produced very limited, heterogeneous and contorted drainage radii. The drainage pathways in the LF reservoir are elongated along directions of high permeability (northwest-southeast) and shortened along directions with lower permeability (northeast-southwest), which indicates that the production wells have greater drainage efficiencies in selected directions. The wells that were shut-in because of water intrusions were seen to have "suffered" from much more water-coning from below than from lateral, up-dip gravity driven water invasion. The use of 4D seismic data has significantly improved the understanding of reservoir dynamics of the LF reservoir, compared to what is possible with the traditional interpretations based on well logs and production history.

References

- Alexander, L., and P.B. Flemings, 1995, Geologic evolution of a Plio-Pleistocene salt-withdrawal minibasin: Eugene Island Block 330, Offshore Louisiana: American Association of Petroleum Geologists Bulletin, v. 79, p. 1737-1756.
- Anderson, R.N., E. Bagdonas, A. Boulanger, L. Xu, and W. He, 1995a, 4D seismic interpretation techniques for the detection of drainage and migration in oil and gas reservoirs: US. Letters Patent Pending.
- Anderson, R.N., A. Boulanger, W. He, Y.F. Sun, L. Xu, 1995b, 4D seismic imaging of drainage and pressure compartmentalization in the Gulf of Mexico, Oil and Gas Journal, part 1, March 28, part 2, April 4.
- Anderson, R.N., P.B. Flemings, and S. Losh, 1995c, The GBRN/DOE Eugene Island Dynamic Enhanced Recovery Project, CD-ROM, Lamont Press.
- Breitenbach, E.A., G.A. King, and K.N.B. Dunlop, 1989, The Range of Applications of Reservoir Monitoring, Society of Petroleum Engineers Paper 19853.
- Domenico, S.N., 1976, Effect of brine-gas mixture on velocity in an unconsolidated sand reservoir, Geophysics, v. 41, p. 882-894.
- Dunlop, K.N.B., G.A. King, and E.A. Breitenbach, 1988, Monitoring of oil/water fronts by direct measurement, Society of Petroleum Engineers Paper 18271.
- Gregory, A.R., 1976, Fluid saturation effects on dynamic elastic properties of sedimentary rocks: Geophysics, v. 41, p. 895-921.
- He, W., R.N. Anderson, and X. Wang, 1994, Constructing 3D porosity and fluid pressure models in the Eugene Island Block 330 Area offshore Louisiana: American Association of Petroleum Geologists Annual Convention Official Program, v. 3, p. 167.
- He, W., and R.N. Anderson, 1995a, Seismic Attribute mapping of the geopressure surface in the Gulf of Mexico, Journal of Geophysical Research, submitted.
- He, W., R.N. Anderson, X. Wang, and Y.-C. Teng, 1995b, Application of finite element seismic modeling in the Eugene Island Block 330 Field offshore Louisiana, Gulf of Mexico: American Association of petroleum geologists Annual Convention Official Program, v. 4, p. 41A.
- Holland, D.S., J.B. Leedy, and D.R. Lammlein, 1990, Eugene Island Block 330 Field-U.S.A. Offshore Louisiana: in Structural traps III: Tectonic fold and fault traps: Treatise of Petroleum Geology, Atlas of Oil and Gas Fields, E.A. Beaumont and N.H. Foster, compilers, American Association of Petroleum Geologists, Tulsa, p. 103-143.
- Lumbly, D., 1995, Seismic monitoring of oil production: a feasibility study: presented at the 1994 Society of Exploration Geophysicist Annual Conference, Los Angeles.
- King, M.S., 1965, Wave velocities in rocks as a function of changes in overburden pressure and pore fluid saturants: Geophysics, v. 31, p. 50-73.
- Nur, A.M., 1982, Seismic Imaging in Enhanced Recovery, Society of Petroleum Engineers Paper 10680.

Nur, A.M., 1989, Four dimensional seismology and (true) direct detection of hydrocarbons: the petrophysical basis: *The Leading Edge of Geophysics*, v. 9, p. 30-36.

Sun, Y.F., 1994, On the foundations of the dynamical theory of fractured porous media and the gravity variations caused by dilatancy, Ph.D. Dissertation, Columbia University.

Taner, M.T., F. Koehler, and R.E. Sheriff, 1979, Complex seismic trace analysis: *Geophysics*, v. 44, p. 1041-1063.

Wang, Z., and A.M. Nur, 1988, Effect of temperature on wave velocities in sands and sandstones with heavy hydrocarbons: *Reservoir Engineering*, v. 3, p. 158-164.

Wang, Z., and A.M. Nur, 1992, Aspects of rock physics in seismic reservoir surveillance: in *Reservoir Geophysics*, R.E. Sheriff, Editor, Society of Exploration Geophysics, p. 285-300.

Wyllie, M.R.J., A.R. Gregory, and G.H.F. Gardner, 1958, An experimental investigation of factors affecting elastic wave velocities in porous media: *Geophysics*, v. 23, p. 459-493.

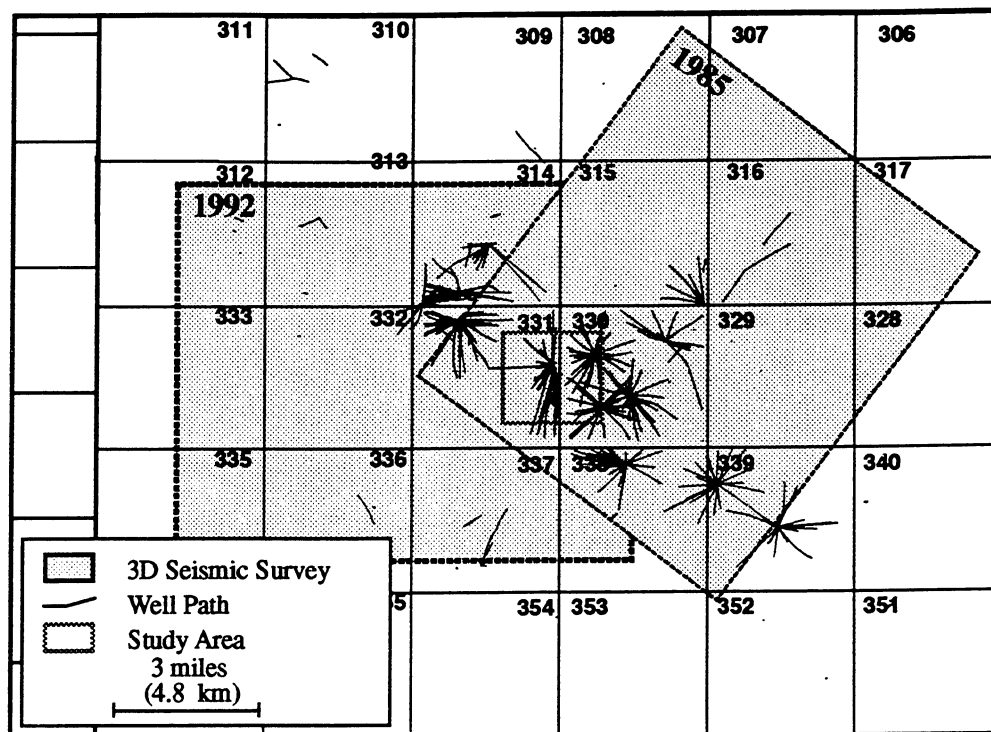


Figure 2.1. Location map of the Eugene Island Block 330 Field, showing two overlapping 3D seismic surveys (yellow). More than 500 wells are also illustrated. The selected study area is outline in red.

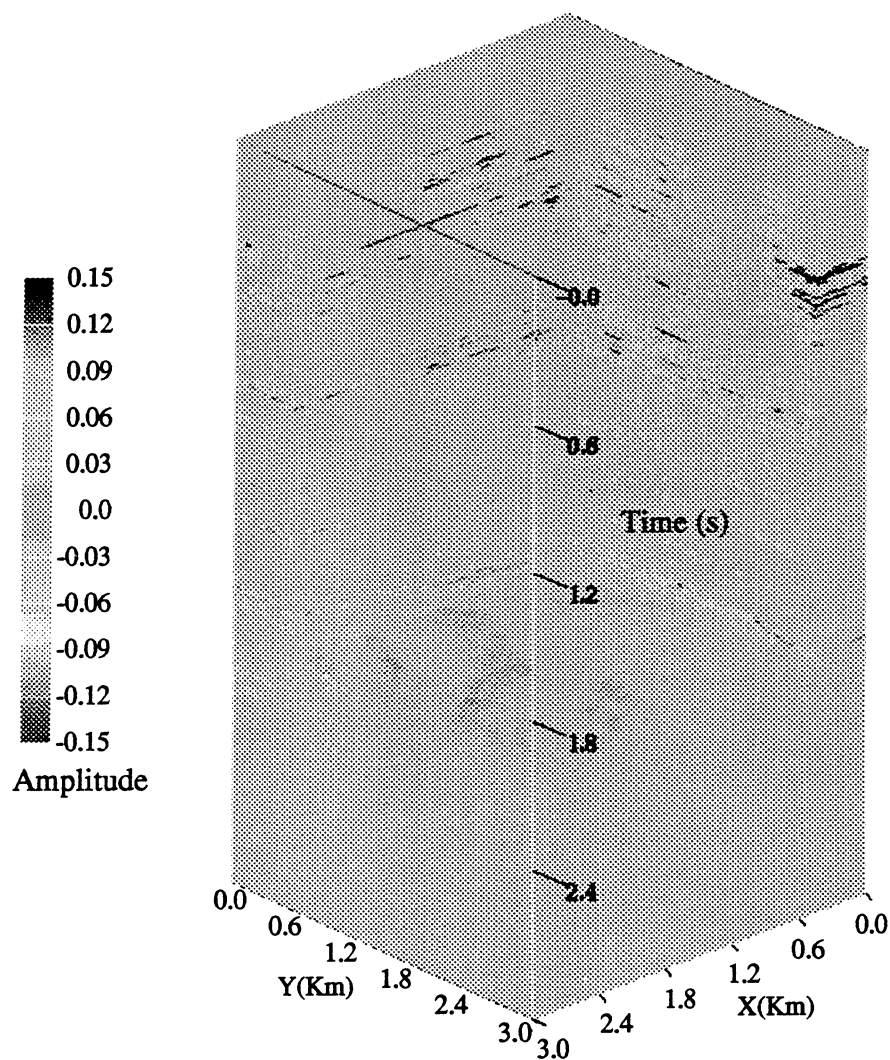


Figure 2.2. The 1985 3D seismic volume is re-oriented into the 1992 3D seismic grid. The seismic amplitudes of the volume are normalized and calibrated using synthetic seismograms generated from sonic and density logs from wells within the volume.

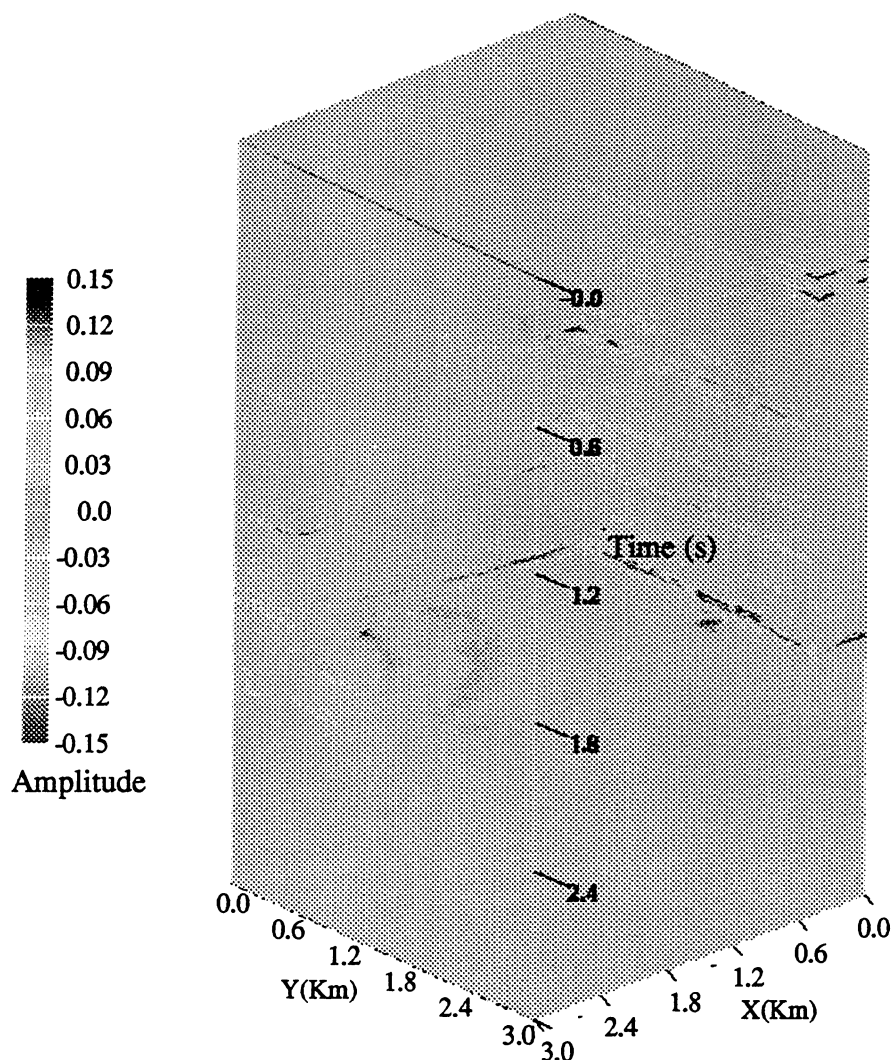
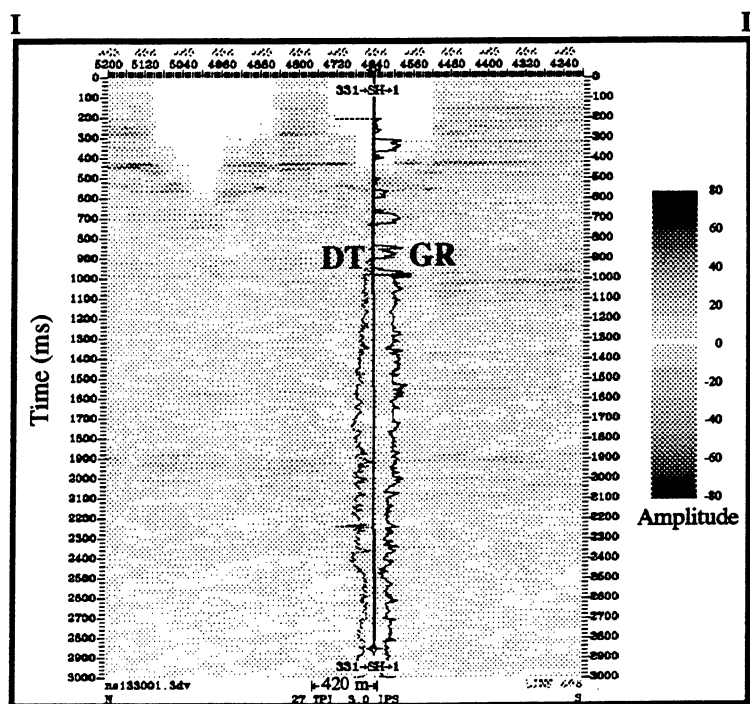
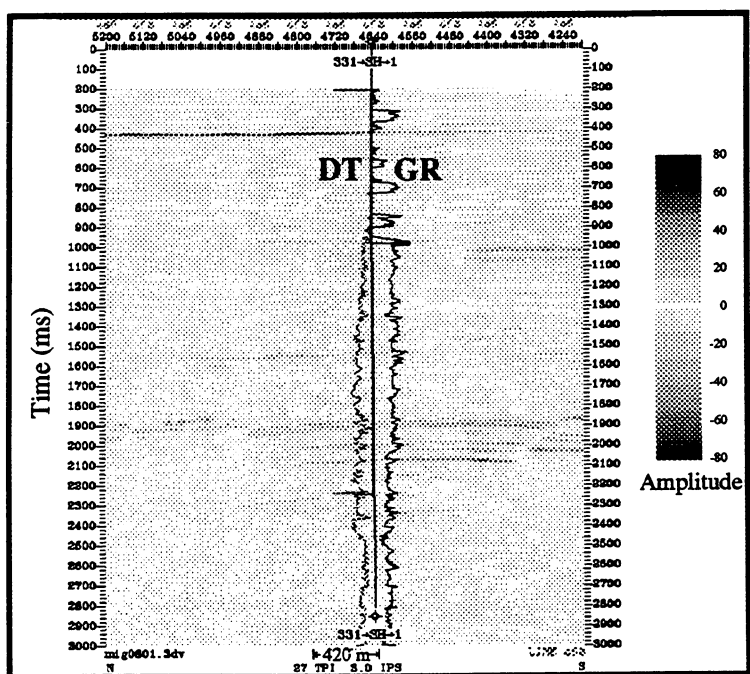


Figure 2.3. The 1992 3D seismic volume is used as the reference grid for inverting 4D seismic datasets because of superior navigation and shooting orientation. The seismic amplitudes of the volume are normalized and calibrated using synthetic seismograms generated from sonic and density logs from wells within the volume. Phase correction is also performed to match the 1985 3D survey.



(a)



(b)

Figure 2.4. I-I' cross-sections are extracted at the same location from the reoriented 1985 (a) and the 1992 (b) 3D seismic surveys (Figure 2.5). Sonic logs (DT) increase from left to right, GR logs increase from right to left. The differences between the 1985 and 1992 data are likely to be caused by hydrocarbon drainage that occurred over the seven years.

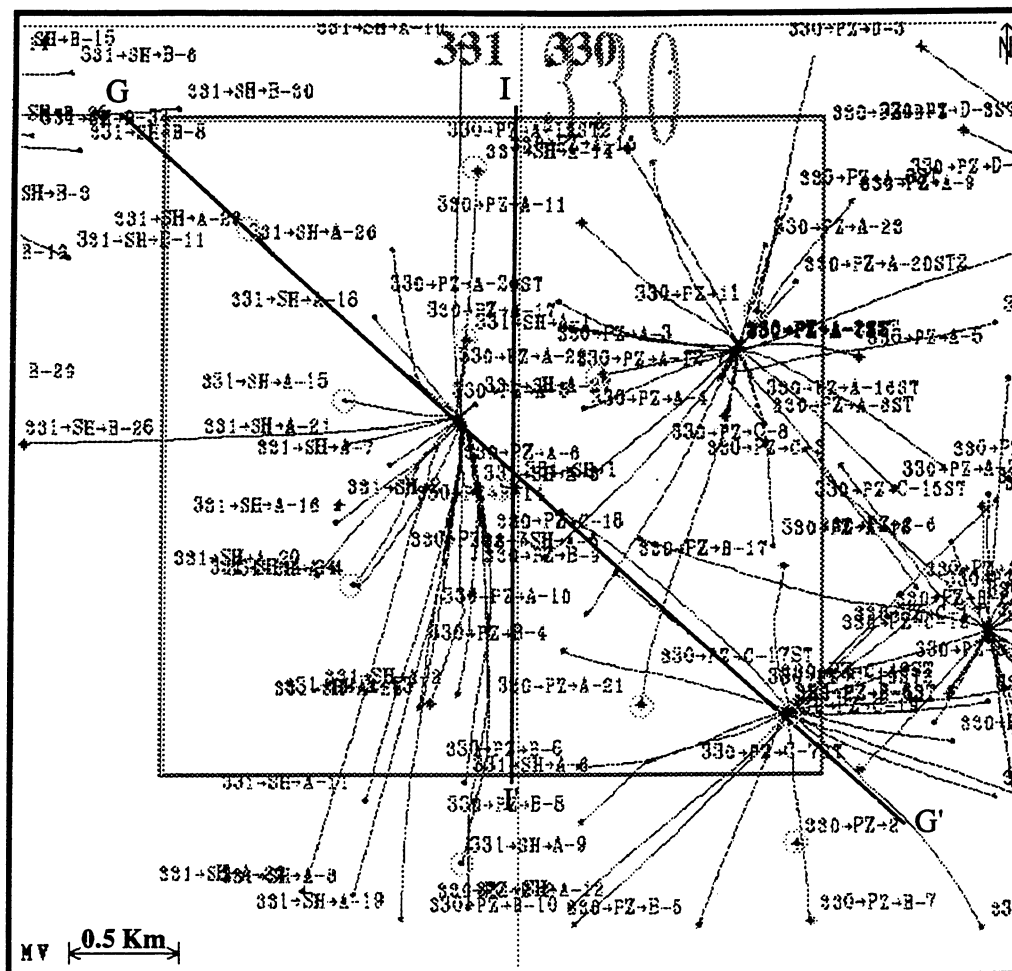


Figure 2.5. Location of seventy-four wells (blue lines) in the study area (red rectangle). The line annotated G-G' is the location of an arbitrary seismic line used for data quality examination. Twelve wells used to construct the *a priori* low-frequency impedance volume are also marked (green circles).

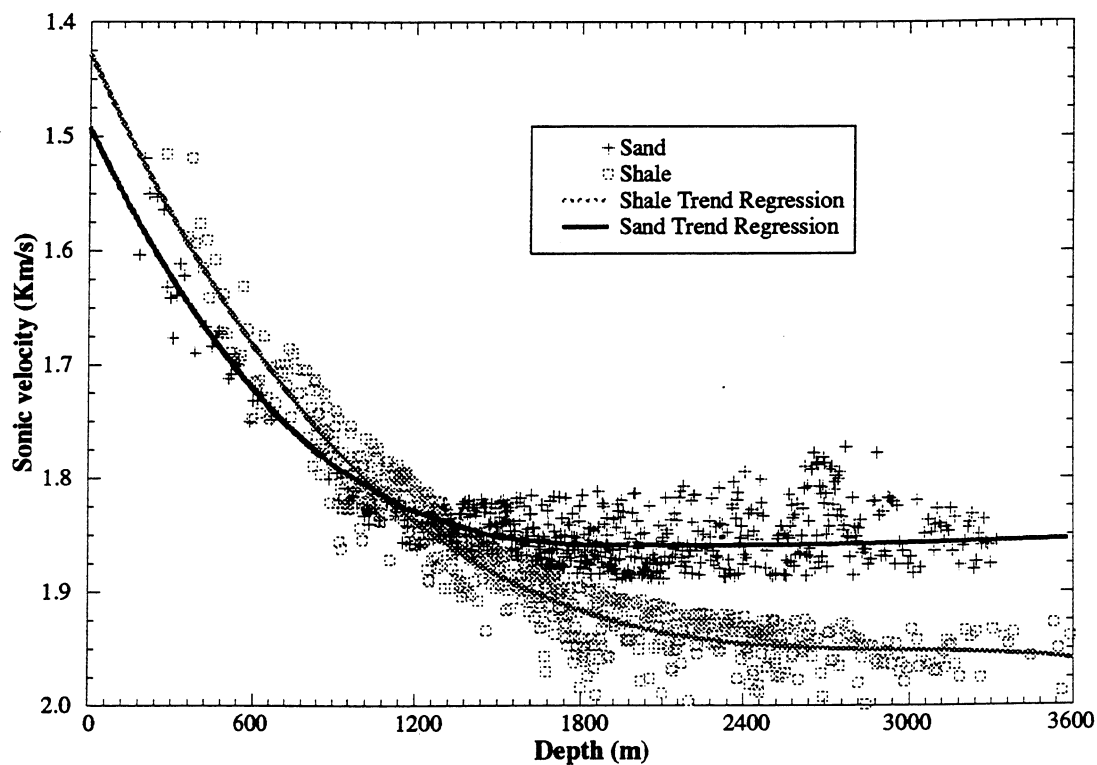
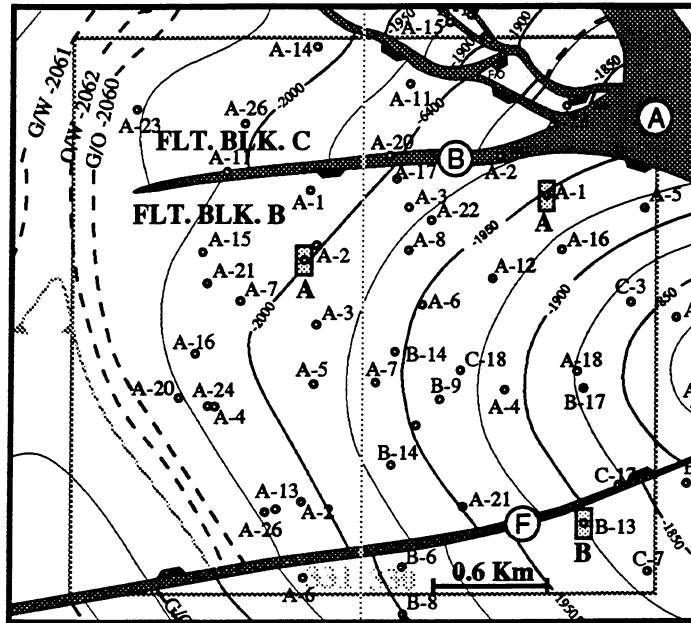
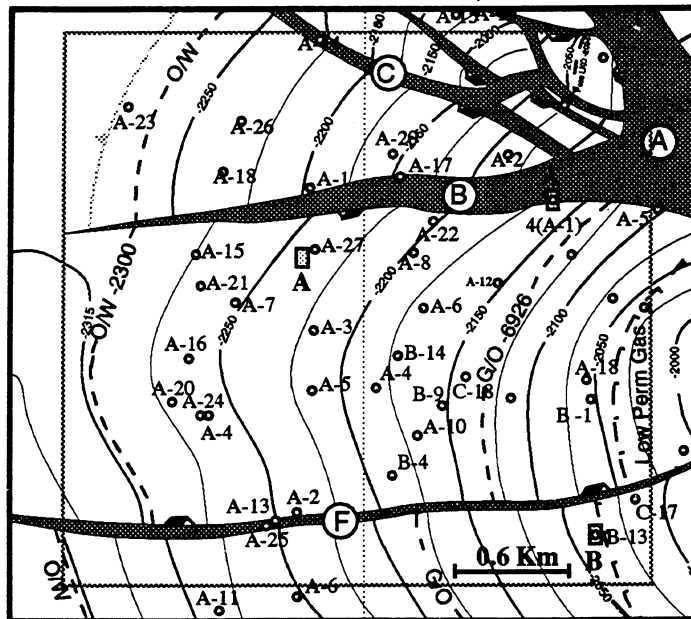


Figure 2.6. The pure sand and shale compaction trends derived from the sonic logging data in the twelve wells. The individual sand and shale points are extracted from sonic velocity every 0.3 m in sand and shale formations. GR logs and SP logs are used as lithology indicators. The sand compaction trend crosses the shale compaction trend at about 1067 m.



(a)



(b)

Figure 2.7. Structures maps of the JD (a) and the LF (b) sand tops (modified from interpretation by Pennzoil Exploration and Production Company). Solid black lines are contours of the structures in meters. Normal faults are in solid red. Oil/water, gas/water, and gas/oil contacts are dotted lines. Yellow circles are production wells, green lines are block boundaries, and blue rectangles are locations of production platform. Faults are annotated by circled letters.

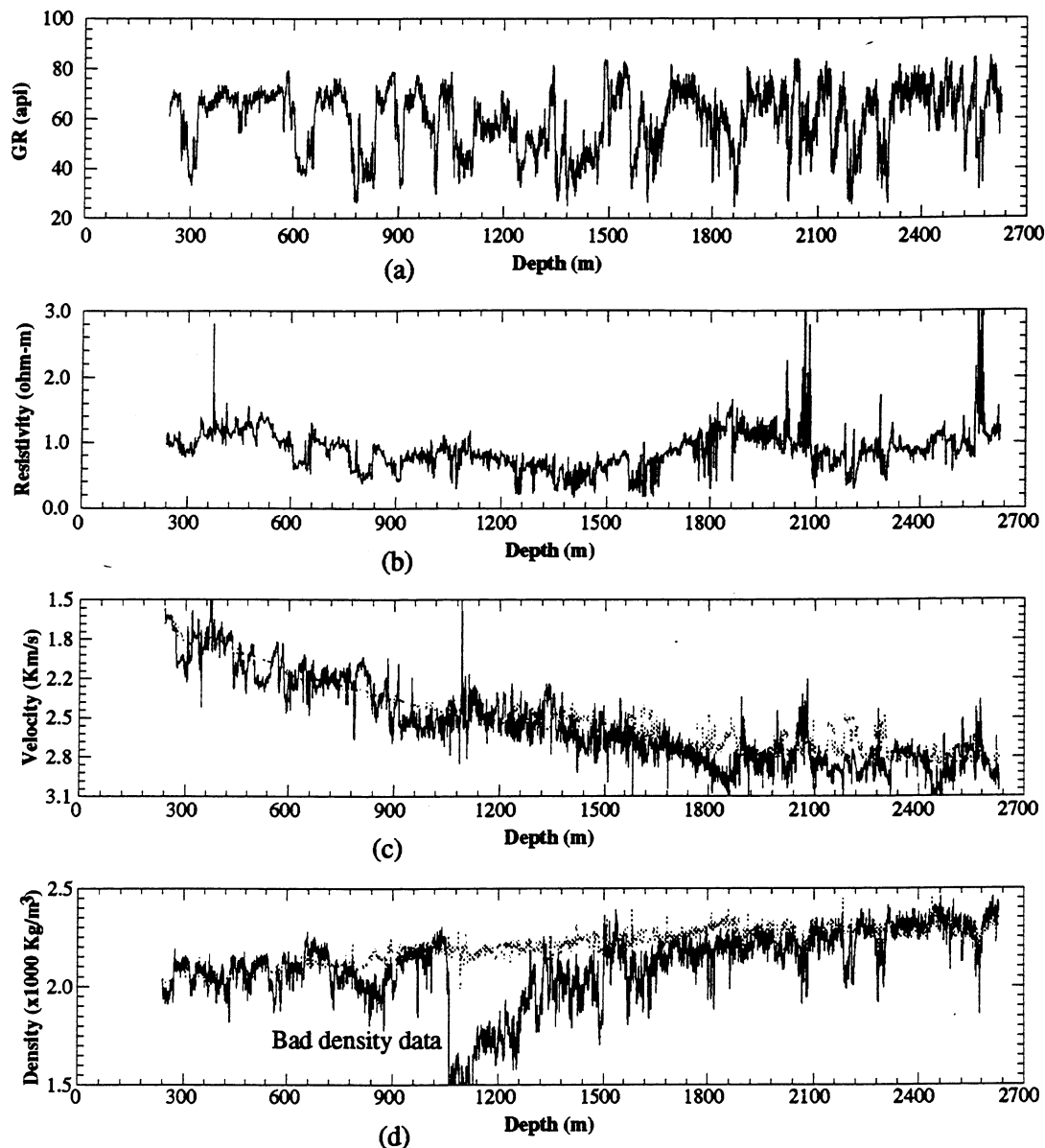


Figure 2.8. The "pseudo" sonic velocity can be estimated from GR and resistivity logs using a dual lithology model. The density log can be estimated from the sonic log using inverse Gardner relationship. Using the sand and shale compaction trends, the estimated sonic log (dashed) from (a) and (b) in well 331_SH_A-1 is superimposed onto the measured sonic log (solid) in (c). The estimated density log (dashed) from measured sonic log (black in c) is superimposed onto the measured density log (solid) in (d). Note the instrumental error in the density log between 1,000 and 1,400 m. The relative errors in the estimation for both cases are less than 7%.

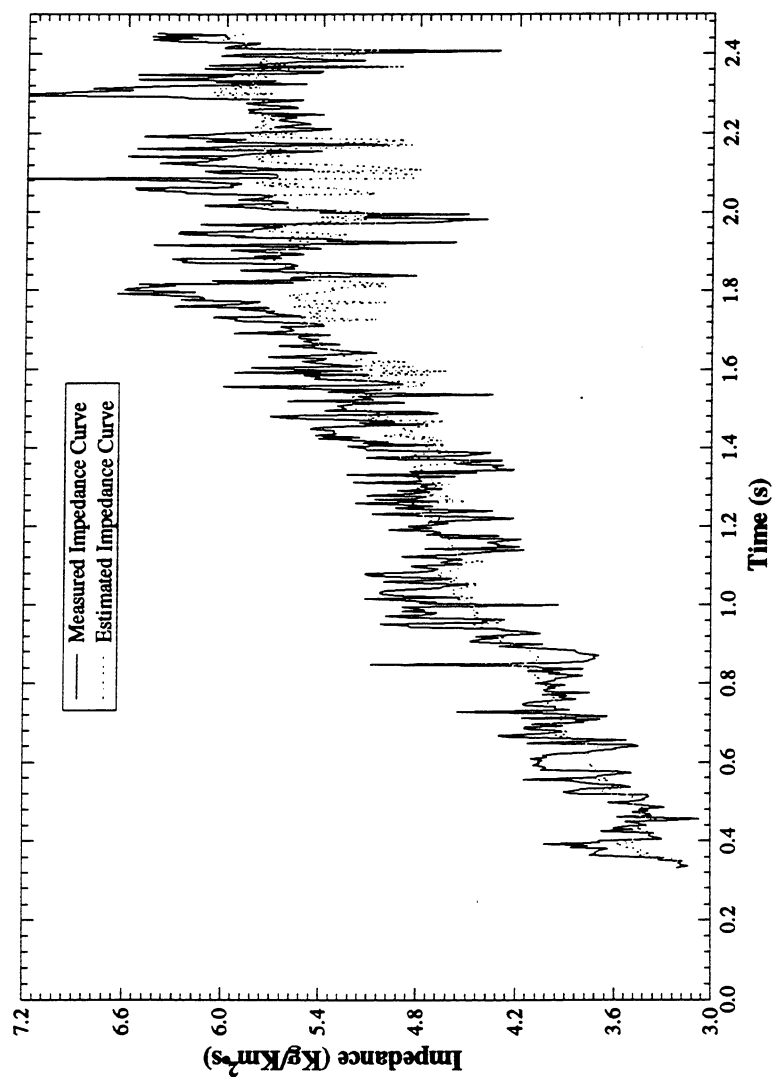


Figure 2.9. The comparison between the estimated and measured acoustic impedance in well 331_SH_A-1. See text for discussion.

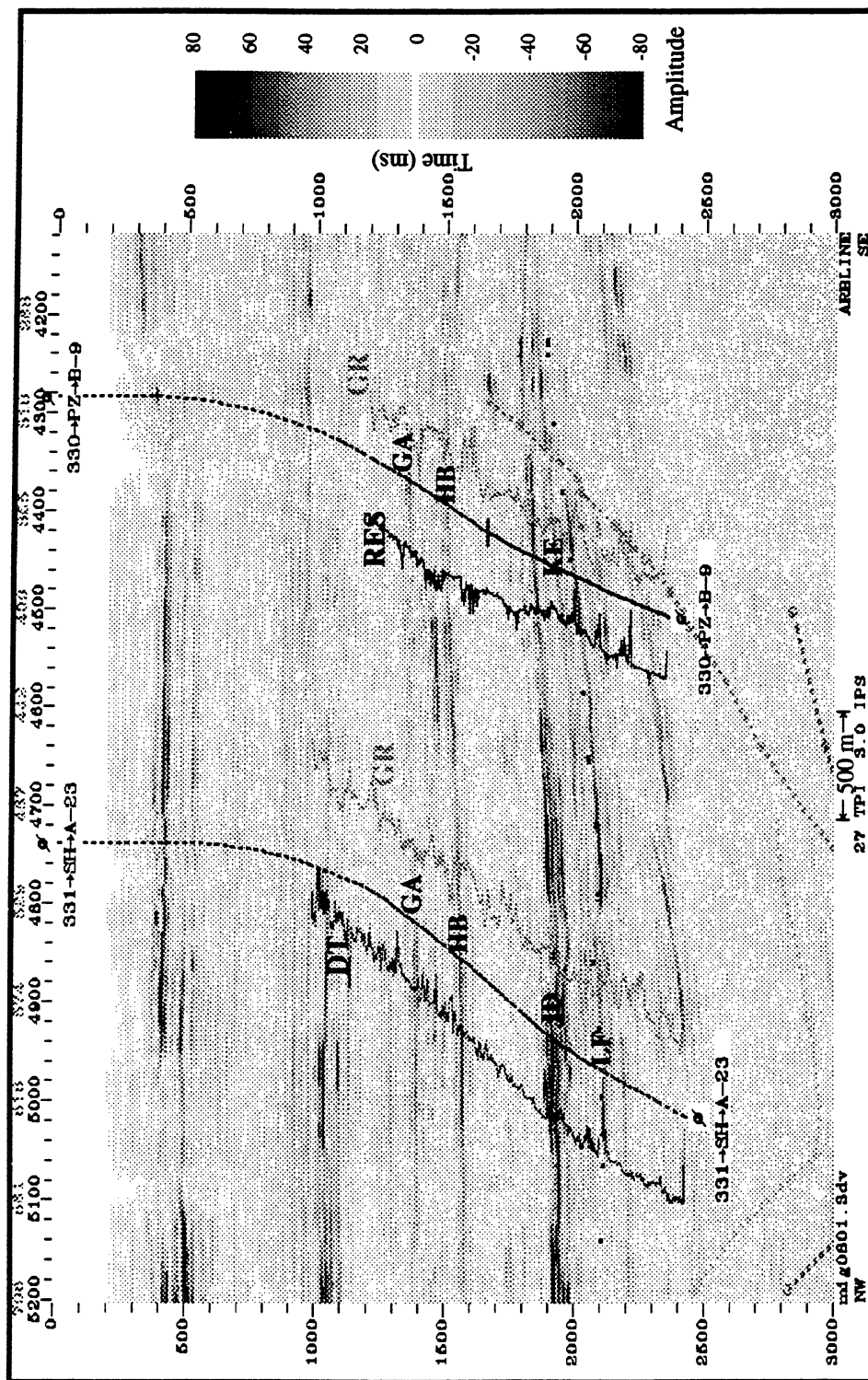


Figure 2.10. Wells 331_SH_A-23 and 330_PZ_B-9 are superimposed on the G-G' cross-section of the 1992 seismic survey. Sonic logs (DT) increase from left to right, GR logs increase from right to left. Resistivity logs (RES) increase from left to right. The depth-time conversions are accomplished using the measured sonic log in well 331_SH_A-23 and the estimated sonic log in well 330_PZ_B-9. The well log features are consistent with major seismic reflectors.

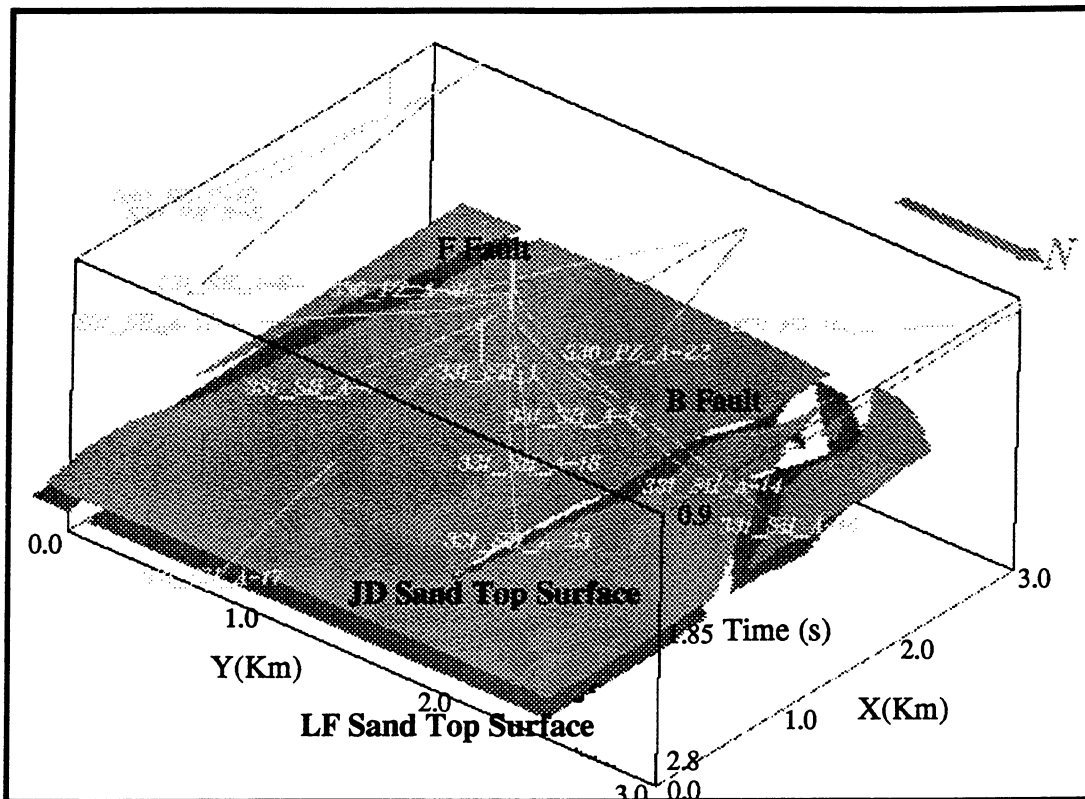


Figure 2.11. The extracted low-frequency impedance trends (blue lines) from the measured and estimated acoustic impedance logs are displayed along the well path (cyan lines) in the study area. The initial impedance model is then interpolated in three dimensions using two horizons, the top of JD sand (purple surface, upper) and the top of LF sand (red surface, lower), as the structural constraints.

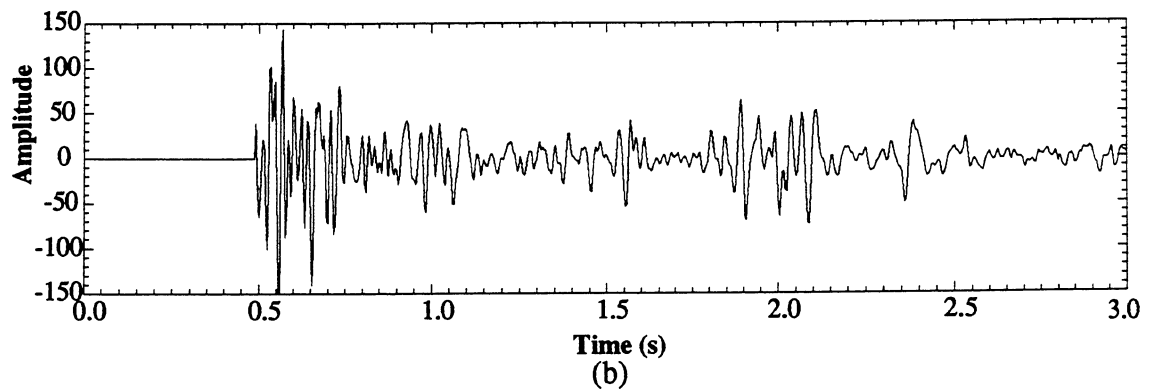
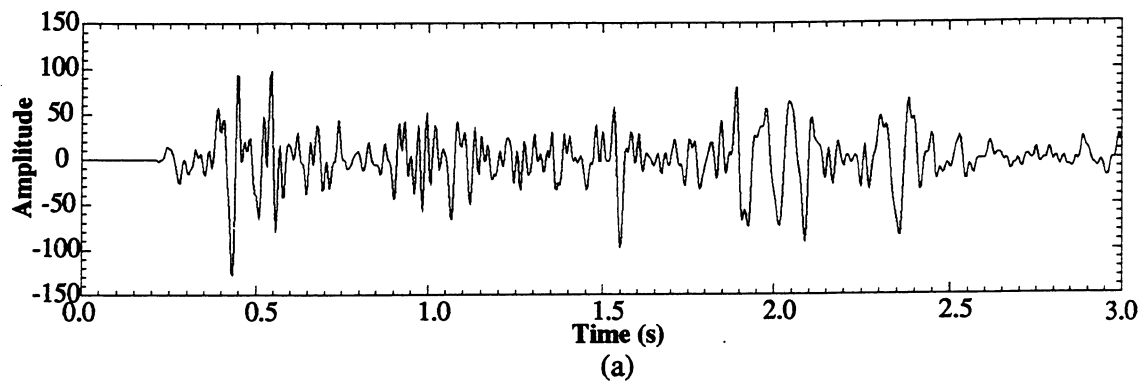


Figure 2.12. Seismic traces extracted from the same location in the 1985 (a) and 1992 (b) 3D seismic surveys.

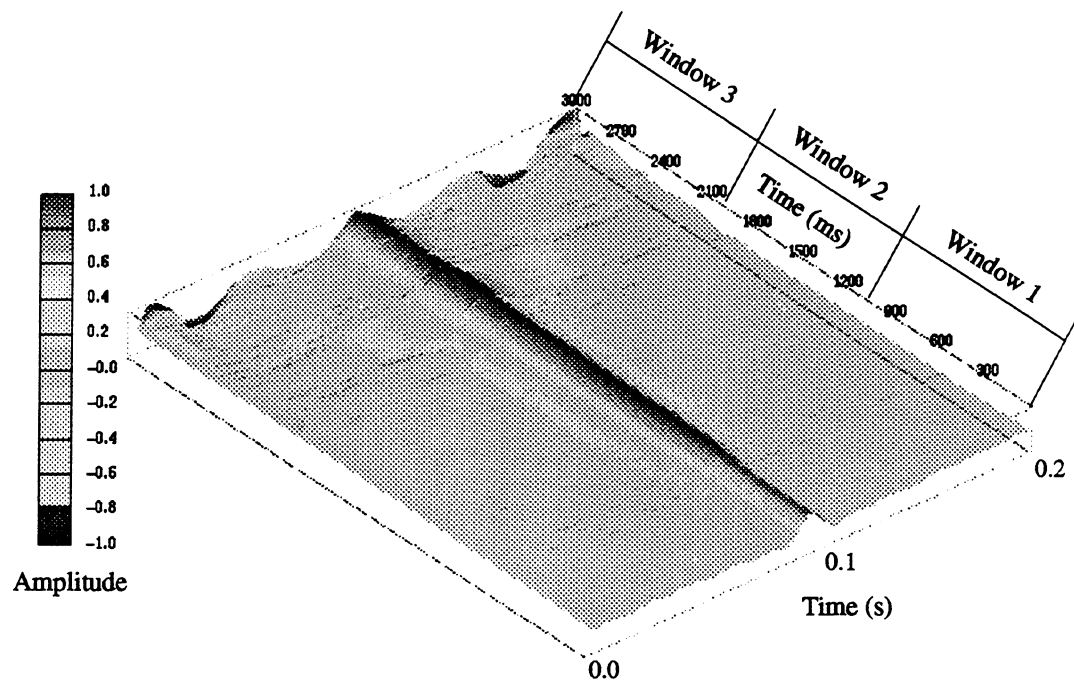


Figure 2.13. The autocorrelation function shown computed from the seismic trace shown in Figure 2.12 (a) from the 1985 survey. During the original processing, three different sets of filters were used evidently in each of three distinct time windows.

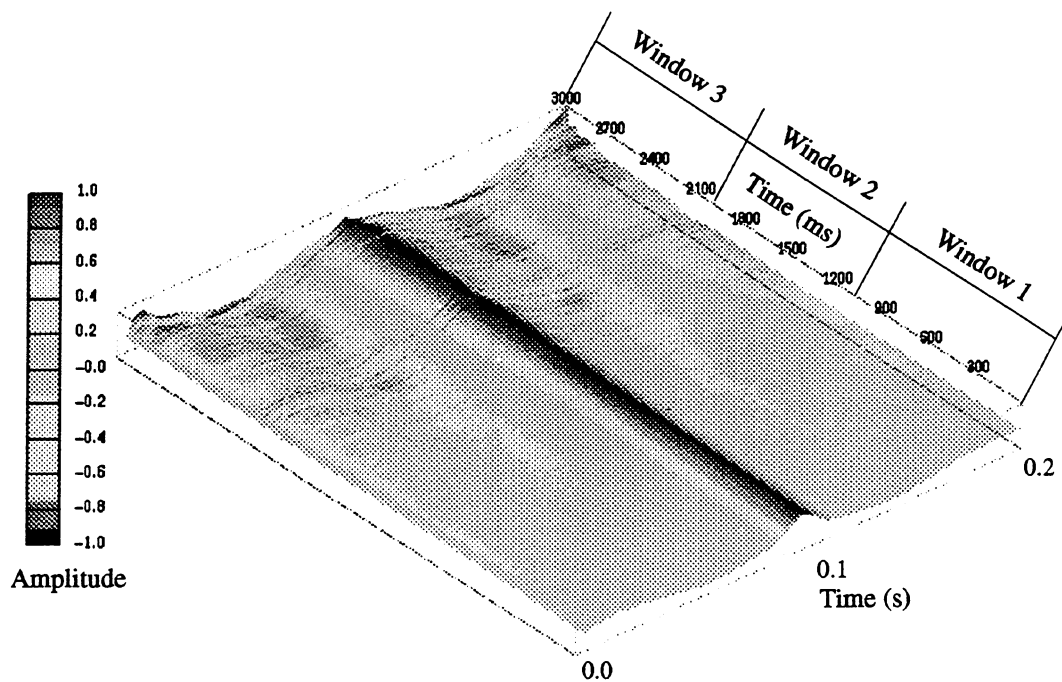


Figure 2.14. The autocorrelation function computed from the seismic trace shown in Figure 2.12 (b) from the 1992 survey.

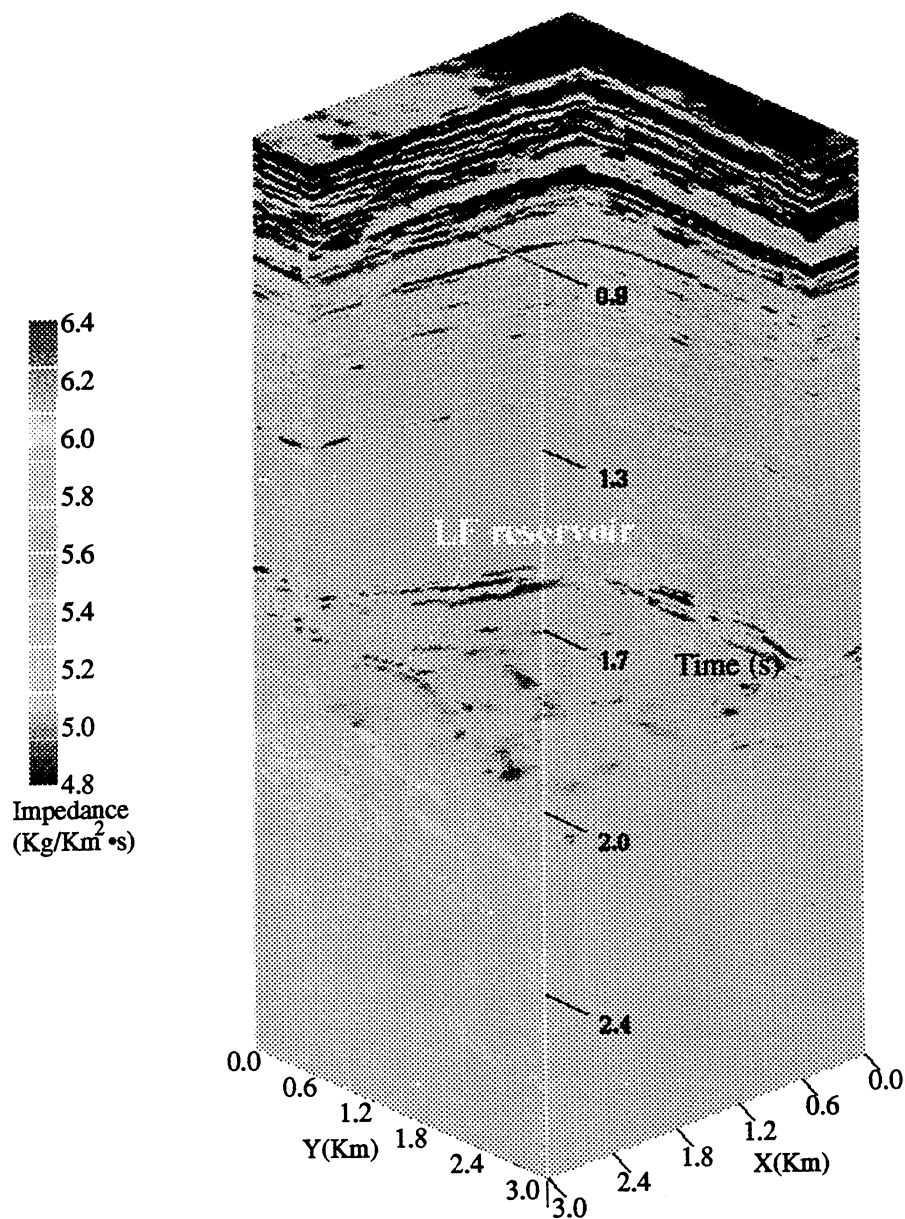


Figure 2.15. The estimated acoustic impedance volume of the 1985 seismic survey in the EI-330 Fault Block B. The slice is cut through the LF reservoir at mid-depth. The low impedance anomalies are correlated to various production reservoirs throughout the volume.

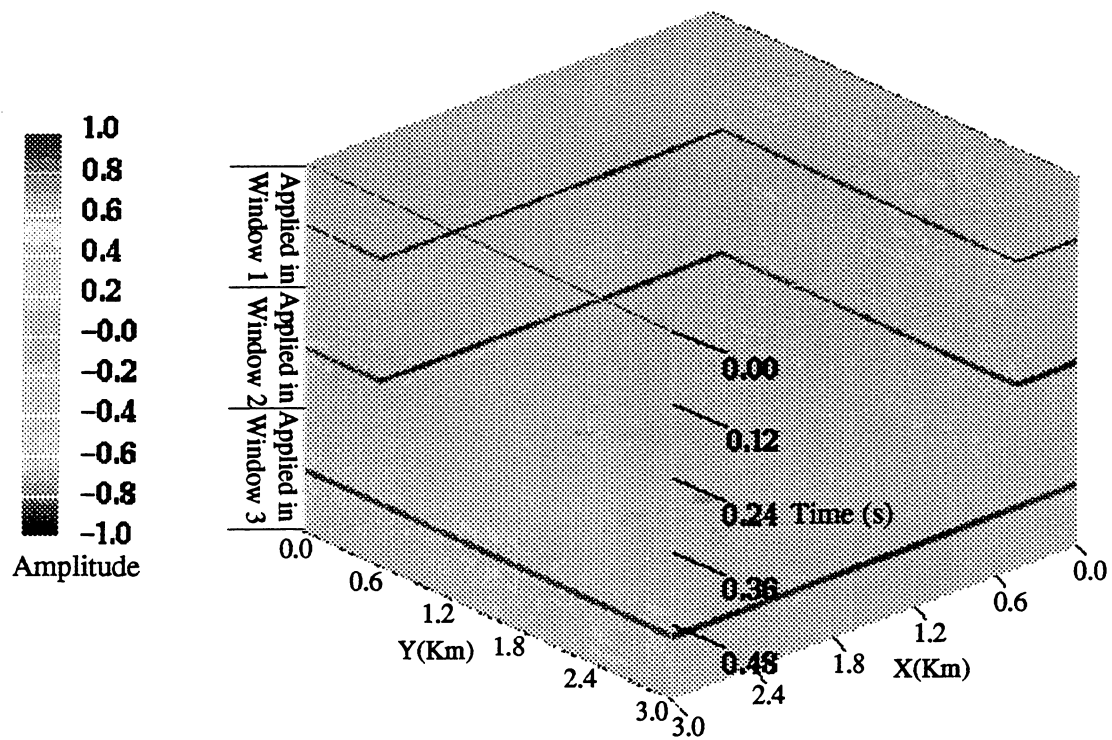


Figure 2.16. Dynamically extracted seismic wavelets from the 1985 seismic survey. The three wavelets extracted in three different windows (Figure 2.13) for each trace are concatenated together.

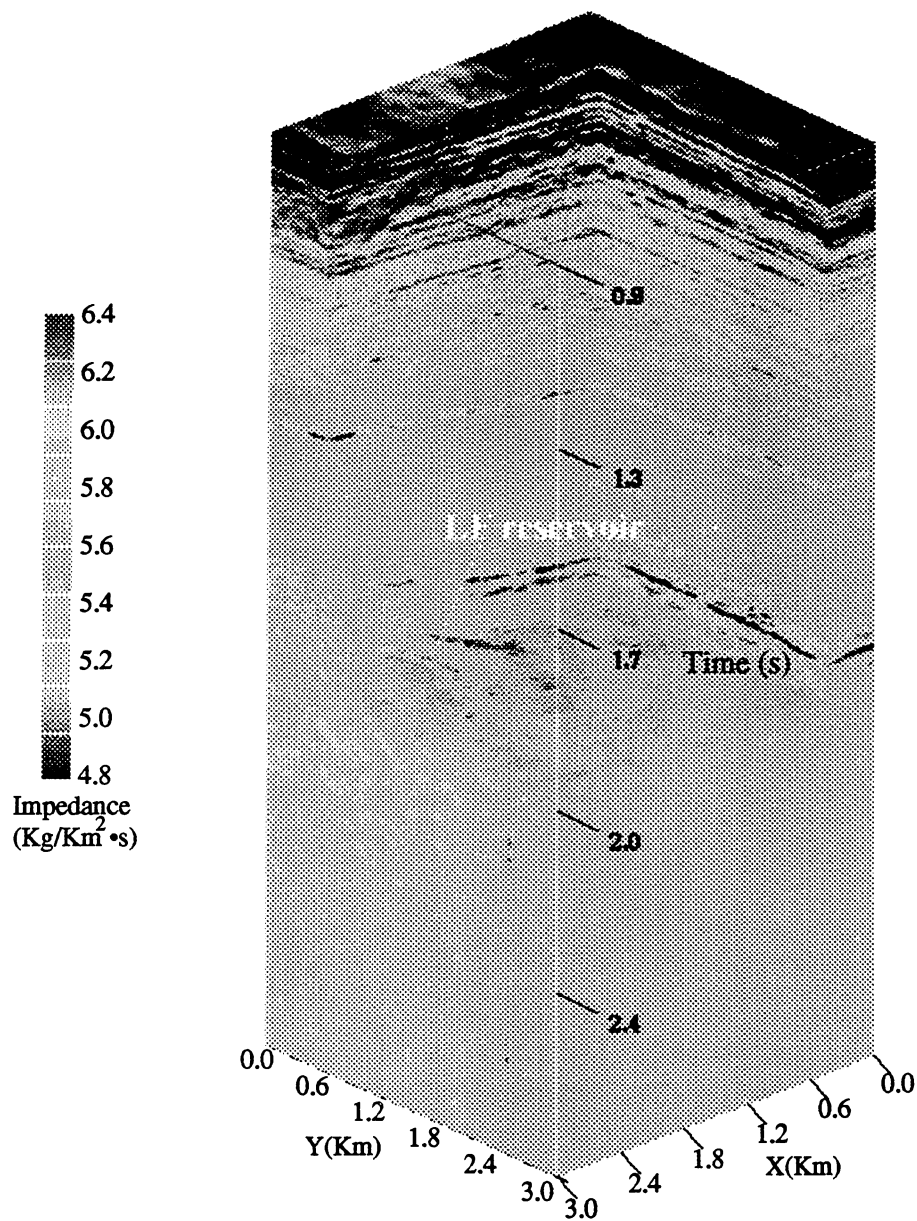


Figure 2.17. The estimated acoustic impedance volume of the 1992 seismic survey in the EI-330 Fault Block B. The slice is cut through the LF reservoir at mid-depth. The low impedance anomalies show very similar patterns to those in the 1985 survey (Figure 2.15).

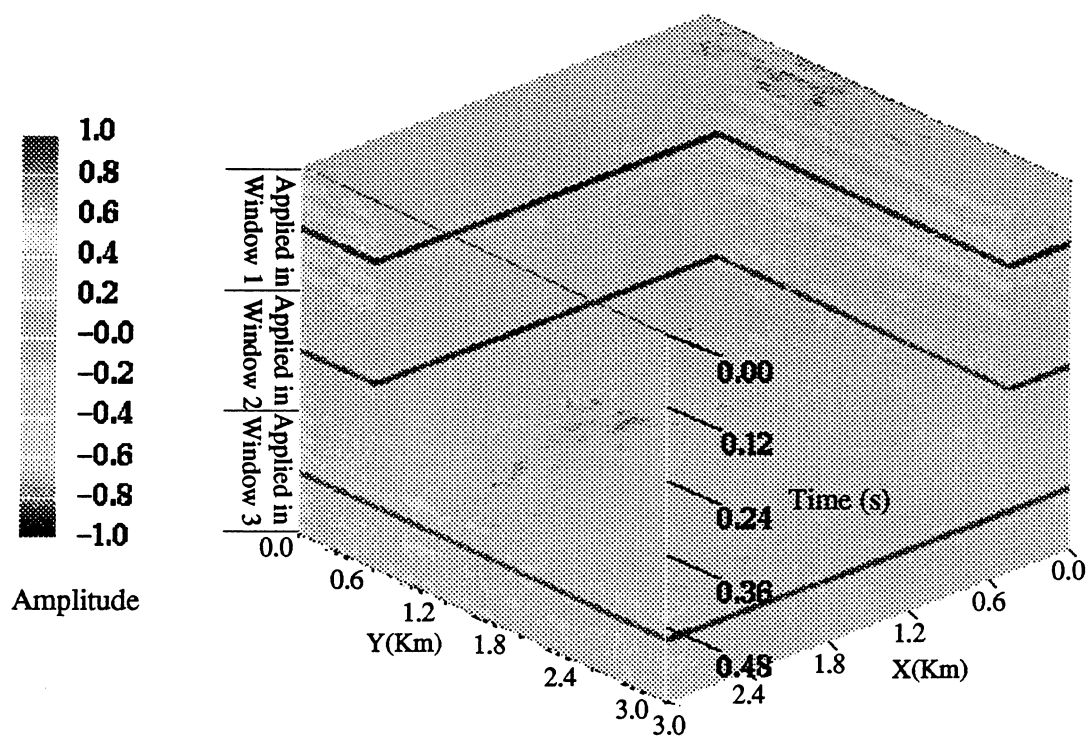


Figure 2.18. Dynamically extracted wavelet volume for inverting the 1992 dataset.

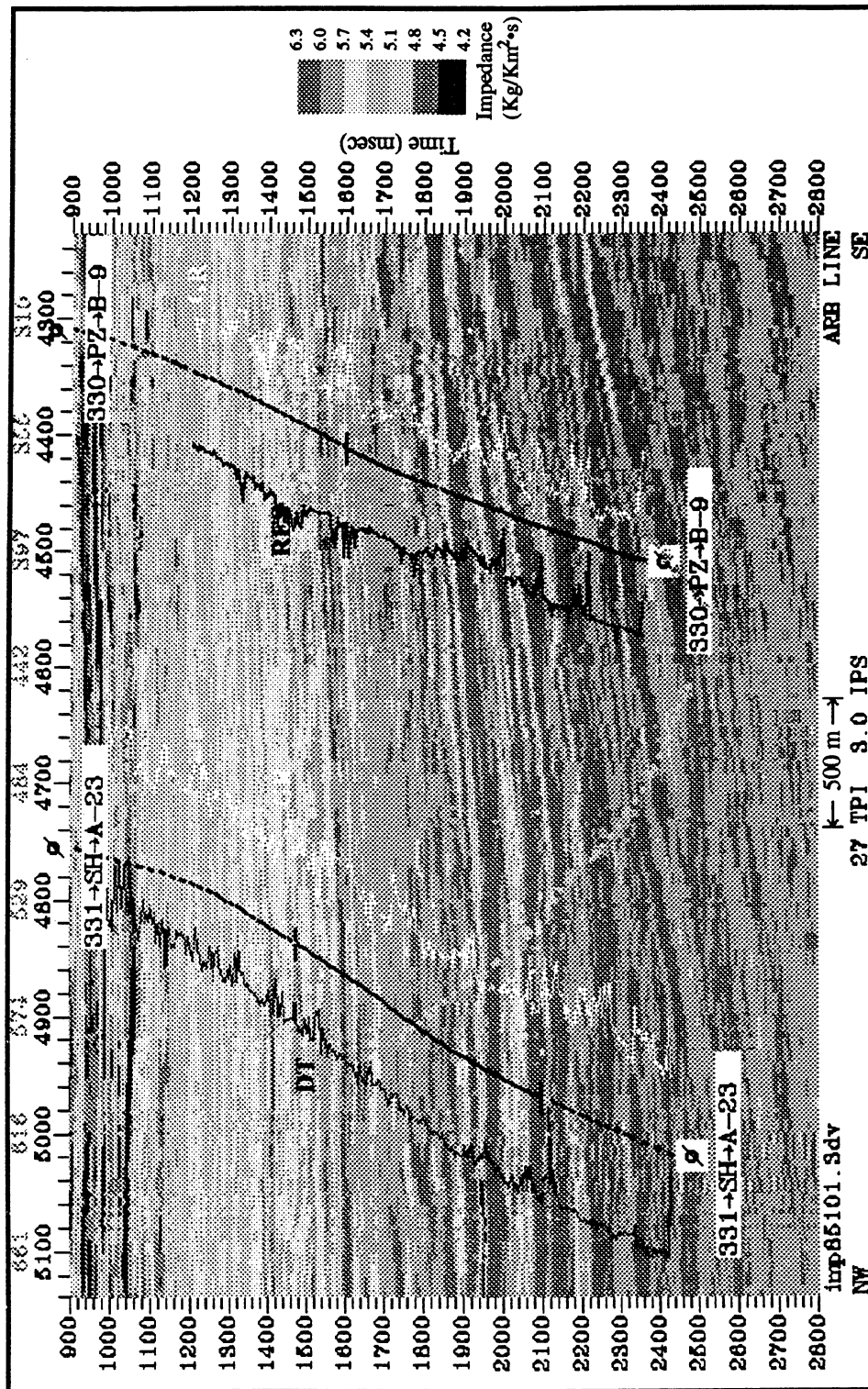


Figure 2.19 (a). Wells 331_SH_A-23 and 330_PZ_B-9 are superimposed on the G-G' impedance cross-section of the 1985 survey. Sonic logs (DT) increase from left to right, GR logs increase from right to left. Resistivity logs (RES) increase from left to right. The major production reservoirs are shown in green to blue indicating that hydrocarbon reservoirs are low impedance anomalies.

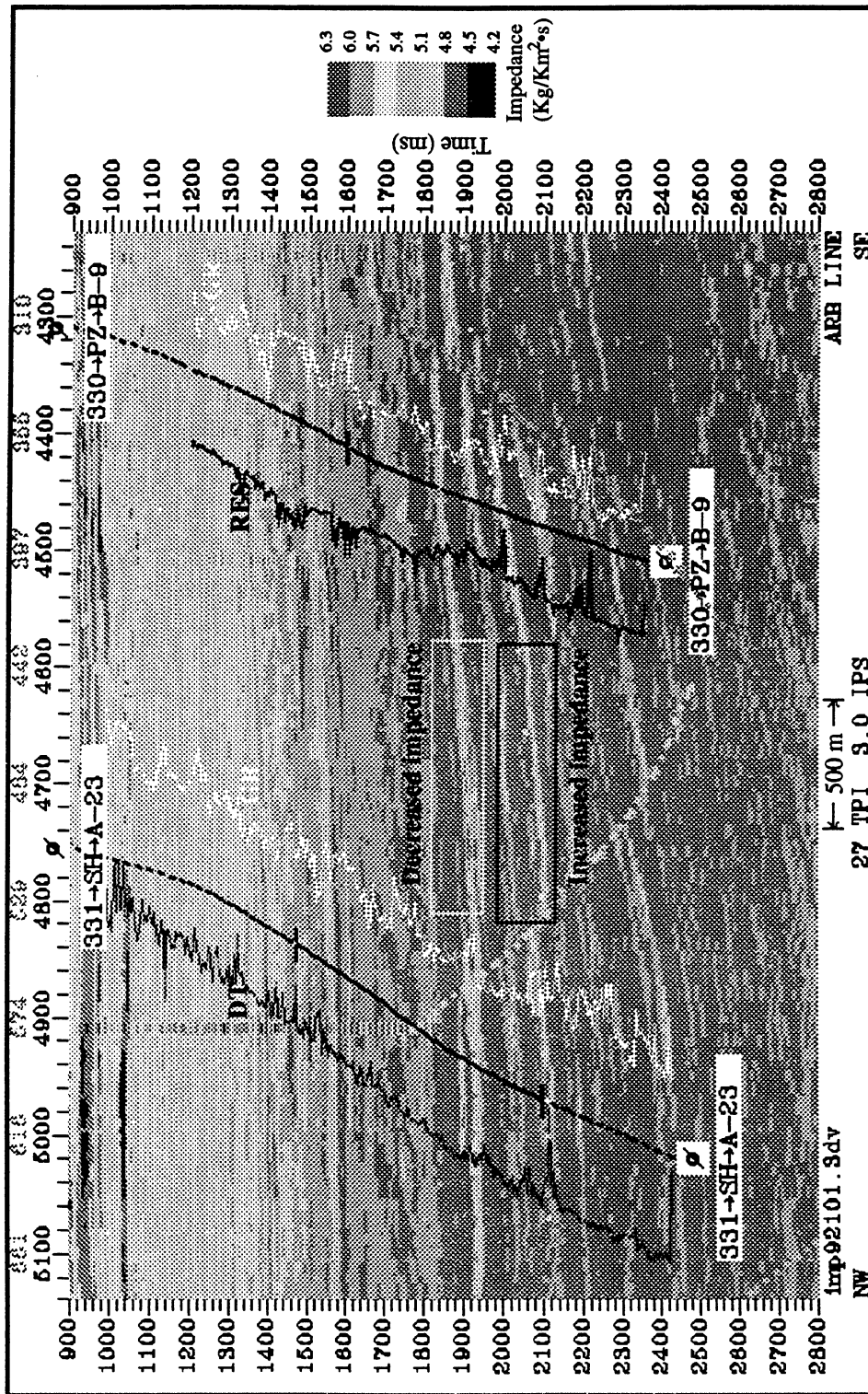


Figure 2.19 (b). Wells 331_SH_A-23 and 330_PZ_B-9 are superimposed on the G-G' impedance cross-section of the 1992 survey. Sonic logs (DT) increase from left to right, GR logs increase from right to left. Resistivity logs (RES) increase from left to right. The production reservoirs can still be identified as low impedance anomalies, but subtle impedance changes are observed when compared to the 1985 impedance cross-section (Figure 2.19 (a)). The banded high frequency features intersecting the A-23 path are caused by numerical errors in the inversion algorithm. They can be eliminated by filtering after inversion.

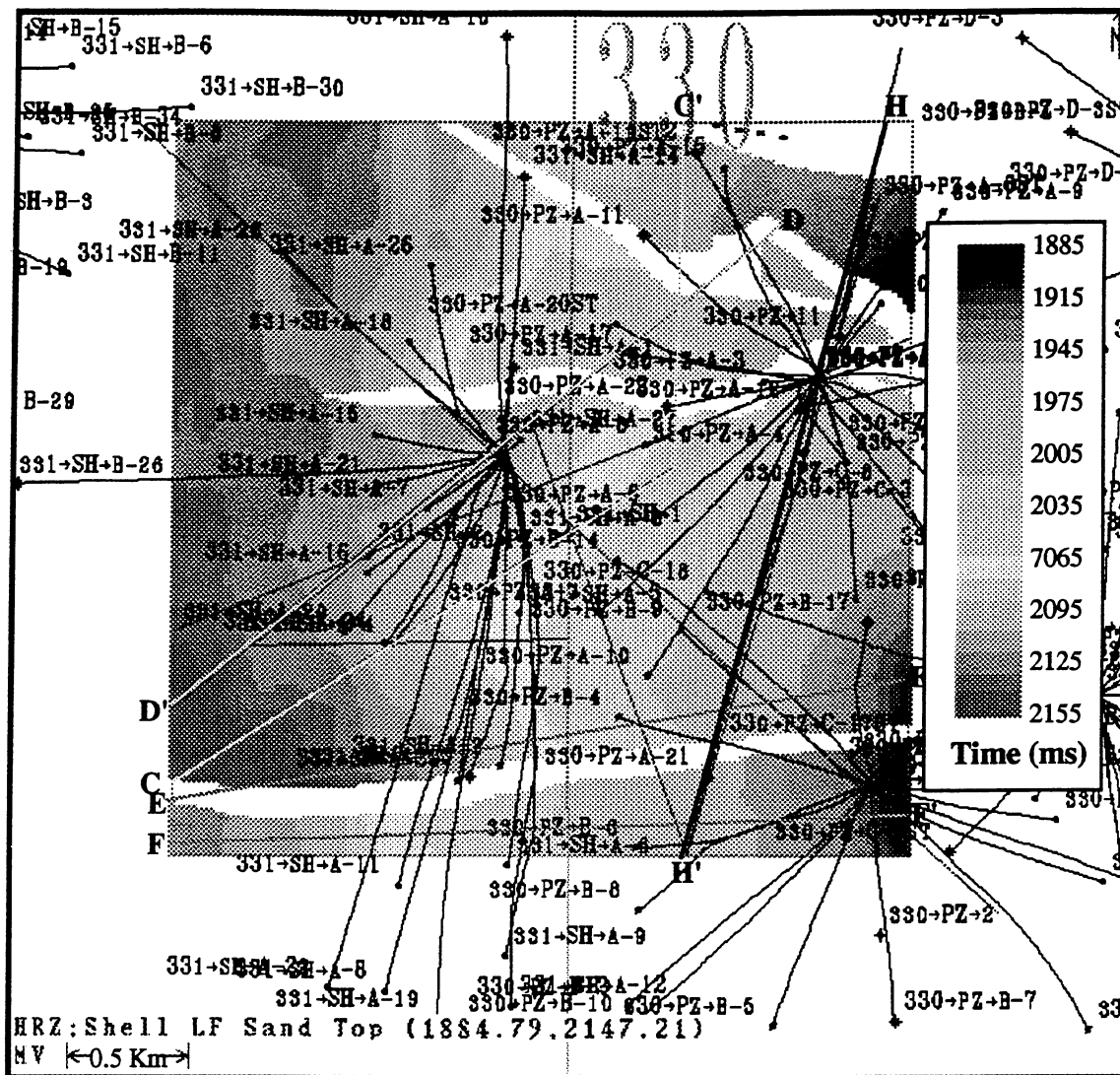


Figure 2.20. Locations of cross-sections where the estimated acoustic impedance volumes are examined are shown with the interpreted two-way traveltime to the top of the LF sand in the study area. The impedance cross-sections extracted from the 1992 impedance volume are annotated as C-C', D-D', E-E', F-F', and H-H'.

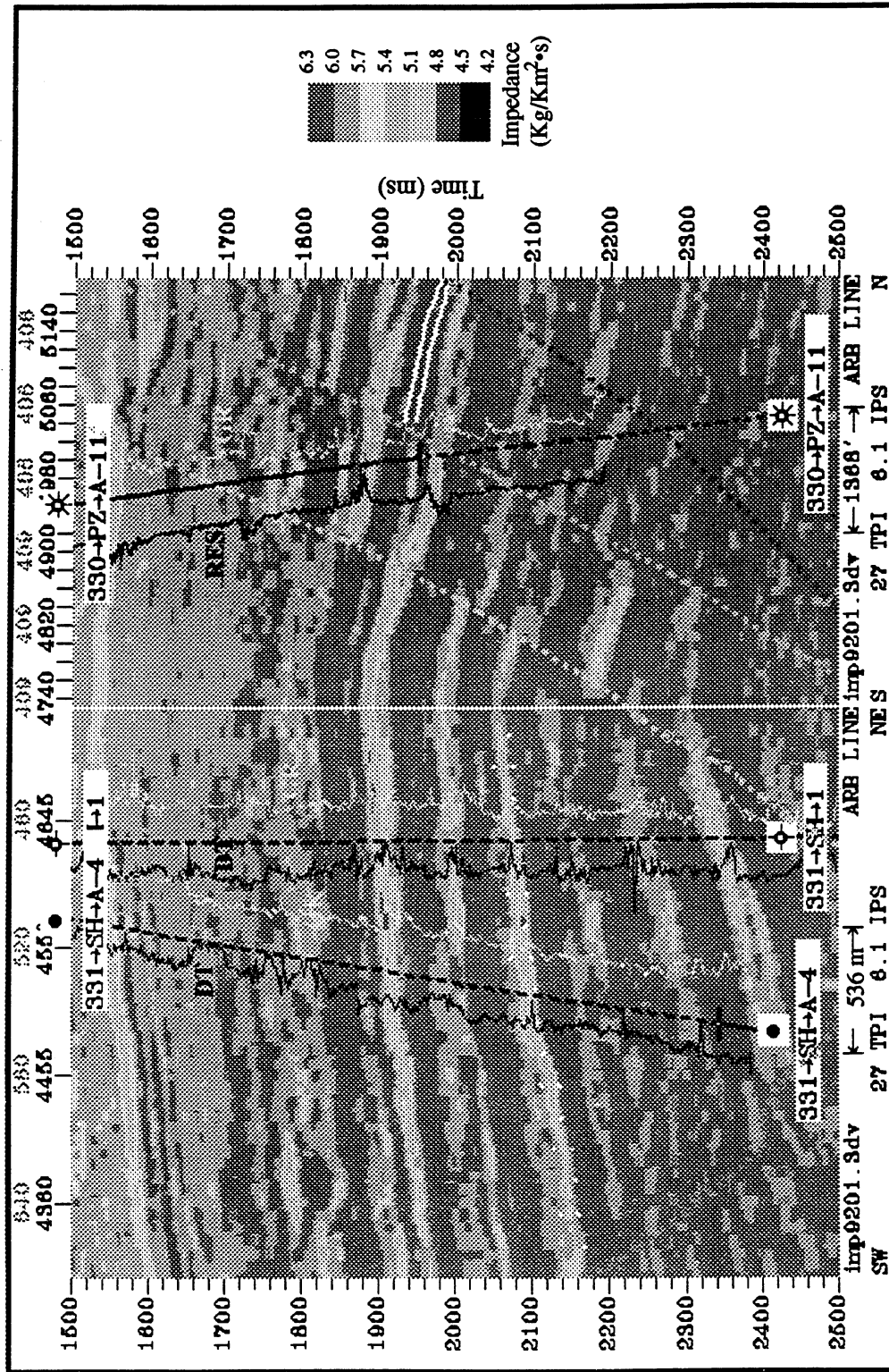


Figure 2.21. Wells 331_A-4, 331_SH_1 and 330_PZ-A-11 are superimposed on the C-C' impedance cross-section of the 1992 survey. The sonic logs (DT) increase from left to right, the GR logs increase from right to left. Resistivity logs increase from left to right.

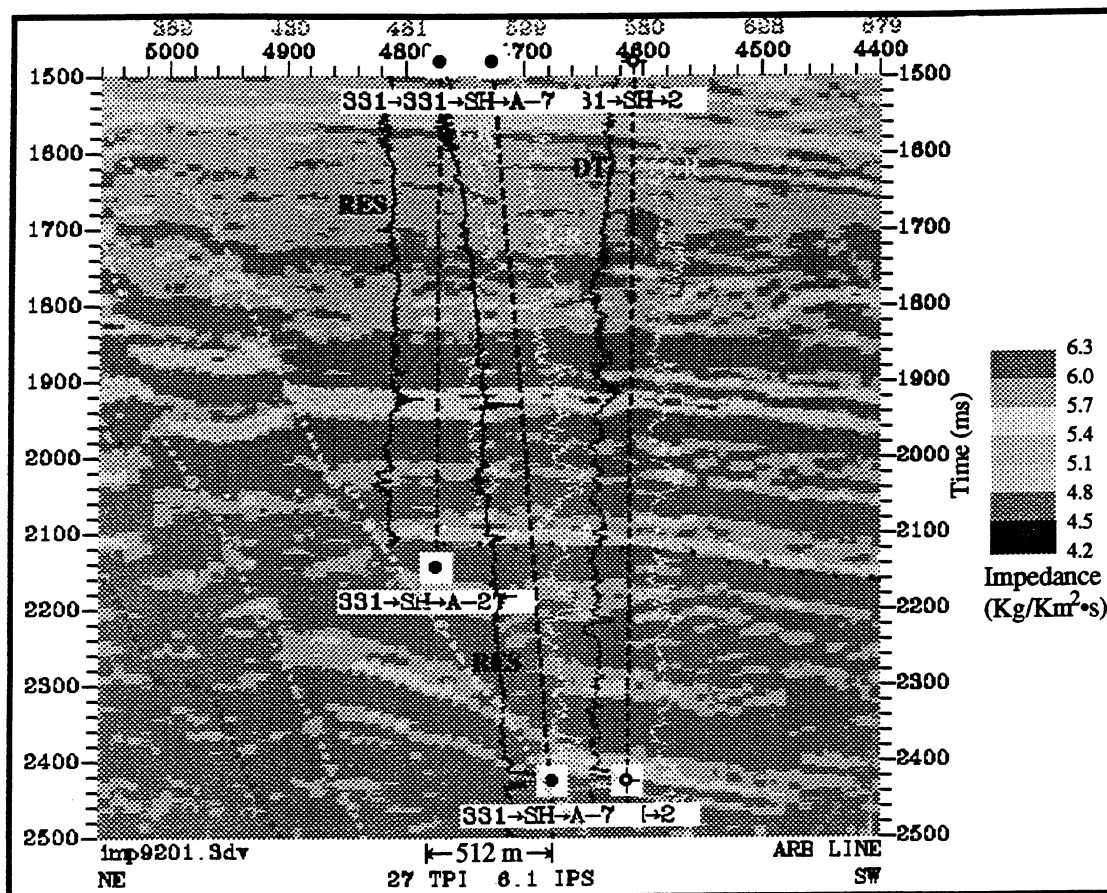


Figure 2.22. Wells 331_SH_A-27, 331_SH_A-7 and 331_SH_2 are superimposed on the D-D' impedance cross-section of the 1992 survey. Sonic logs increase from left to right, GR logs increase from right to left. Resistivity logs increase from left to right.

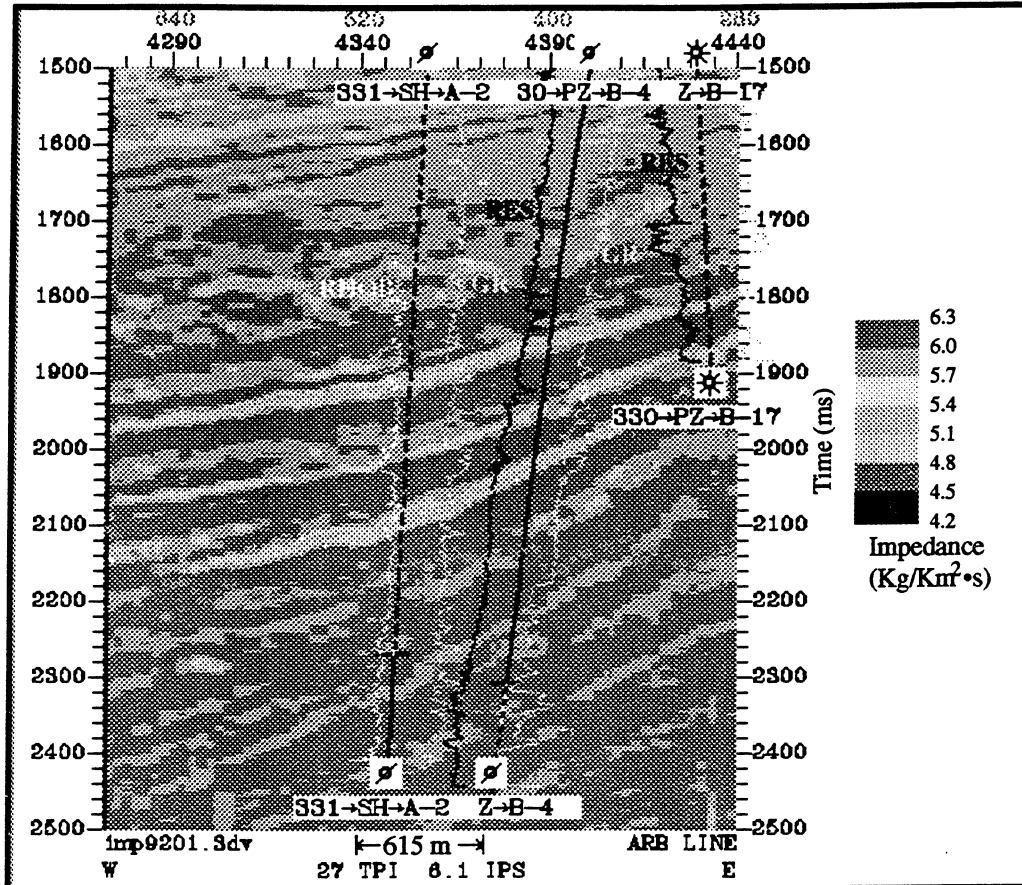


Figure 2.23. Wells 331_SH_A-2 and 330_PZ_B-4 are superimposed on the E-E' impedance cross-section of the 1992 survey. Sonic logs increase from left to right, GR logs increase from right to left. Both density and resistivity logs increase from left to right.

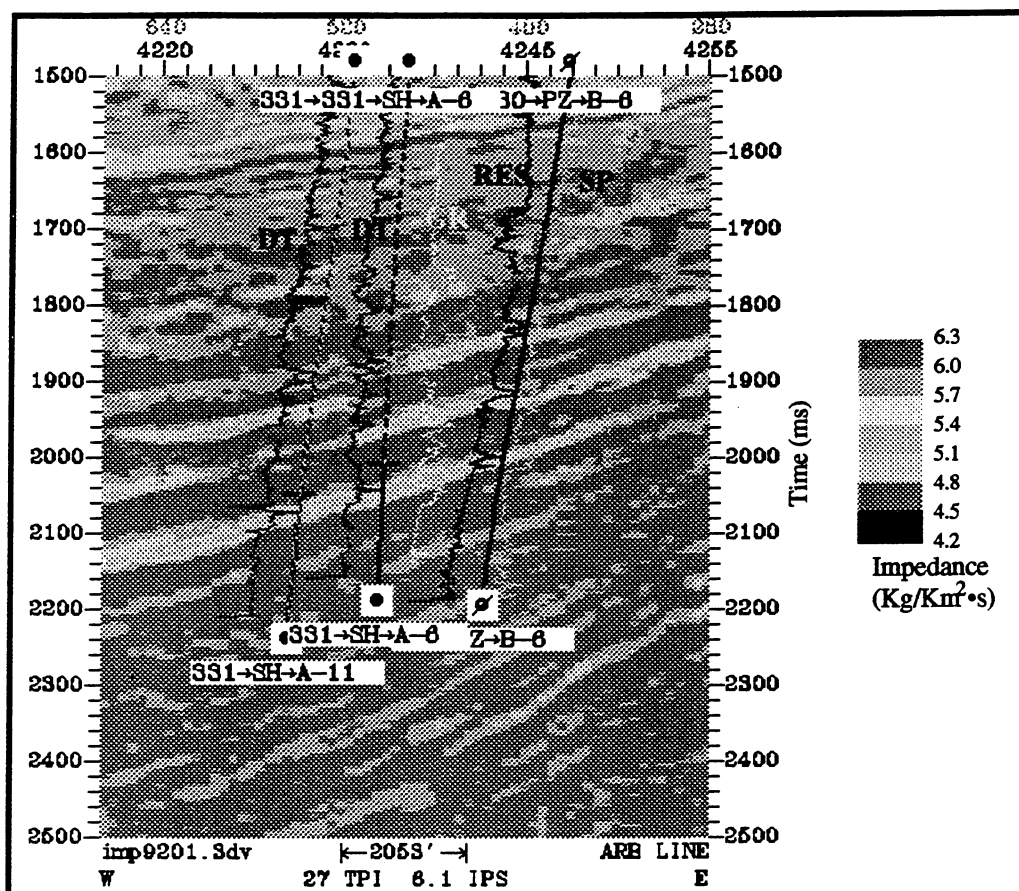


Figure 2.24. Wells 331_SH_A-11, 331_SH_A-6 and 330_PZ_B-6 are superimposed on the F-F' impedance cross-section of the 1992 survey. Sonic logs increase from left to right, GR logs increase from right to left. Resistivity logs increase from left to right, and SP logs increase from right to left.

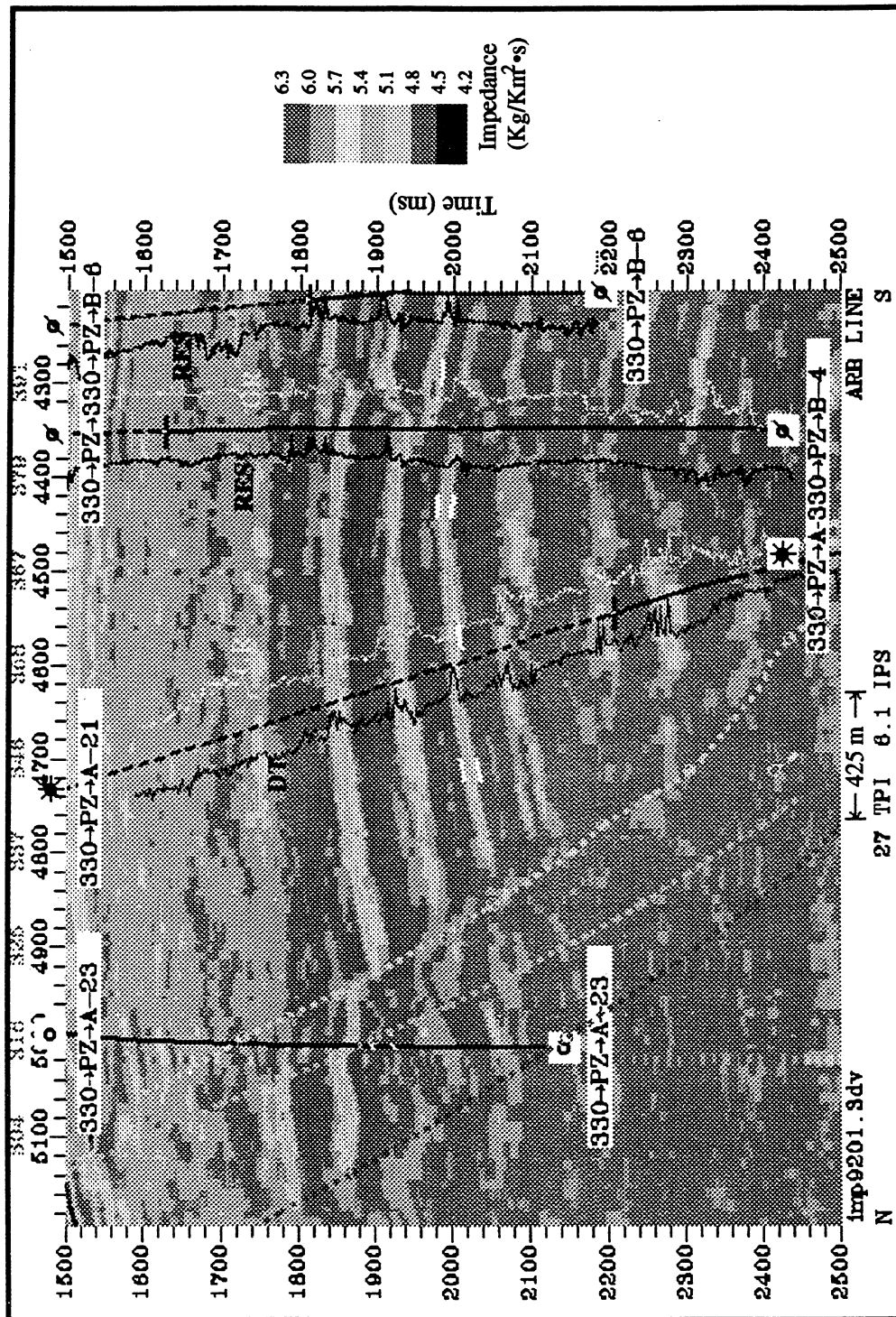


Figure 2.25. Wells 330_PZ_A-21, 330_PZ_B-4 and 330_PZ_B-6 are superimposed on the H-H' impedance cross-section of the 1992 survey. Sonic logs increase from left to right, GR logs increase from right to left, and resistivity logs increase from left to right.

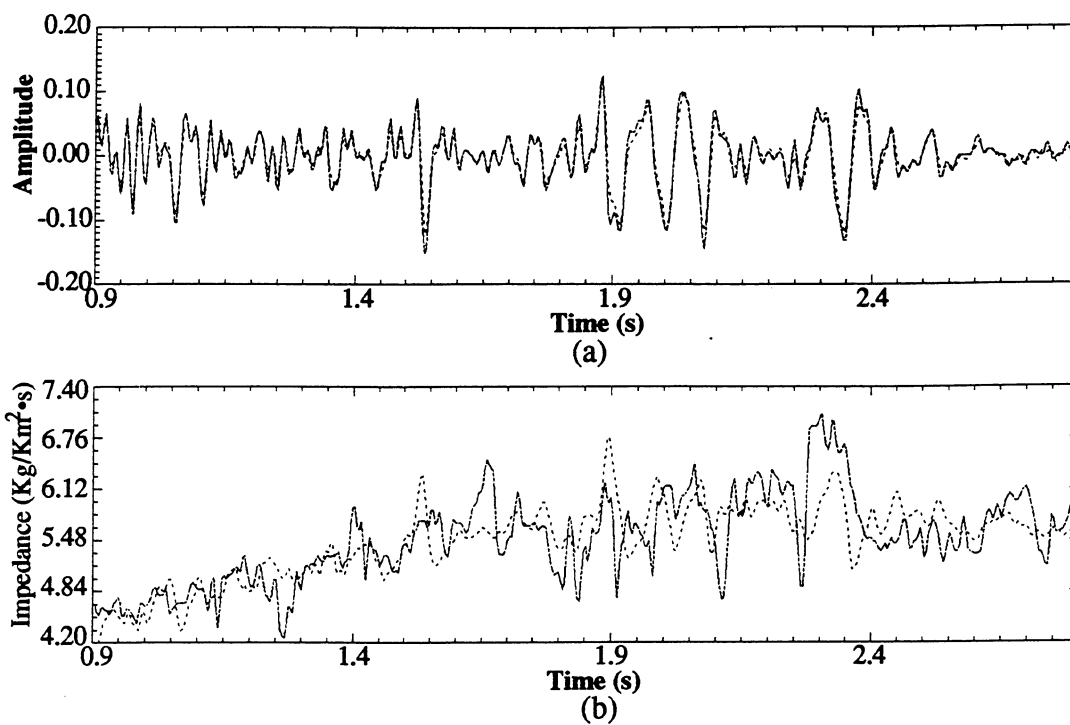


Figure 2.26. Inversion results. (a) The predicted seismic trace (dotted line) is almost identical to the observed seismic trace (solid line). (b) The estimated acoustic impedance function (dotted line) shares the same low-frequency trend as the measured impedance log (solid line). The high-frequency major features also match fairly well.

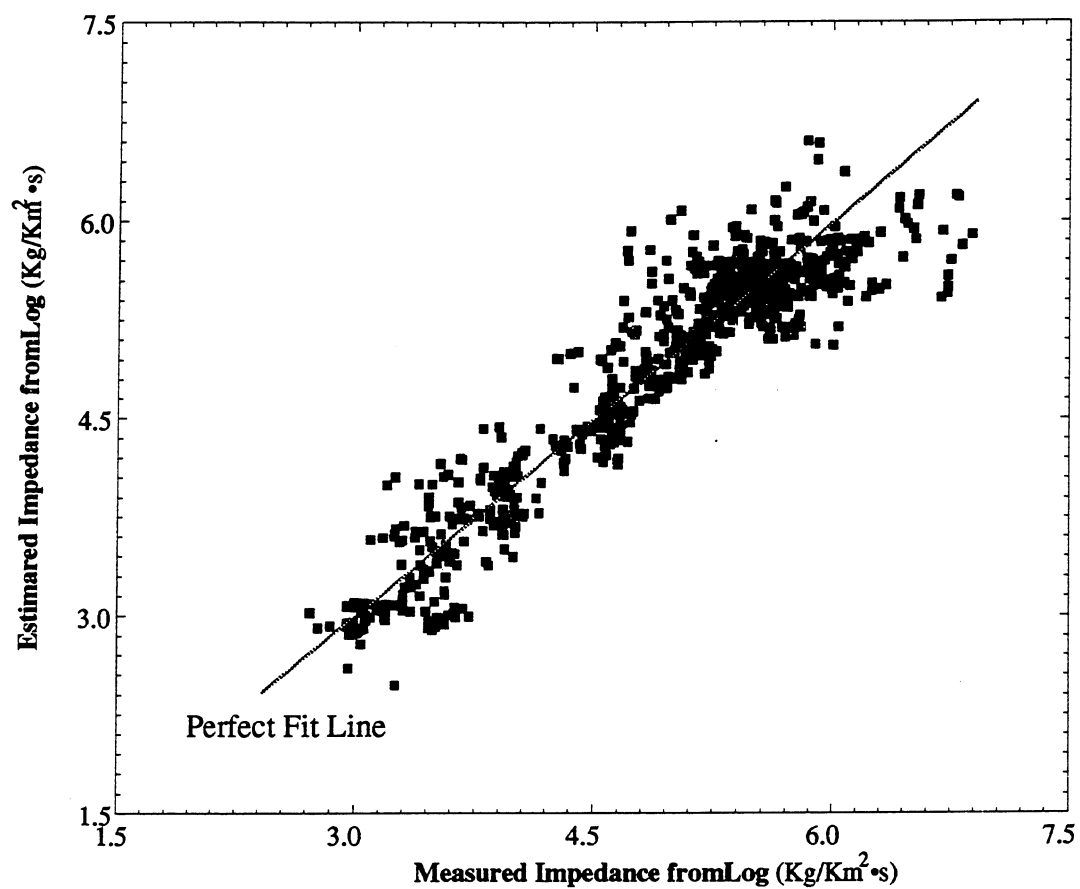


Figure 2.27. The estimated acoustic impedance from inversion compared with the measured impedance log in well 331_SH_1. The relative error is less than 10%.

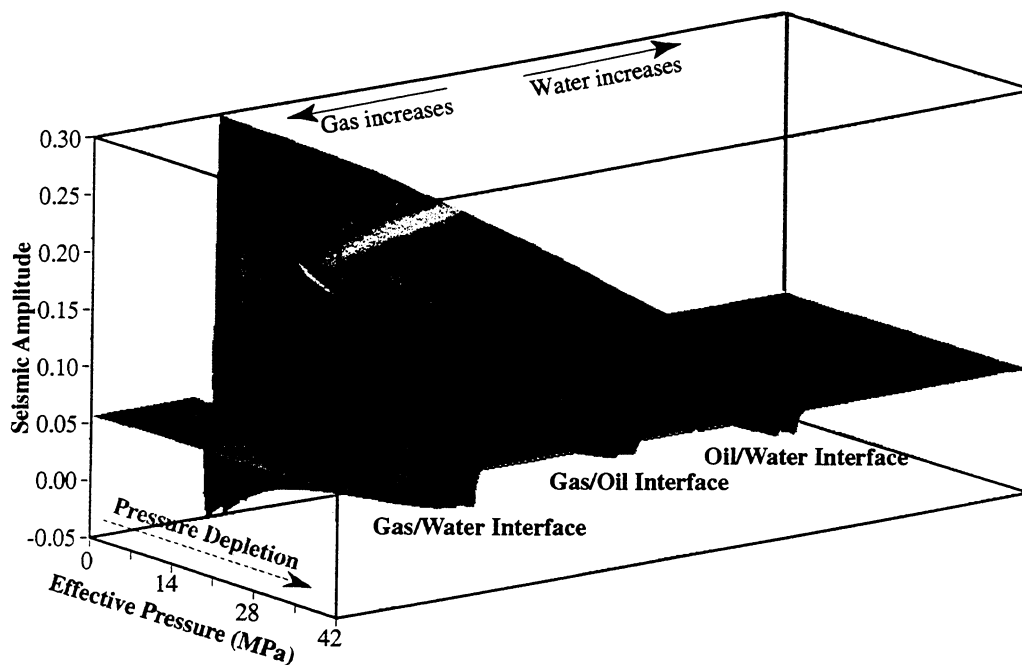
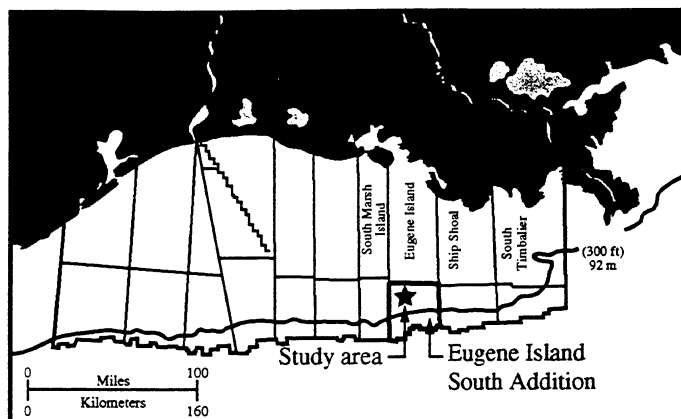
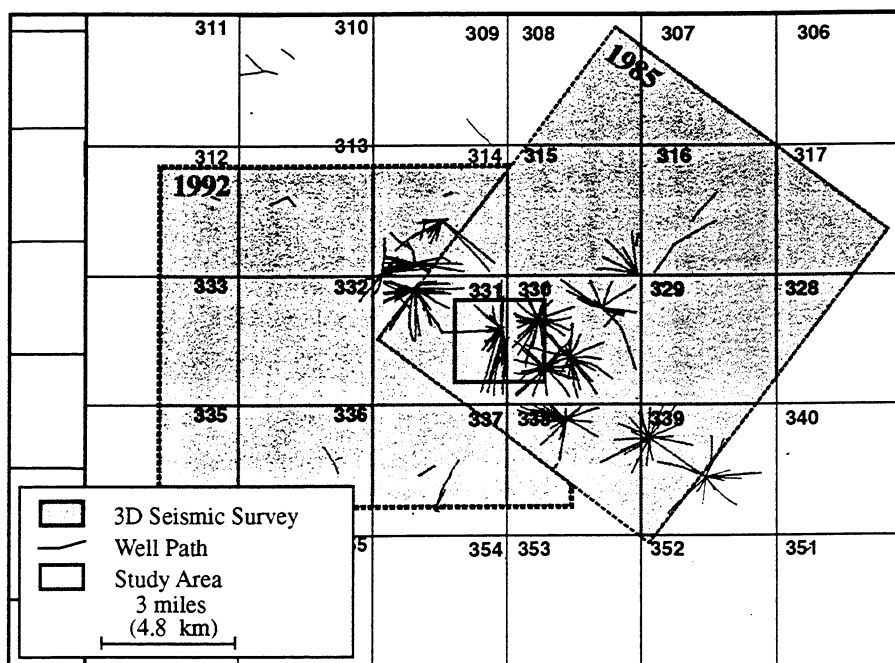


Figure 3.1. A generic seismic forward model is constructed to illustrate the effects of hydrocarbon production on reflection seismic amplitude. The horizontal axes can be considered as the fluid substitution process. The predicted amplitude change surface is nonlinearly interpolated from the amplitudes of three interfaces.



(a)



(b)

Figure 3.2. Geographic location of the Eugene Island 330 Field is shown in (a), and the orientations (coverage) of the 1985 and the 1992 3D seismic surveys and more than 500 wells are shown in (b). The study area is the red rectangular area in the center of (b).

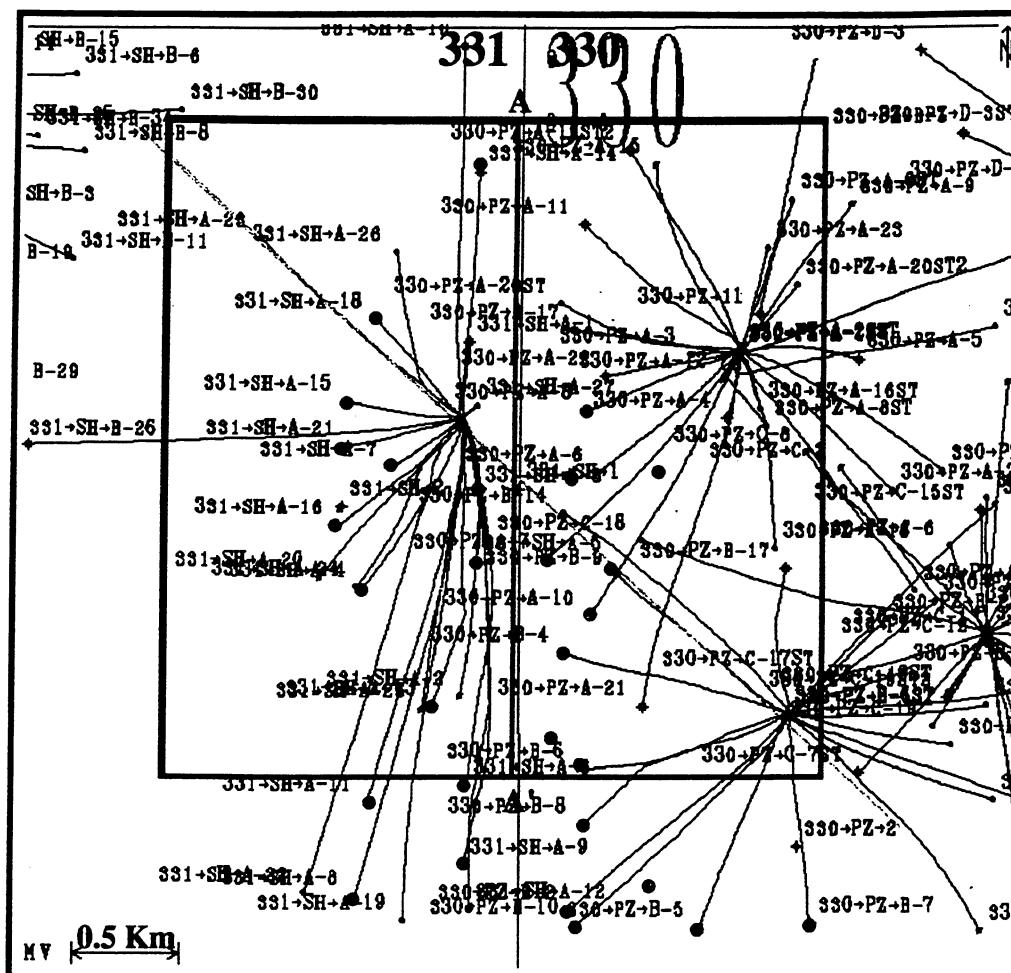


Figure 3.3. There are a total of seventy-four wells in the study area (outlined by red rectangle). Production data were collected in the wells marked (red circles filled with blue). Nineteen wells within the study area are used in this study. The black line denotes the location of profile A-A' a seismic cross-section used to show comparison between the 1985 and the 1992 3D seismic surveys in Figure 3.11.

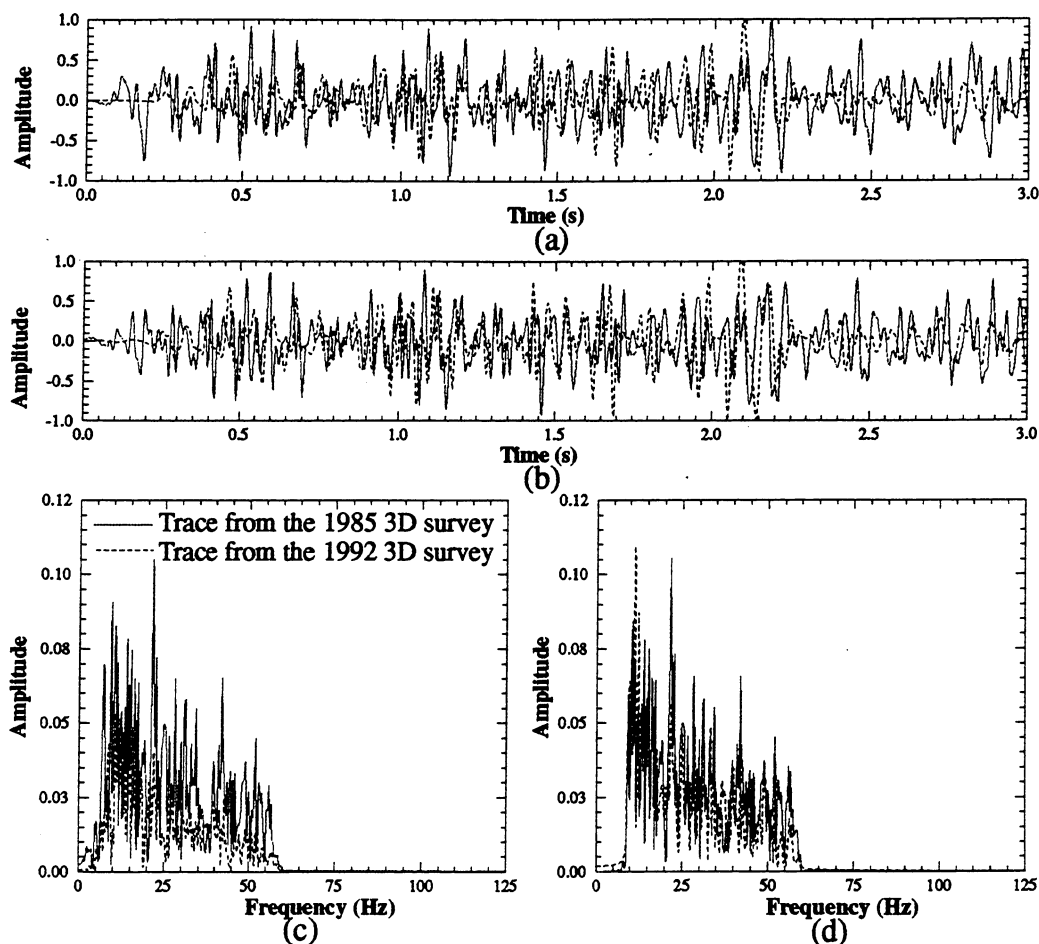


Figure 3.4. The spectral matching of our 4D seismic technique is applied to two seismic traces (a) extracted at the same location from the two seismic volumes. A zero-phase bandpass filter with the common frequency bandwidth is determined from the Fourier spectra of the two traces. The filtered traces are shown in (b). The frequency spectra before and after filtering are shown in (c) and (d), respectively.

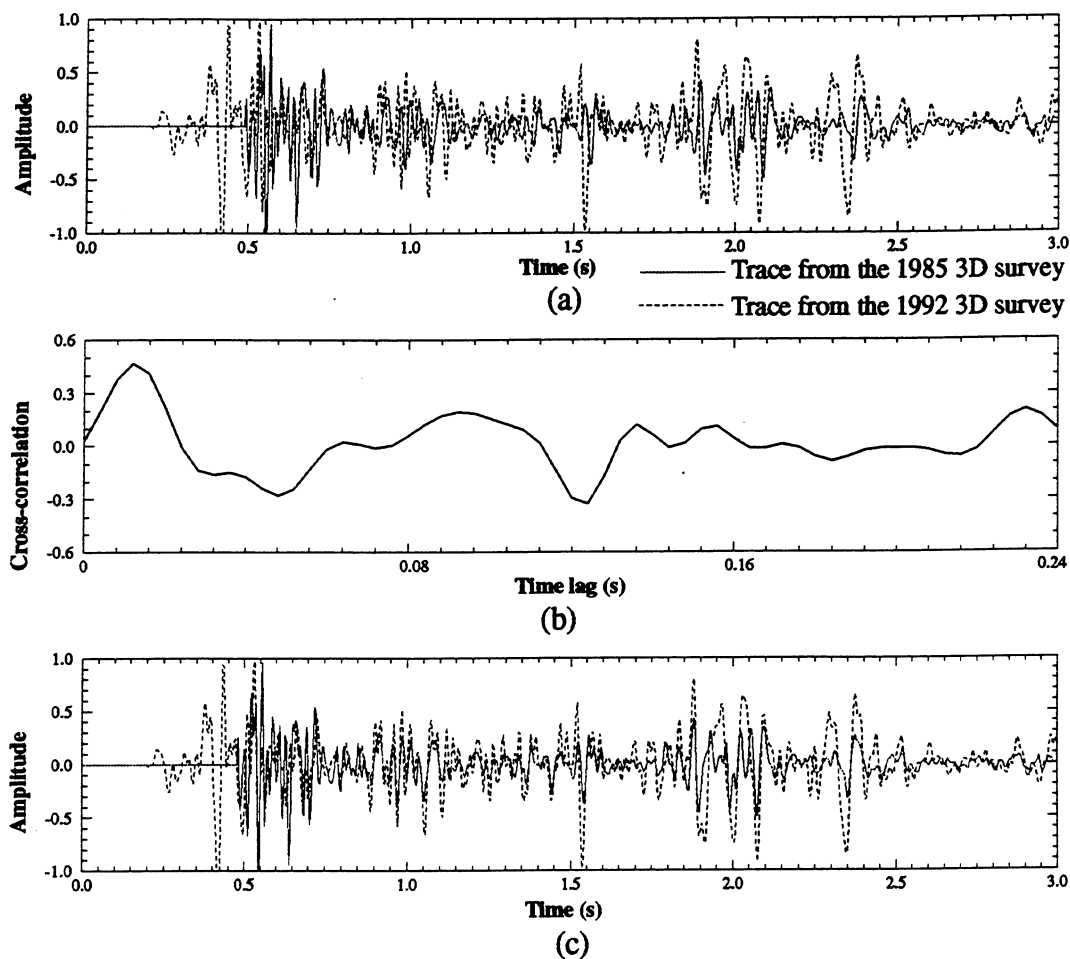


Figure 3.5. The static shift (misfit) is corrected using a cross-correlation technique applied in the vertical direction to two 3D seismic surveys. Two seismic traces extracted at the same location from the 1985 and the 1992 surveys are shown in (a). The cross-correlation of the two traces is shown in (b), and the corrected traces are shown in (c).

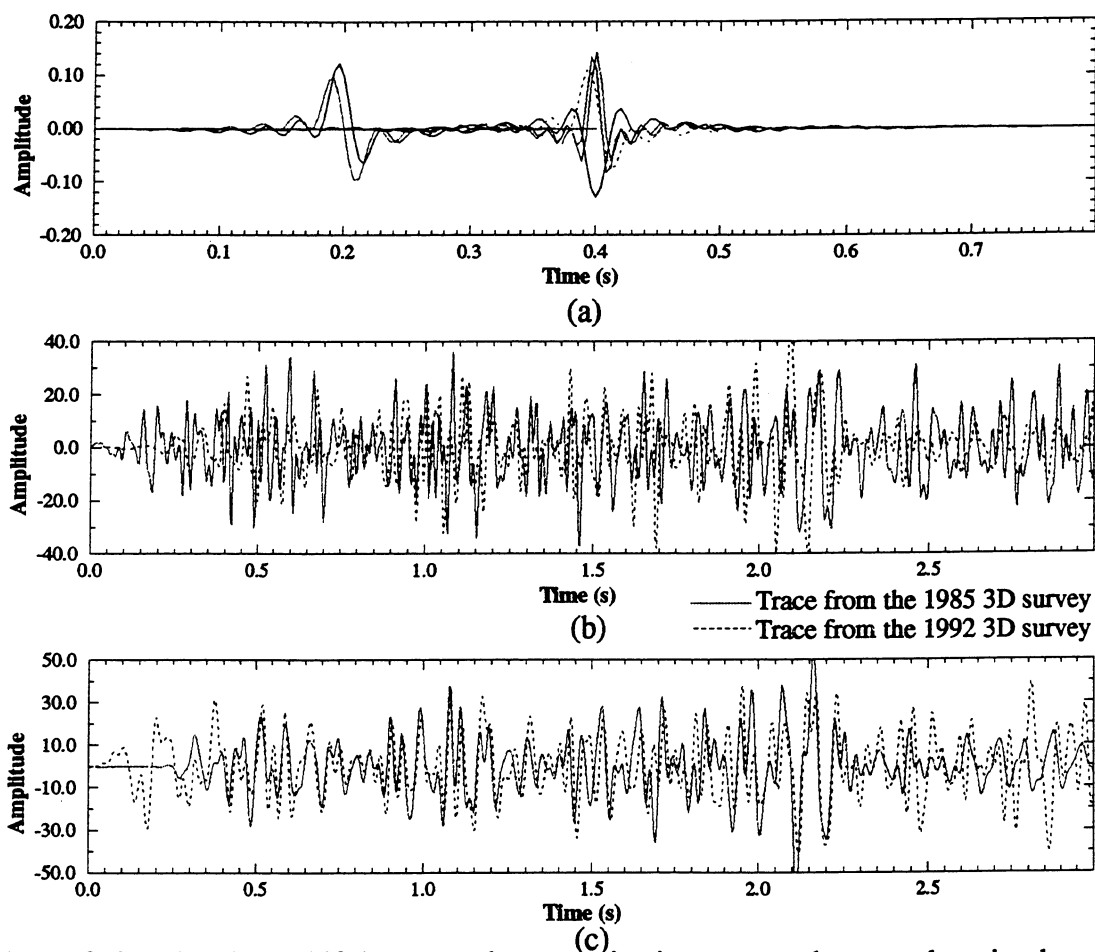
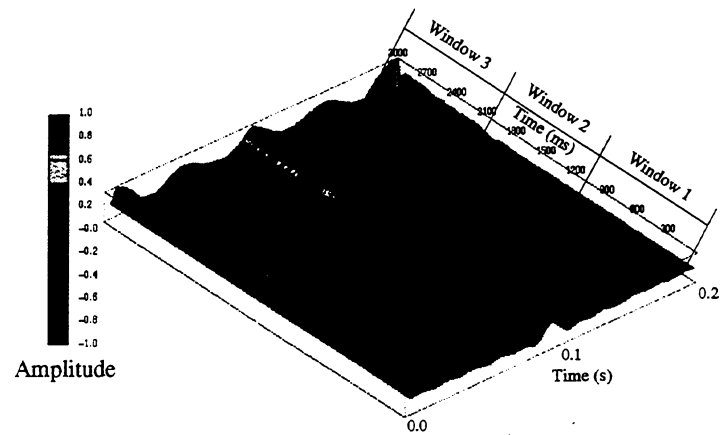
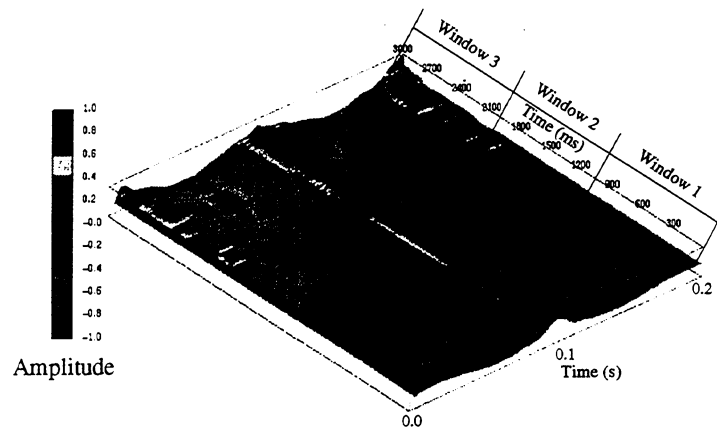


Figure 3.6. The phase shift between the two seismic traces at the same location but from two seismic surveys (b) is determined using a cross-correlation technique in our study. Several bandpass filters with the same common frequency bandwidth and different phase angles are shown in (a). The corrected seismic traces are shown in (c).



(a)



(b)

Figure 3.7. The time-variant autocorrelation function of two traces extracted from the 1985 and the 1992 seismic volumes are shown in (a) and (b), respectively. The waveform characteristics revealed indicate that frequency bandwidth of the two seismic traces are time-variant, i.e., depth-dependent. Three time windows, namely, 0-1, 1-2 and 2-3 seconds of two-way traveltime, have different frequency bandwidths.

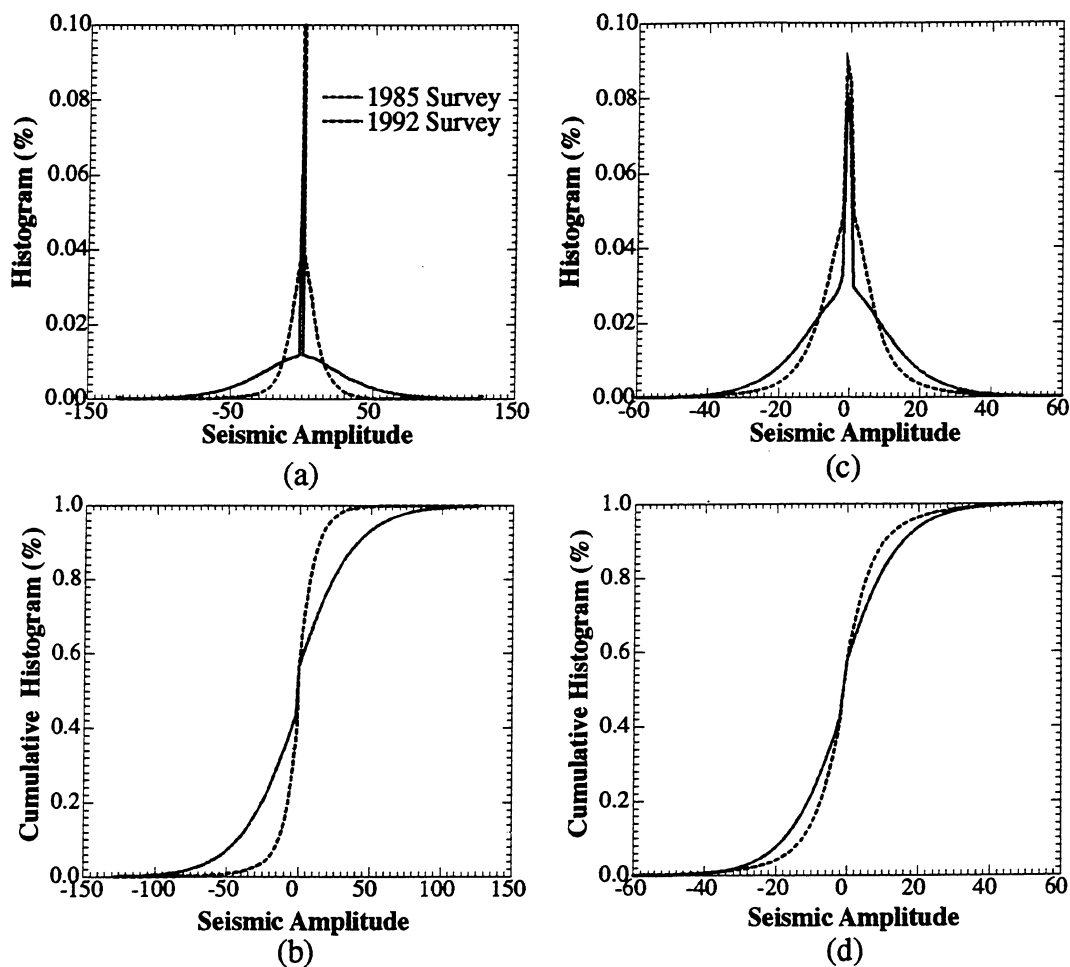


Figure 3.8. (a) Histograms of the 1985 and 1992 seismic volumes. (b) Cumulative histograms. The final distributions after rescaling are shown in (c) and (d). The residual differences are believed to be the real differences, which can be used to monitor hydrocarbon drainage over time.

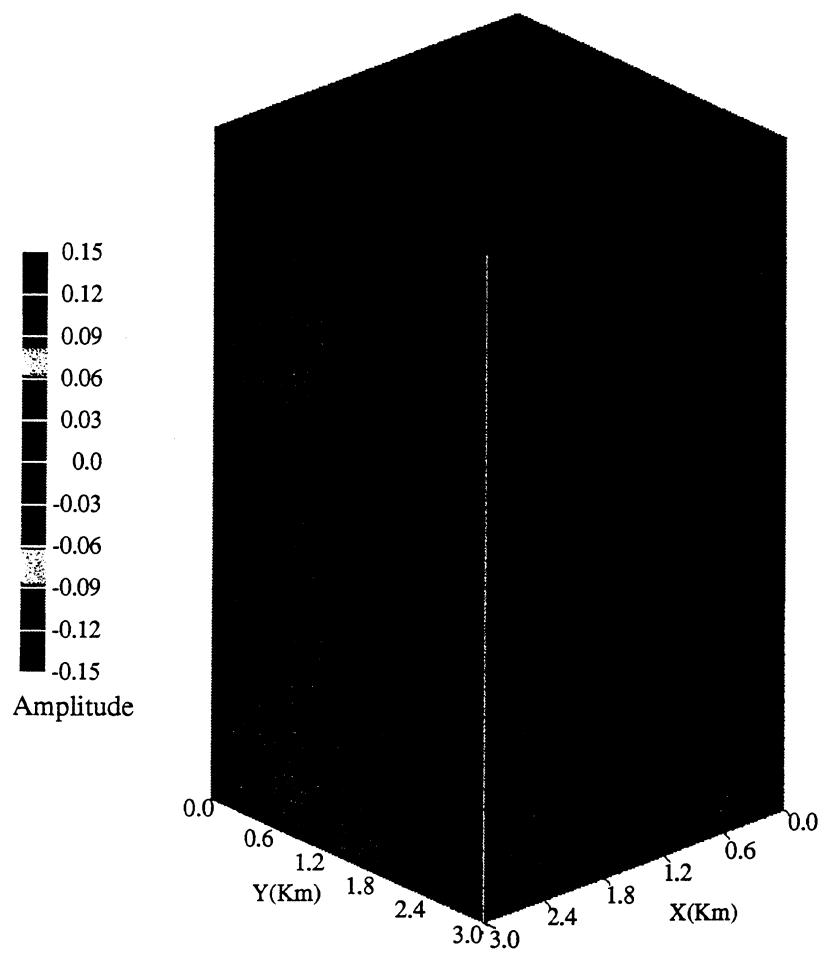


Figure 3.9. The pre-processed 1985 3D seismic survey, which matches the 1992 3D seismic survey (Figure 3.10).

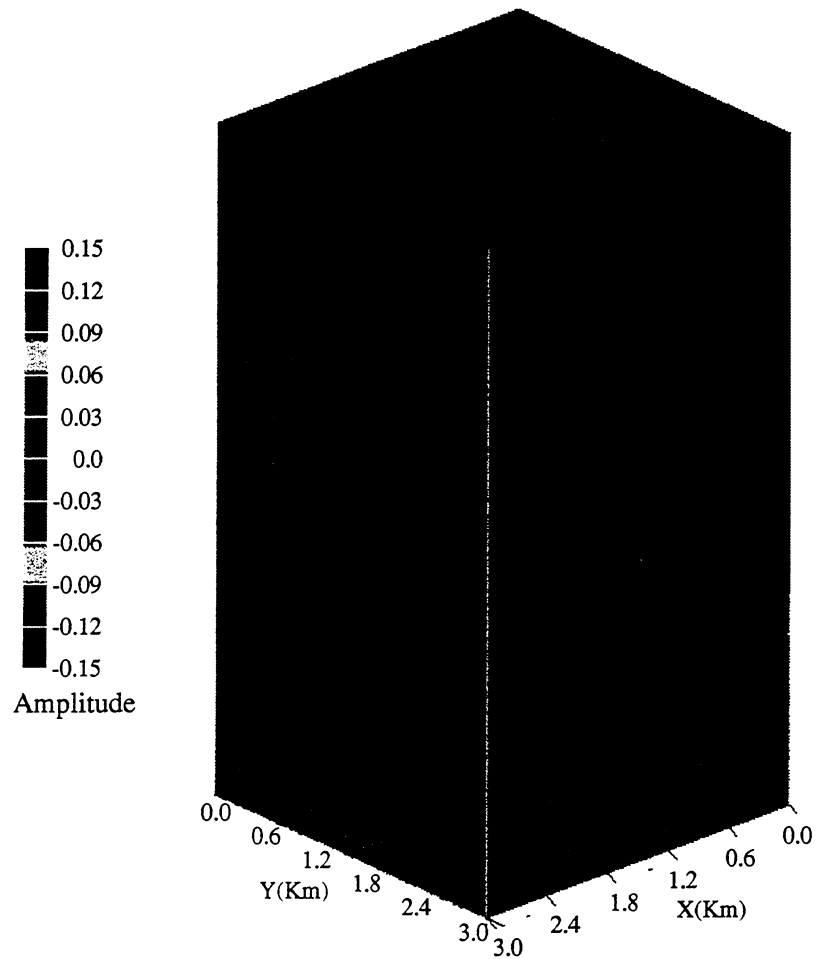
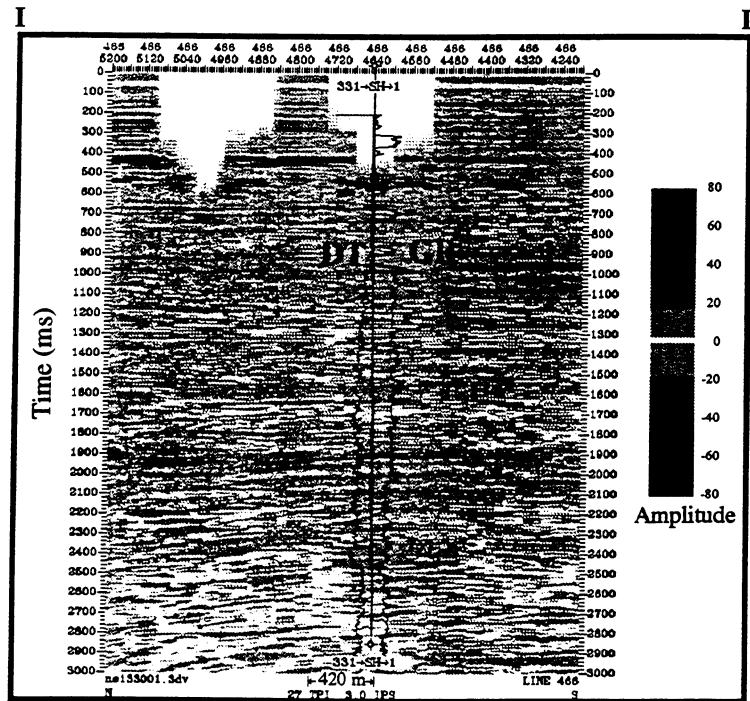
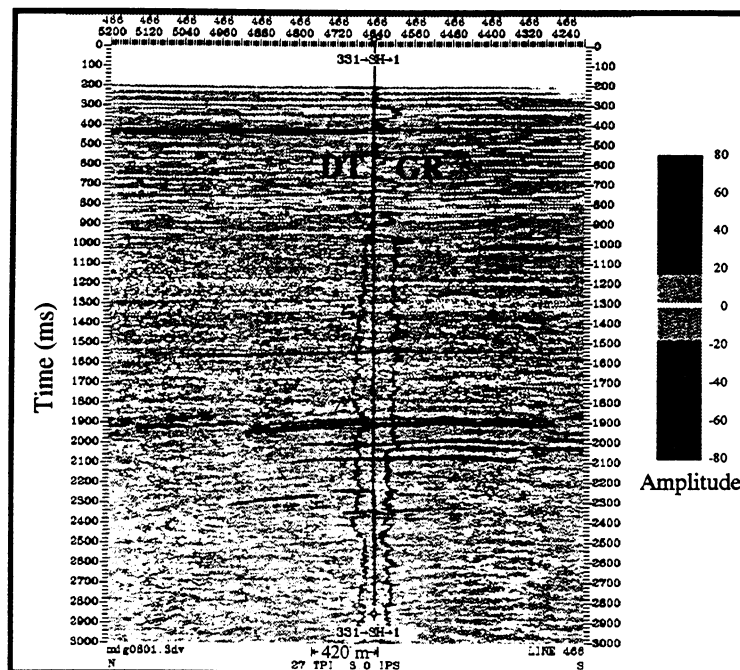


Figure 3.10. The pre-processed 1992 3D seismic survey. Seismic amplitudes of both volumes (the 1985 and 1992 surveys) are normalized and calibrated using synthetic seismograms generated from sonic and density logs from wells within the volume.



(a)



(b)

Figure 3.11. The seismic cross-sections along A-A' profile (Figure 3.3) are extracted at the same location from the reoriented 1985 (a) and the 1992 (b) 3D seismic surveys. Sonic logs (DT) increase from left to right, GR logs increase from right to left. Although these datasets were acquired seven years apart, they show structural similarities. The differences observed within the reservoirs are likely to be caused by hydrocarbon drainage between 1985 and 1992.

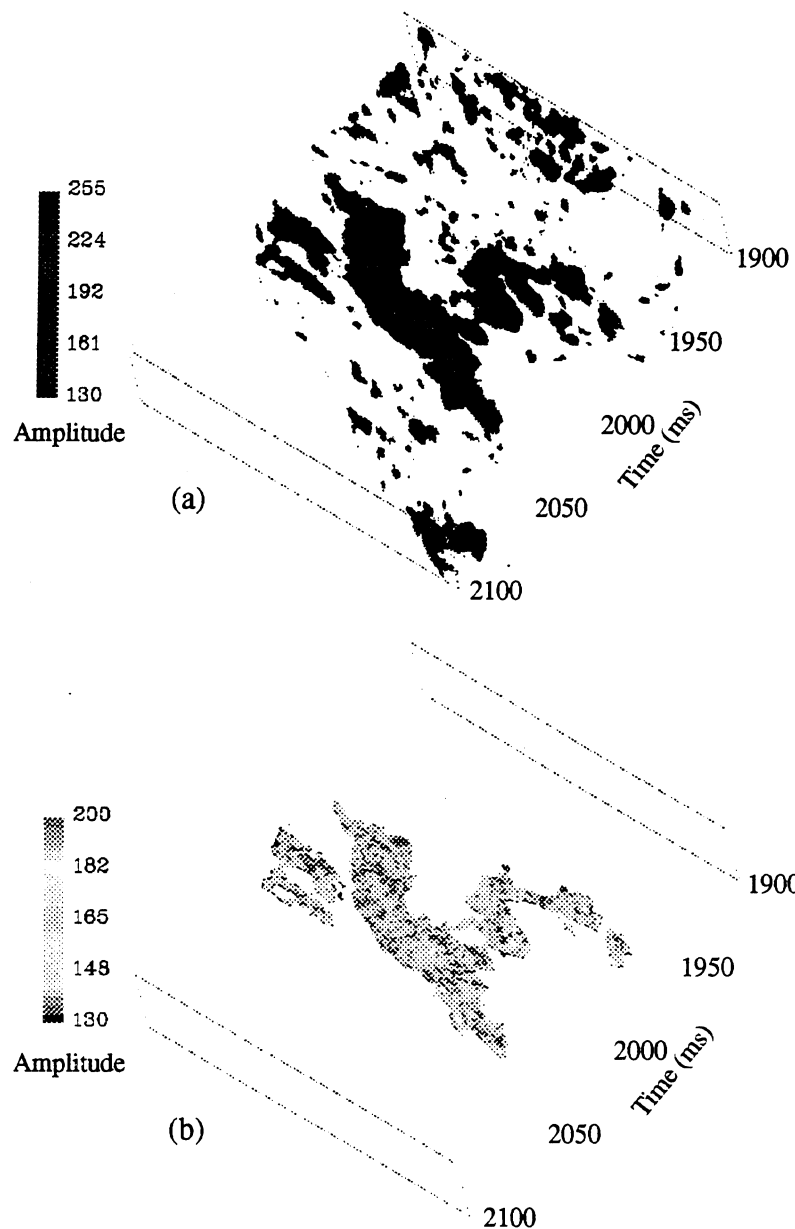


Figure 3.13. The comparison between the conventional isosurface technique (a) and our region-growing technique for the LF reservoir in the EI-330 Filed.

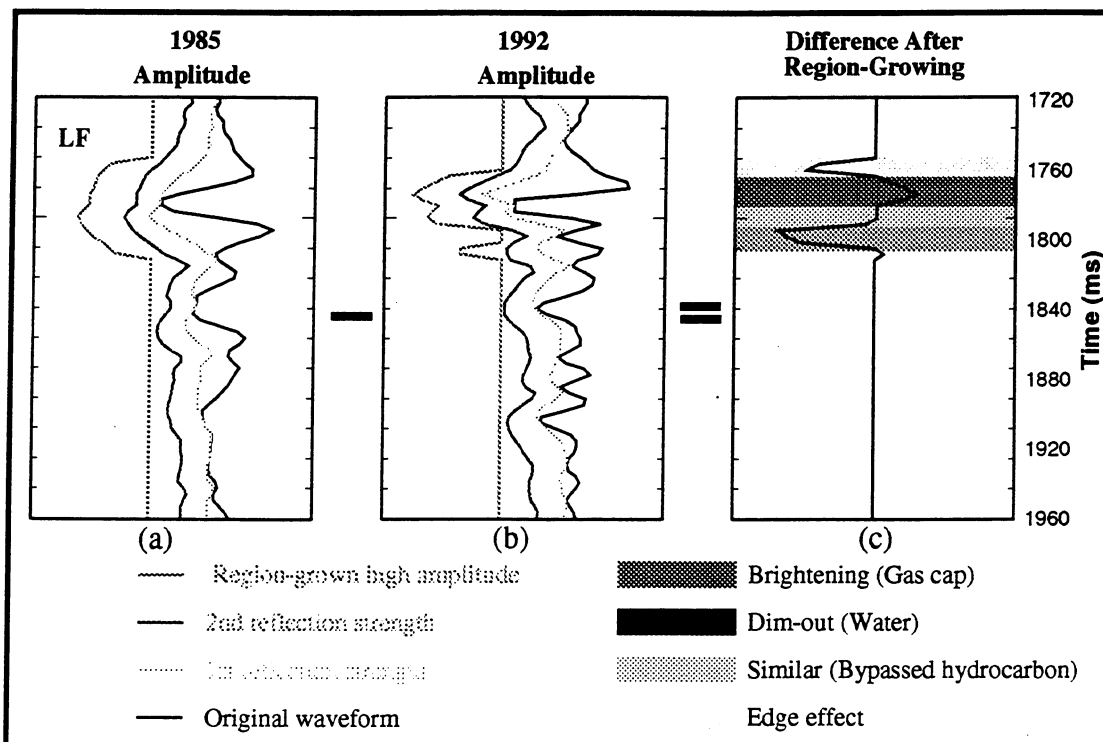
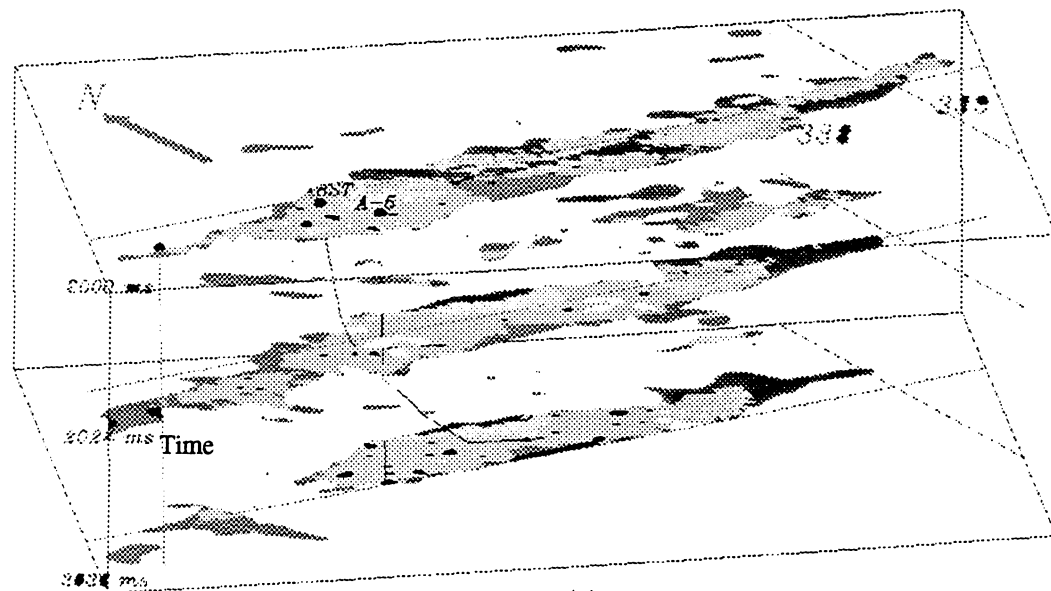
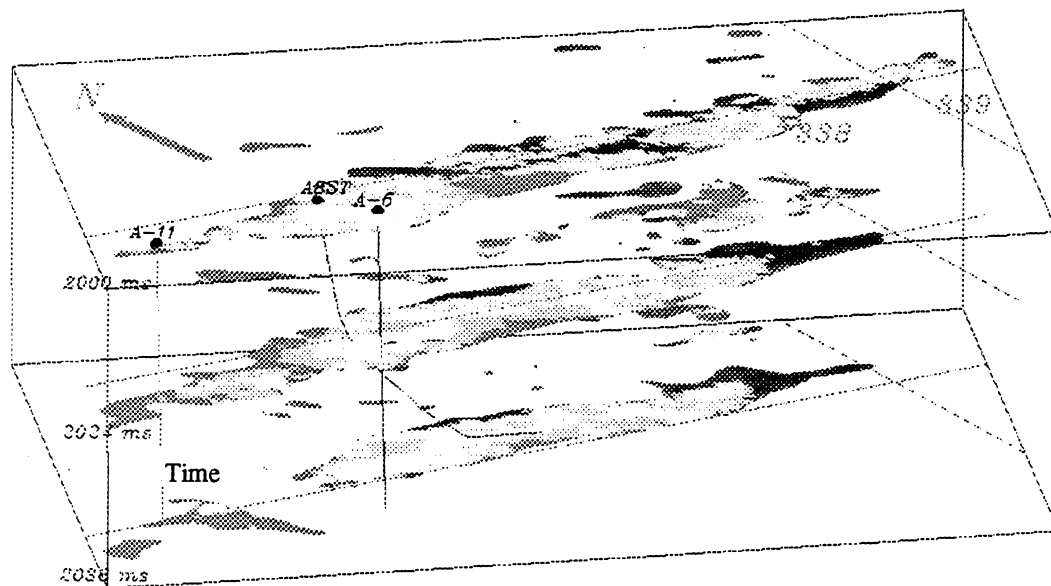


Figure 3.14. Our 4D seismic amplitude analysis technique uses region-growing algorithms to extract patterns and features from the reflection strength difference between two seismic datasets. The region-growing technique applied to a seismic trace of the 1985 volume is shown in (a), the application of the technique to a trace at the same location in the 1992 volume is shown in (b), and the differentiated amplitude within this high amplitude regions of the LF reservoir is shown in (c). Using this technique, we can minimize the possibility of noise contamination in the original seismic waveforms.



(a)



(b)

Figure 3.15. Within the LF reservoir, two scales can be used to present the differentiated amplitude volume depending on the visualization requirement. As an example, we display time slices through the top, middle, and bottom of two time-lapse 3D seismic datasets (1985 and 1988 3D surveys in the eastern LF reservoir, Anderson et al, 1995) in rough (a) and fine (b) scales of the amplitude differences. In (a), green is no change in high amplitudes indicating locations of possible bypassed pay, whereas the blue is dimmed-out from production, red is from areas of amplitude increase caused by gas/oil ratio increase with production. In (b), yellow denotes region within the HAR with no measurable change (<10%). Green is the region that still has high amplitudes, but within which some changes have been detected (10-30%).

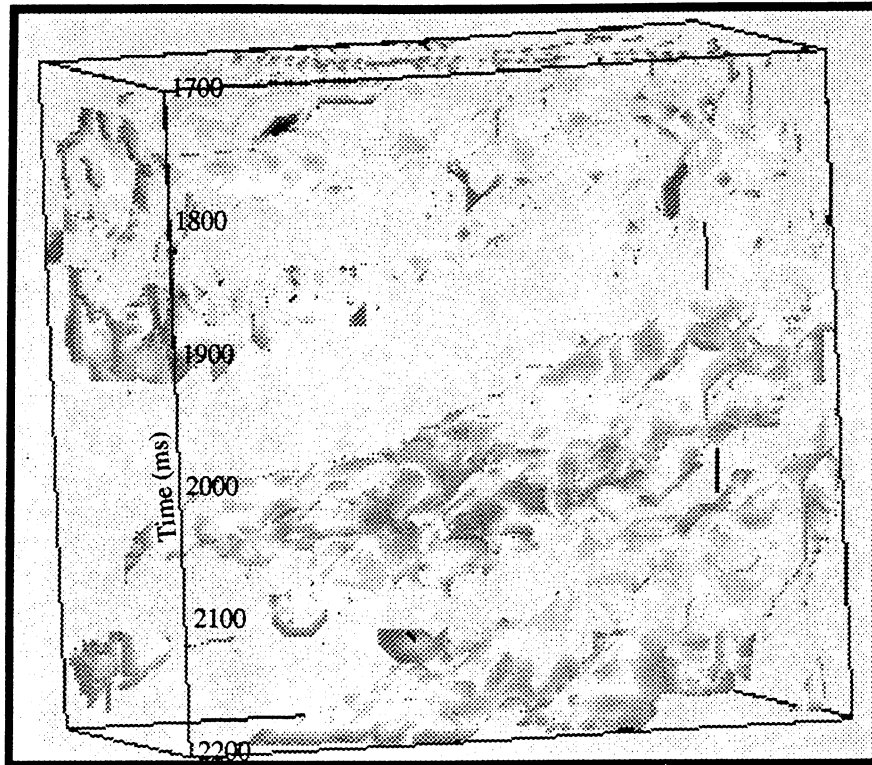


Figure 3.16. Hydrocarbon reservoirs can be constructed from seismic amplitudes using our region-growing algorithms. Four stacked reservoirs built from a seismic reflection strength volume in the study area are shown in this figure. Colors represent seismic amplitudes. Note the spatial connectivity and variations of the amplitude of each hydrocarbon reservoir as defined by our high amplitude regions (HARs).

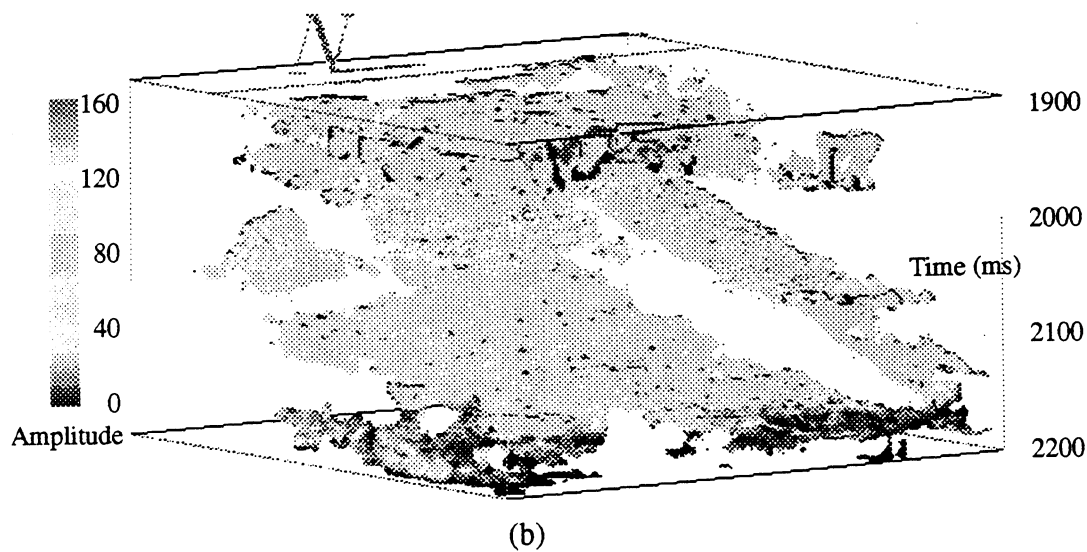
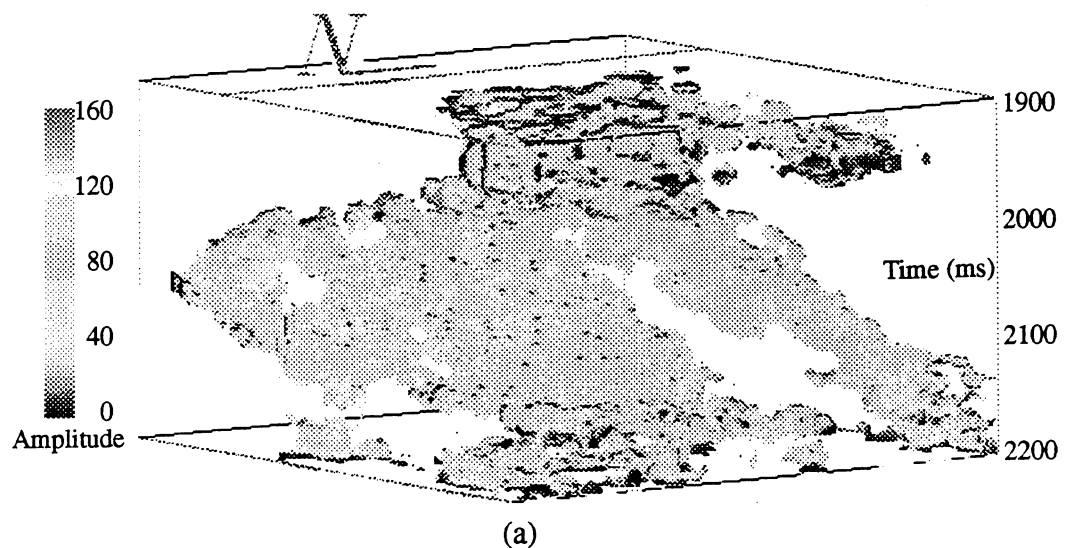


Figure 3.17. The hydrocarbon reservoirs in Fault block B are computed and segmented on the 1985 (a) and 1992 (b) reflection strength volumes. The blank areas in these volumetric representations are areas with amplitudes that are lower than specified amplitude threshold (non-reservoirs).

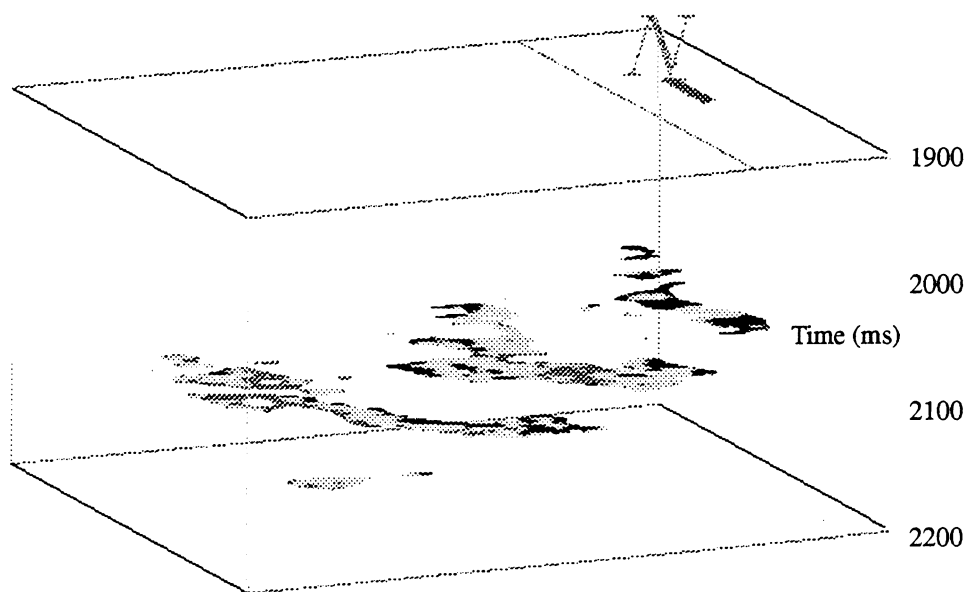
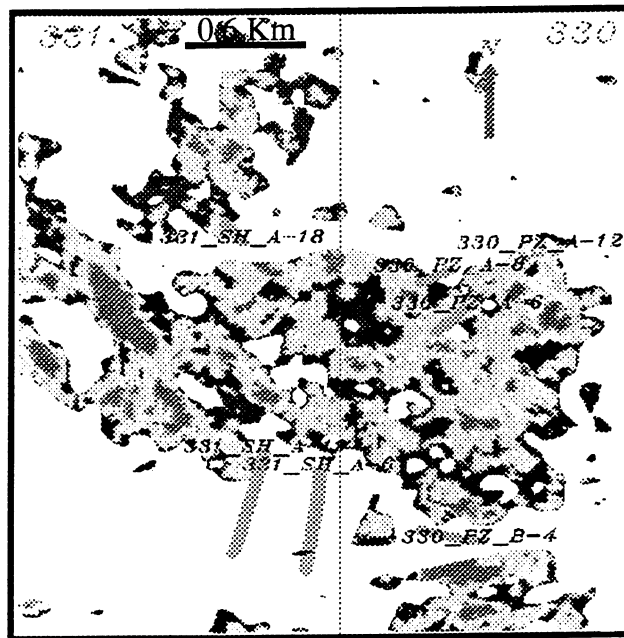
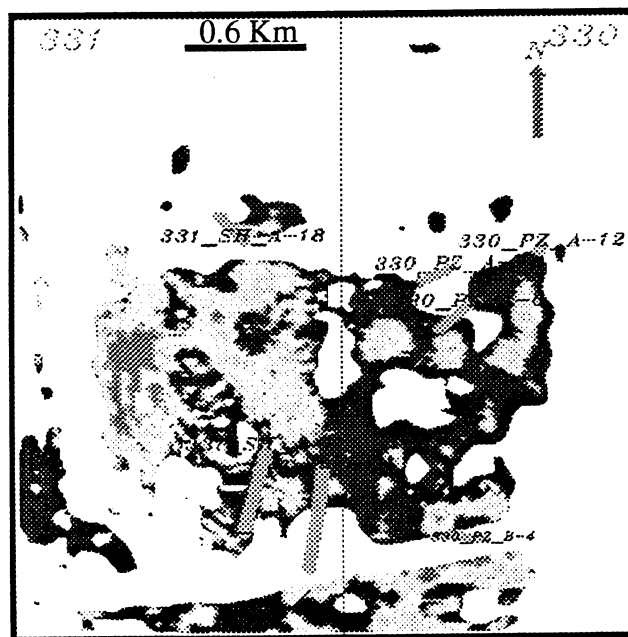


Figure 3.19. Three time slices show selected internals within the LF reservoir as extracted from the amplitude difference volume between the 1985 and 1992 region-grown amplitudes. Using the same color scheme as shown in Figure 4.18, red denotes areas with increased amplitudes from 1985 to 1992. Blue denotes areas with decreased amplitudes. Green and yellow denote areas with unchanged ($<10\%$) amplitudes.



(a)



(b)

Figure 3.20. The extracted, region-grown amplitudes along the top of the LF reservoir structure from the 1985 (a) and 1992 (b) are direct hydrocarbon indicators. Red and yellow are regions with high amplitudes, and the regions with relatively low amplitudes are coded as blue.

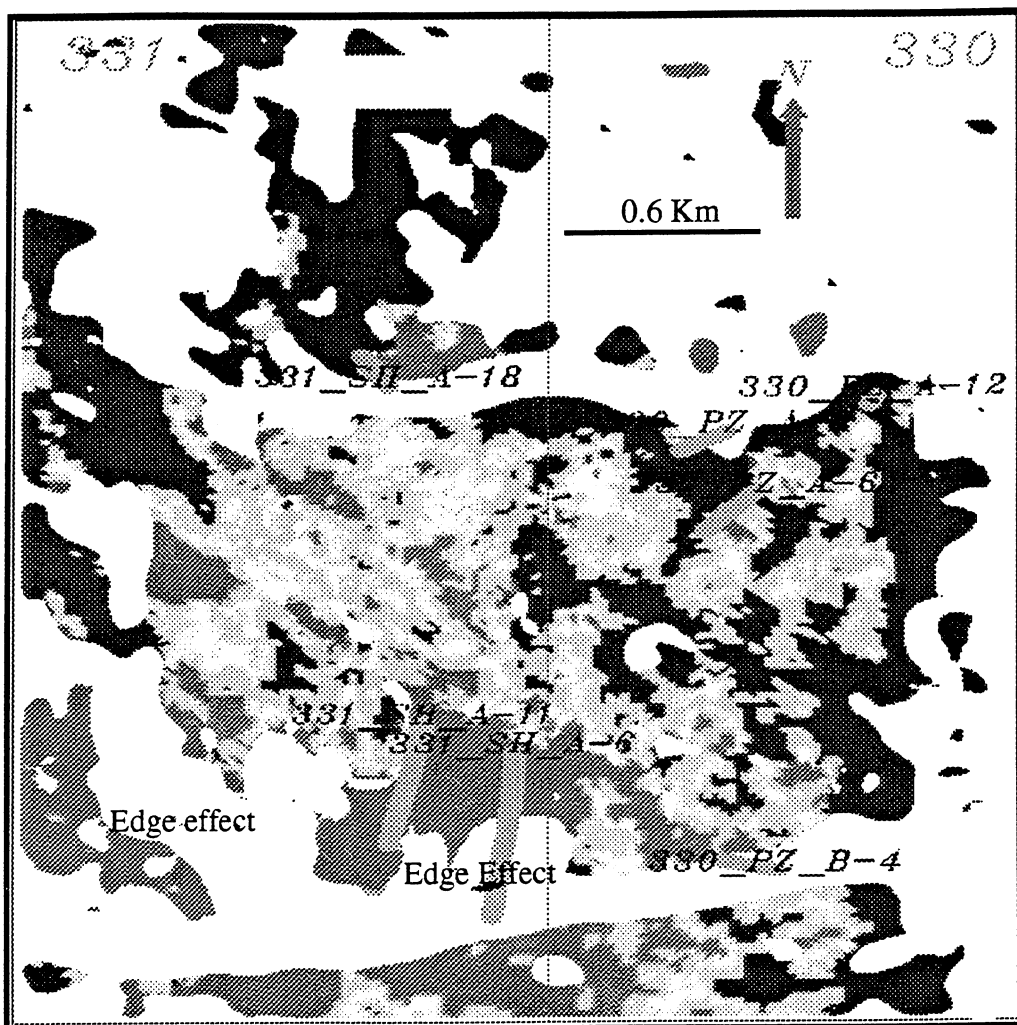


Figure 3.21. The amplitude differences derived from the 1985 and 1992 region-grown amplitudes along the top of the LF reservoir structure. Red indicates regions with increased amplitudes, blue indicates regions with decreased amplitudes, and yellow and green indicate regions with very little amplitude changes (<10%). The solid red regions in the west and the south are caused by edge effects, or misalignment.

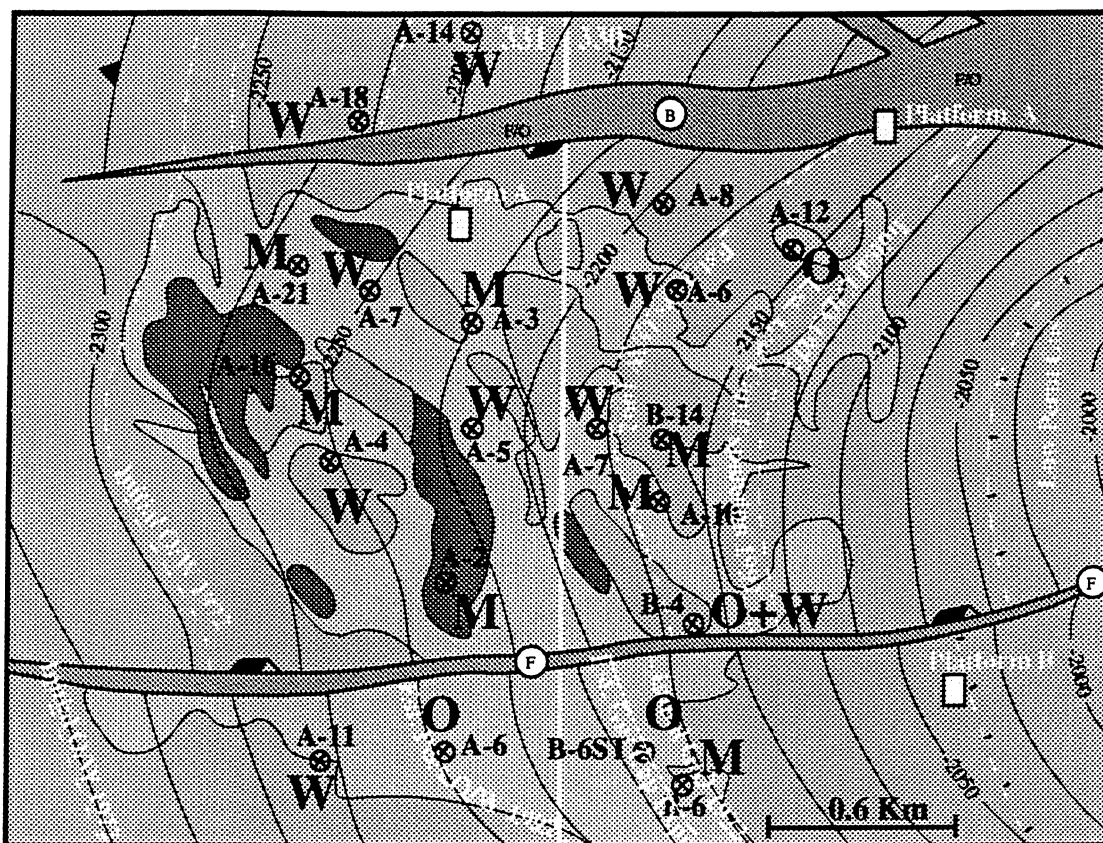


Figure 3.22. Interpreted drainage patterns of the LF reservoir are derived from our 4D seismic amplitude analysis (from Figures 3.19-3.21). The results are projected onto the top of the volume, on which the identified amplitude anomalies at the upper-, mid-, and lower-LF reservoir slices (Figure 3.23) are outlined. Green denotes areas filled with bypassed hydrocarbons (unchanged seismic amplitudes), blue denotes areas with water-sweeping (decreased amplitudes), and red denotes areas with gas development (note that increased amplitudes are down-dip). Yellow dashed lines are the estimated initial and present G/O, O/W contacts from well production data. Edge effects were excluded in the figure.

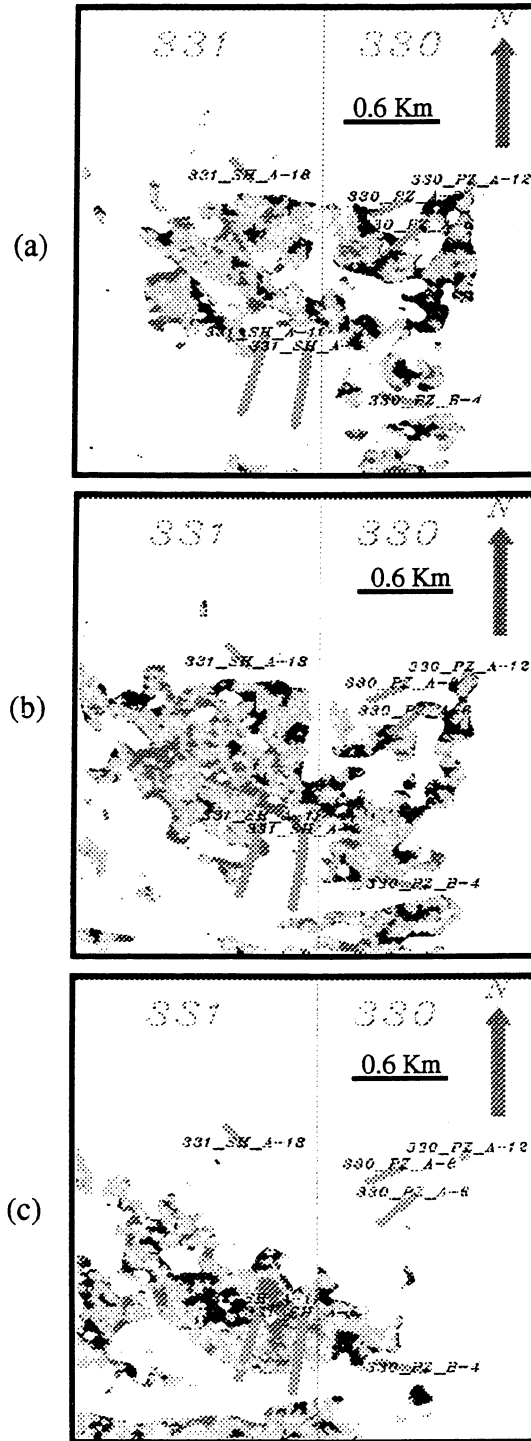


Figure 3.23. The extracted amplitude difference slices along the upper-, mid- and lower-depth of the LF reservoir are illustrated in (a), (b), and (c), respectively. Blue represents regions with decreased amplitude from 1985 to 1992. Red represents regions with increased amplitudes, and green and yellow represent regions with amplitude changes less than 10%.

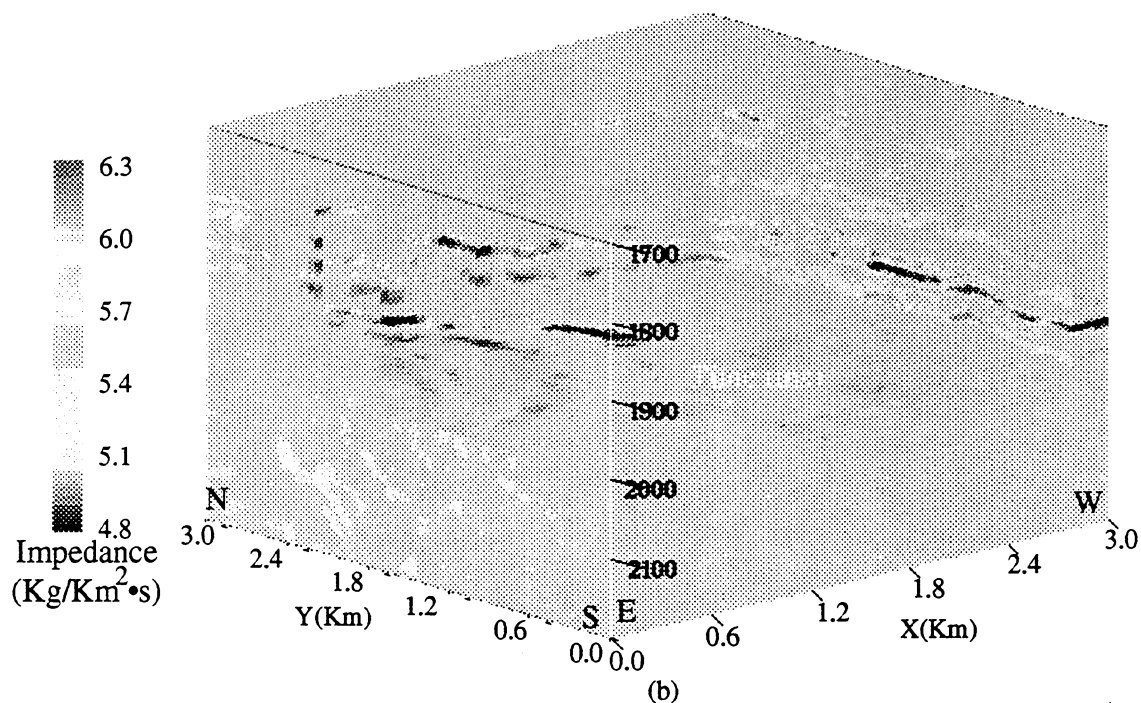
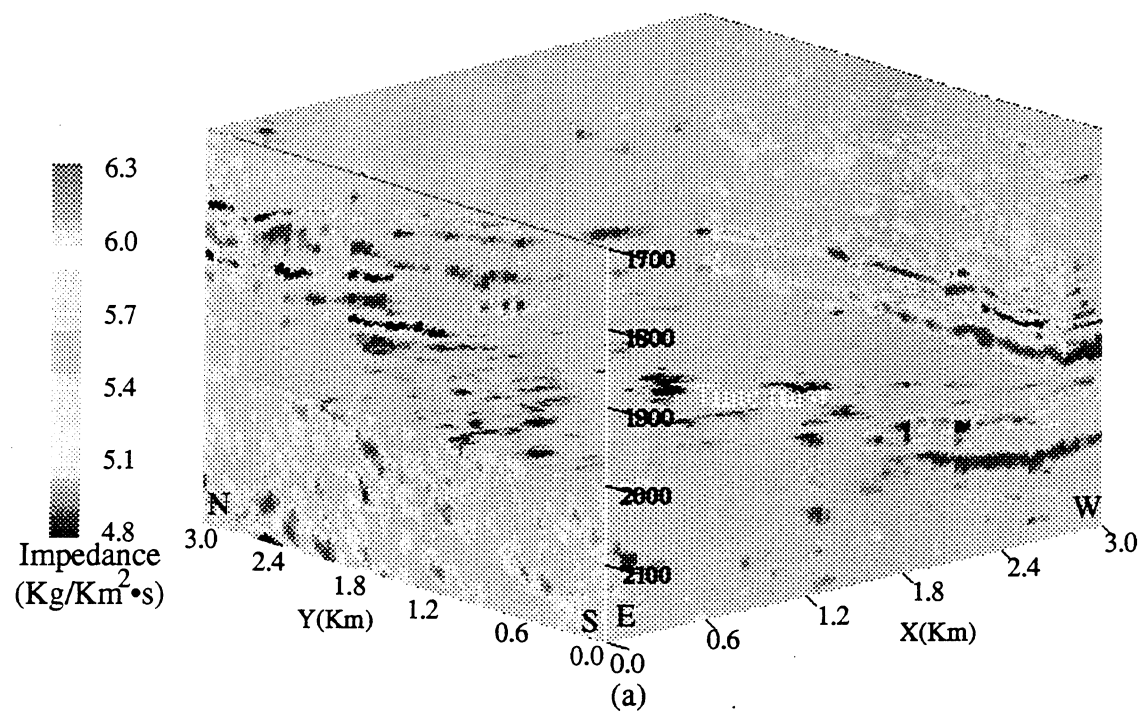


Figure 3.24. The estimated acoustic impedance volumes of the 1985 (a) and 1992 (b) seismic surveys using our nonlinear seismic inversion. Oil and gas reservoirs are low impedance anomalies (blue). The depth in chair display of both (a) and (b) is at mid-depth of the LF reservoir.

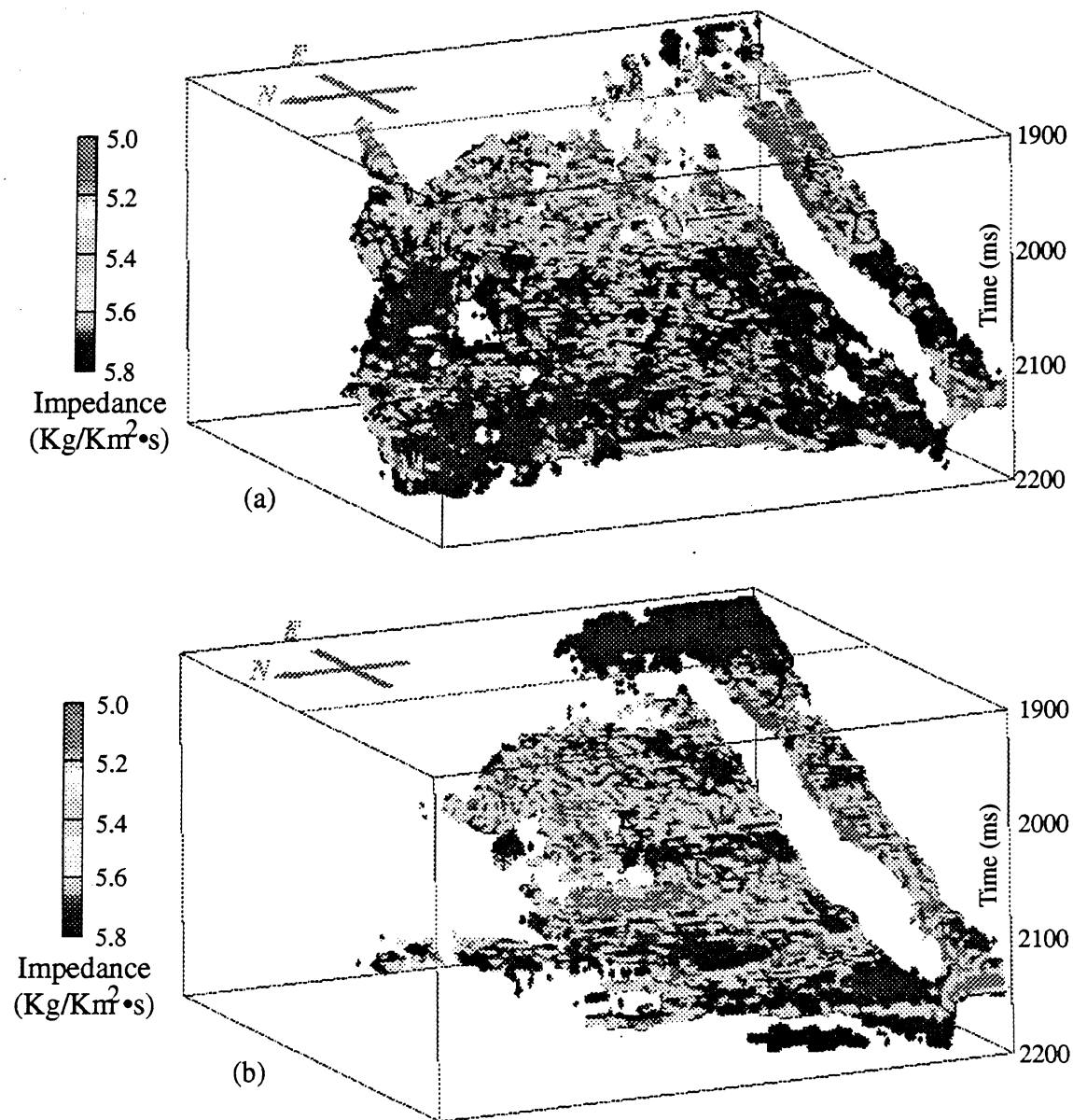


Figure 3.25. The LF reservoir is constructed from the region-grown 1985 acoustic impedance (a) and 1992 acoustic impedance (b) volumes using our 4D seismic reservoir building algorithm. The region-growing algorithms were applied to extract Low Impedance Regions (LIRs) within the acoustic impedance volumes. Note how much "cleaner" the 1992 reservoir is.

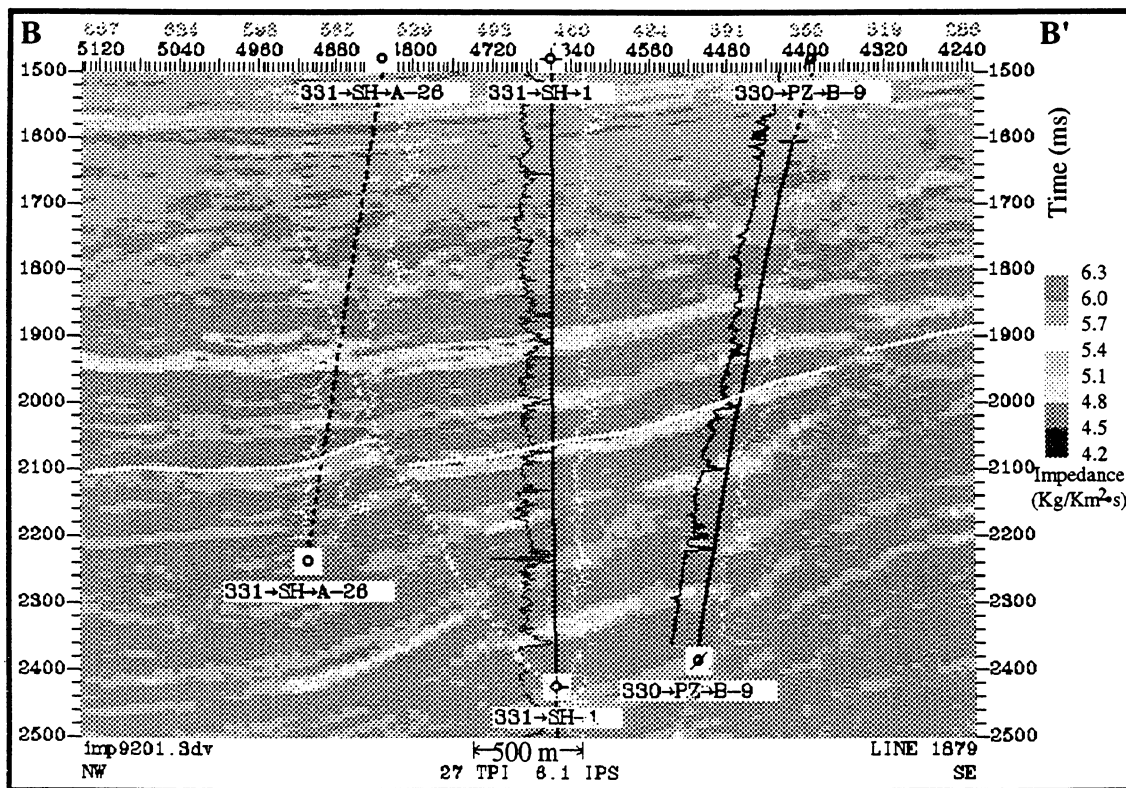
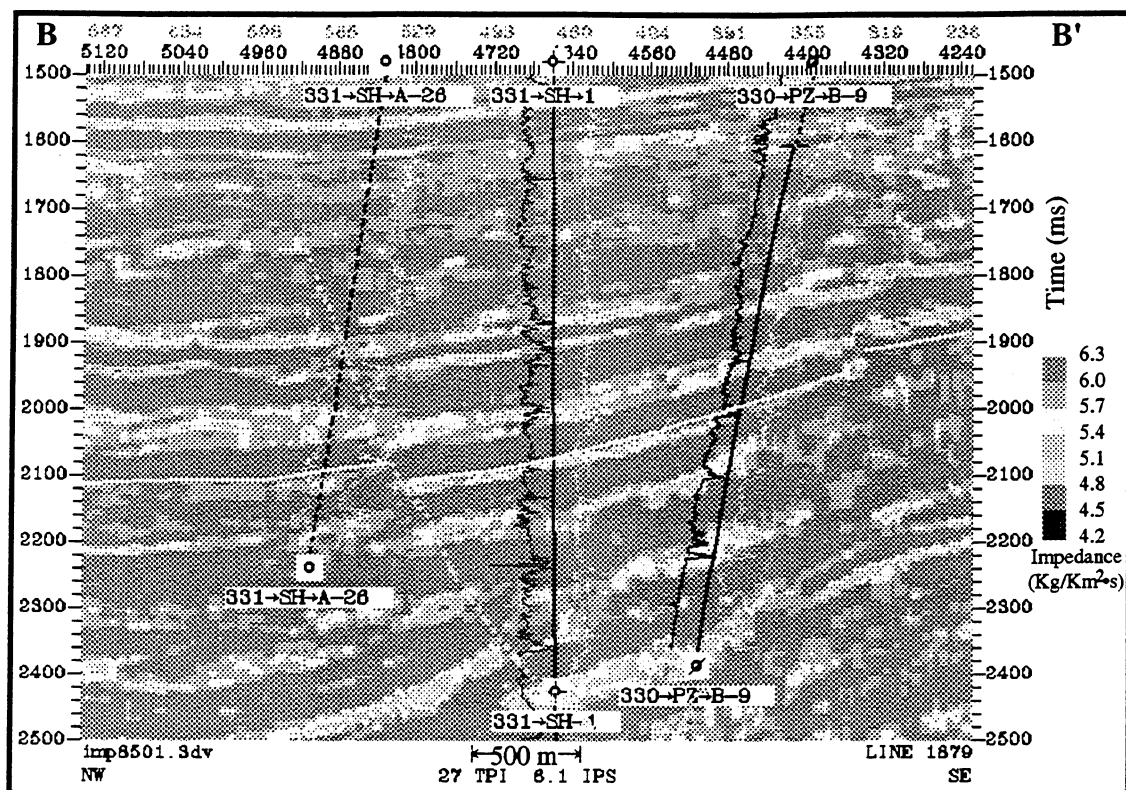
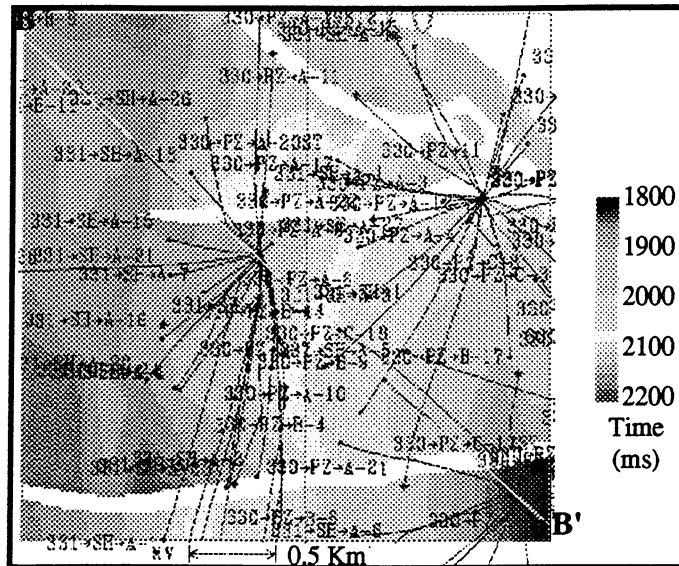
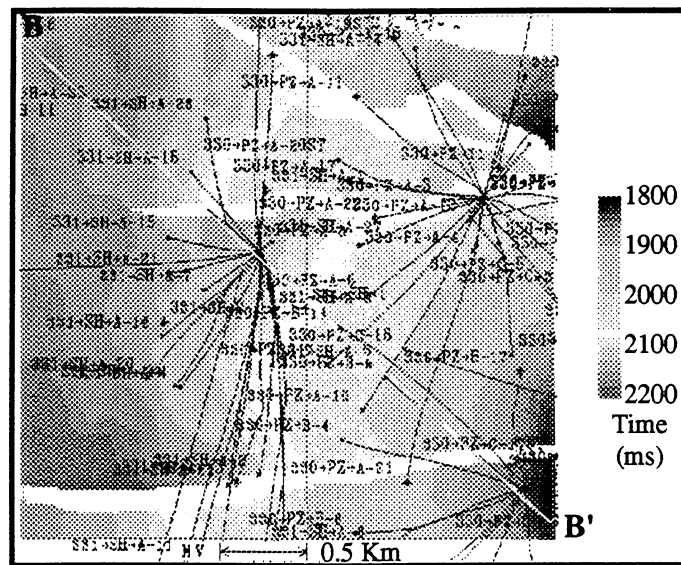


Figure 3.26. The interpretation of the LF reservoir on the 1985 (up) and 1992 (down) inverted acoustic impedance volumes. Location of the line is shown in Figure 3.27.



(a)



(b)

Figure 3.27. The top of the LF reservoir is interpreted using both the 1985 (a) and 1992 (b) acoustic impedance volumes. These two surfaces are consistent in most places. However, time differences caused by changes in velocity from production of shallower reservoirs between 1985 and 1992 are observable near the center of the fault block B. Line B-B' is the location of the cross-section shown in Figure 3.26.

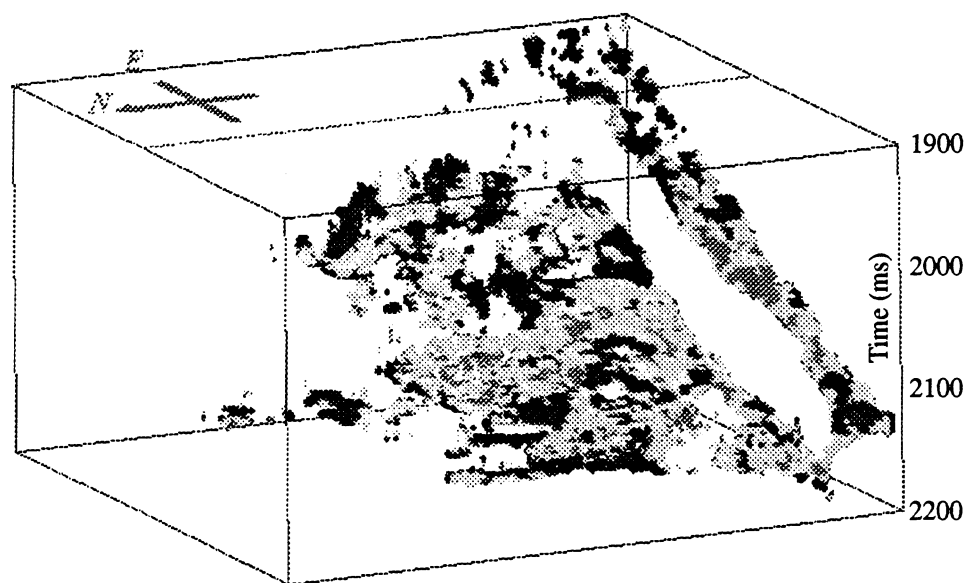


Figure 3.28. The volumetric representation of the region-grown acoustic impedance differences between the 1985 (Figure 4.25 (a)) and the 1992 (Figure 4.25 (b)) estimated impedance volumes. Red denotes areas with increased amplitudes from 1985 to 1992. Blue denotes areas with decreased amplitudes. Green and yellow denotes areas with unchanged (<10%) amplitudes.

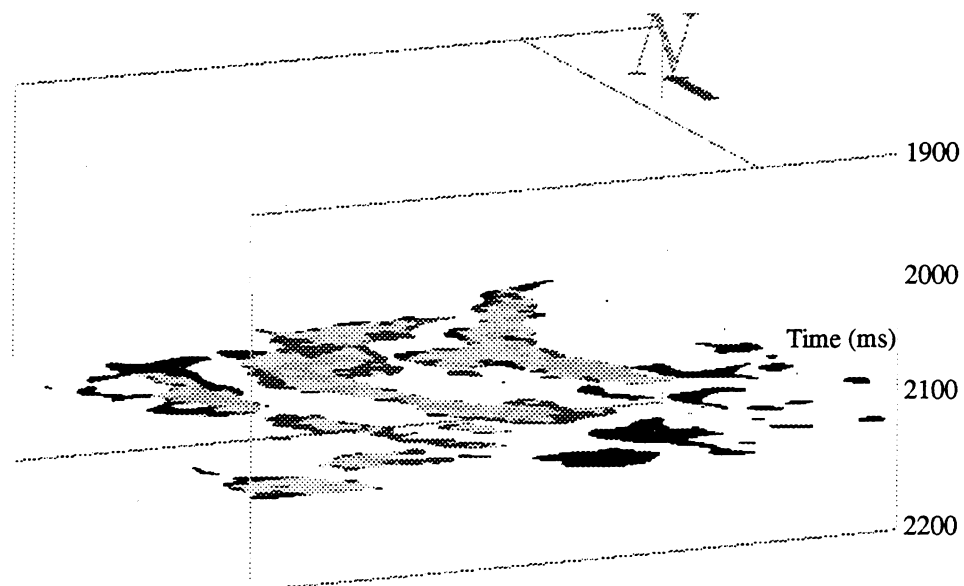
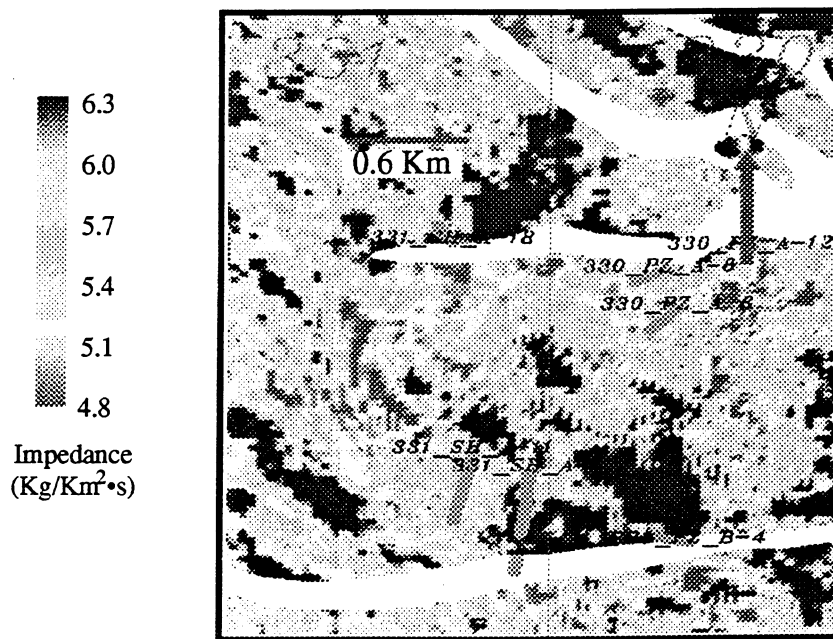
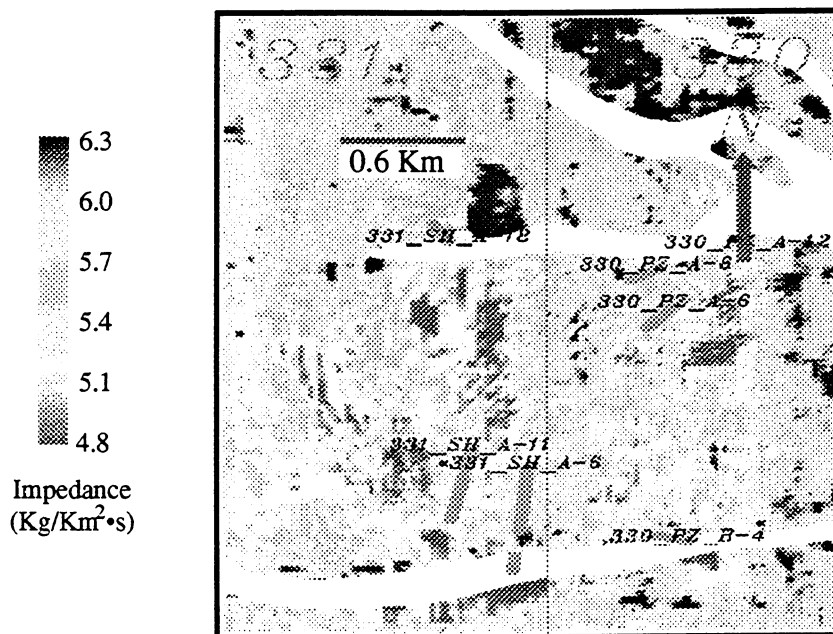


Figure 3.29. The acoustic impedance difference volume is sliced by three time slices at upper-, mid- and lower-depth interval of the LF reservoir in the fault block B. Red denotes areas with decreased impedances from 1985 to 1992. Blue denotes areas with increased impedances. Green and yellow denote areas with unchanged (<10%) impedances.



(a)



(b)

Figure 3.30. Extracted acoustic impedances of 1985 (a) and 1992 (b) along the top of LF reservoir structure. Red and yellow are regions with low impedances, and blue are region with high impedances. Hydrocarbons are associated with the former regions.

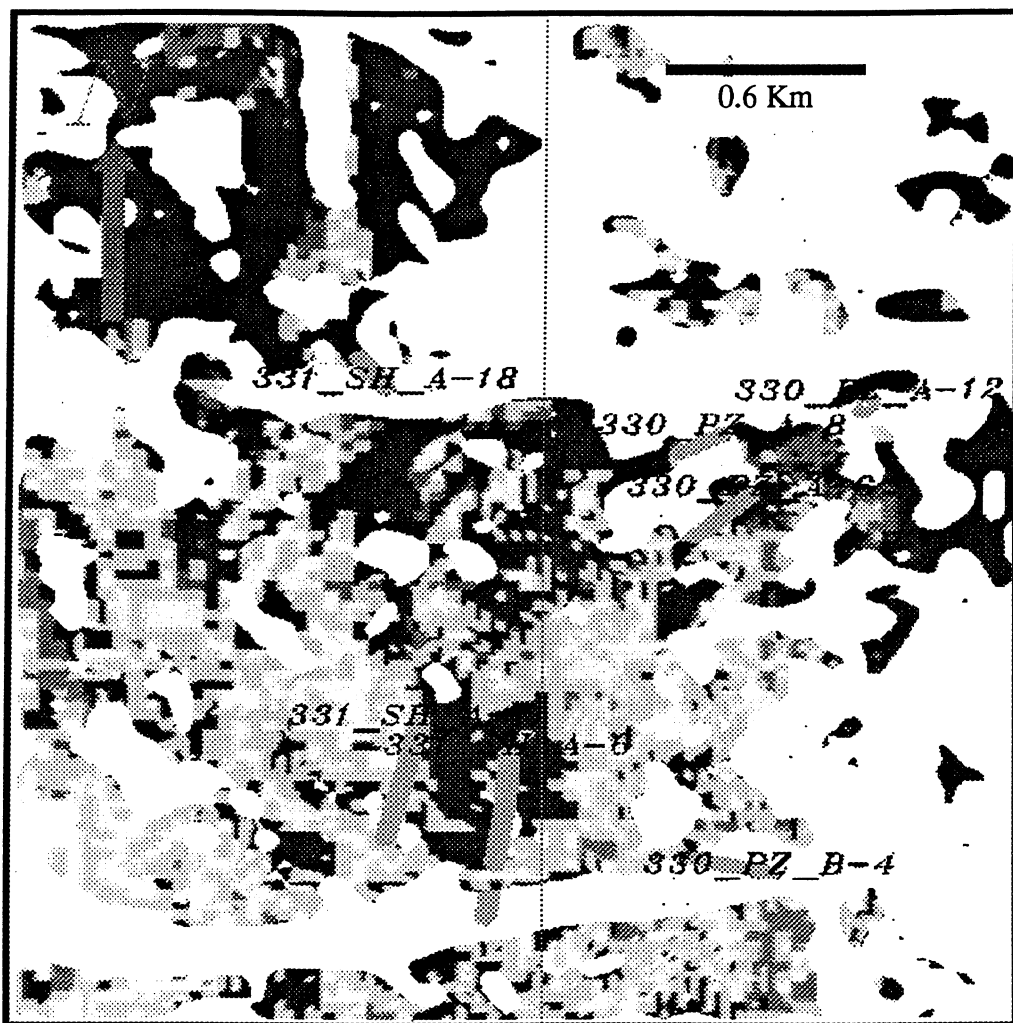


Figure 3.31. The acoustic impedance differences along the LF reservoir top. Red indicates regions with decreased impedances, blue indicates regions with increased impedances, and yellow and green indicate regions with very little impedance changes (<10%).

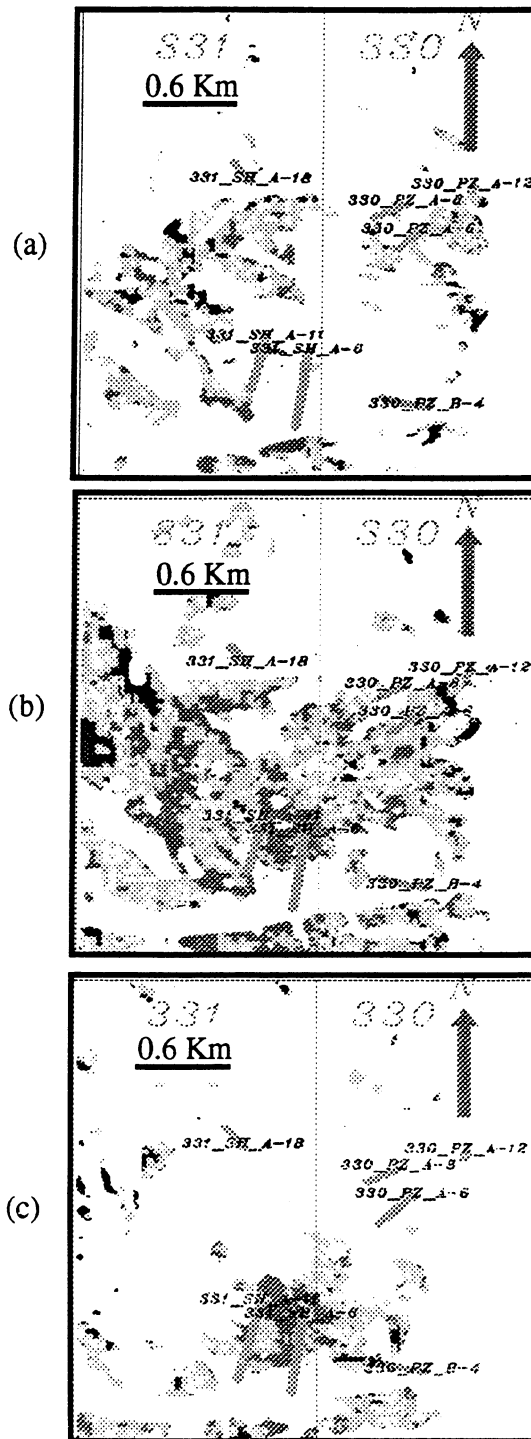


Figure 3.32. The extracted acoustic impedance difference slices along the upper-, mid- and lower-depth of the LF reservoir are illustrated in (a), (b), and (c), respectively. Blue represents regions with increased impedances from 1985 to 1992. Red represents regions with decreased impedances, and green and yellow represent regions with unchanged impedances (changes are less than 10%).

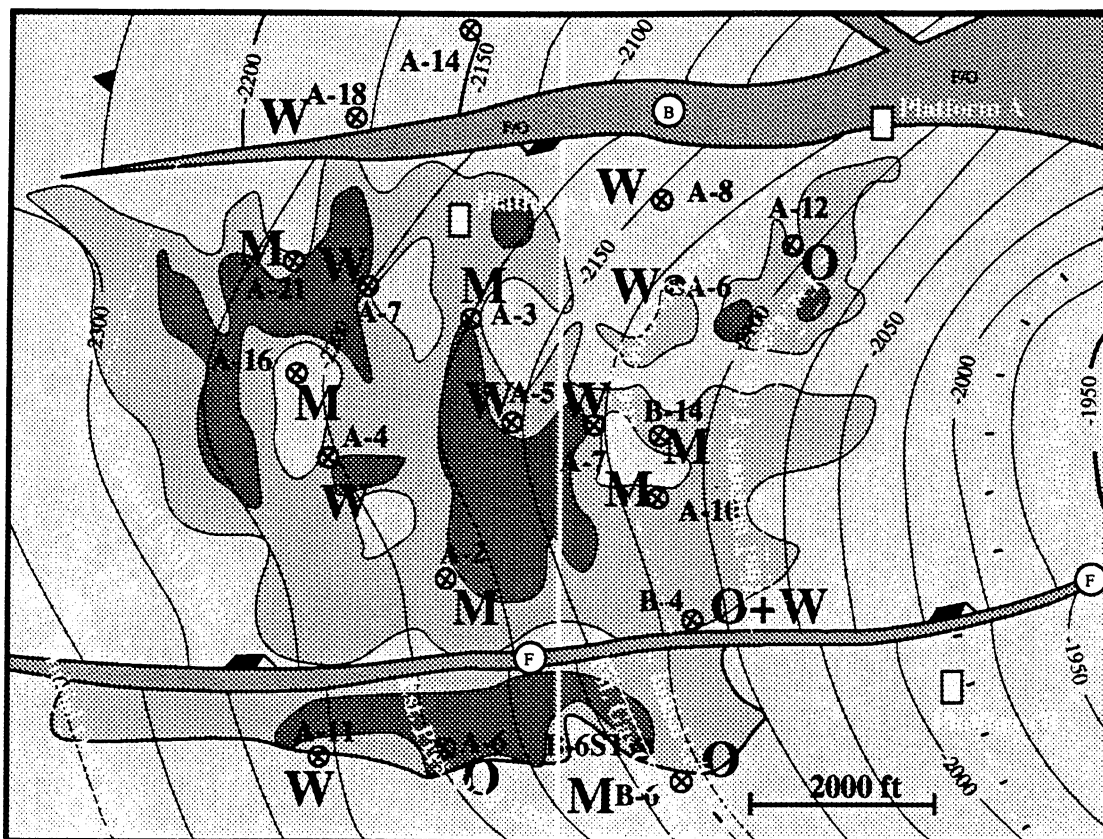


Figure 3.33. Drainage patterns of the LF reservoir are derived from our 4D impedance analysis. The results are projected onto the top of the volume, on which the identified impedance anomalies at the upper-, mid-, and lower-LF reservoir slices (Figure 3.32) are outlined. Green denotes areas filled with bypassed hydrocarbons (unchanged acoustic impedances), blue denotes areas with water-sweeping (increased impedances), and red denotes areas with gas cap development (decreased impedances). Yellow dashed lines are the estimated initial and present G/O, O/W contacts from production data.

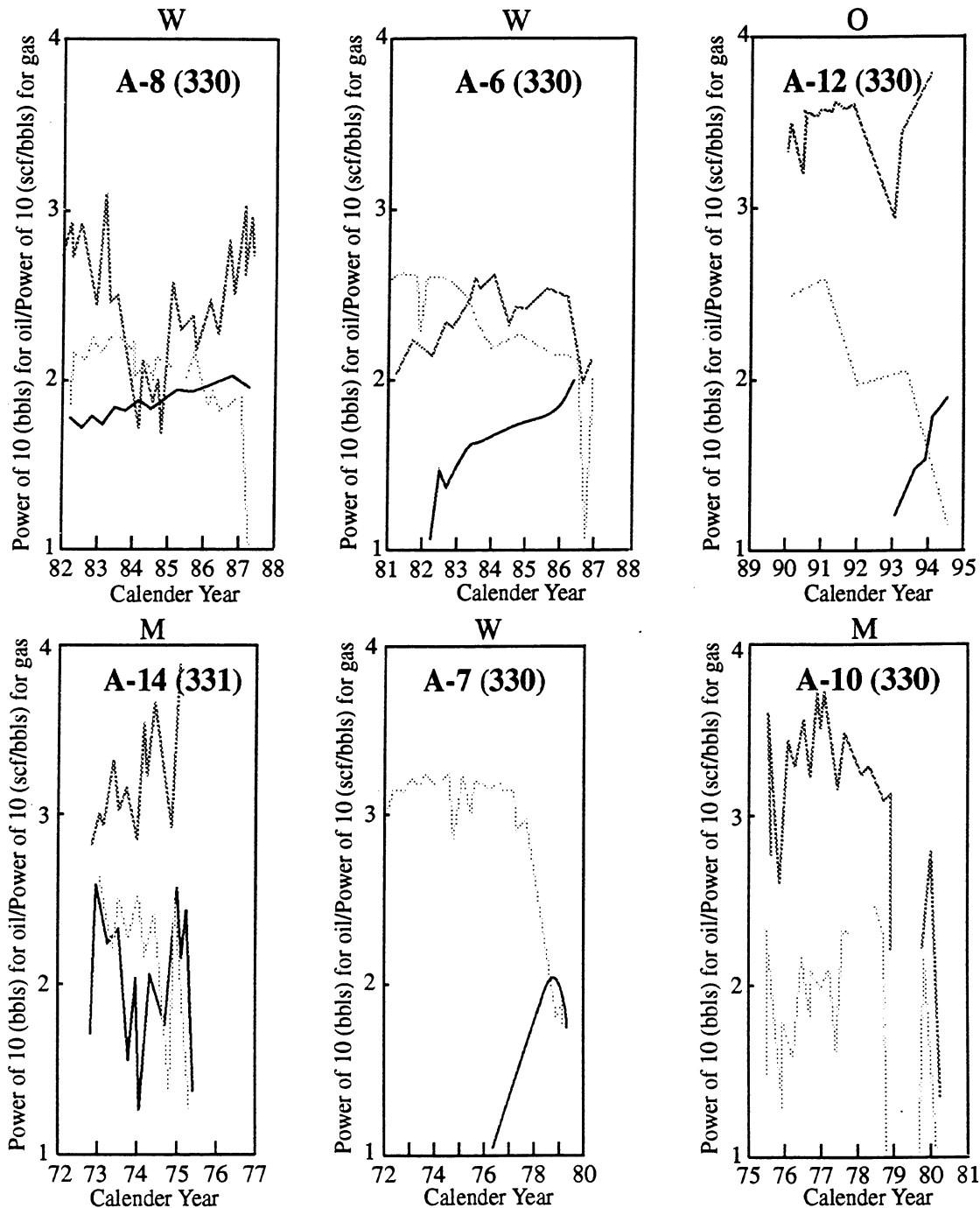


Figure 3.34. Production data of the 19 production wells in the study area are shown in yearly scale. Green is the volume of oil, blue is the volume of water, and red is the volume of gas. The status of each well during 1985 and 1992 is also marked as O = oil production continuing, W = watered out, and M = mechanical problems caused shot-in, respectively. (The rest of the wells available are illustrated in the following figures). 1 bbls (barrel) = 0.15898 m³.

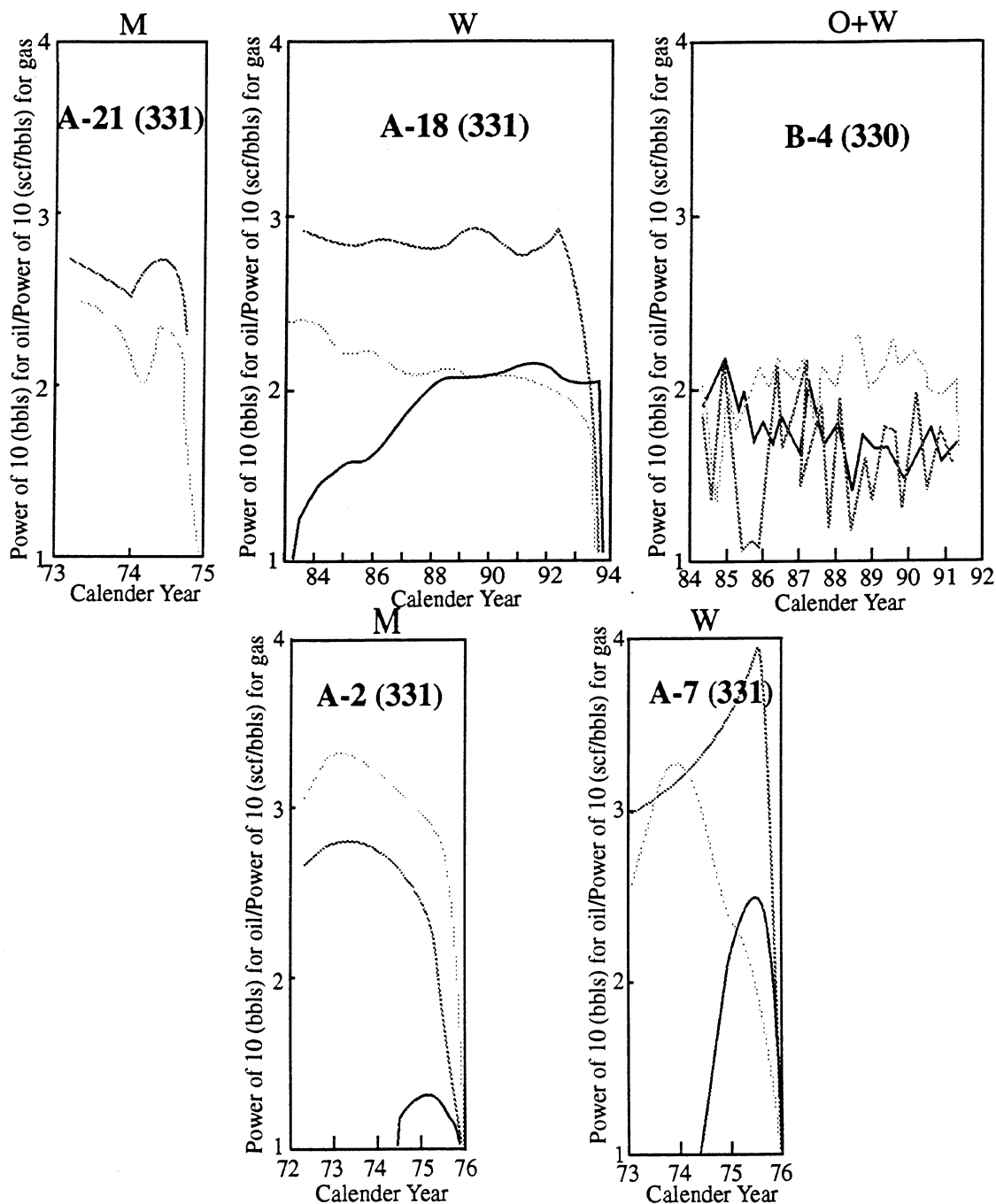


Figure 3.34. (Continuing from the previous page) Green is the volume of oil, blue is the volume of water, and red is the volume of gas produced from each well within the LF study area. The status of each well during 1985 and 1992 is also marked as O = oil production continuing, W = watered out, and M = mechanical problems caused shot-in, respectively.

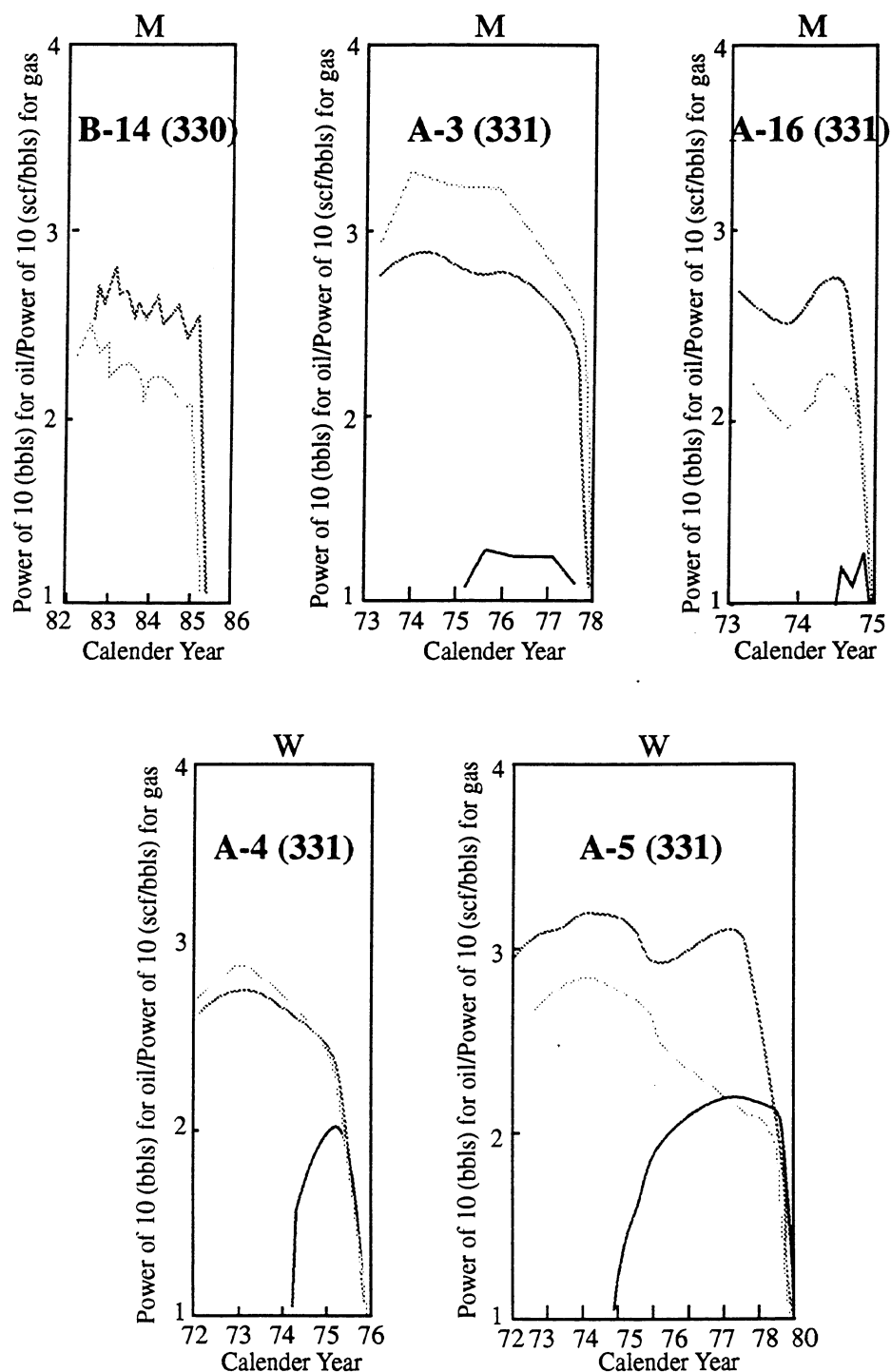


Figure 3.34. (Continuing from previous page) Green is the volume of oil, blue is the volume of water, and red is the volume of gas produced from the LF study area. The status of each well during 1985 and 1992 is also marked as O = oil production continuing, W = watered out, and M = mechanical problems caused shot-in, respectively.

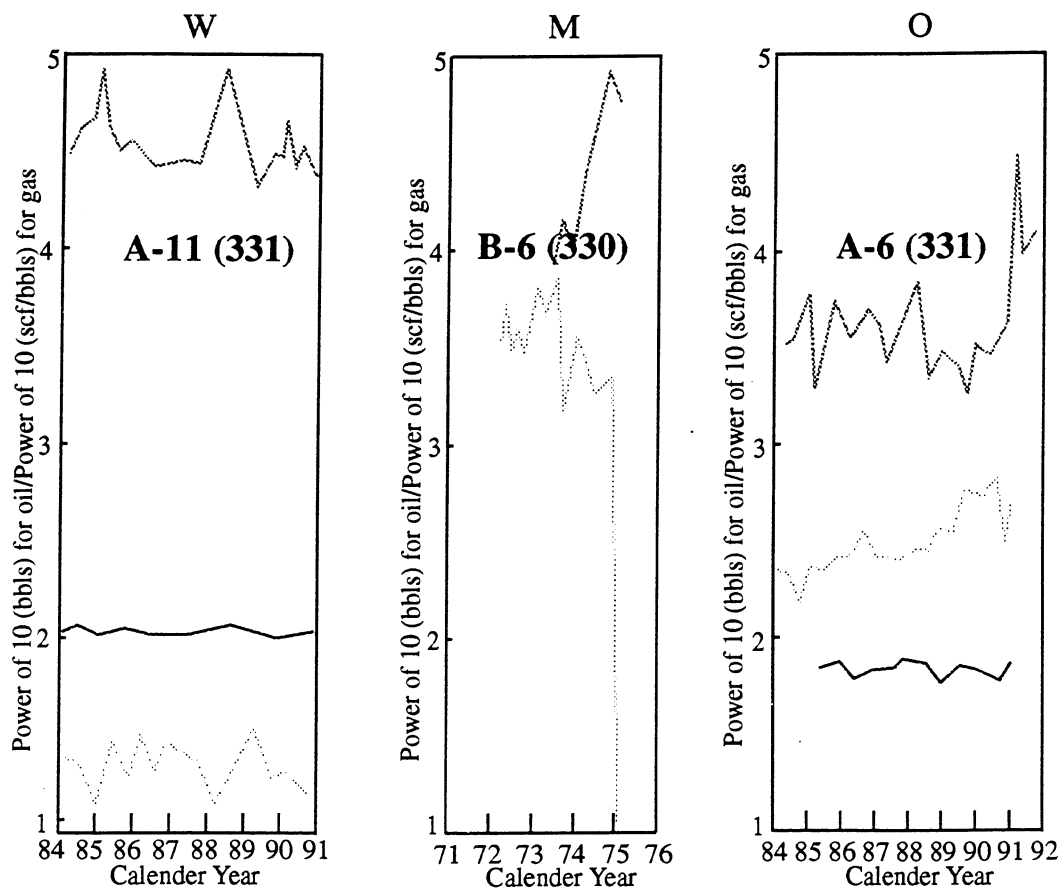


Figure 3.34. (Continuing from previous page) Green is the volume of oil, blue is the volume of water, and red is the volume of gas produced from the LF study area. The status of the wells during 1985 and 1992 for each well is also marked as O = oil production continuing, W = watered out, and M = mechanical problems caused shot-in, respectively.

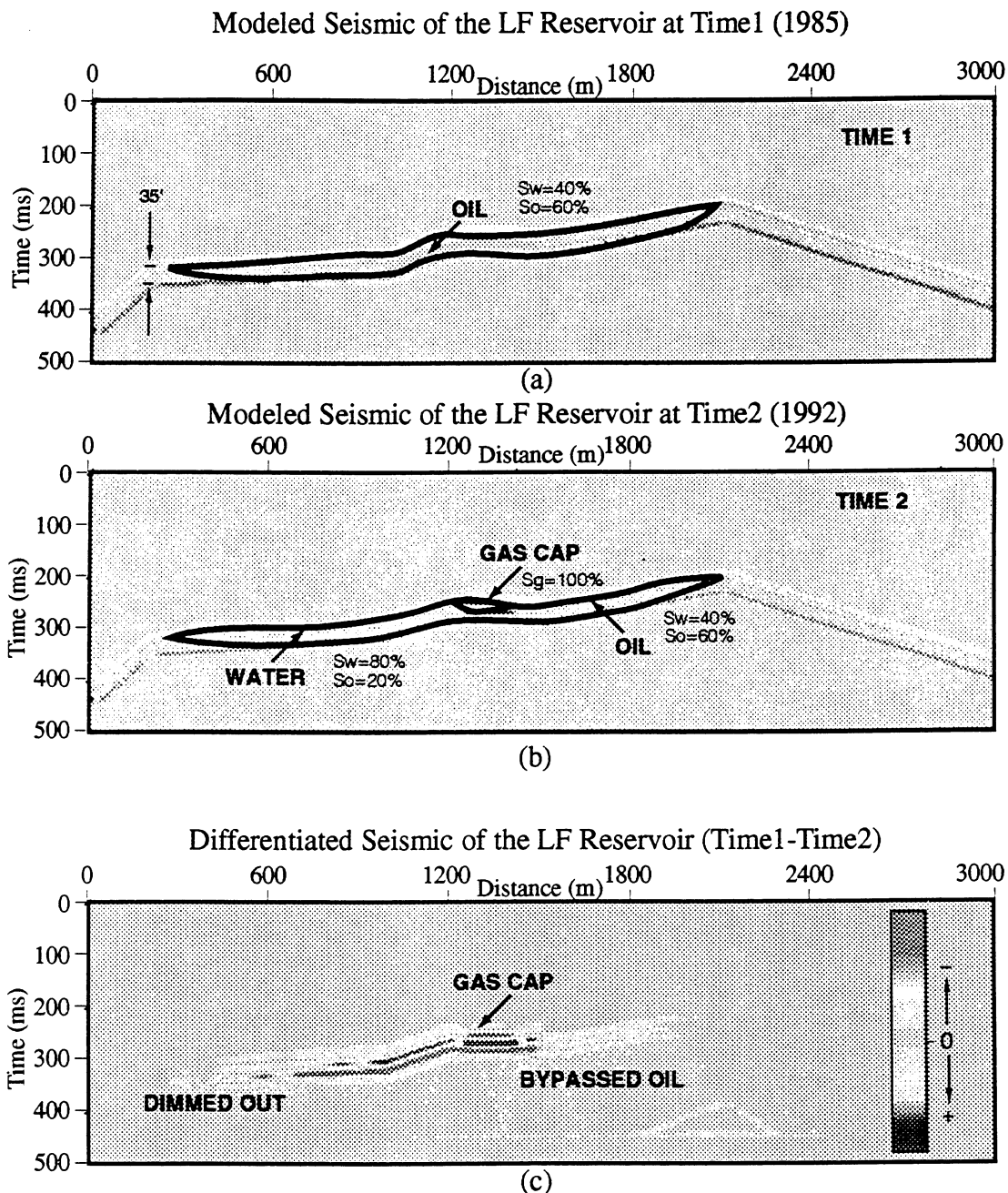
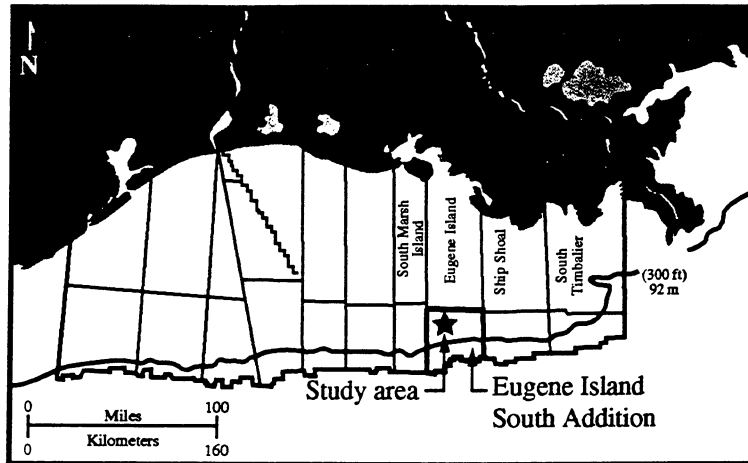
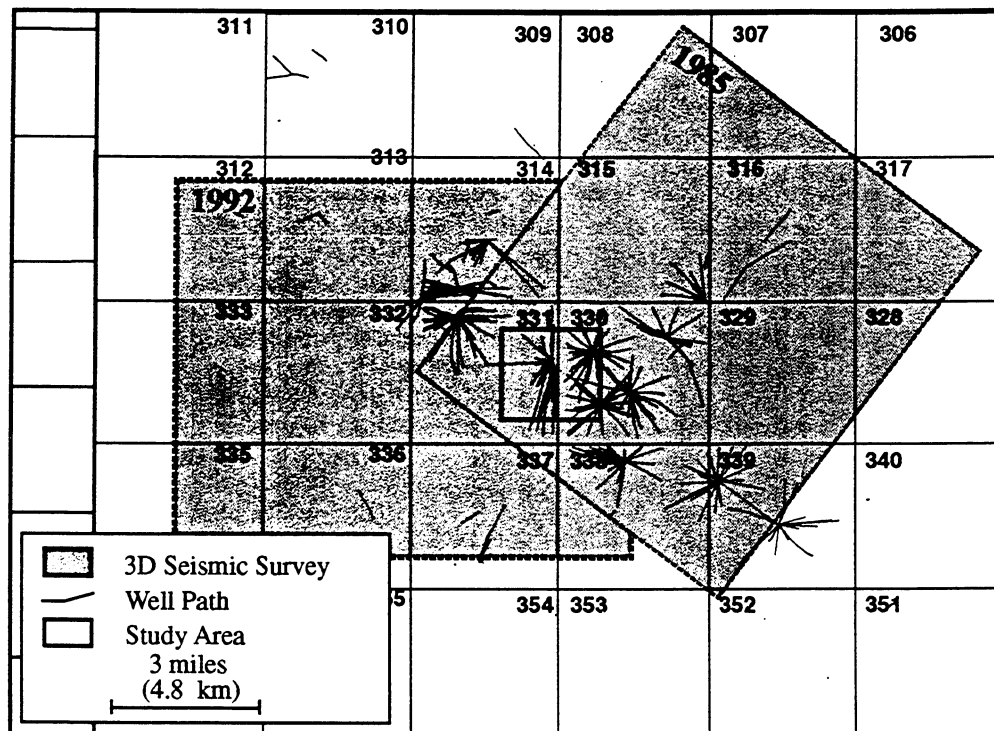


Figure 3.35. A 2D finite element seismic forward model is used to simulate the seismic response of the drainage effects due to production in the LF reservoir. Average properties of the LF reservoir are used in the modeling: porosity = 30%, thickness = 40 ft, which is close to the turning thickness of a 30 Hz, zero-phase wavelet.



(a)



(b)

Figure 4.1 Geographic location of the Eugene Island 330 Field is shown in (a), and the orientations (coverage) of the 1985 and the 1992 3D seismic surveys and more than 500 wells are shown in (b). The study area is the red rectangular area in the center of (b). The estimated acoustic impedance from the 1992 seismic survey is used in the reservoir characterization of the LF reservoir because of better data quality.

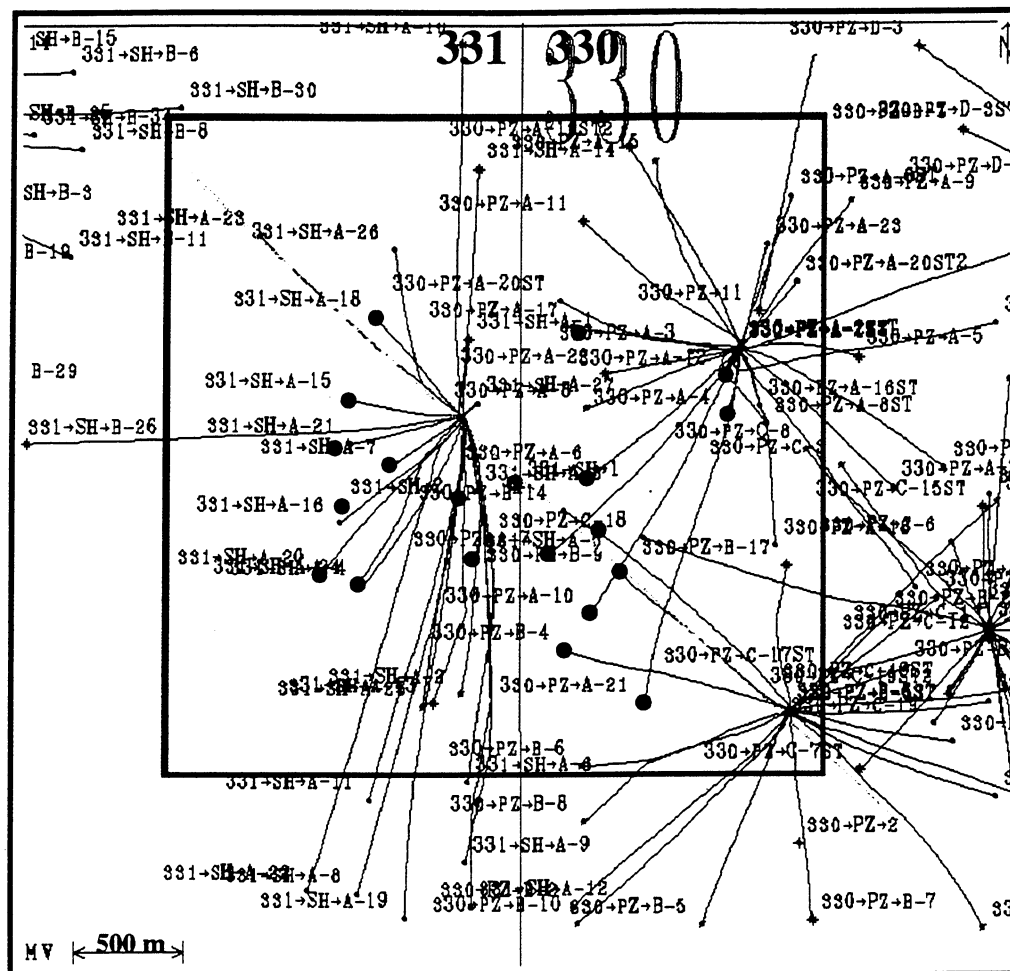


Figure 4.2. There are a total of seventy-four wells in the study area, the red rectangular area shown in this figure is the same as in Figure 4.1 (b). We use twenty wells in the fault block "B" to characterize the LF reservoir in our study. The wells used are annotated by filled black dots.

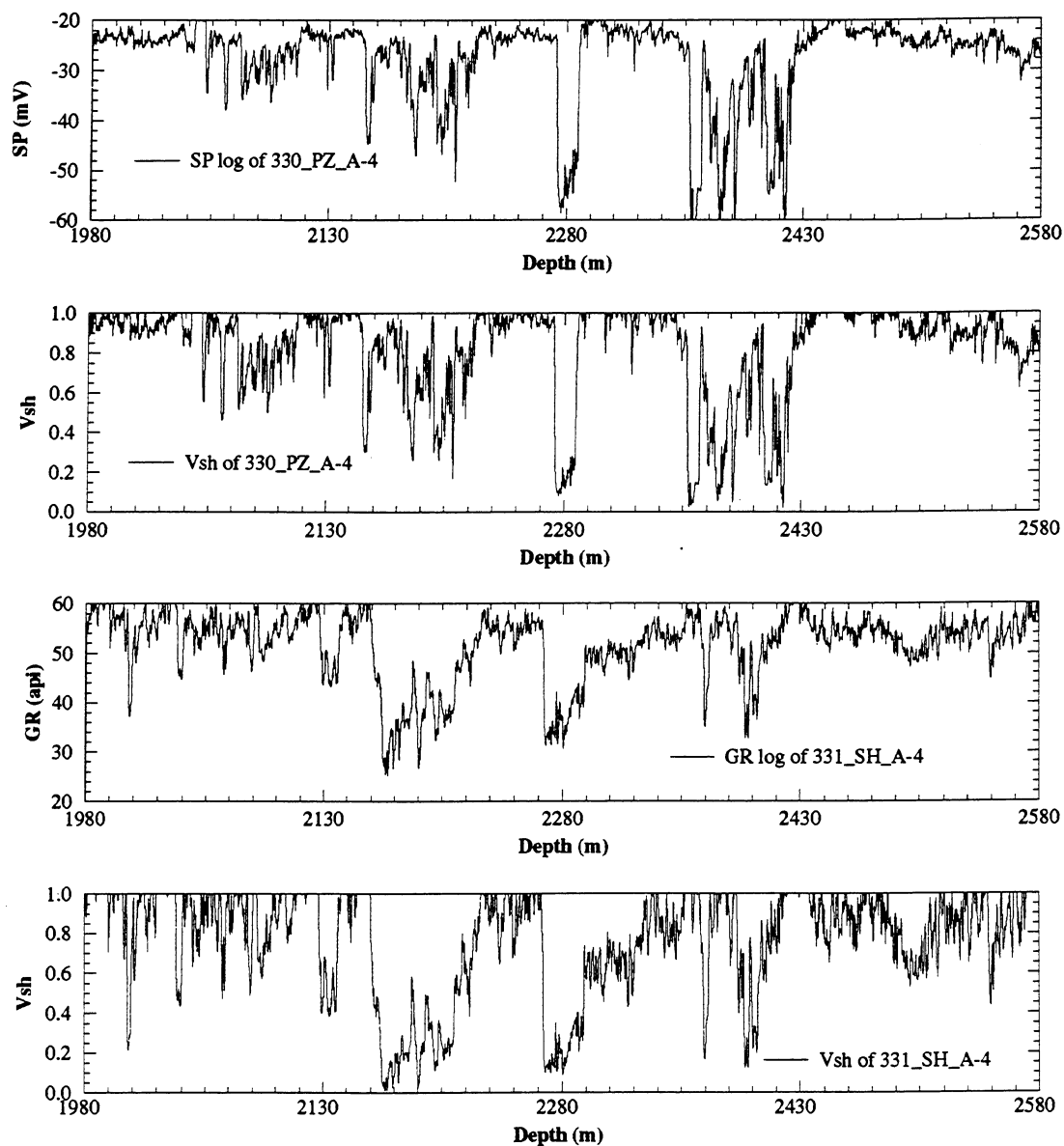


Figure 4.3. The spontaneous potential log (SP) of EI well 330_PZ_A-4 and the gamma ray log (GR) of EI well 331_SH_A-4 are converted to shale volume fractions.

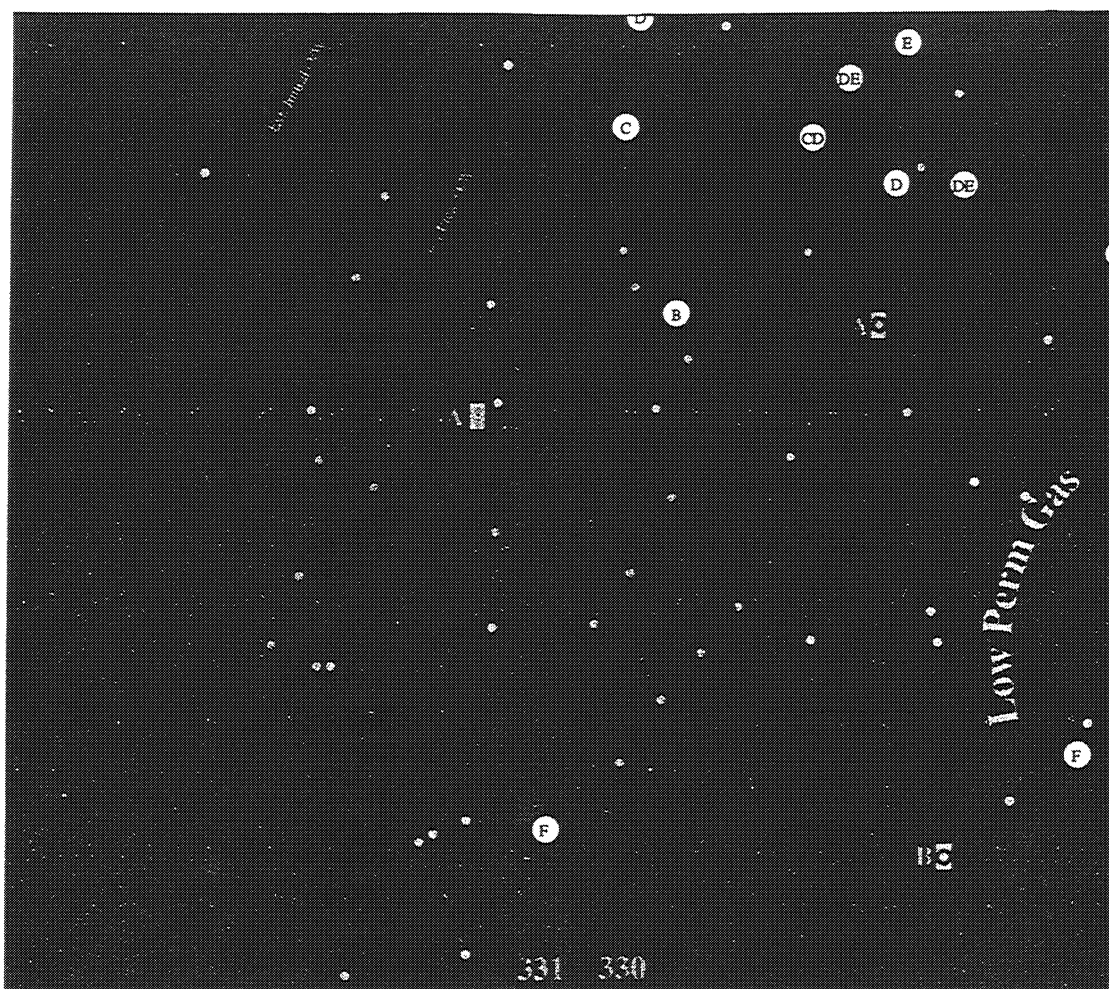


Figure 4.4. The structure map of the LF sand top interpreted from wireline logging data by Pennzoil Exploration and Production Company. Black lines are contours in meters. Regions in dark blue are water defined by initial O/W contact, regions in light blue were originally oil and have been replaced by water by 1992. Original (1972) gas cap is coded by red, and gas cap expansion is coded by light pink. Low permeability gas cap is coded in dark pink. Regions with oil in 1992 are coded by green. O/W and G/O contacts are thick dashed lines.

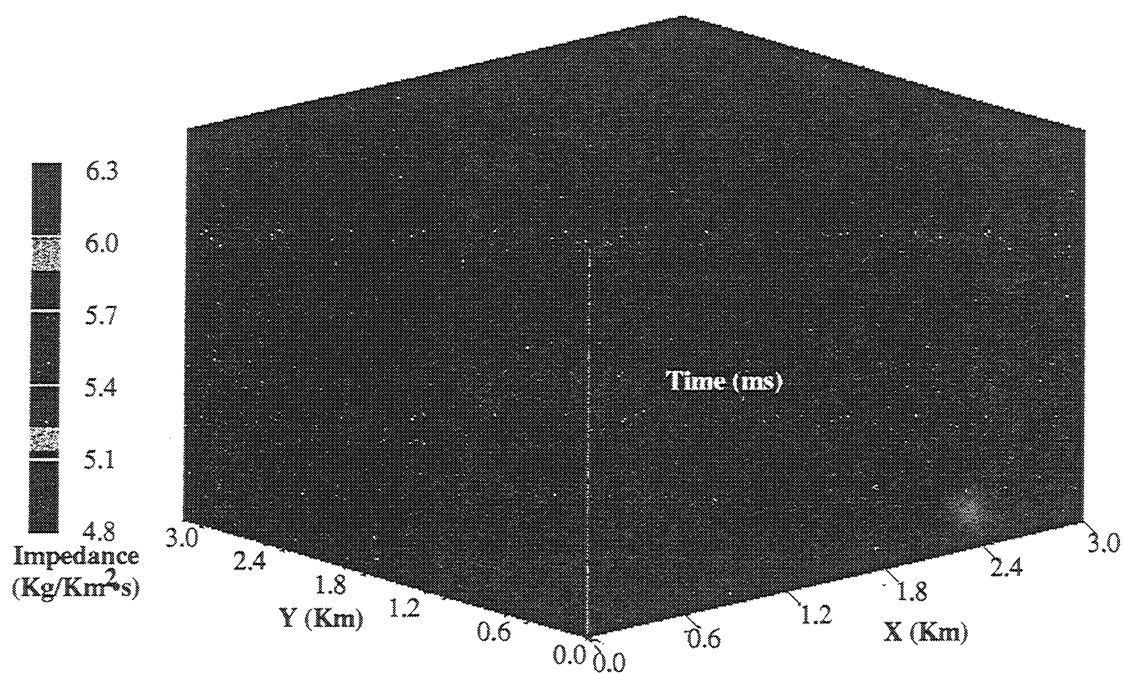


Figure 4.5. The estimated acoustic volume from the 1992 3D seismic survey in the study area. The three hydrocarbon reservoirs, i.e., JD, KE, and LF, are covered in this acoustic impedance volume. These hydrocarbon reservoirs are low impedance anomalies (blue) in the impedance volume.

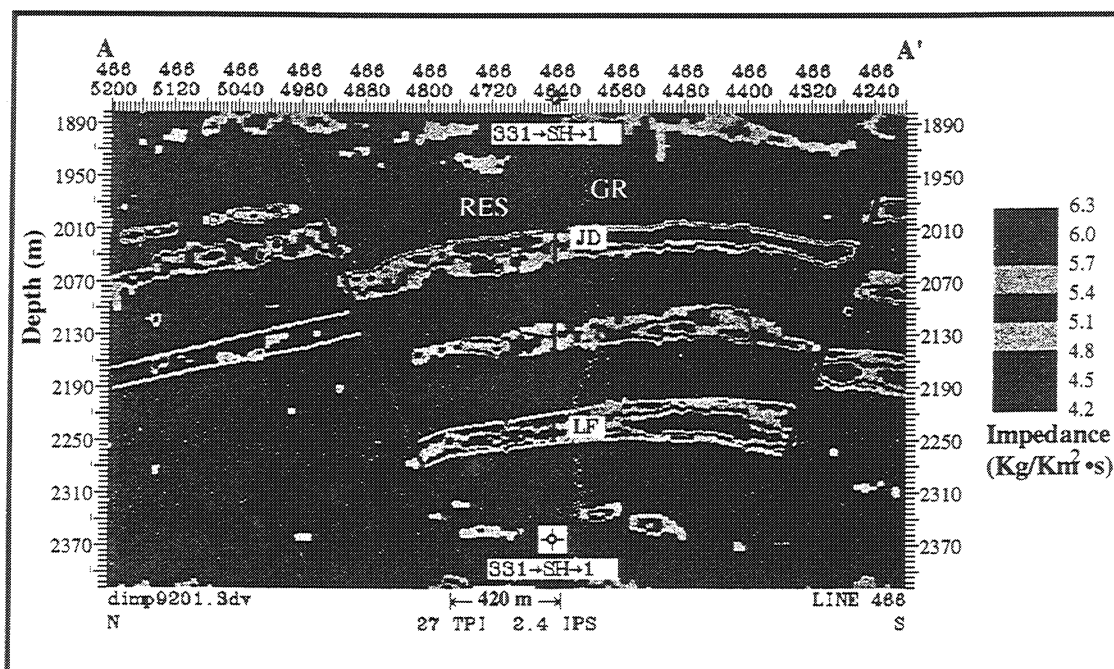


Figure 4.6. The top and bottom of the LF reservoir were interpreted in the converted impedance depth volume through correlating the low impedance anomalies. Resistivity and gamma ray logs of EI well 331_SH_1 are also superimposed, note the excellent match between the well tops interpreted in the well and that interpreted from the impedance depth volume.

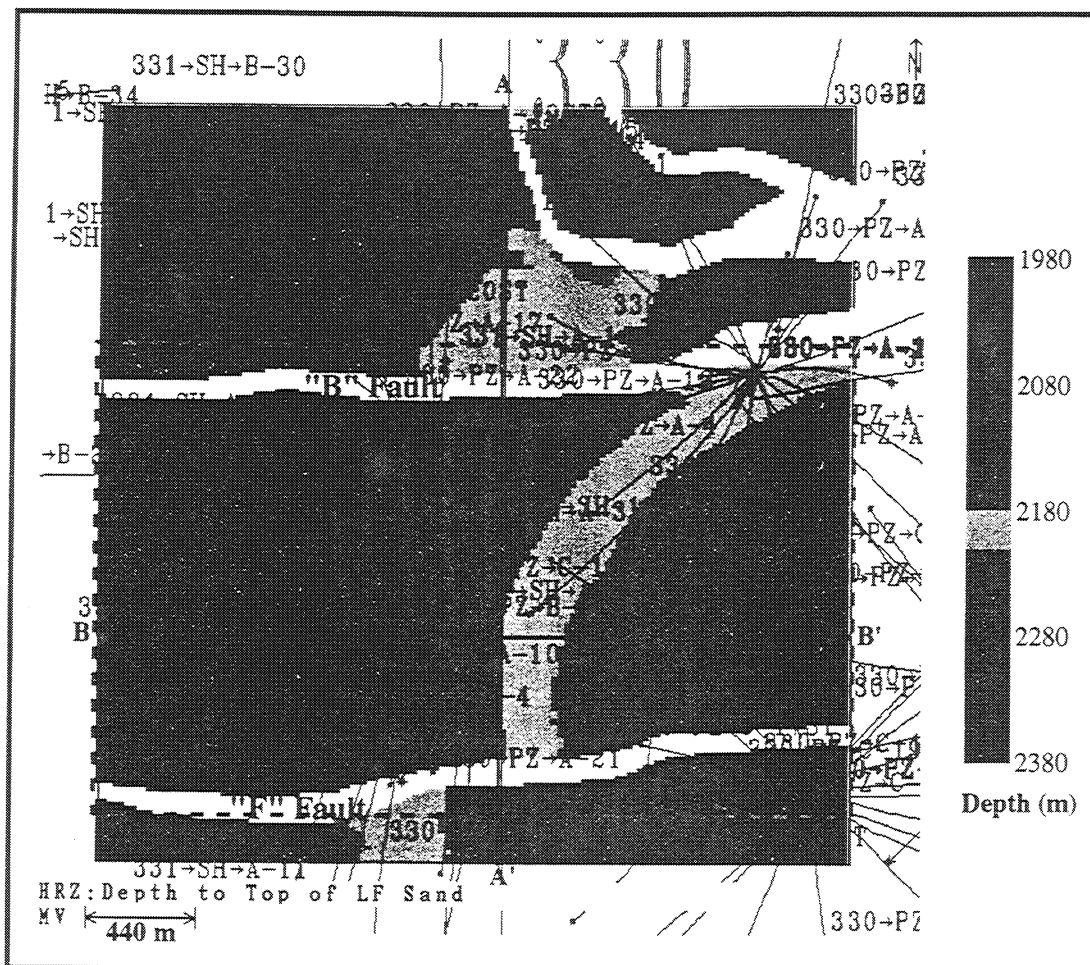


Figure 4.7. The interpreted top of LF structure map from the acoustic impedance volume. The A-A' cross-section is shown in Figure 4.6, and the B-B' cross-section is shown in Figure 4.11. Our reservoir characterization and analysis are performed only in the fault block "B", which is the rectangle illustrated by dashed line.

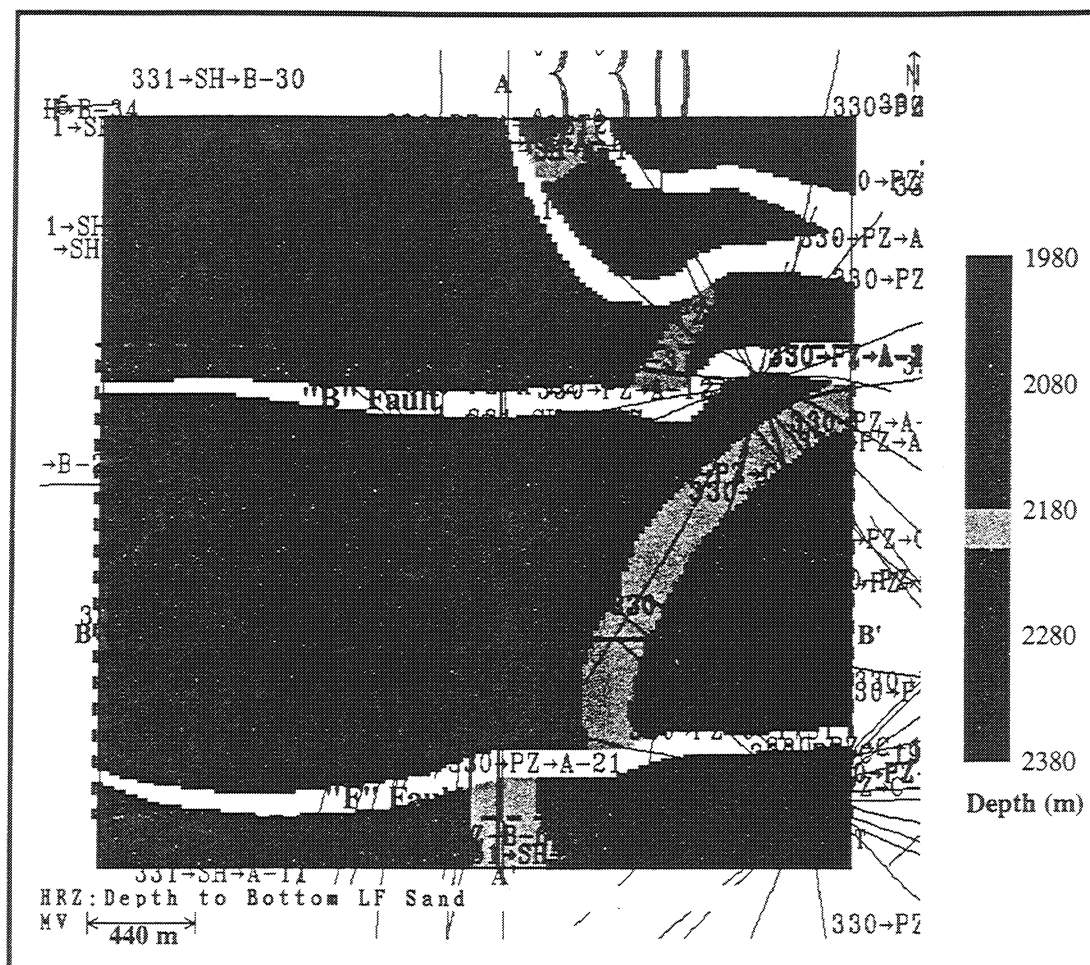


Figure 4.8. The interpreted bottom of LF structure map from the acoustic impedance volume. The bottom structure of the LF sand is similar to the top of the LF sand except in the central area (west of the block boundary) just above the "F" fault, the contours are much deeper than those close to the "B" fault in the north.

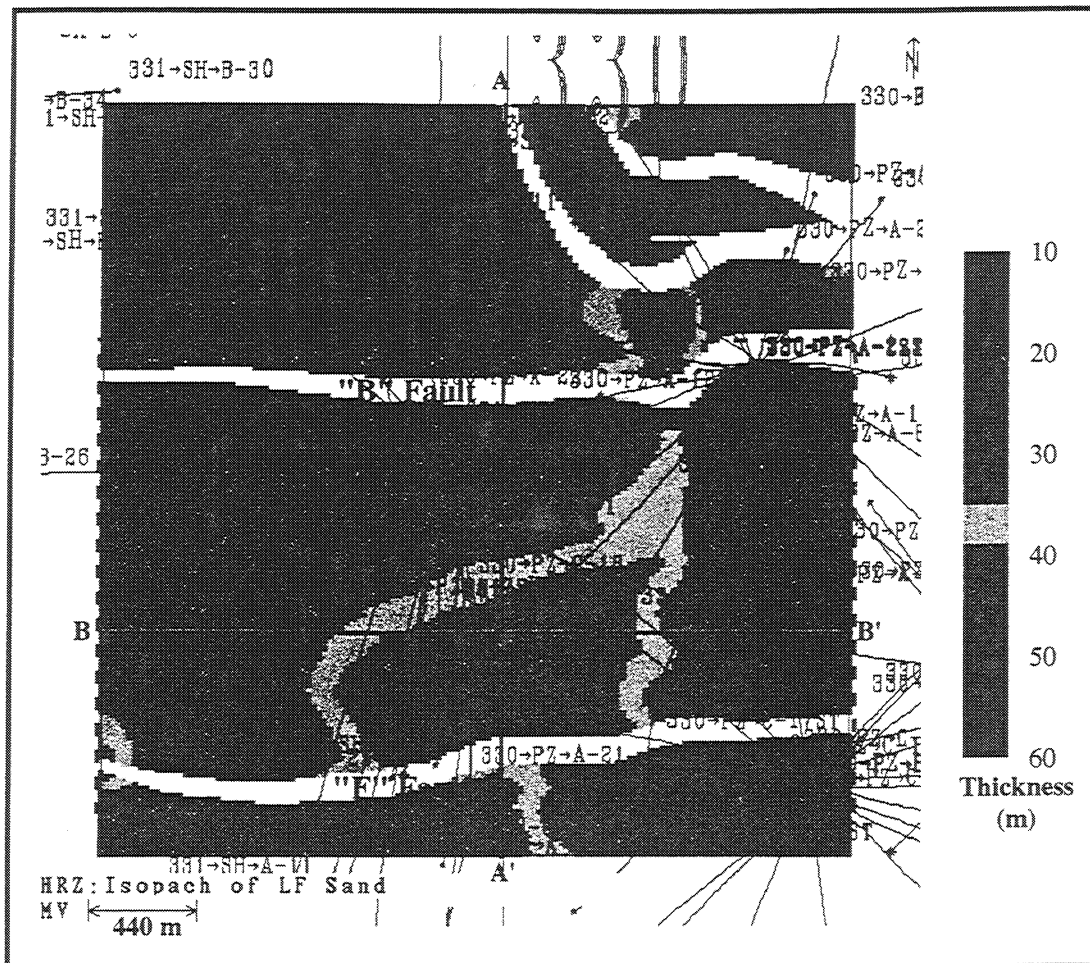


Figure 4.9. The isopach map of the LF sand is calculated from the top and bottom of the LF structure map. The depocenter of the LF sand appears to be in the south-west, and the thickening of the LF sand runs along the north-east to south-west direction. The "F" fault separated the main LF sand body into two compartments, i.e., the fault block "A" in the south and the fault block "B" in the north.

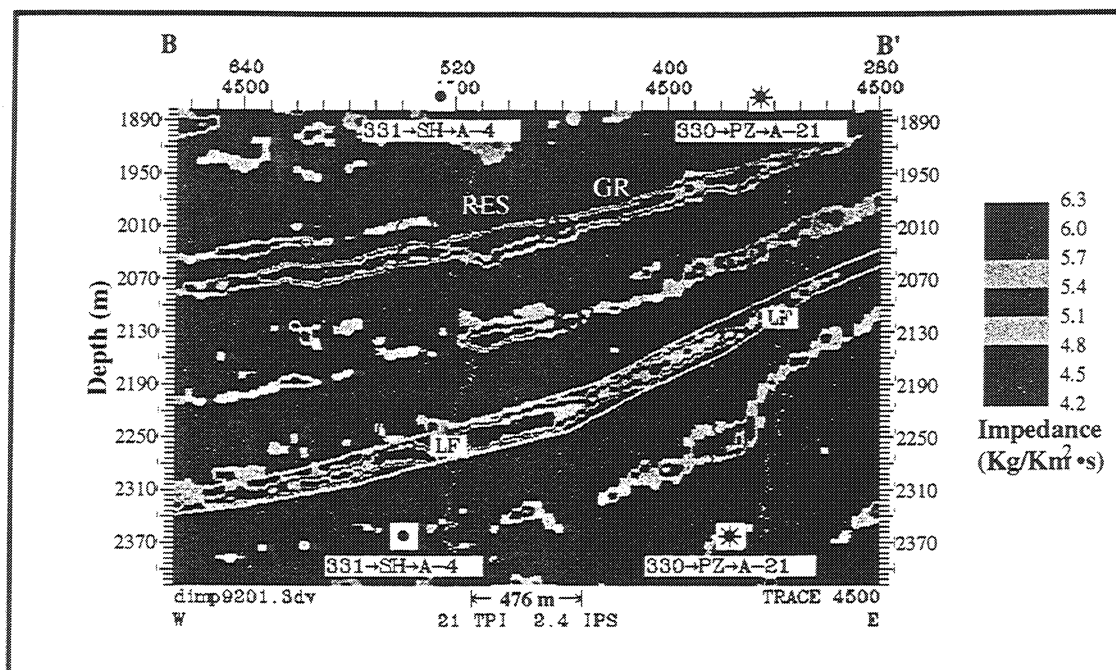


Figure 4.10. The west-east impedance cross-section shows that the sand thickness of the LF sand gradually decreases toward the crest of the rollover anticline in the east. The JD and KE sands also show the same pattern. The resistivity and gamma ray logs of EI well 331_SH_A-4 and 330_PZ_A-21 are also shown in the figure. The shaliness of the LF sand increases updip across the section from west to east. We also see that the LF reservoir is a low resistivity pay. The location of the cross-section is shown in Figure 4.7.

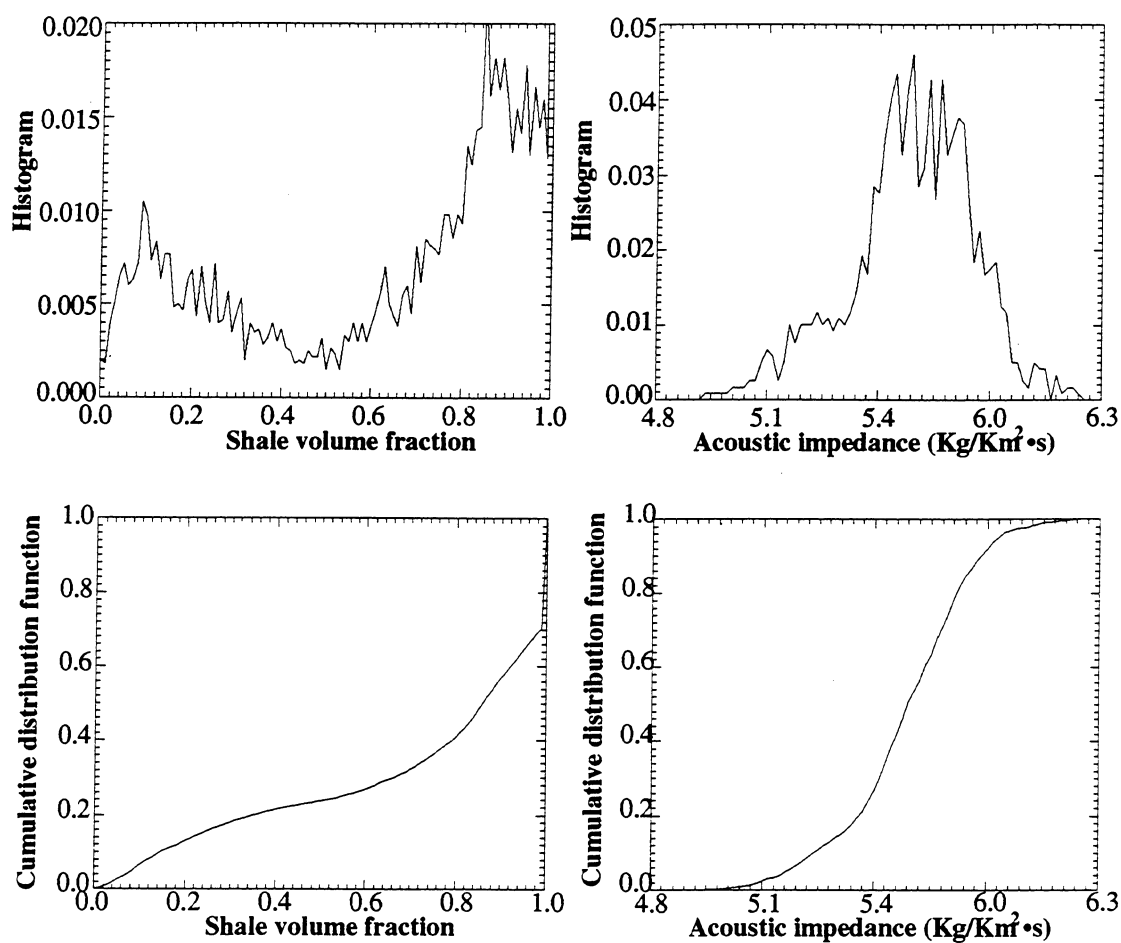


Figure 4.11. Histogram and cumulative histogram of the measured shale volume fractions in the twenty wells and the extracted acoustic impedances at the same locations. The shale volume fractions have a broad bi-modal distribution, and the impedances appear to be a biased single-modal distribution with a long tail at the low impedance end.

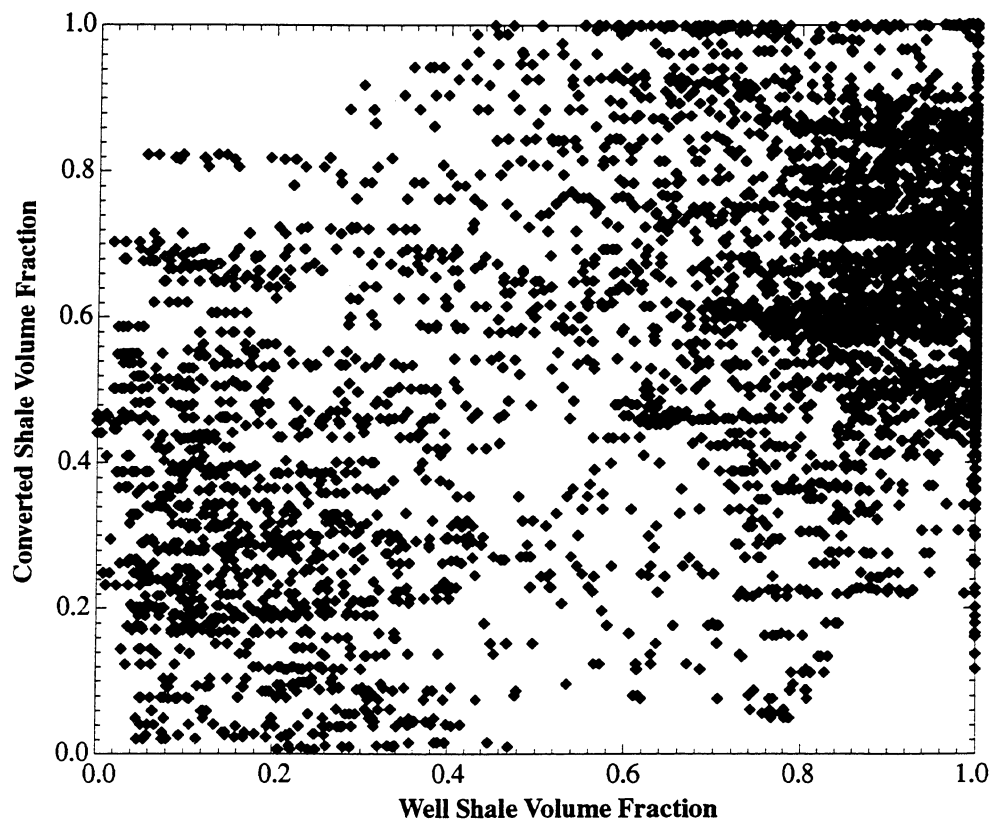


Figure 4.13. The crossplot of the converted, or, soft shale volume fractions from acoustic impedances versus the measured shale volume fractions at wells. The converted shale volume fractions are used with those measured as the calibration dataset in the stochastic simulation of lithology.

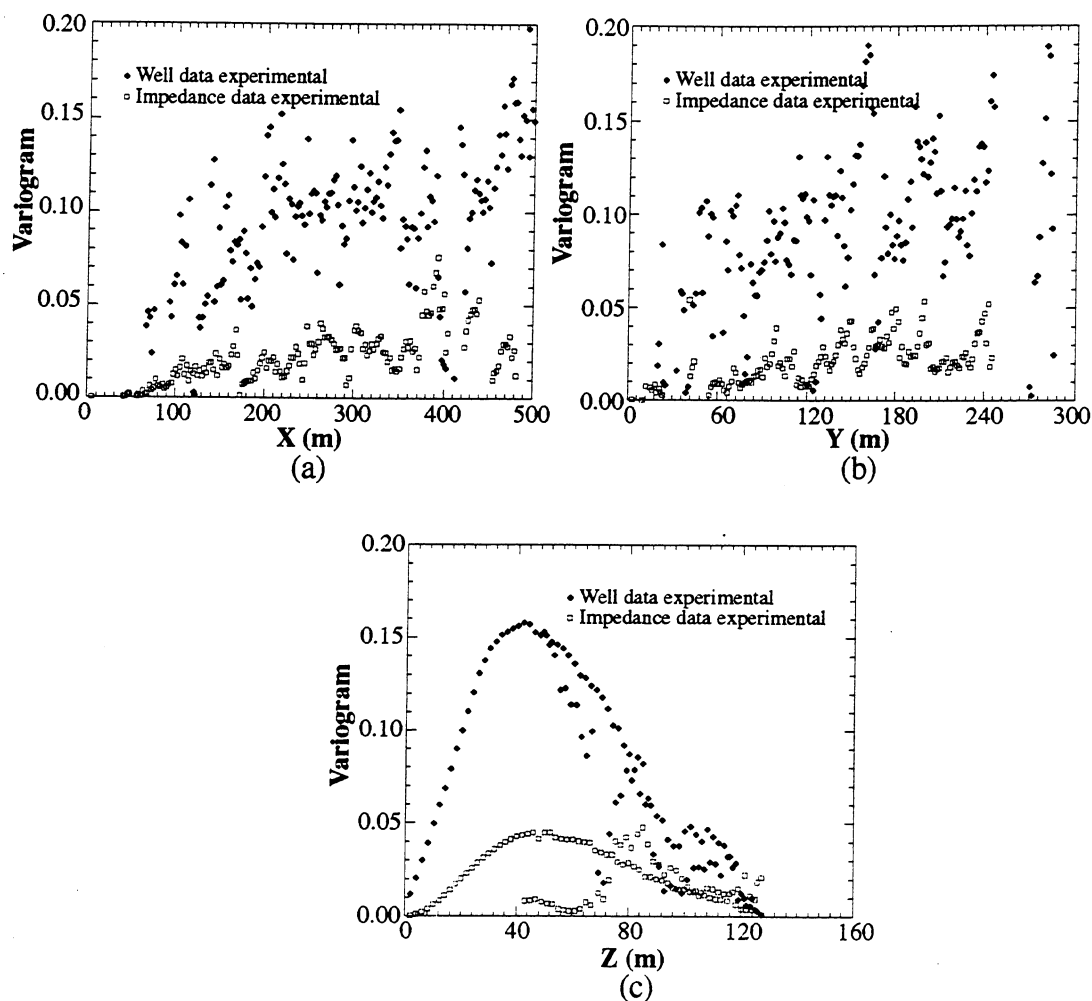


Figure 4.14. Semivariograms of the well shale volume fractions (hard data) and the converted shale volume fractions from acoustic impedances (soft) are analyzed in the the transformed X (a), Y (b) and Z (c) directions. The hard data show greater variabilities in all these three directions. Decrease of covariances in Z disrection is caused by the layering of lithology.

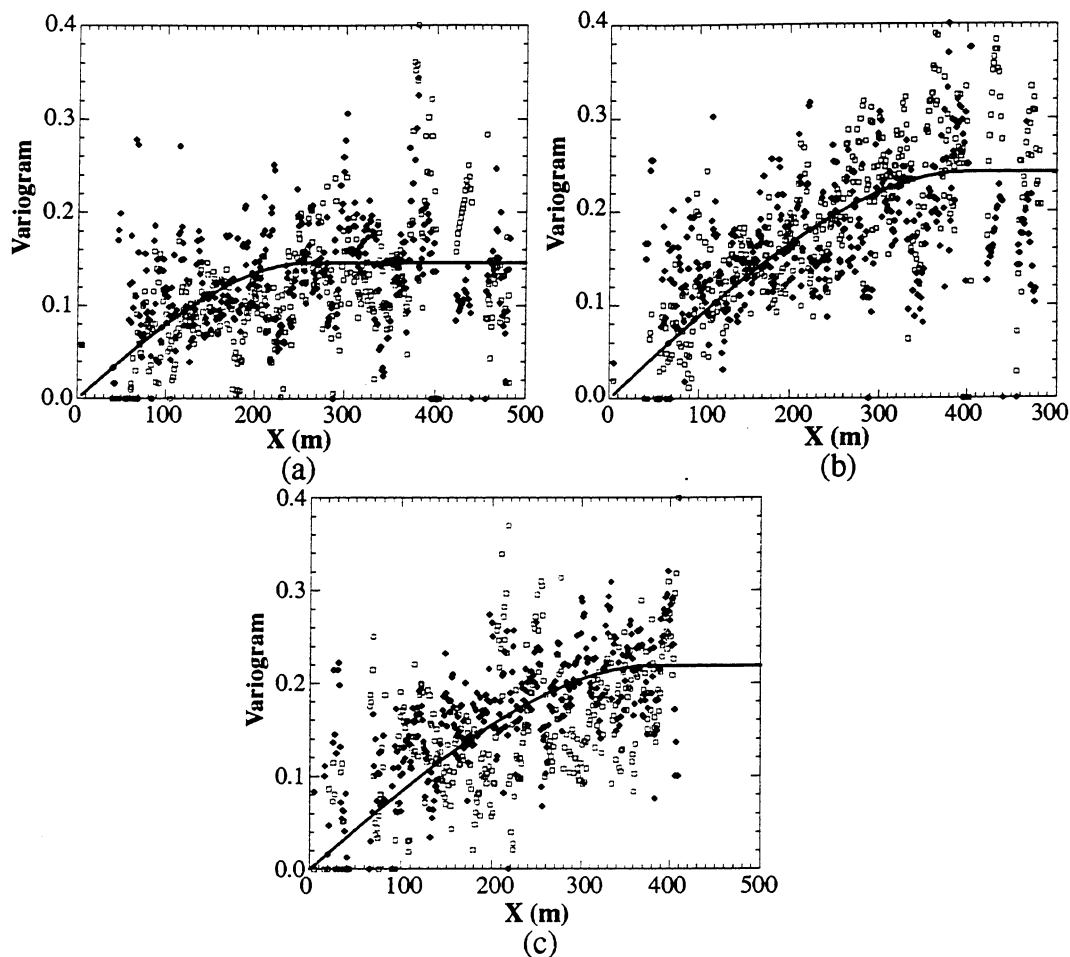


Figure 4.15. Semivariograms of the cutoffs 0.25, 0.5 and 0.75 for both hard and soft data in the transformed east-west direction (X) are shown in (a), (b), and (c), respectively. The hollow squares are the shale volume fraction samples converted from acoustic impedances (soft data), and the solid diamonds are the measured shale volume fractions in wells (hard data). The fitted theoretical spherical models are shown as solid lines.

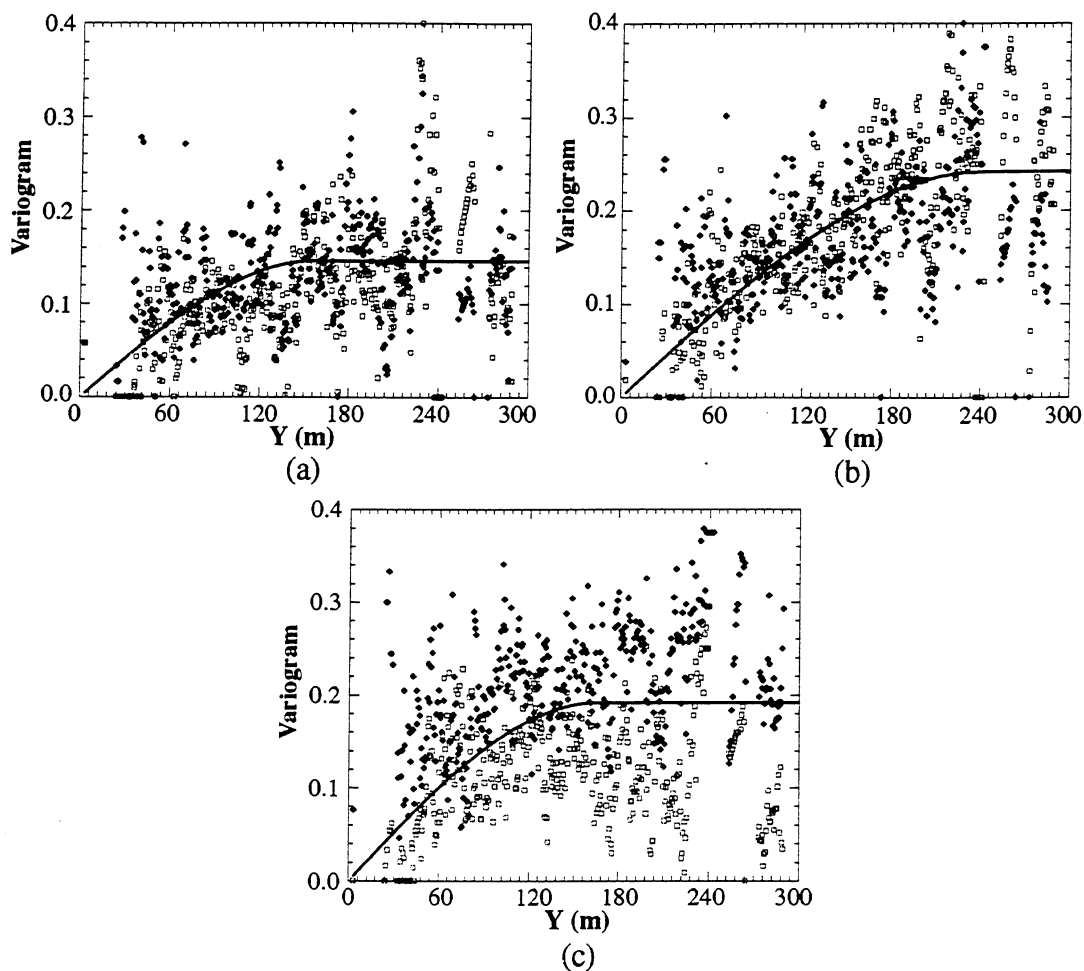


Figure 4.16. Semivariograms of the cutoffs 0.25, 0.5 and 0.75 for both hard and soft data in the transformed north-south direction (Y) are shown in (a), (b), and (c), respectively. The hollow squares are soft data, and the solid diamonds are hard data. The fitted theoretical spherical models are shown as solid lines.

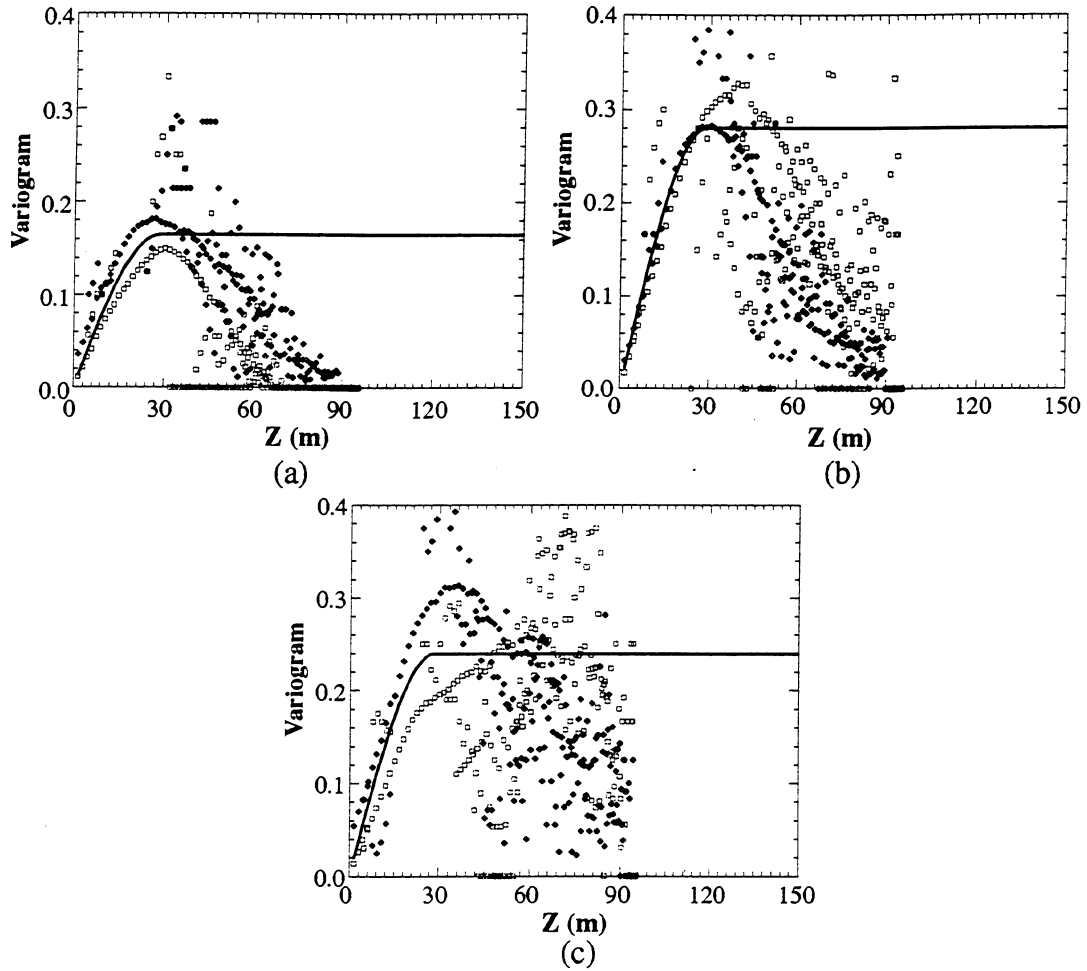


Figure 4.17. Semivariograms of the cutoffs 0.25, 0.5 and 0.75 for both hard and soft data in the transformed vertical direction (Z) are shown in (a), (b), and (c), respectively. The hollow squares are soft data and the solid diamonds are hard data. The fitted theoretical spherical models are shown as solid lines. These fitted directional semivariograms shown in Figures 4.15, 4.16 and 4.17 are then used in stochastic simulation as the spatial distribution structures for the defined cutoffs.

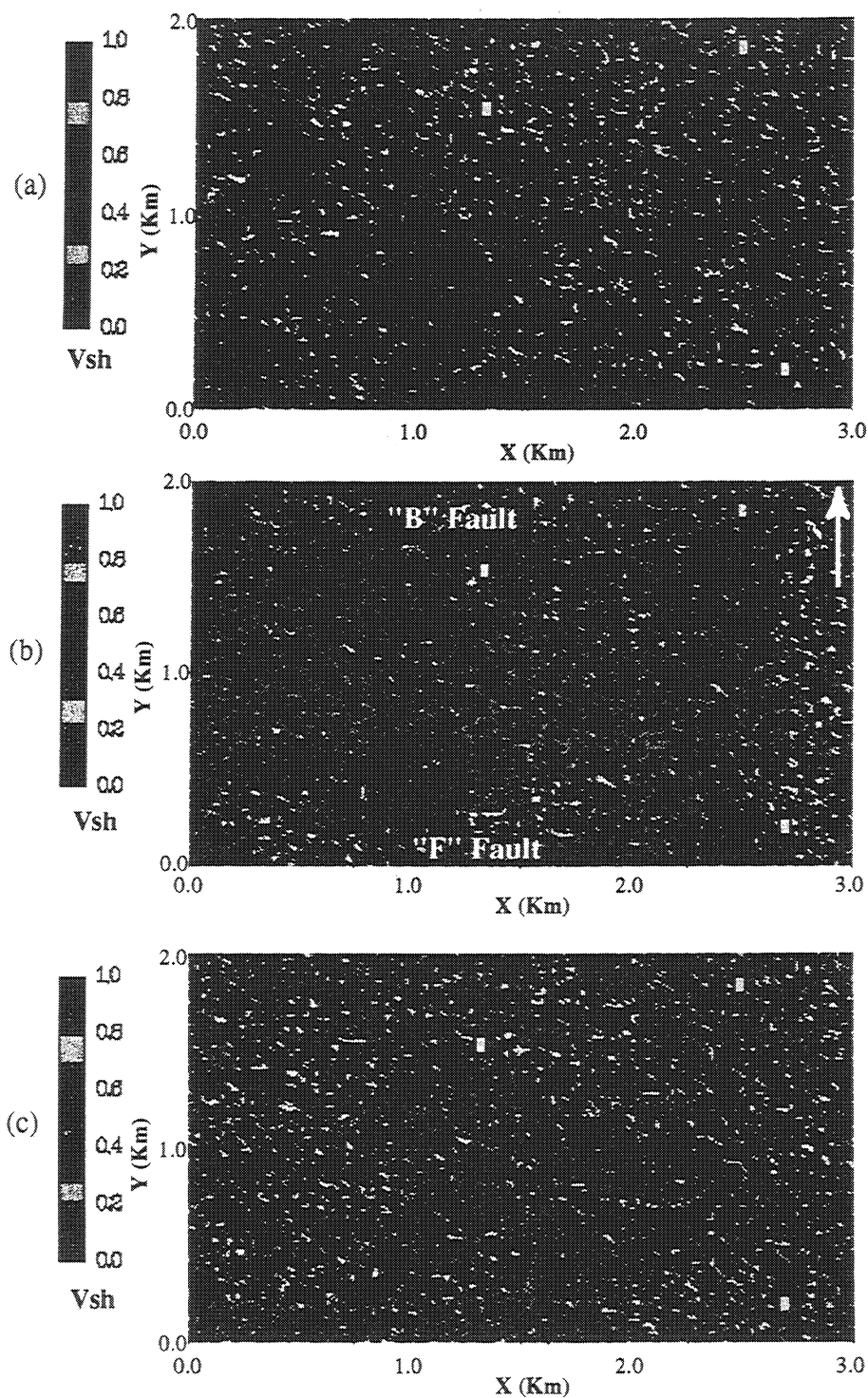


Figure 4.18. Simulated shale volume fraction volume of the simulation 1 using the first random seed point is sliced at the upper (a), middle (b), and lower (c) LF sand. Sand and shale are the two dominant lithologies in the simulated volume. The faults B and F can be clearly seen in the middle slice. Black circles are hard data locations.

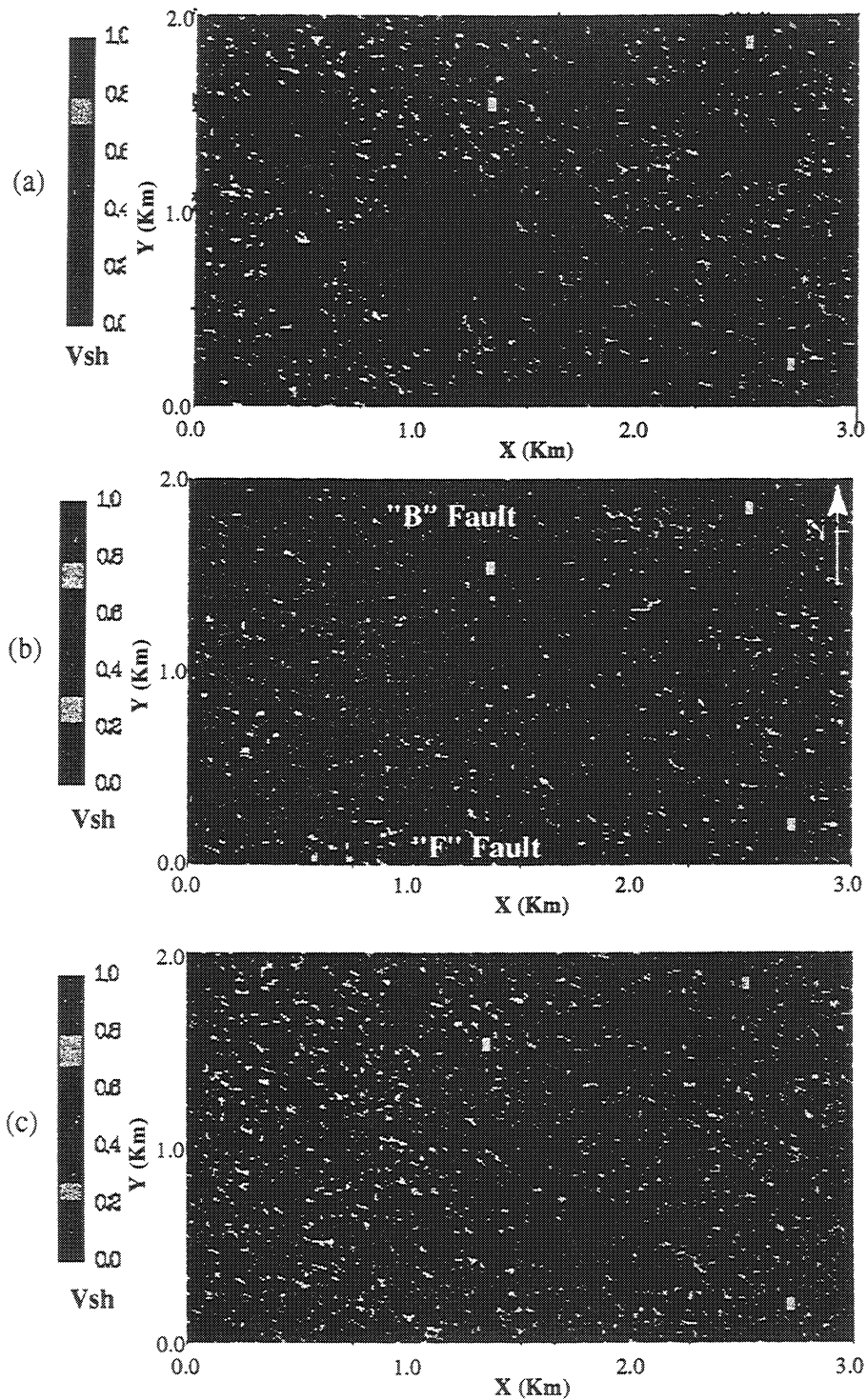


Figure 4.19. Simulated shale volume fraction volume of the simulation 1 using the second random seed point is sliced at the upper (a), middle (b), and lower (c) LF sand. Sand and shale are the two dominant lithologies in the simulated volume. The faults B and F can be clearly seen in the middle slice.

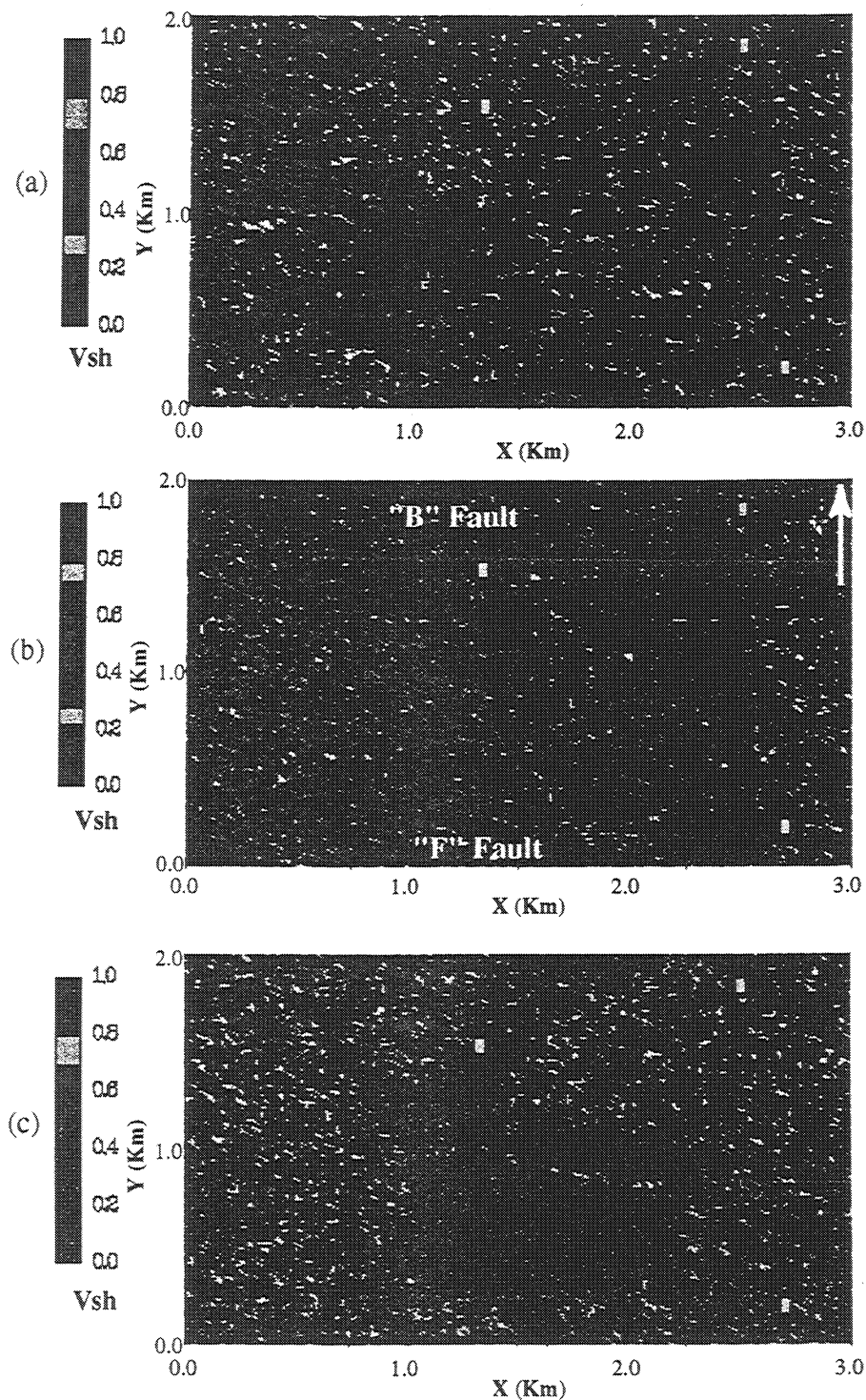


Figure 4.20. Simulated shale volume fraction volume of the simulation 1 using the third random seed point is sliced at the upper (a), middle (b), and lower (c) LF sand. Sand and shale are the two dominant lithologies in the simulated volume. The faults B and F can be clearly seen in the middle slice.

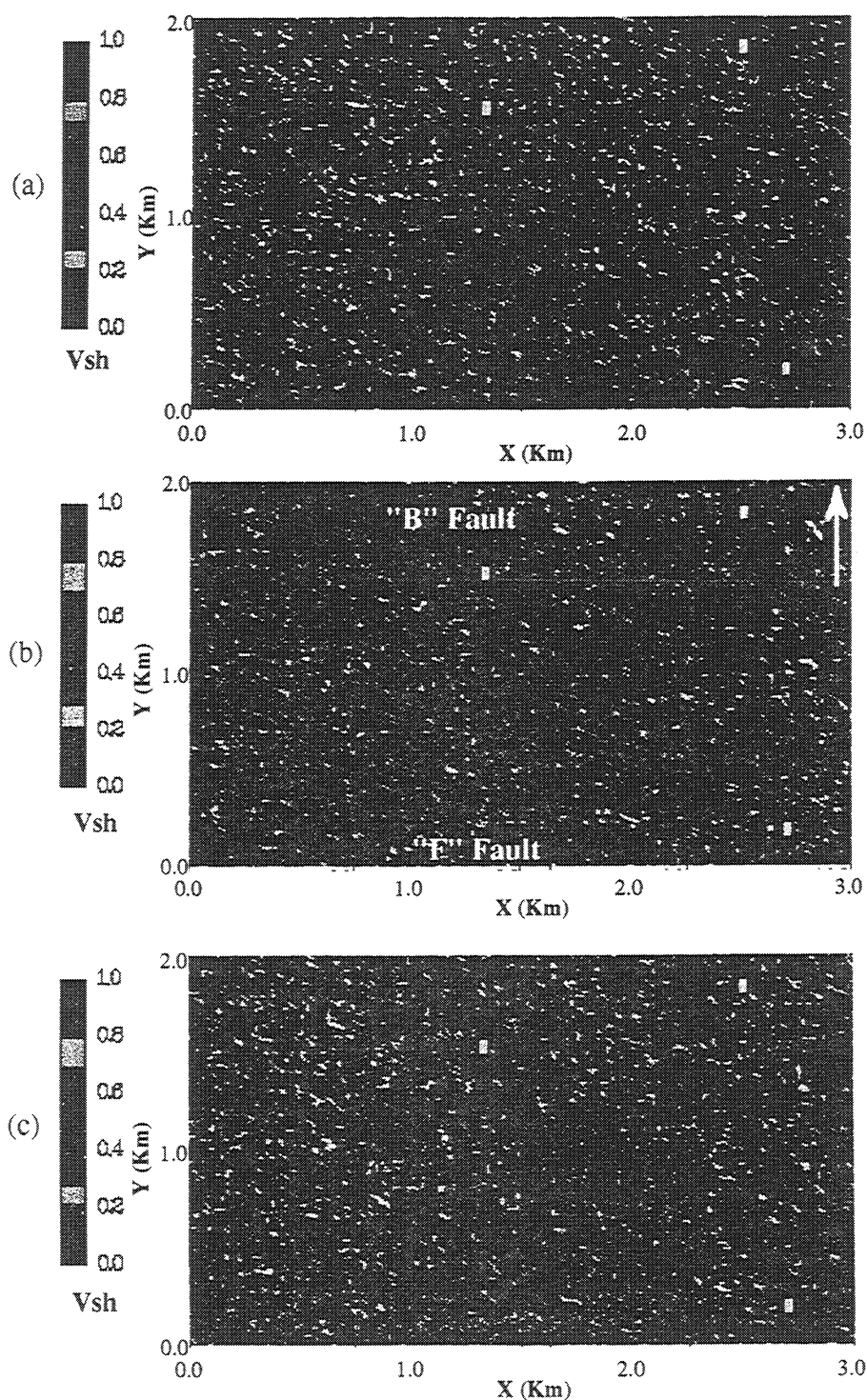


Figure 4.21. Simulated shale volume fraction volume of the simulation 1 using the forth random seed point is sliced at the upper (a), middle (b), and lower (c) LF sand. Sand and shale are the two dominant lithologies in the simulated volume. The faults B and F can be clearly seen in the middle slice.

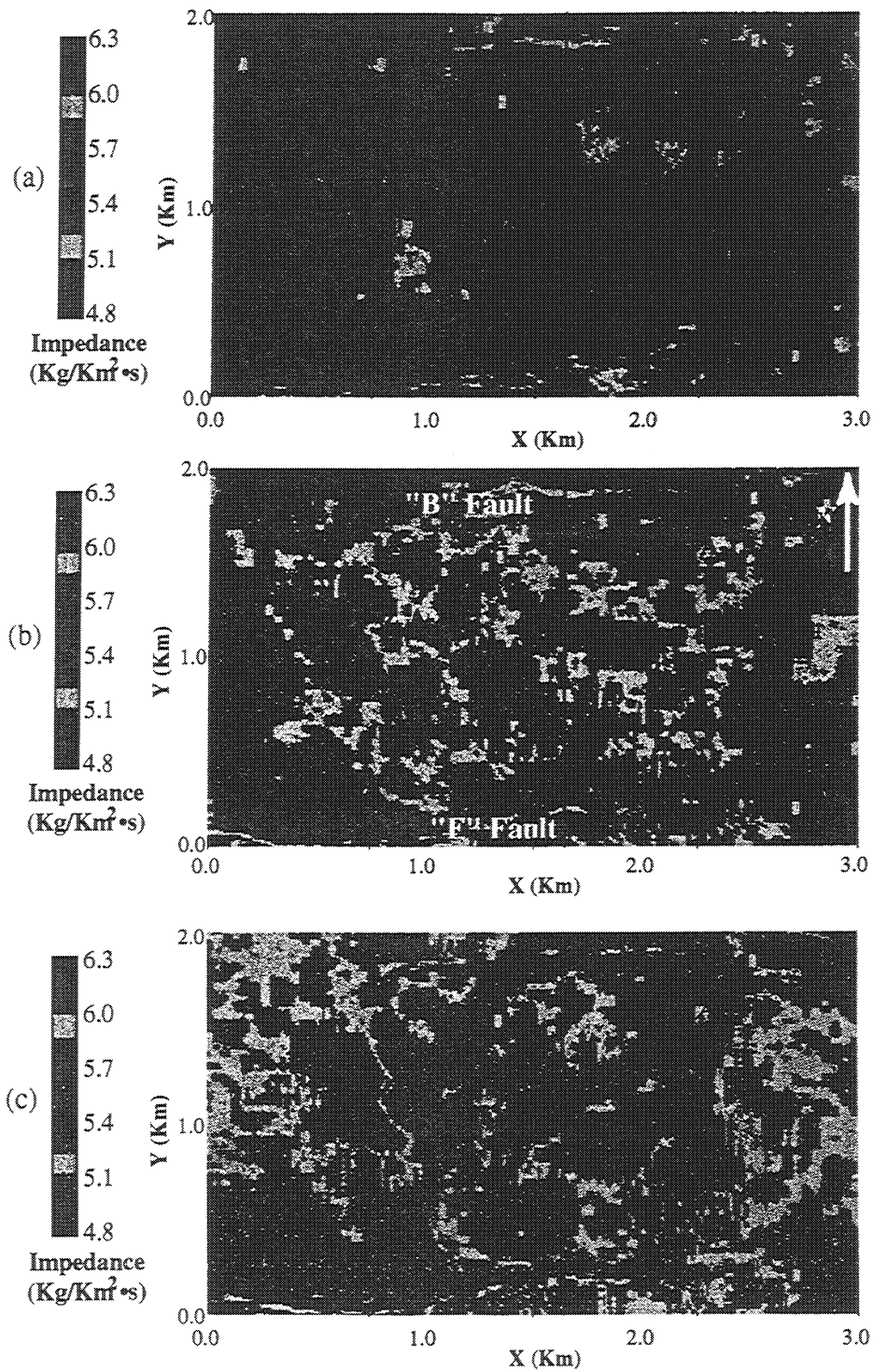


Figure 4.22. The estimated 1992 acoustic impedance volume is sliced at the upper (a), middle (b), and lower (c) LF sand. Compare them with the simulated lithology distributions.

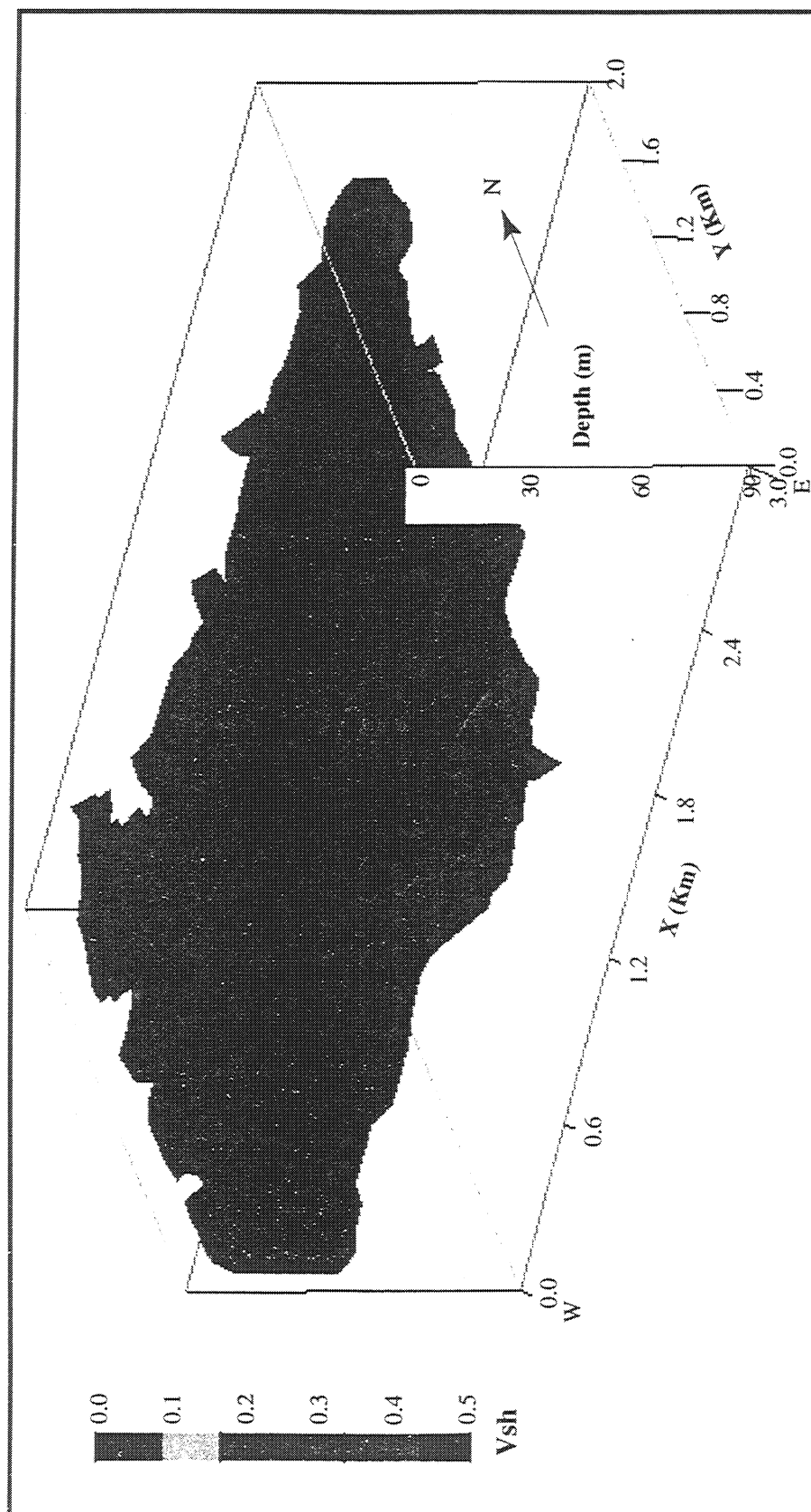


Figure 4.23. The final lithology model of the LF reservoir in the fault block B is computed using the arithmetic average of the 20 simulated shale volume fraction models. Only the sand and shaly sand are rendered in this volumetric representation of the LF reservoir. The volume is flattened using the interpreted top of the LF sand (Figure 4.7) from the acoustic impedance volume.

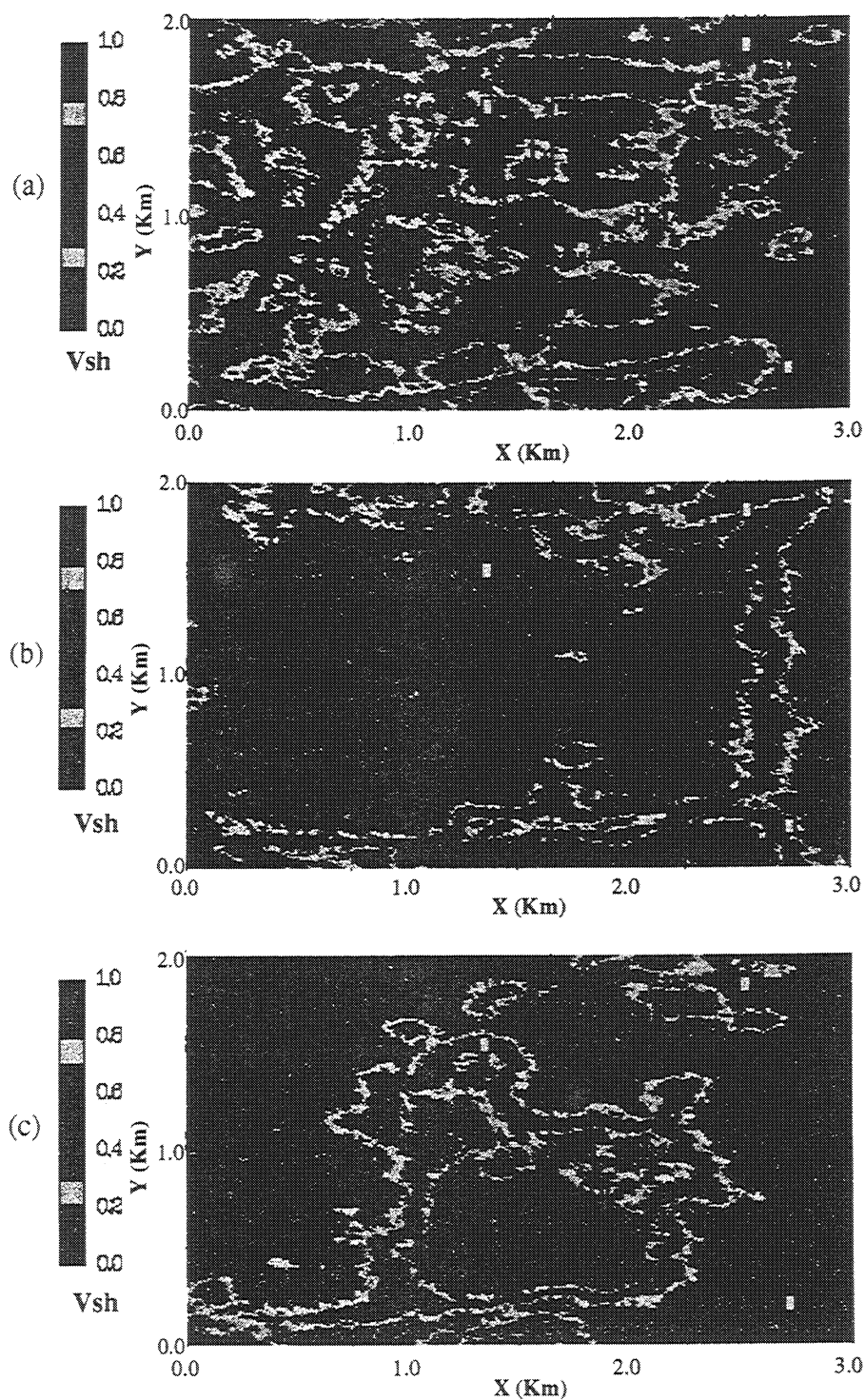


Figure 4.24. The final lithology volume of the LF reservoir is sliced at the upper (a), middle (b), and lower (c) LF sand. The arithmetic average smoothed out the sharp sand and shale boundaries shown in the individual simulations. However, the consistency of the randomly simulated sand and shale distributions suggest that the simulation algorithm used is indeed robust.

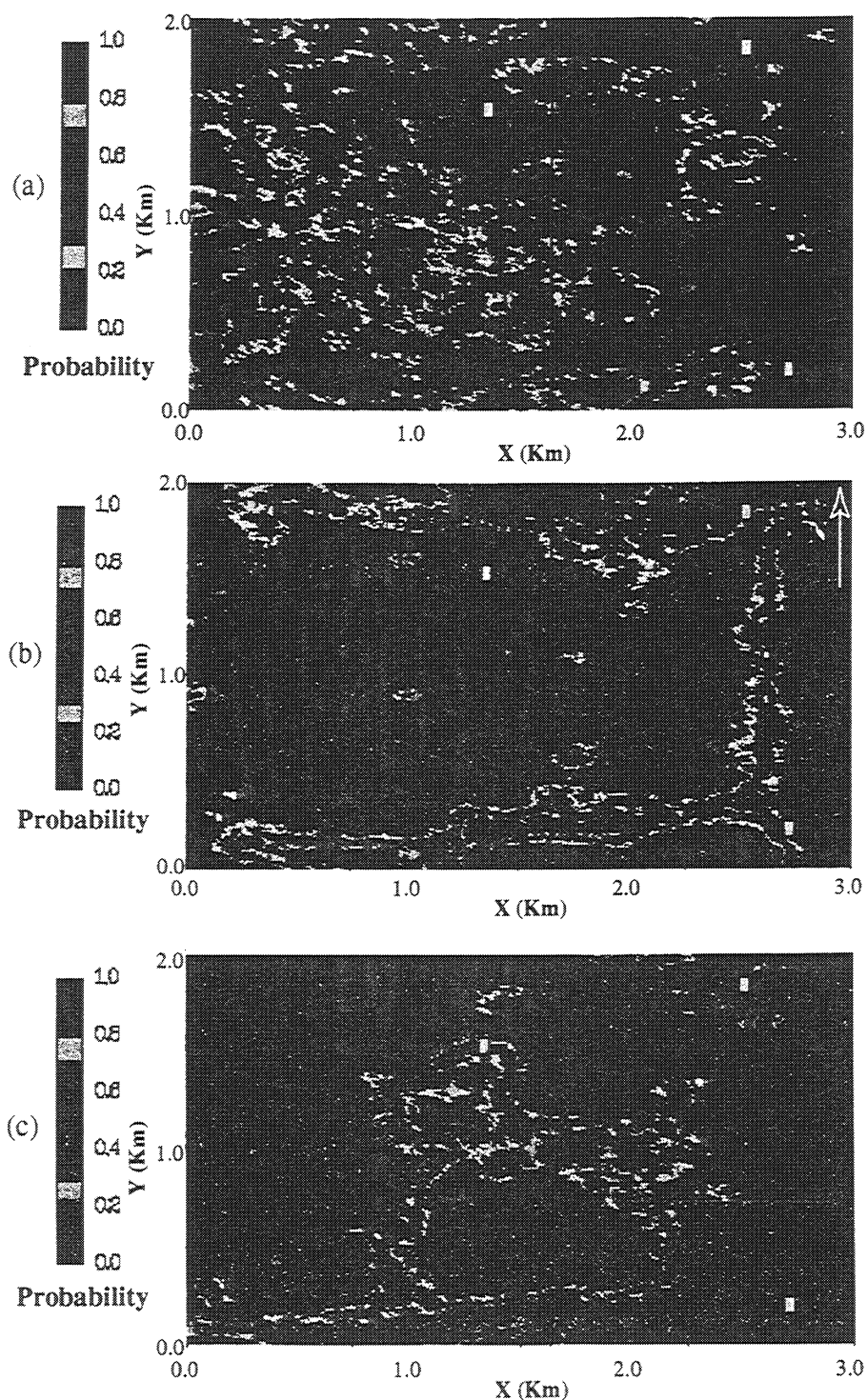


Figure 4.25. The probability slices of sand distribution corresponding to the lithology slices shown in Figure 4.24. The probability volume is computed using the 20 simulated lithology models at each grid point in 3D. These maps provide the confidence level of whether a particular volume in the LF sand is a clean sand or dirty sand body.

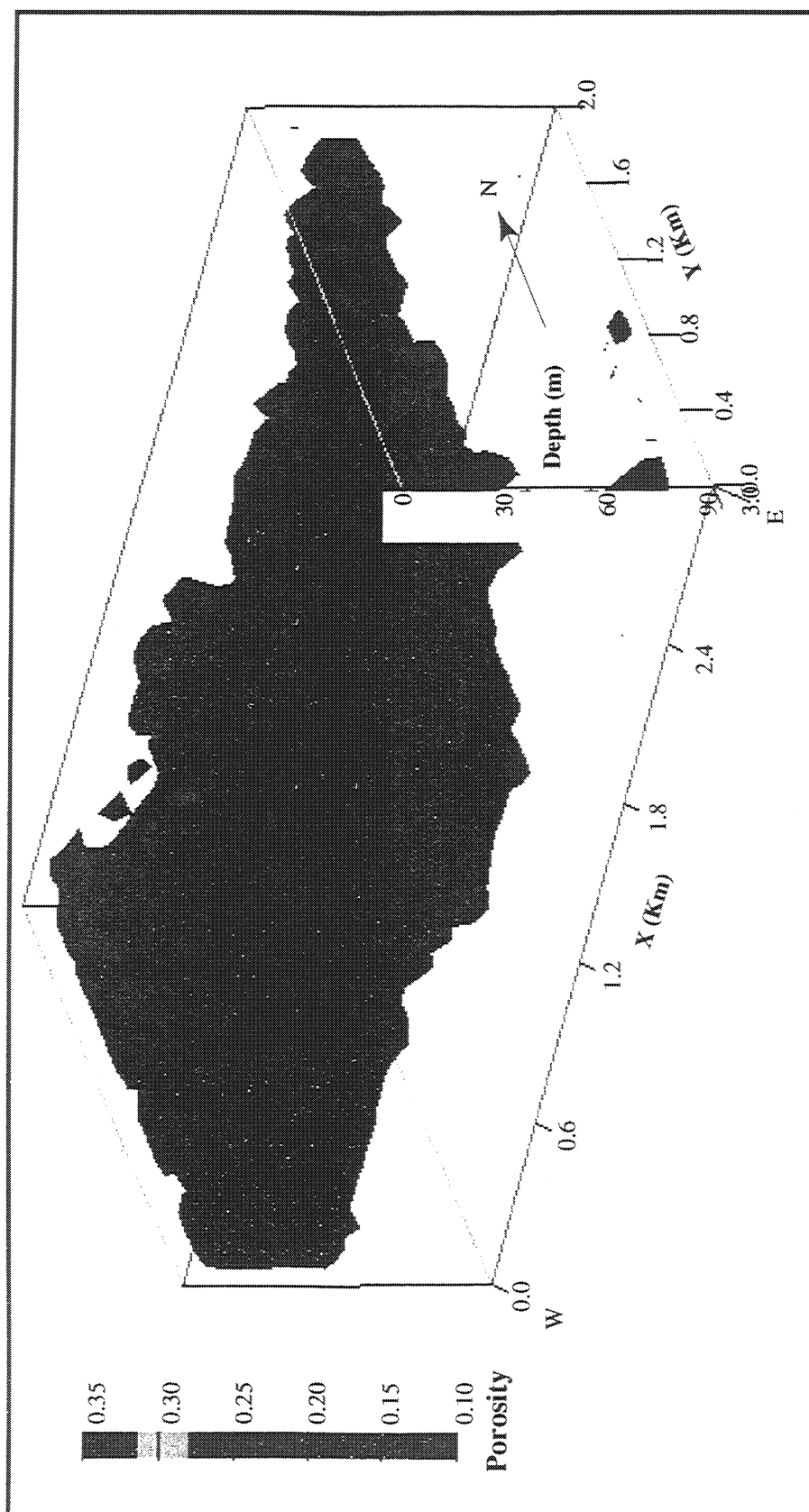


Figure 4.26. The computed porosity model of the LF reservoir in the fault block B using Eq. 4.16 in the context. The computation uses both the constructed lithology model (Figure 4.23) and the inverted acoustic impedance volume, the acoustic impedance of pore fluids is the water acoustic impedance, therefore, the computed porosity also contains the oil and gas saturation information.

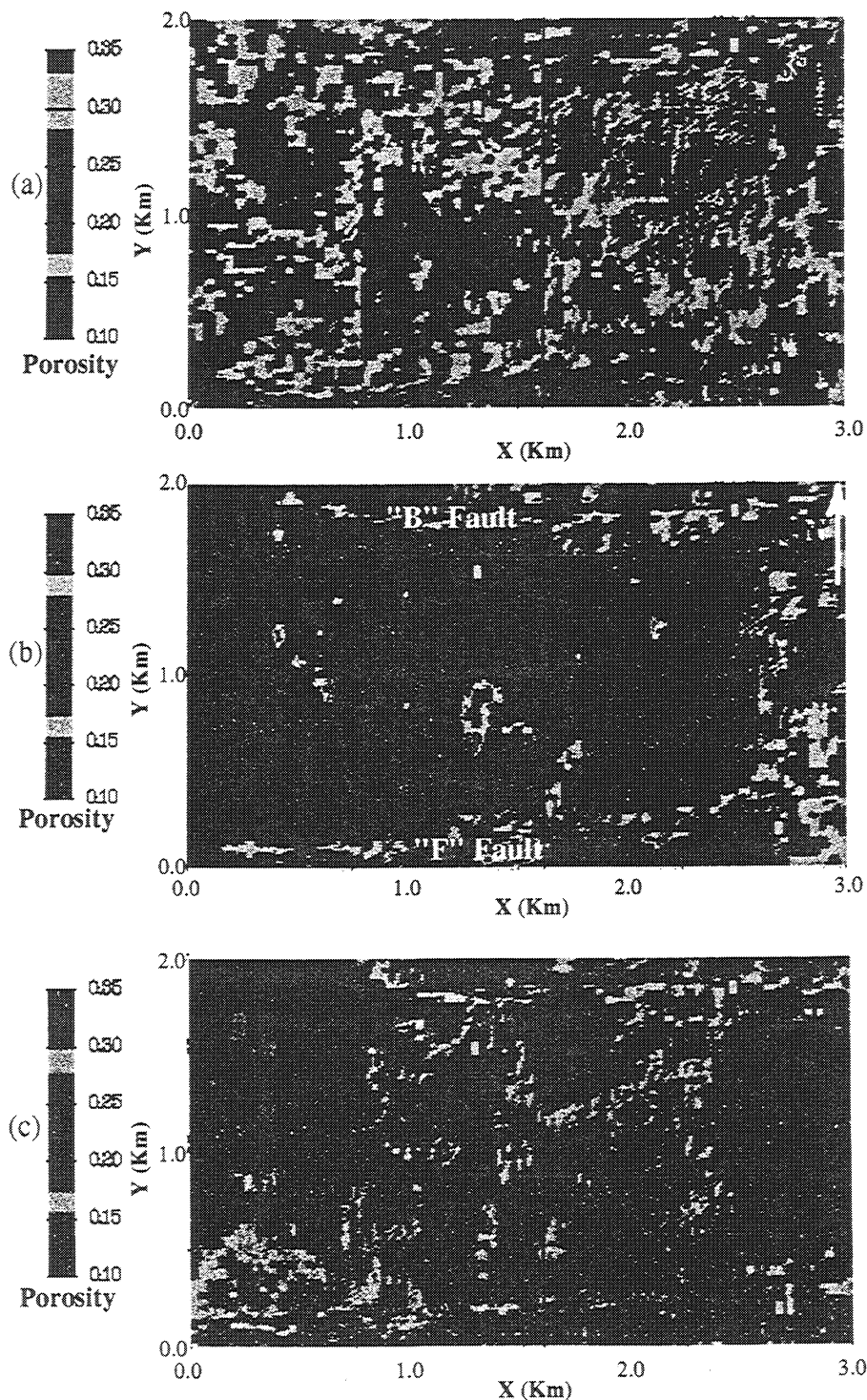


Figure 4.27. The porosity slices of the LF sand corresponding to the lithology slices shown in Figure 4.24. The porosity distribution is more sensitive to the lithology variations, the faults "B" and "F" are clearly seen in all the three slices because of the shale volume fraction corrections applied to the porosity computation.

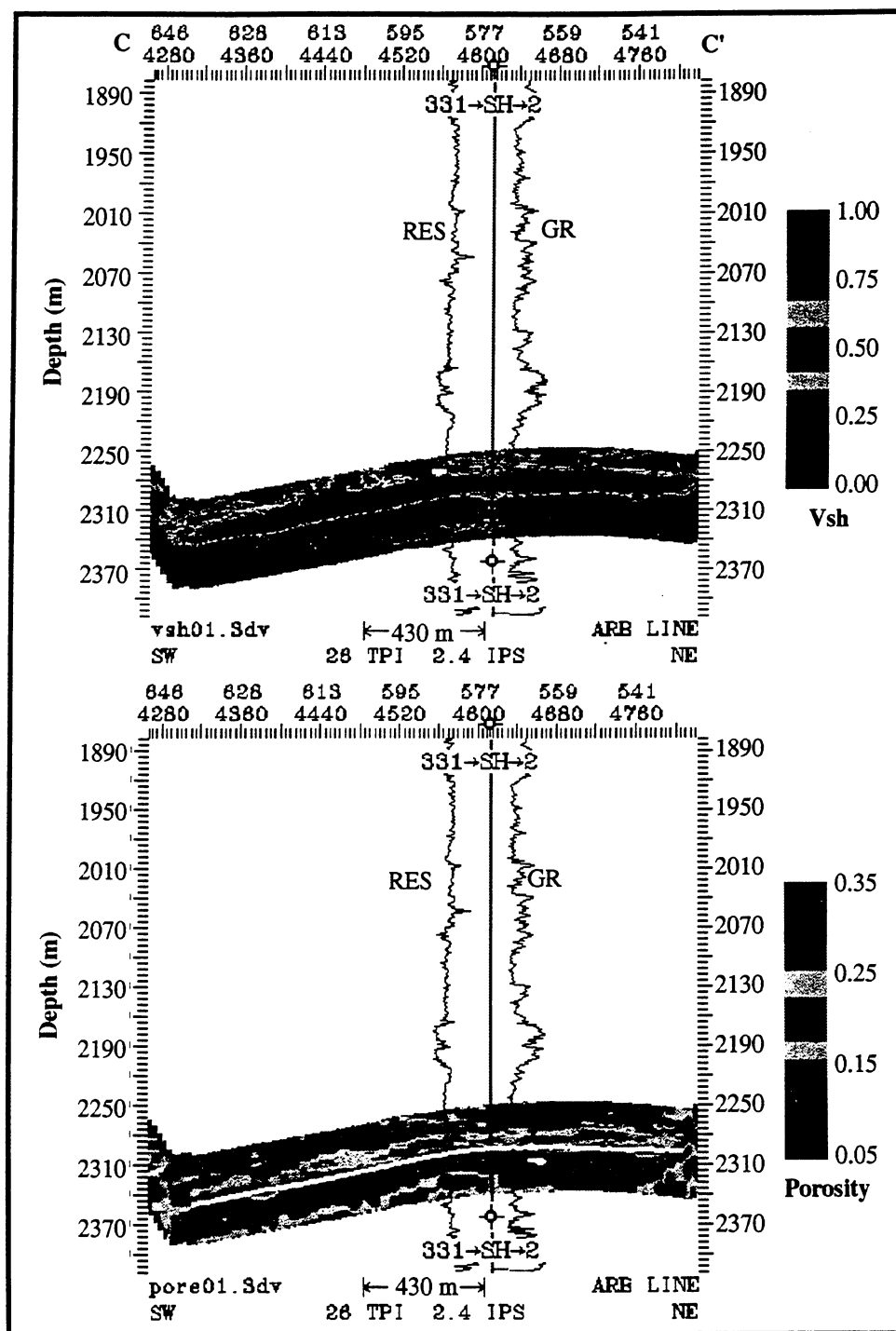


Figure 4.29. The C-C' cross-sections of shale volume fraction (top) and estimated porosity (bottom) are shown with the resistivity (RES) and gamma ray (GR) logs in EI well 331_SH_2. Excellent agreement between the estimated and measured lithology and porosity can be clearly seen.

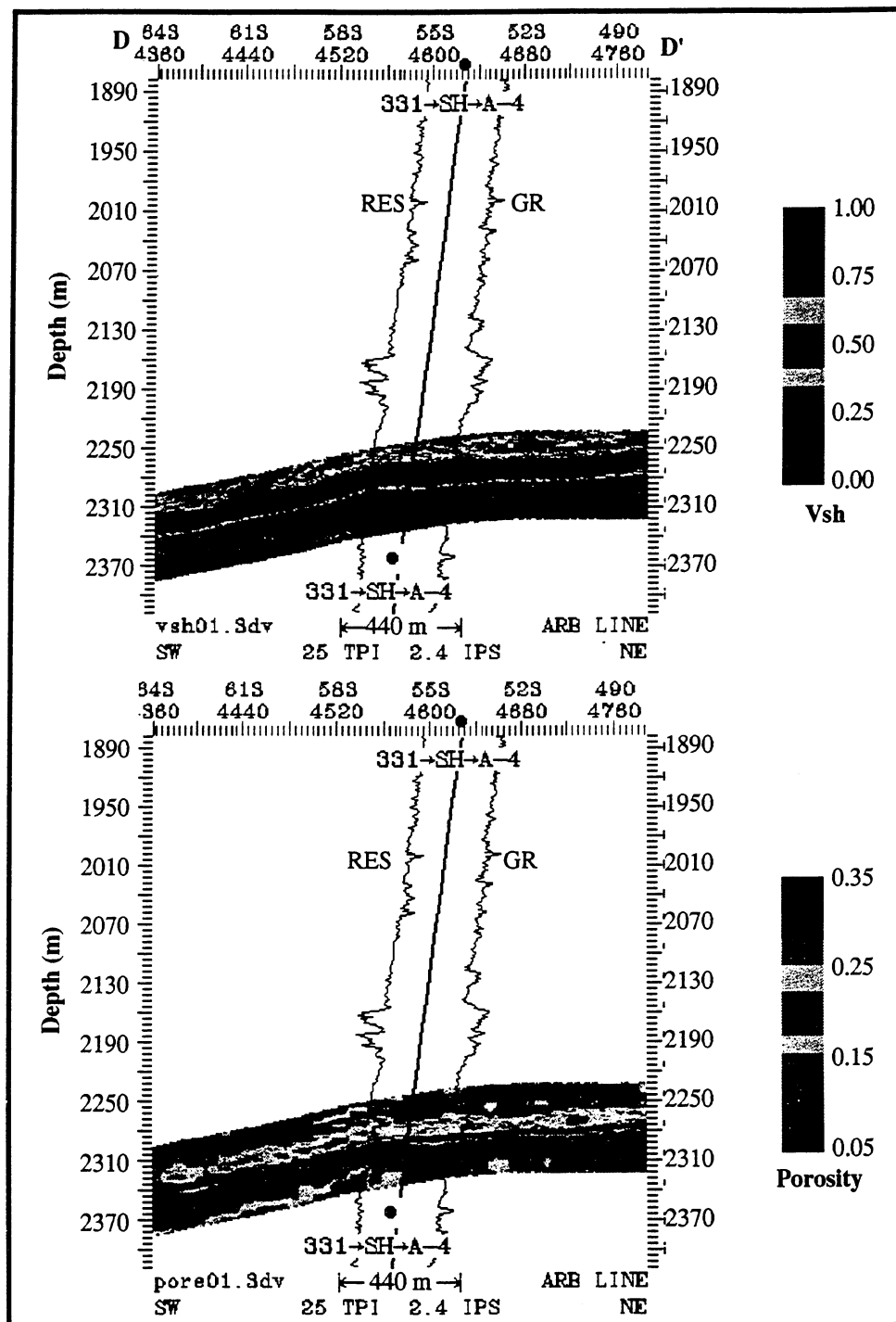


Figure 4.30. The D-D' cross-sections of shale volume fraction (top) and estimated porosity (bottom) are shown with the resistivity (RES) and gamma ray (GR) logs in EI well 331_SH_A-4.

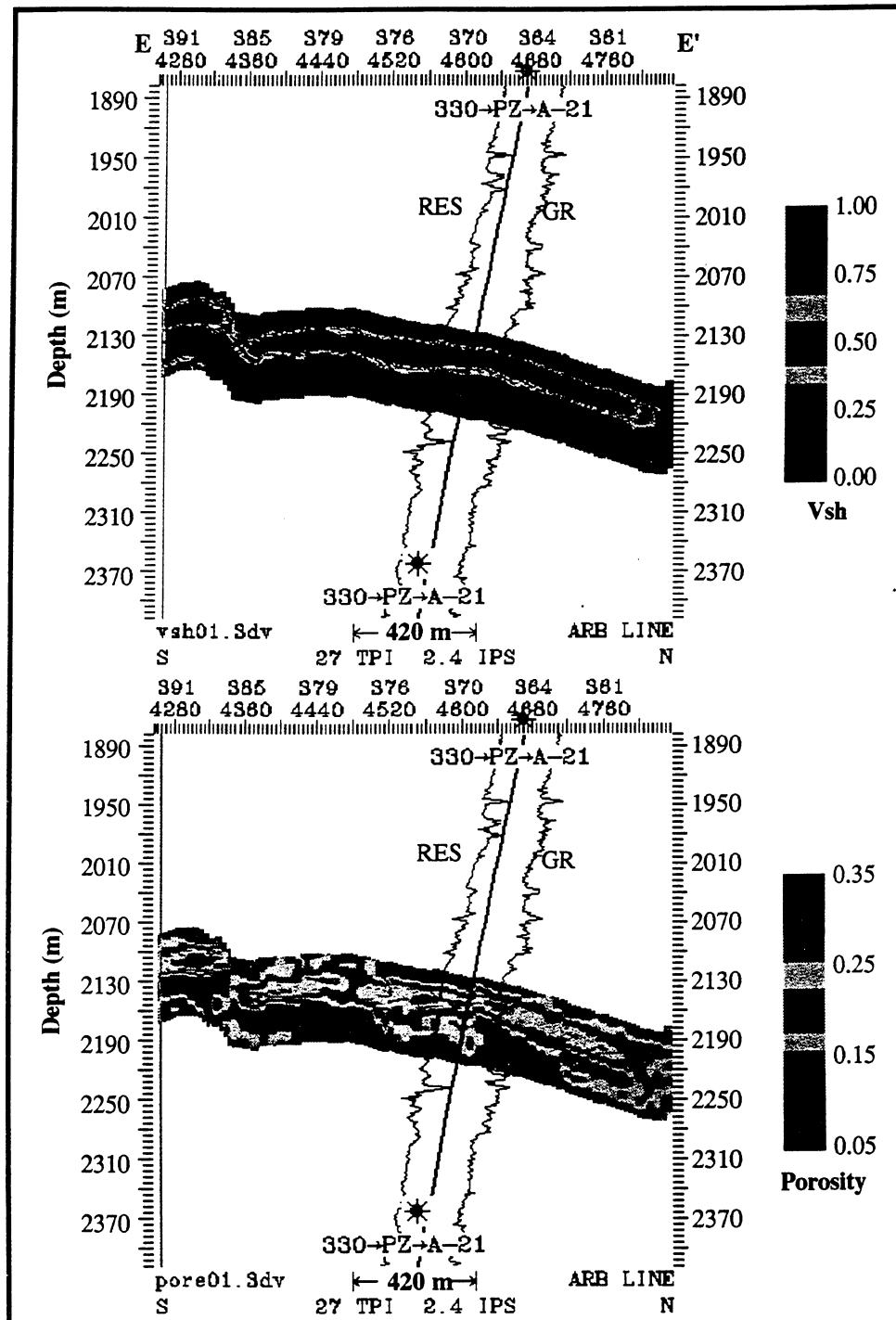


Figure 4.31. The E-E' cross-sections of shale volume fraction (top) and estimated porosity (bottom) are shown with the resistivity (RES) and gamma ray (GR) logs in EI well 330_PZ_A-21.

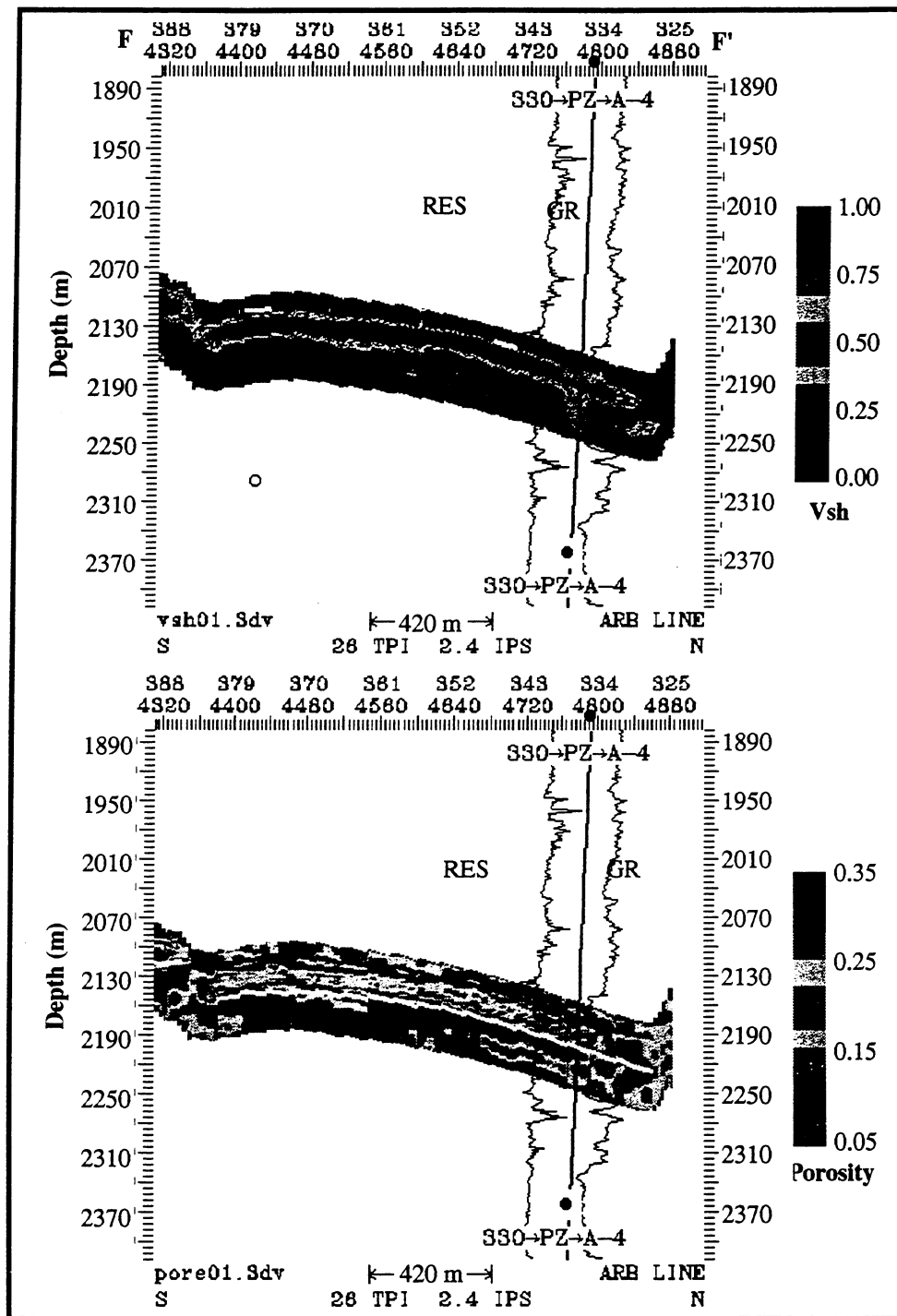


Figure 4.32. The F-F' cross-sections of shale volume fraction (top) and estimated porosity (bottom) are shown with the resistivity (RES) and gamma ray (GR) logs in EI well 330_PZ_A-4.

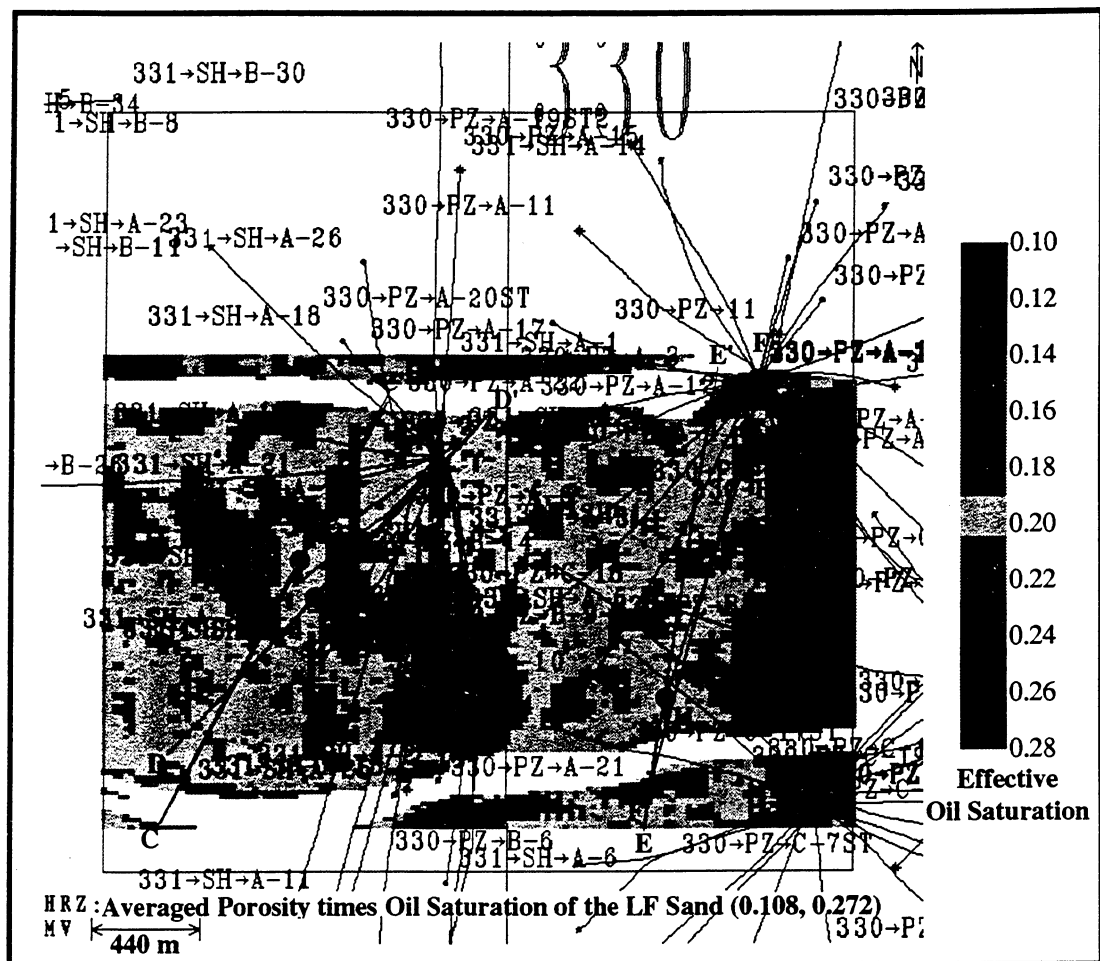


Figure 4.33. Porosities calculated using Eq. 4.12 and saline impedance as the pore fluid impedance can also be considered as effective oil saturation, which is essentially the product of porosity and oil saturation. The average effective oil saturation map of the LF reservoir is thus computed. It shows remarkable similarities to the bypassed hydrocarbons obtained from our 4D acoustic impedance analysis, which used two acoustic impedance volumes inverted from the 1985 and 1992 3D seismic surveys in the study area (see Figure 4.34).

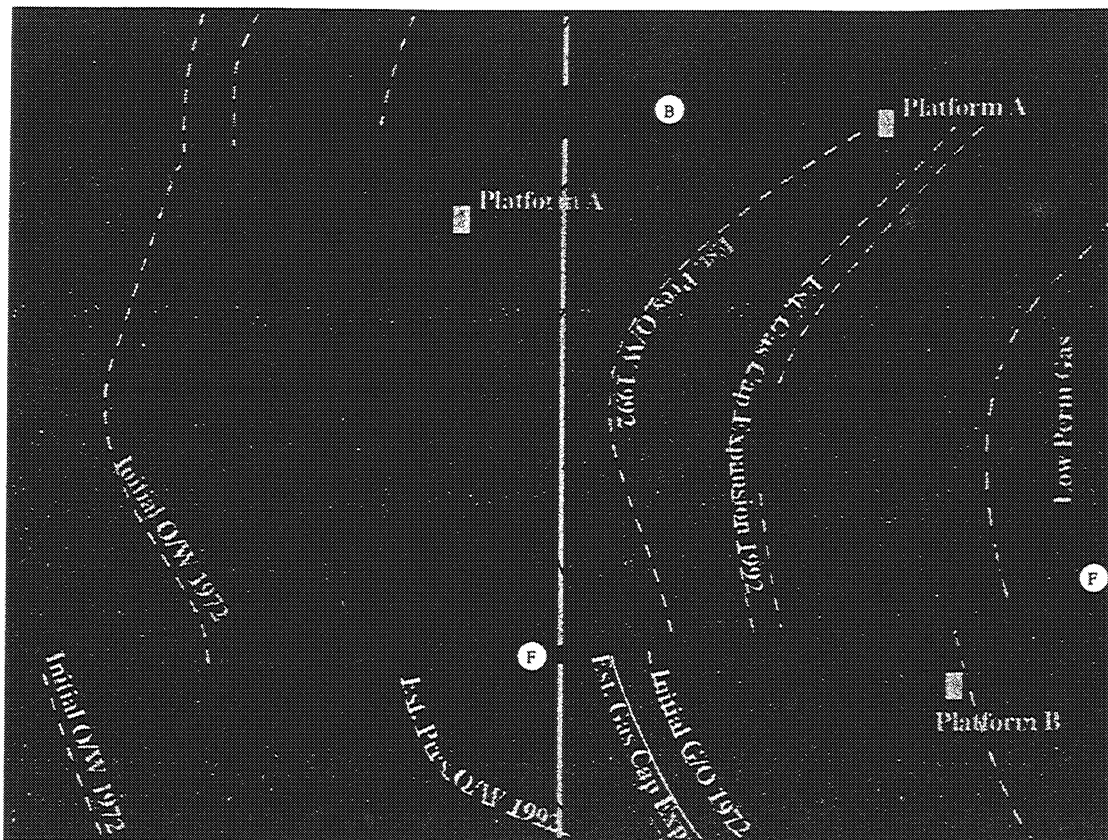


Figure 4.34. Drainage patterns of the LF reservoir derived from our 4D impedance analysis show great similarities to the result obtained from our reservoir characterization (Figure 4.33). The areas of the bypassed hydrocarbons are consistent with the areas of greater porosity and/or effective oil saturation shown in Figure 4.33. Water is shown as light blue, oil is in green, and the decreased impedances (possible gas caps) over the time are shown in red.

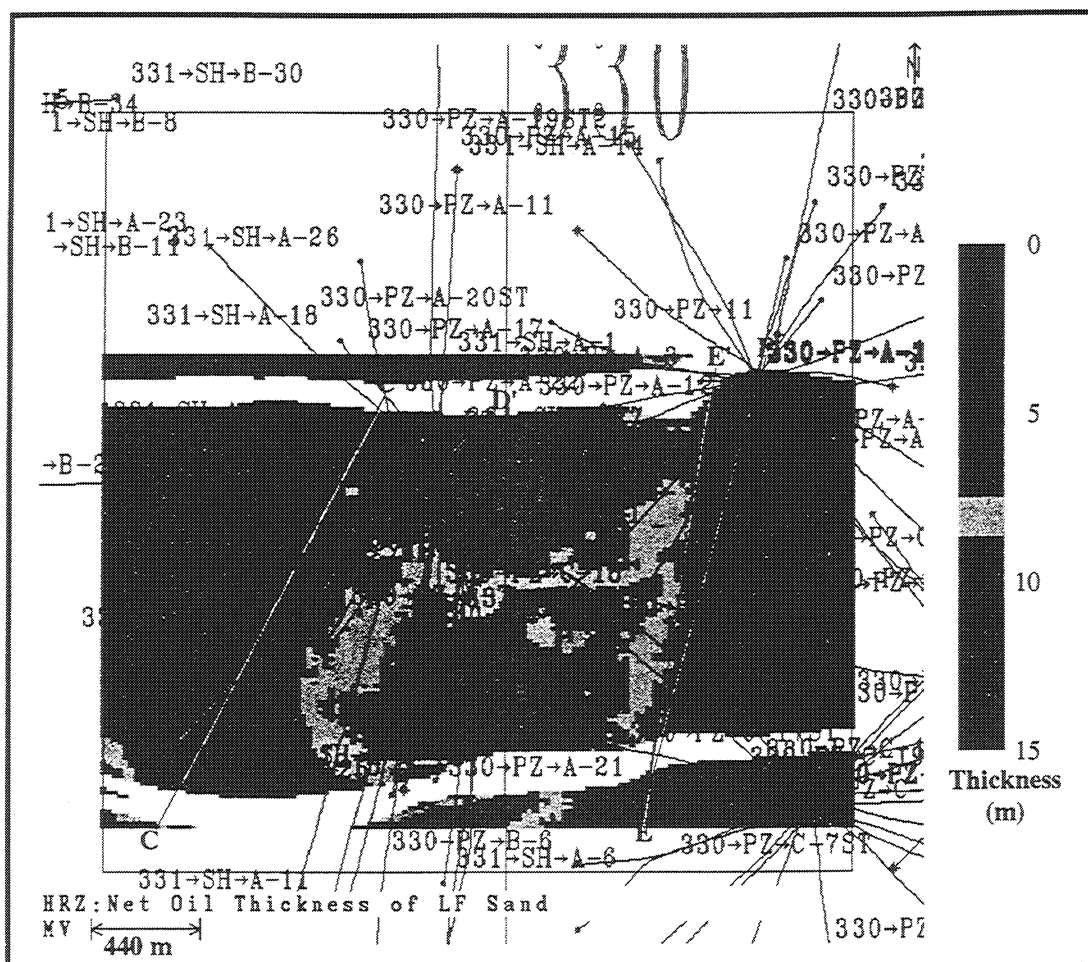


Figure 4.35. The net oil thickness map of the LF reservoir in the fault block B is calculated using the isopach map times the average effective oil saturation factor (Figure 4.33) within the LF interval.

Task Three - Field Demonstration Experiment

Roger N. Anderson - Task Manager

OBJECTIVE:

The objective of task three was to drill one well extension to test the Dynamic Enhanced Recovery Technologies objectives of this project. In November and December, 1993, we drilled into the fault zone in Eugene Island Block 330 (A20-ST) and performed the following experiments: whole coring, wireline logging, sidewall coring, formation pressure tests, stress tests, completion with frac-pack, flow test, and pressure transient test.

SUMMARY:

3.1 Environmental Assessment: Sub-task 3.1 is completed and was discussed in 10/15/93 technical quarterly report.

3.2 Field Demonstration Well: Sub-task 3.2 is completed and was discussed in 1/15/94 technical quarterly report. Technology transfer of the field demonstration experiment data and results are discussed in Task 7 of this report. The declination of the Columbia funding supplement request by the Pittsburgh office has caused Pennzoil and partners to absorb the added expenses of the Pathfinder well tests. because the contract was represented as a "Cost-Reimbursement" contract by DOE, and because the actual costs of the Field Demonstration Experiment were within 3 % of the budgeted estimate, the oil companies were expecting DOE to pay the overage. The declination has resulted in Pennzoil writing explicitly in the contract for continued support of the 4-D seismic monitoring Joint Industry Consortium that no Federal funds will be sought in the future by the consortium.

3.3 Interpretation of Results of Well Experiments: The A-20ST "Pathfinder" well was drilled by Pennzoil Exploration and Production Co., on behalf of partners Exxon, Mobil and Cockrell, into the OI-4 reservoir just above the "Red" growth fault zone that forms the northern boundary of the Eugene Island 330 minibasin. The well was then extended across the fault zone and into the footwall with DOE funding. The GBRN Field Demonstration Project consisted of three phases: whole coring, extensive logging, and stress and production testing in the Pathfinder extension. Measurements were made to determine in-situ conditions within and surrounding the fault zone and to test the hypothesis that hydrocarbons could be produced from a fault zone.

We found and sampled oil and gas from silty shales within the fault zone and discovered that the oils have similar chemistry to those being produced from the reservoirs directly above the fault zone. Whole coring revealed that faulting and fracturing extended at least 350 feet into the shales of the upthrown block. Many of the faults and fractures contained oil. Hydrocarbons would not flow at economically viable rates during drill-stem tests. The larger the drawdown pressure applied across the perforations, the lower the permeability of the fault zone became.

Where the A-20ST crossed the fault zone, the horizontal closure stress was found to be 500 psi greater than the fluid pressure. An increase in the pore pressure of 500 psi was then found to induce significant permeability within the fault zone.

A related well, the A-10ST, was drilled into the fault zone in EI 330 in October, 1993, in anticipation of the Pathfinder well, completely with industry funds. In contrast to the "tight" fault encountered in the Pathfinder well, fluids flowed strongly when the fault zone was penetrated by the shallower A-10ST well. Fluid flow within the high-pressured fault zone was sufficient to cause differential sticking and the loss of two bottom-hole assemblies in the well. A pulsed-neutron, Thermal Decay Time log run through the stuck drillpipe recorded increased gamma ray radiation from oxygen activation indicating that water was flowing at rates of up to 700 barrels/day within the fault zone.

Introduction

The Global Basins Research Network (GBRN) is an electronic "Internet" organization that was formed to solve two very specific fluid flow problems: 1) the identification of expulsion mechanisms by which hydrocarbons migrate up fault zones from deep, geopressured strata into shallower reservoirs, and 2) the imaging of these hydrocarbon migration pathways so that wells can be drilled into these "streams" located within fault zones. As part of a GBRN/Department of Energy/oil industry cost-sharing project, we are experimenting with methodologies by which hydrocarbons can be economically produced from these natural conduits into deeper, as yet unexploited reservoirs. These deep reservoirs are targets of the sub-salt play currently receiving so much attention in the exploration community.

The specific hypothesis we are testing is that fluid pressures periodically exceed rock failure strength within the geopressured zone, reopening fault zones which become transient conduits for fluids to rapidly exit the pressure chambers. The shallower reservoirs are filled by hydrocarbons that have migrated up these fault zones, but the timing, migration pathways, and rates of migration remain poorly understood. To address this hypothesis, we integrated a wide variety of geophysical, geochemical, geological and reservoir engineering technologies in order to image these ongoing fluid-flow processes in the Eugene Island 330 Field (Figure I.1), and to site the test wells in Block 330 itself. In cooperation with the operator Pennzoil and partners Exxon, Mobil and Cockrell, we drilled, logged, sampled, Frac-Packed, and drill-stem tested a 700 foot extension of a development well into the deep fault zone (the A-20ST) in November-December, 1993, and logged an earlier extension of the A-10ST into the fault zone at a shallower level (Figure I.2).

The Eugene Island 330 Field

We chose the Eugene Island 330 field for our oil migration study because it is the largest Pleistocene oil field in the world, it is geologically well-characterized, and most importantly, it shows a variety of indications of geologically recent hydrocarbon migration (Holland et al, 1990 and Whelan et al, 1994). The Eugene Island 330 Field is a typical Gulf of Mexico mini-basin (Alexander and Flemings, 1994) (Figure I.2). Structurally, a regional growth-fault system (the "Red Fault Zone") forms the northern boundary of alternating sequences of Plio-Pleistocene sands and shales overlying deep-water turbidites and basin-floor fan deposits from the ancestral Mississippi River delta. As the Red Fault Zone accommodated extension toward the deep-water Gulf of Mexico, the sediments in the depobasin formed rollover anticlines that are now filled with oil and gas. Extension was caused by withdrawal to the south of an extensive salt sill initially present near the surface of the mini-basin from 6 to at least 2.2 Ma (Rowan, Weimer and Flemings, 1994). A counter-regional, down-to-the-north fault zone forms the southern boundary of the mini-basin. A thick shale sequence separates the shallow-water shelf sands from geopressured, deep-water deposits (Alexander and Flemings, 1994).

Remnant salt feeder stocks and remobilized salt diapirs bound the mini-basin, exclusively upthrown to the bounding fault system (Figure I.2). The deep turbidites are still geopressed (He and Anderson, 1994), even after the removal of the impermeable salt seal, because high sedimentation rates combined with the thick, deepwater shale accumulations in the Pliocene resulted in rapid burial and permeabilities too low for the excess pore fluids to escape (Mello, et al, 1994).

Migration of hydrocarbons is occurring today in the Eugene Island 330 Field (Anderson, et al, 1993). Seeps are active at the sea floor outcrop of the Red Fault Zone system. Oil and gas are being produced in reservoirs as young as 400,000-years-old beneath these seeps. Geochemical monitoring over the last twenty years has recorded temporal changes in the composition of the oils being produced from the shallow reservoirs; these changes may reflect recent injection of wet gas and gasolines (Whelan, et al, 1994). Also, biodegraded oils have been replaced by less biodegraded oils over time in the shallowest reservoirs.

Locations of the A-20ST Pathfinder and A-10ST Wells

Migration pathways of hydrocarbons can be imaged within the 3-D seismic surveys in the Eugene Island 330 Field by mapping high amplitude connectivity throughout the volume (Anderson, et al, 1993). The northern growth fault system is particularly involved in the migration of hydrocarbons, although the conduits are convoluted and more like 3-D "streams" than uniform, permeable, 2-D fault zone flow planes (see Figure I.6, below).

The GBRN focused on a strategy of testing the fault zone play concept by deepening appropriate development wells being drilled during the normal ongoing operations of the Eugene Island 330 Field. This strategy, though far more economical than drilling dedicated research wells, places practical limits to the targets available to the GBRN. In the A-20ST Pathfinder well, we penetrated the tightest, most shale-prone portion of the fault zone just beneath the deepest known reservoirs trapped against the Red Fault Zone in EI 330 (the OI-4 and 5 sands) (Figure I.3). In this location, the stress field was predicted to be the most constrictive to fluid migration (Flemings, et al, 1994), and by testing the fluid flow properties here, we could better understand the migration process itself.

In addition, we were able to participate in the logging of the A-10ST well that Pennzoil and partners drilled into the fault zone to the southeast of the A-20ST (Figure I.2). At this location, the fault zone was intersected at a shallower depth, and the seismic signature was of two splays 180 feet apart with a high seismic amplitude anomaly trapped inbetween.

The Field Demonstration Experiments in the A-20 ST Pathfinder Well
Pennzoil and partners primary economic target in the A-20ST well was the OI-4 sand located between the "D" and "A" fault splays of the Red Fault Zone (Figure I.3). The well was spudded on November 2, 1993, and Pennzoil, as operator, drilled to 7035' Total Vertical Depth (TVD) and set 9 5/8" casing. They then drilled-out and penetrated a section of the OI-4 pay that was 50 feet thicker than the downdip section of this sand that is currently on-production in the A-23 well. Pennzoil and partners agreed to log-while-drilling the well extension from the 9 5/8" casing point through their OI-4 and OI-5 pay zones to the point where the GBRN began to core the fault zone. The GBRN/DOE extension was begun on November 23, at 7300' TVD, and ended at 8075' TVD on December 25, 1993. Experiments were carried out in three stages.

Stage I: Whole Coring

We cored the next 350 feet of the well below the OI-5 pay, and though the upper 60 feet of the cored interval was dominated by down-to-the-southwest, slickensided faults, the major deformation zone imaged by the logging tools (see below) was just above this interval. We used an experimental anti-whirl PDC bit developed by Baker Hughes Inteq. and Amoco Production Co. that had not yet been used in a well. We coupled this new coring bit with a full-closure core catcher, and a water-based polymer mud containing a 3% synthetic, non-fluorescing oil additive developed by M-I Drilling Fluids Co. to prevent adhesion of clays to the bit (balling). A 60' core barrel with a 4" aluminum inner tube was chosen over the usual 30' barrel normally used in the Gulf. We obtained a total of 343' of 4 1/4" diameter core from an attempted interval thickness of 360', a 95% recovery rate. The cutting rates averaged better than 70'/hour and at times exceeded 150'/hour in these "gumbo" shales, and the entire coring operation took less than three days. The core was split into alternating 3' chilled and frozen sections, and is available for further study at the GBRN Core Repository at the Pennsylvania State University.

The cored interval was from 7330' to 7680'TVD, and overall, the rock consisted primarily of silty shale with minor sand beds. The Formation MicroImager (FMI) log indicates the cored interval begins just below the deformation zone mapped as the Red Fault Zone, and extends across a second, minor fault not imaged by the seismic surveys. Beds in the cored interval dip between 20 and 30 degrees to the north-northwest. The core sampled three primary structural domains. An upper faulted zone extends from 7330' to 7490', and containing slickensided faults at moderate to high angles. Many are filled with drilling mud, indicating fracture permeability. A middle zone from 7490' to 7560' is relatively unfaulted, and consists of silty shale, shaly silt, and thin, yellow fluorescing sand beds, the thickest measuring 9". Much of this interval corresponds with a slight increase in resistivity, and may be low resistivity pay. Finally, a lower fault zone was encountered from 7560' to 7680'TVD, consisting of silty shales with gouge zones that intersect the well at high angles. Slickensided faults are also present, and dip at a variety of angles. Much more fluorescence is apparent in both low- and high-angle structures in the lower fault than in the upper fault zone (Figure I.4). The lowermost faulted zone in the core may reflect deformation associated with a fault beneath the Red Fault Zone.

The planning and execution of the coring stage of the project was a collaborative effort involving not only the GBRN scientists, but also many supporting oil and service companies, and the success was directly attributable to this collaboration. For example, an Exxon coring specialist, Mike Wooten, oversaw the on-site coring effort while Texaco, Chevron, Conoco, and M-I Drilling Fluids provided mud composition advice, CoreLabs processed and archived the core, a Chevron scientist collected gases, Shell and Exxon provided CAT-scanning of the core and other analyses, GERG/ Texas A&M and Woods Hole, the organic geochemistry, Cornell, the structural and fracture mapping, Penn State, the acoustic correlation with seismic, Schlumberger, major element chemistry, the University of Michigan and Michigan Tech, the pore water chemistry of wells near the A-20ST, the University of Rochester, age dating of the pore fluids, Pennzoil, the paleontology and biostratigraphy, Woods Hole and Chevron, Mobil, Exxon and the University of Virginia, gas source and maturity analyses.

Stage II: Wireline Logging

The GBRN then logged from TD at 8010' to casing at 7046' TVD with a full suite of acoustic, nuclear and electrical "imaging" logs from Schlumberger to obtain as complete a picture of the fault zone as possible. The acoustic measurements made in the wellbore were from the dipole sonic log, which recorded compressional, shear, and stoneley waveforms throughout the open-hole portion of the well. The fault zone was

distinguished by a marked decrease in sonic velocities from the downthrown (shallower) to the upthrown (deeper) blocks. While compressional velocities decreased by 10% across the fault zone, the shear velocity decreased by more than 20% (Figure I.5). The dipole shear source excited a shear wave only slightly faster than the stoneley wave. Fracturing, observed in the core, is thought to be the cause of the low shear velocities, and extensive acoustic measurements are planned at in situ conditions for the core samples.

An experimental nuclear geochemical logging tool developed by Schlumberger was then lowered across the fault zone. Using a controlled source of neutrons, this logging tool measures the elemental composition of the rock by neutron activation, in real time. The distribution of elemental abundances into a normative mineralogy model verifies that the rocks both above and below the fault zone are shales (quartz contents are less than 20% and clay mineral contents are greater than 40% in a rock with 25% porosity) (Figure I.5). The fault zone itself appears to be somewhat more silty with quartz contents of slightly more than 25%. This logging tool also recorded neutron porosity and gamma ray density.

The electrical logs obtained were array induction and Formation MicroImager (FMI); the latter measures resistivity variations with resolution down to mm-scale along four orthogonal swaths along the wellbore wall. A fluxgate magnetometer orients the four pads relative to true north. Possible pay was indicated within the Red Fault Zone by the induction log, and the FMI showed that a considerable part of the OI-5 pay, thought to be above the fault zone, was in fact, significantly disrupted by movement downthrown to the fault zone. As indicated by dip "tadpoles" (Figure I.3), the OI-4 sand has normal, 10-20 degree regional dips to the north. Below this, the OI-5 dips first steeply to the west, then steeply to the east, before the fault zone top is encountered at 7270' TVD. The fault zone is defined by 40' of southwest-dipping faults imaged by the FMI. Below 7310', footwall deformation is seen to 7350', below which 20-30 degree dips to the north are the norm. No further southwest-dipping fractures are imaged by the FMI until the small fault zone, seen in the lower two cores, is encountered at 7560-7680' TVD. However, the core revealed that many such small faults exist throughout the footwall section.

In fact, the first core was repeatedly cut by down-to-the-southwest, slickensided faults that were too small to be imaged by the FMI. The FMI revealed that the lower half of the OI-5 target was within the fault zone itself, and consequently, we had begun our coring program about 10' BELOW the deepest down-to-the-southwest fracture within the fault zone imaged by the FMI.

From the bottom of the Red Fault Zone upward (Figure I.6), the FMI revealed a zone of interbedded shales and silts with gentle dip, but cut by southwest dipping faults with increasingly more throw until a distinct surface dipping 55 degrees to the southwest was mapped at 7280' TVD. Above this discontinuity, highly deformed silty shale is found, cut by and rotated along an antithetic fault. Three large vertical fractures were mapped above this deformation zone, and each was found to have high electrical resistivity, possibly indicative of hydrocarbon charge. These natural fractures strike in the orientation of the fault zone, and may connect the fault zone hydraulically with the overlying OI-4 and 5 pay zones in the downthrown block (Figure 1.7). The composition of the oils recovered from the fault zone are identical to the OI-4 oils currently being produced in the A-23 well (see below).

The modular dynamics formation tester (MDT) was next run in the well. We intended to use this tool to obtain at least 12 pressures throughout the well extension, but because of the hole conditions, the MDT was stuck obtaining the first pressure measurement. Pennzoil then acquired 75 sidewall cores from 7157'-7661' TVD in three coring runs in the hole, including valuable samples from within the major deformation zone of the fault zone.

Stage III: Stress and Production Testing

On December 2, 1993, we ran a 7 5/8" liner into the well extension. As a result of an incomplete cement job, we were required to squeeze cement through casing into the intervals directly above and below our test zone to insure isolation. Stress tests were performed below the fault at 7380-7384', within the fault at 7270-7310', and above the fault at 7240-7244' to obtain pore pressures and tectonic stress magnitude variations across the fault zone.

The difference between the minimum compressional stress (S3) and the fluid pressure (P) controls the hydraulic conductivity of the fault zone. As the fluid pressure converges upon the minimum horizontal stress, significant fracture permeability may be created. Our stress and pore pressure experiments allowed us to measure these in situ conditions above, below, and within the fault zone (Figure I.7). We measured pore pressures that were 0.8 of the vertical stress (S1) above and 0.95 of S1 below the fault zone. Direct measurements of the stress field using hydraulic fracturing experiments (see Part IV) show that fluid pressures of an additional 500 psi would be required to reopen fracture permeability and allow significant fluid flow within this segment of the fault zone.

It is also interesting to note that the maximum hydrocarbon columns in the OI reservoirs result in buoyant pressures of approximately 500 psi. Thus, it is possible that these large OI columns are in dynamic equilibrium with the closure stresses along the fault. This, in turn, implies that any new hydrocarbons migrating up the fault from depth would be able to naturally hydrofracture into lower pressured reservoirs. We believe the natural vertical fractures imaged just above the fault zone by the FMI log reflect this migration pathway (Figure I.7). A fundamental question we continue to address is whether this process of ongoing vertical migration is presently occurring.

Drill-Stem Tests in the Fault Zone

We then perforated, frac-packed and flow tested a 40' interval within the fault zone. On December 14, 1993, the tubing conveyed perforating gun was fired at 7270-7310'. Since only a trickle of flow-back was seen at the surface, low permeability of the formation was assumed. We then hydraulically fractured the perforated interval using Dowell's new telemetry capability in which the test was monitored in real-time in the Dowell offices in Lafayette, Louisiana. The procedures followed were: a) an acid job was performed to clean the perforations and formation near the wellbore, b) a mini-fracture was created using stepped-rate injection into the formation, and several constant rate stress tests followed (essential for the final design of the frac-pack), then c) the well was shut-in to retrieve the downhole data recorded on the Schlumberger DataLink system. The fracture design was then finalized, and the hydraulic fracture completed. However, the fracture pumps stalled-out at the beginning of the final injection stage, preventing the downhole completion of the fracture job. Although a tip screen-out was thought to be observed at the surface, later retrieval of the downhole DataLink records showed that the increased surface pressure was from frictional loss and not from fracture completion in the formation. Although the highest permeability recorded after the fracture was only 120 md, fluids began immediately to flow to the surface at a rate of 2 bbl/hr at 400 psi against a 16.3 lb/gal zinc bromide completion fluid. Then the drill-stem testing assembly was tripped into the hole to flow test the fault zone interval. The flow test began with flow to the surface at a rate of 8 bbl/hr, but within two hours, the rate had dropped to less than 2 bbl/hr. Pennzoil then used a coiled tubing unit to "jet-in" the well with nitrogen. Once this procedure began, the flow rate increased to 8 bbl/hr again but would not sustain itself, dropping within 24 hours to zero net flow. We did, however, recover several barrels of oil at the surface; hydrocarbons that came from

within the fault zone. Fifteen gallons of this fault zone oil were collected for geochemical analysis, and samples are available through GERG/TAMU or WHOI.

As the nitrogen jetting drew higher and higher differential pressures against the formation, the well flowed at smaller and smaller rates, until it completely stopped at more than 5000 psi of drawdown differential. In other words, the more underbalanced we were, the less the formation flowed (Figure I.8). At the end of each drawdown experiment, we shut-in the well to measure the permeability of the formation from the pressure rebound.

The fracture permeability in the fault zone is strongly pressure dependent (Figure I.8), and as we drew-down the pressure in the wellbore, the fracture network supplying the permeability within the fault zone closed tighter and tighter. This observation was verified on the rig when we shut down the jetting, re-equilibrated the wellbore, then pumped fluid into the formation through the perforations to verify that they were not plugged-off. The fault zone took fluid easily at about 500 psi over ambient fluid pressures.

Pennzoil then plugged the fault zone interval on December 25, 1993, and will complete in their economic target, the OI-4 formation in 1994.

The Logging of the A-10ST Well

In preparation for the A-20ST well, and to examine targets on the upthrown side of the Red Fault, Pennzoil and partners extended the A10-ST well through the fault zone in October, 1993. The A-10ST well is located approximately 1300 feet shallower and 1000 feet to the southeast from the A-20ST (Figure I.2).

In the A-10ST well, the first splay of fault zone was encountered at 7500' MD (6000 ft TVD), (Figure I.9), and a clear fault break was observed by the mudlogger. Significant shows of oil and gas (2000 units, with C1 through C4 components present) soon followed. One of the Show Reports is shown in Figure I.10. The volumes of oil that flowed into the mud pits were estimated by the mud engineer to be 1% of 730 bbl of 14.2 lb/gal mud being cut by gas to 12.5 lb/gal in one 12 hour interval, and 2% of 530 bbl of 15.8 lb/gal mud cut to 13.5 lb/gal in 14 hours of circulation. An oil chromatogram of fault zone oil recovered from the mud pits was measured at GERG/TAMU, and it shows that the oil is unbiodegraded and does not have the light n-alkanes or gasolines stripped-off (as do the Pathfinder oils, see the Geochemistry Section, below). The A-10ST oils are as complete, chromatographically, as any found in the producing reservoirs of EI-330.

The drillpipe became stuck as the second splay was being encountered 180 feet into the fault zone. Pennzoil backed off and whipstocked, re-entering the fault zone with significantly heavier mud (16.2 lb/gal). Again, oil and gas (3000 units) shows were reported at the surface, this time against mud weights up to 16.5 lb/gal mud.

An open hole Array Induction resistivity log was then attempted, but was stopped by a borehole bridge 50 feet beneath the first splay of the fault zone. However, a clear fault zone break was observed at 7500' MD, (6010' TVD), in the Gamma Ray and Spontaneous Potential logs, with an oil show in shaley sand indicated by the resistivity log at the top of the fault zone (Figure I.11).

While trying to clear this bridge, the drillpipe became stuck again at 7650' MD (6200' TVD), within 8 feet of the previous event. We believe the sharp lithologic break encountered at 7500' MD (6010' TVD) is the first splay of the fault zone, with porous and permeable, hydrostatically pressured IC sands of the downthrown block juxtaposed against low permeability shale or shale gouge. The resistivity log indicates high resistivity in the shale just below the fault break (Figure I.11). Beneath this first splay, a slightly sandier zone was encountered at 7550-7570' MD (6060-6080' TVD). The second splay of the fault zone could be indicated by the low Sigma and low porosity logged from 7630-7660' MD (6140 to 6170' TVD).

A dual-burst, Thermal Decay Time (TDT) log was then run through the stuck drillpipe to TD. Lithologies determined from gamma ray and neutron capture cross-section (Sigma) measurements indicate that the fault zone consists of shaly sand interbedded with shale streaks near the top and bottom of the fault zone. Gas (Neutron Porosity, NPHI <10% porosity) and possible oil shows were indicated by the minima in the Sigma capture cross-section log at 7550-7570' MD (6060'-6080' TVD) and 7630-7660' MD (6140-6170' TVD) (Figure 1.11). A water-wet, shaly sand was found at the base of this upper show at the center of the fault zone, with possible gas and oil shows measured both above and below. Gas continued to cut the mud from 16 to 13 lb/gal while the pipe was stuck. The oil-finding capability of the thru-pipe TDT was then verified by successfully logging the IC pay shallower in the well -- thru pipe, mud, casing, and cement.

Transient Fluid Flow from within the Fault Zone

In the most significant finding from the A-10ST, active, transient, fluid flow was recorded during four repeated TDT logging runs and subsequent station measurements within the fault zone (Figure 1.11). Water flow was detected by means of neutron activation of oxygen nuclei to produce the radioactive isotope $^{16}\text{Nitrogen}$ (Schnorr, 1993). The use of the oxygen activation technique to measure water flow in boreholes has been known since 1967 (Wichmann, et al, 1967), and an impulse-activation technique for the TDT log has been applied successfully in Alaska (Scott, et al, 1993, McKeon, et al, 1993). Water contains abundant oxygen atoms, but no oxygen atoms reside within the structure of hydrocarbons, so any possible oil/gas mix traveling with the flowing water was not determined by the following observations.

Gamma ray counts recorded by the natural gamma ray logging tool (NGT) in the TDT were routine during the lowering of the logging tool to the bottom of the well. Shales were emitting about 80 api units of natural radiation, as expected, and sands were recorded at about 60 api units. Then, at the bottom of the well, the neutron generator was activated and began to pulse neutrons into the formation as the logging tool was pulled up the hole at 12 feet per minute. A 10 millisecond burst of 10^8 neutrons was followed by a 100 millisecond quiescence as the photoelectric accumulator was counting gamma rays returning to the logging tool. The total capture cross-section (Sigma) of the formation is the intended measurement of the TDT tool.

As the TDT was logging Pass 1 across the fault zone, gamma ray counts quickly jumped to >200 api units above background, and steadily increased until at 7580' MD (6095' TVD), a maximum radiation level of 290 api units was recorded--far in excess of the natural radiation level of any sedimentary rock. The gamma ray count then slowly decreased to 200 api units at 6030' TVD (7520' MD), then dropped to 60 api units at 7470' MD (5980' TVD), and remained near these background values that had been recorded on the trip into the hole for the rest of Pass 1 (Figure 1.11). The minitron was then turned off, and the TDT logging tool lowered back to the bottom of the well. Normal gamma ray counts of 60-80 api units were recorded again on the trip back to the bottom of the hole with the neutron source turned off. Passes 2 and 3 repeated the cycle of logging up the hole with the pulsed neutron source activated. Pass 2 recorded the highest gamma ray counts from the bottom of the hole to the most radioactive depth at 7580' MD (6095' TVD), but then the count rate dropped more precipitously from there to the top of the fault zone at 7500' MD (6010' TVD), where this time normal gamma ray counts were recorded by the TDT even with the minitron still pulsing neutrons. Pass 3 resulted in gamma ray counts that fall between those of Passes 1 and 2. Pass 4 was then recorded without turning the neutron source on, and only normal gamma ray counts were recorded by the tool. Clearly, some transient fluid flow phenomenon was being observed (Figure 1.11).

We believe this to be the first recorded case in which the TDT log measured water flow by oxygen activation while the tool was moving upward during a logging operation. The previous water flow studies reported in the literature (c.f., McKeon, et al, 1991, Scott, et al, 1993, Schnoor, 1993) all utilized the tool in stationary locations within the wellbore.

In our case, the TDT was activating oxygen nuclei within flowing water, sending radioactive ^{16}N isotopes streaming uphole. The water must have been flowing at much faster rates than the logging tool was moving (12-17 ft/min) in order for the gamma rays emitted by the decay of the ^{16}N isotopes, which have a half-life of 7.13 seconds, to overtake and be recorded by the gamma ray detector which was 14.5 feet above the neutron source (McKeon, et al, 1991, Scott, et al, 1993, Schnoor, 1993) (Figure I.11).

The flux of gamma rays counted by the detector within the TDT logging tool quantitatively recorded the variations in water flow within the fault zone between the three activation passes logged in the well. That is, the number of oxygen nuclei streaming past the detector during the passes varied, and was measured directly by the TDT log.

As shown by McKeon, et al, 1991, fast neutrons generated by the neutron generator have energies of approximately 14 MeV, high enough to activate oxygen nuclei to produce radioactive ^{16}N isotopes. ^{16}N decays by beta emission, emitting a 6.13 MeV gamma ray in most cases (69% of the time). Because of its high energy, the 6.13 MeV gamma rays penetrate several inches of borehole fluid, casing, drillpipe, and cement. However, these gamma rays are not ordinarily recorded by the natural gamma ray detector because it is 14.5 feet above the minitron source, and logging is done while moving the tool uphole at 12-17 feet/minute. Water must be flowing at faster than the logging speed for the gamma ray detector to record the gamma rays emitted by this decay of ^{16}N .

McKeon, et al, (1991) report the development of a Monte Carlo neutron transport code that can be used to estimate the velocity and volume of the water flowing outside the drillpipe. Assumptions are that the 1 11/16" TDT logging tool is centered in the 5 1/2", 15.5 lbm/ft drillpipe, and stationary. The formation is assumed to be 30 porosity units of sandstone with water in the pore spaces. The flow channel is a 2" thick annulus immediately outside the drillpipe.

The total number of activated oxygen nuclei passing the detector is proportional to a scaling factor and Avogadro's Number (there are 6.03×10^{23} oxygen nuclei in each gram molecular weight of water). Thus, the measurement appears, at first glance, to be independent of the flow velocity. However, the time that each activated nucleus remains in the vicinity of the detector is inversely proportional to the flow velocity, and since the activated ^{16}N signal decays exponentially after activation and before gamma rays reach the detector, the flow velocity can be estimated from the gamma ray detector count rate. The specific geometry of the flow pathway itself is irrelevant to the velocity calculation. The gamma ray count rate above background (C_t) is proportional to water flow velocity (v) by $e^{(-\lambda L/v)} / v$, where λ is the ^{16}N decay constant, and L is the distance from source to counter.

Thirteen station measurements were made after pass 4, and after a 17.5 lb/gal "kill-slug" was circulated to the bottom of the hole (Table 1). In this mode, the TDT tool is held stationary in the wellbore while the minitron bursts neutrons for 10 msec, then passively counts for 100 msec, then the cycle is repeated many times (see Schnoor, 1993). Much slower flow rates were encountered overall after the kill-slug, but "bursts" of radioactive fluid were periodically encountered in 4 stations adjacent to the fault top. In these bursts, radioactivity first increases dramatically, then decays exponentially as the ^{16}N flu is dissipated across the stationary detector (Figure I.12).

These velocity-versus-gamma-ray-count ratios were used to approximate the flow velocities logged by the moving TDT tool (Table 1), although the gamma ray counts

recorded by the moving tool were considerably higher than those recorded during the stations (because of the different mud weights in the wellbore). The assumption made is that the fluid flow was all in the same direction as the tool was moving. In fact, the tool velocity was added to the calculated flow velocity (Table 1). Variations in water flow velocities are predicted for the gamma ray variations logged by the TDT to have been up to 160 ft/minute (Figure I.13).

Flow volumes are somewhat more complicated, because an estimate of the open annulus is required. However, we can estimate the volume flux if we assume the geometry used in the McKeon, et al (1991) Monte Carlo technique. The flow rate (Q) is again given by McKeon, et al (1991):

$$Q = [Av^2e^{(L/v)/aSN}] C(t)$$

where A is Avogadro's Number times a scaling factor, a is the geometric factor, and SN is the total neutron output of the minitron. Since we were stuck, the assumed annulus of 2" outside the drillpipe is obviously incorrect somewhere along the wellbore. The logging service provided these calculations for the station measurements (Table 1), and we can estimate the variations in volume flux by again extrapolating from the station ratios to the logging values. Volume fluxes of up to 225 bbl/day are predicted for flow in the fault zone of the A-10ST well (Figure I.13).

The variations in volume flux up the hole versus depth are interesting (Figure I.13). The flux increases from about 150 bbl/day at TD to a peak at 7580' MD (6095' TVD). The maximum flow was encountered in all three activation passes at this depth, which is also the minimum Sigma "peak" within the fault zone. Flow up the wellbore then steadily decreases between there and the top boundary of the fault zone. Very little flow is observed from the fault zone into the hydrostatically pressured IC sands above the fault zone (less than 50 bbl/day, Figure I.13). The differential sticking of the drillpipe seems likely to have occurred where fluid was exiting the wellbore as the flow rate decreased within the wellbore from 7500' to 7680' MD (6010' to 6200' TVD). Variations in the water flow were monitored by three separate repeat logging runs, and each time the maximum upward flow rate was encountered where the minimum neutron capture cross-section (Sigma) was found in the fault zone. However, the flow rate was variable, with the maximum flux encountered during the first pass (Figure I.13), but the minimum measured by the second pass. By the time of the third pass, the flow rate had increased again (Figure I.11).

An 18 lb/gal kill slug was then pumped downhole, and verification that flow had stopped was made by active TDT logging that reproduced the normal gamma ray values recorded from the fault zone and by several stations. The "activation after kill" gamma ray log shown in Figure I.11. The drillpipe was then severed, and the bottom of the well cemented-off.

In summary, what we believe happened in the bottom of the A-10ST well is that, after crossing the first fault splay a very large pressure increase was encountered (8.8 to 16 lb/gal equivalent). Then as the well penetrated deeper into the second bounding splay of the fault zone, strong fluid flow began with water entering the wellbore from below the fault zone sand and moving uphole to exit the wellbore between the sand and the top-bounding fault splay. Interestingly, little of the flow appears to have gone into the overlying hydropressed sands, but instead was confined to the interval between the fault splays. This fault zone is clearly capable of producing fluids at high rates, especially if it were part of an interconnected fluid migration network.

Geochemistry of Hydrocarbons Recovered from EI 330 Reservoirs and the Red Fault Zone

All of the biomarker and aromatic hydrocarbon maturation parameters measured to date in the Eugene Island 330 reservoir oils are consistent with these oils having been

generated and expelled approximately from the beginning to the middle of the oil generation window, equivalent to a vitrinite reflectance, R_o , of about 0.75 to 0.8%, depending on the exact type of kerogen present. However, gases from the same GOR mixes in wells have much higher maturity (1.1% to 1.2% R_o , equivalent vitrinite reflectances, Whelan et al, 1994), suggesting a much deeper source for the gases. The biomarker maturation values from the A-20ST Pathfinder well's fault zone oils are also very constant and the same as those for the deeper "standard" EI reservoir oils from the KE, LF, MG, and OI reservoirs.

The ratio of $(nC_3 + nC_4) / nC_{17}$ was used by Whelan et al. (1994) to represent ratios of wet gas to oil. High wet gas to oil ratios may be diagnostic of recent hydrocarbon reinjection into reservoirs in EI 330, since the lighter hydrocarbons are also more prone to escape from a reservoir undergoing leakage. In addition, in any reservoir undergoing active biodegradation which produces "humpane" type baselines, such as those observed for the GA and HB reservoirs, it would be expected that nC_3 and nC_4 should also be absent. These low molecular weight compounds are easily and preferentially lost by biodegradation, as well as by a number of other processes, including water washing and evaporative fractionation (Thompson, 1983; 1987; 1988). Therefore, high $(nC_3+nC_4)/nC_{17}$ ratios observed in the GA and HB oils of Eugene Island 330 are consistent with recent active oil migration and/or remigration.

Changes are noticeable over time as well, particularly in the ratios of light (C_3 - C_5) to heavier (C_7 - C_8) components among samples taken in 1984, 1988, and 1992, with an ever higher proportion of lighter components being present in 1994. Ratios of B (toluene to n-heptane), F (n-heptane to methylcyclohexane), H (a maturity ratio based on the ratio n-heptane to the sum of branched and cyclo to n-alkanes), and I (ratio of branched C_7 compounds to the sum of cyclic C_7 dimethylcyclopentanes) also show systematic changes over the 6 year period indicative of changes in reservoir hydrocarbon composition and possibly of dynamic injection of hydrocarbons from deeper sources into the reservoirs over this interval time, (Whelan et al, 1994).

The whole oil chromatograms of the A-20ST Pathfinder fault zone oils (Fig I.13) are virtually identical to those of the deeper KE through OI oils recovered from other "A" platform wells, and particularly the A-23 oils from the nearest reservoir "updip" to the fault zone, the OI-4. However, the Pathfinder oils from the fault zone show very low wet gas to oil ratios, suggesting no recent hydrocarbon injection of light hydrocarbons in this particular fault zone interval. In contrast, the A-10ST oils (Figure I.13) are from an interval of the fault zone with higher seismic amplitudes than are present in the Pathfinder fault zone penetration, implying higher gas contents. Indeed, analyses of the A-10ST oils show them to have higher wet gas to oil ratios than do the Pathfinder oils. Perhaps the A-10ST oils are closer to a light hydrocarbon migration pathway within the fault zone than the A-20ST Pathfinder oils, or the Pathfinder oils have been stationary for long enough to lose their light components (Figure I.13).

During drilling of the A-20ST Pathfinder well, gas samples were obtained by Martin Schoell, Chevron, using a new gas sampler technology. Initial molecular and isotopic compositions for these gases (Figure I.14) show that the gases from the cored interval beneath the fault zone contain a progressively higher biogenic versus thermogenic component with increasing depth. The biogenic gas represents that generated in organic rich sediments of the footwall at much shallower depth which was then carried down and buried. Diffusive mixing is indicated, with more thermogenic gas entering the sediments through the fault zone at the top of the cored interval and mixing with biogenic gases in the shales from the upthrown block. Thus, the $\delta^{13}C$ methane values for the Pathfinder well show that no significant fluid flow is occurring from the high pressure foot wall to the lower pressure reservoirs of the hanging wall sediments. Also, the source of the thermogenic gases found within the fault zone appears to be from deeper along the fault zone trajectory.

How to Produce Oil and Gas from a Fault Zone Conduit

Our current working hypothesis for hydrocarbon migration in the EI 330 area is that deep in the geopressured turbidites, formation pressures periodically increase until fracture-reopening stresses are overcome in the fault zones that connect into these "chambers". At such times, large volumes of hydrocarbons are released rapidly in transient bursts up the fault zones towards the surface, and then the faults close back up. Put another way, with added pressure, oil is expelled up the fault zones, but then the very act of releasing the fluids drops the pressure and the faults become tight again. Over and over, the cycle repeats. Evidence from the Pathfinder well to support this hypothesis is that the fracture permeability within the fault zone is strongly pressure dependent. We have shown that oil and gas are present even in the tightest portion of the Red Fault Zone in Eugene Island 330, and that these would flow under fluid pressures 500 psi higher than those measured within the fault zone today. We have demonstrated that such pressurization increases the permeability of the fault zone to darcy values. However, we have also found that the fluid-release from such a pressurized fault zone immediately lowers the permeability by several orders-of-magnitude. In addition, the A-10ST well provides strong evidence that once fluid flow is established within the fault zone, transient behavior can be expected.

The GBRN/DOE Field Demonstration Experiments have provided tests of likely strategies for future production:

- 1) Locate wells into high permeability pathways within the fault zones that have high-seismic amplitudes,
- 2) change the angle of penetration from perpendicular to parallel to the fault zone in order to expose more surface area, such as drilling along a fault isolated sand lobe (such as the LF sand penetrated by the A-8ST well along the EI 330/338 boundary, see Anderson, et al, Part I). Such strategies are likely to be profitable, since they increase permeability by drilling higher seismic amplitudes and increase thickness by drilling along the plane of the fault zone.

We believe that technology transfer of the GBRN/DOE methodology of integrating geophysical and geochemical dynamics with the more traditional stratigraphic and structural techniques will lead to a more complete hydrocarbon-system view of the deep subsurface. In addition, these technologies lead to a new play concept that could help locate and exploit large volumes of deep, geopressured reserves not only in the Gulf of Mexico, but also in other sedimentary basins where hydrocarbons are currently migrating out of deep geopressured chambers, such as in Nigeria, the North Sea, Indonesia and the Caspian Sea.

Task Four - Reservoir Characterization
Peter Flemings - Task Manager

OBJECTIVE:

The purpose of this task was to integrate the geological and geophysical data to construct the minibasin and reservoir models in the SEI 330 Area in order to understand the hydrodynamics of the minibasins. The minibasins are analyzed through stratigraphic interpretation, salt analysis, pressure and temperature mapping. Temporal seismic amplitude analysis is to monitor the dynamic changes occurred in the reservoir.

SUMMARY:

This is the second and final annual report summarizing the completed research in the Reservoir Characterization Task. Detailed results are presented in Attachments 1 through 3. A summary of accomplishments is discussed below.

An outline of the individual tasks are provided below. Primary responsibility for tasks are shown in parentheses: PSU = Penn State University, CU = University of Colorado- Boulder, LDEO = Lamont-Doherty Earth Observatory. Completed tasks are indicated by a pound sign (#).

Task #	Name	Start	Finish	Status
Task 4:	Reservoir Characterization	10/92	10/95	#
4.1:	Stratigraphic Interpretation			
	4.1.1: 16 Block 2-D Analysis (PSU)	10/92	4/94	#
	4.1.2: 4 Block 3-D Analysis (PSU)	10/92	11/94	#
	4.1.3: North-South Transects (CU)	10/92	5/94	#
4.2:	Salt Analysis and Paleogeographic Reconstruction			
	4.2.1: North-South Transects (CU & PSU)	10/92	3/94	#
	4.2.2: 16 Block 3-D Restoration (CU)	10/92	12/95	
4.3:	Fluid Potential Analysis			
	4.3.1: Fault Plane Mapping (PSU)	10/92	1/95	#
	4.3.2: Structure Maps (PSU)	10/92	10/94	#
	4.3.3: 3-D Permeability Pathways (PSU)	8/94	10/95	#
	4.3.4: Pressure Mapping (PSU)	10/92	6/94	#
	4.3.5: Temperature Mapping (G. Guerin, LDEO)			#
4.4:	Amplitude Mapping Analysis (R. Anderson, LDEO)			#

Through the final year of the project we continued to acquire important data for the 330 field. These included: 1) complete wire- line data for Blocks 338 and 339 (donated by Texaco), 2) fracture completion data, and leak off data for Blocks 330, 338, and 339, and 3) the entire 316 A-12 core (now housed in the Penn State Core Repository) which was recently drilled by Pennzoil. Throughout the year, Beth Bishop and Amanda Shaw have continually updated the Landmark Openworks project and distributed data to all of our colleagues in this DOE-funded project.

4.0 Progress Made by Subtask

4.1: Stratigraphic Interpretation

4.1.1: 16 Block 2-D analysis (PSU)

Started: 10/92

Completed: 4/94

This subtask has been completed. Details of this work will be published in the December 1995 issue of the AAPG Bulletin in a paper entitled "Stratigraphic Architecture and Evolution of a Plio-Pleistocene Salt Withdrawal Mini-Basin: Eugene Island, South Addition, Block 330, Offshore Louisiana." This paper was included in last years annual report.

4.1.2: 4 Block 3-D analysis (PSU)

Started: 10/92

Completed: 11/94

Work on this subtask is complete. Details of this work will be presented in two forms:

- 1) Hart, B.S., Sibley, D.M., Flemings, P.B., Reservoir Compartmentalization by Depositional Features in a Pleistocene Shelf Margin (Lowstand) Delta Complex, Eugene Island Block 330 Field, Louisiana Offshore, accepted to 3-D Seismic Interpretation Atlas, (P. Weimer and T. Davis, eds.)
- 2) Hart, B.S., Sibley, D.M., Flemings, P.B., Seismic Stratigraphy, Facies Architecture and Reservoir Character of a Pleistocene Shelf Margin Deltaic Complex, Eugene Island Block 330 Field, Louisiana Offshore, accepted to AAPG Bulletin

4.1.3: North-South Transects (CU)

Started: 10/92

Completed: 5/94

This subtask is complete. See Task 4.2.1 for reporting.

4.2: Salt Analysis and Paleogeographic Reconstruction

4.2.1: North-South Transects (CU & PSU)

Started: 10/92

Completed: 3/94

This subtask is complete. Details of this work, and the results from Subtask 4.1.3, will be presented in three parts:

- 1) Rowan, M. G., Weimer, P., Flemings, P.B., "Three-dimensional geometry and evolution of a composite, multi-level salt system, western Eugene Island, offshore Louisiana," submitted to Gulf Coast Geological Societies, v. 44, pp. 641-648.
- 2) Rowan, M. G., Weimer, P., Flemings, P.B., "Deformation of a composite salt system: controls on the structural and stratigraphic evolution of the Eugene Island Block 330 minibasin, Gulf of Mexico," to be submitted to AAPG Bulletin.
- 3) Rowan, M. G., Weimer, P., Budhijanto, F., Flemings, P.B., "Integrated Regional Stratigraphic Sequence and Structural Framework and Geological Evolution of the Eugene Island Block 330 Area, Offshore Louisiana"

4.2.2: 16 Block 3-D Restoration (CU)

Started: 10/92

Projected Completion: 12/95

This is the only task that has not been completed to date. It is still uncompleted because Tasks 4.3.1 and 4.3.2 were much more involved than was originally predicted. However, we are continuing to work on this task which is now 75% complete and plan to submit the results to the AAPG Bulletin late this year.

4.3: Fluid Potential Analysis (PSU)

4.3.1: Fault Plane Mapping (PSU)

Started: 10/92

Completed: 10/95

This task is now complete. Please see attachment 1 by Rowan et al..

4.3.2: Structure Maps (PSU)

Started: 10/92

Completed: 10/94

This task is now complete. Please see attachment 1 by Rowan et al..

4.3.3: 3-D Permeability Pathways (PSU)

Started: 8/94

Completed: 10/95

This subtask is complete. The paper describing these interpretations is being prepared for publication in the Journal of Geophysical research. In addition, the results can be found in the Rowan et al. report (attachment 1) and on the 'Results of the Pathfinder Drilling Program Into a Major Growth Fault' cd-rom volume published by the GBRN.

4.3.4: Pressure Mapping (PSU)

Started: 10/92

Completed: 6/94

Work on this subtask is complete. More details of this work can be found in:

Hart, B.S., Flemings, P.B., and Deshpande, A. Porosity and pressure: Role of compaction disequilibrium in the development of geopressures in a Gulf Coast Pleistocene basin. *Geology* 23 (1):45-48(1995).

The following work was performed by Parvel Peska of Stanford University as consulting services to Columbia's Lamont-Doherty Earth Observatory from April 1, 1994 through July 31, 1995:

4.3.4.1. CONSTRAINING IN SITU STRESS IN THE SOUTH EUGENE ISLAND FIELD, GULF OF MEXICO

4.3.4.1.1. Pathfinder well

We analyzed data from the GBRN/DOE Pathfinder well, block 330 of the South Eugene Island field (extension of the Pennzoil A-20ST production well, offshore Louisiana). The data include: 4-arm caliper, leak-off/minifrac, pore pressure, FMI and hole orientation data.

Four-arm caliper measurements associated with an FMI log run in the Pathfinder well indicated systematic borehole enlargements from a depth interval 2158-2180 m, about 150 m above the main growth fault. The breakouts occur at an azimuth of N55°E if projected onto a horizontal plane. At these depths, the wellbore deviates 32° from the vertical at an azimuth N35°E.

A leak-off test from a depth of 2148 m provides an estimate of the minimum principal stress, S_3 , of 37.1 MPa. The corresponding vertical stress, S_v , is 43.0 MPa (computed from average density given by the density log), and the estimated formation pore pressure, P_p , is 29.0 MPa (Hart et al. 1994). These observations represent information that is typically available in many offshore reservoirs. The occurrence of naturally-occurring vertical extension fractures on the FMI log near the depth of interest indicates that S_v is a principal stress. Thus, to fully determine the stress state, two stress components are still unknown: the magnitude and azimuth of SH_{max} (or azimuth of Sh_{min}).

The subsequent analysis revealed that the azimuth of Sh_{min} must be between N37°E and N49°E and the corresponding values of SH_{max} must be between 39.5 MPa and 43 MPa. No other values satisfy the observed wellbore breakouts ($\pm 5^\circ$) and the known values of S_v , Sh_{min} and P_p . Although it is commonly assumed that $SH_{max} = Sh_{min}$ in the Gulf Coast, the SH_{max} value determined in this case departs significantly from Sh_{min} . The computed azimuth of Sh_{min} deviates from the azimuth of observed breakouts (whereas in a vertical well the breakouts are at the same azimuth of Sh_{min}) and it appears to be quite reasonable as it is orthogonal to strike of the major growth fault passing through the hole just below the measurement depth. No knowledge of either rock strength or elastic moduli was necessary in these computations.

Once the range of allowable magnitudes of SH_{max} and azimuths of Sh_{min} is computed, the uniaxial rock strength necessary to prevent borehole failure can be estimated. The occurrence of breakouts implies a strength less than about 22 MPa if $SH_{max} = 39.5$ MPa and less than ~32 MPa if $SH_{max} = 43$ MPa. These are reasonable values considering the sediments in question are poorly-indurated and clay-rich (Anderson et al. 1994).

The results of the study were presented in the paper "In situ stress and rock strength in the GBRN/DOE Pathfinder well, South Eugene Island, Gulf of Mexico" (Zoback and Peska 1995).

4.3.4.1.2. Surrounding well

Analysis of borehole breakouts detected in deviated wells by caliper logs was extended from the Pathfinder well to other wells in the South Eugene Island field where the logs were available (wells A2, A6, A20, A21, A22, #11 in the block 330, wells A11 and A12 in the block 316 and well A8 in the block 338). Borehole enlargements at azimuths which do not correlate with the hole inclination were detected in the wells A6, #11, A12 and A8 at depths of 6000'-8000'. The caliper difference was relatively small and subsequent stress analysis revealed that either the breakouts are not stress-induced or the stress state is highly heterogeneous in the region of interest.

4.3.4.1.3. Miscellaneous

As a part of the stress studies in the South Eugene Island field, we also performed compilations on stress magnitudes in the Gulf Coast, particularly on fracture gradients and pore pressures as a function of depth, which revealed that the Mohr-Coulomb frictional model controlling stress magnitudes in crystalline rocks in many parts of the world (e.g. Zoback and Healy 1984) is not working for overpressured formations in the Gulf Coast

unless the coefficient of friction is extremely low. A theoretical model of stress distribution in overpressured sedimentary basins was developed to demonstrate changes in stress magnitude and orientation with depth in areas where gravitational sliding controls the extensional faulting. Also, a FORTRAN code was written for inverting breakout orientation data from deviated boreholes (based on the method proposed by Qian and Pedersen (1991)).

4.3.4.2. ANALYSIS OF THE RELATIONSHIP BETWEEN IN SITU STRESS AND BOREHOLE FAILURE FOR STRESS DETERMINATION AND BOREHOLE STABILIZATION

An integrated methodology was developed to analyze the relationship between the in situ stress and failure of inclined boreholes. We have conducted a comprehensive series of calculations of the occurrence of borehole breakouts and drilling-induced tensile wall-fractures in arbitrarily-inclined boreholes and showed how such observations can be used to determine stress orientation and magnitude, effective rock strength and the optimal mud weight for borehole stability. The results are summarized in the paper "Compressive and tensile failure of inclined wellbores and direct determination of in situ stress and rock strength" (Peska and Zoback 1995).

Optimally, there is a two-step procedure how to apply this methodology in practice:

- 1/ Utilize observations of wall failures in inclined holes to constrain the in situ stress and effective rock strength assuming that independent information such as on the least principal stress, pore pressure and overburden is available.
- 2/ Utilize the knowledge on the stress field from the previous step to predict optimal wellbore trajectories and mud weights to stabilize the wellbore.

Computer codes were written in Matlab programming environment to implement the methodology. The computations are based on the assumption that the rock is isotropic and it behaves elastically to the point of failure which is controlled by the Mohr-Coulomb criterion.

The *GetStress* program computes the orientation and magnitude of the stress tensor (principal stresses are assumed to act vertically or horizontally) from the azimuth of borehole breakouts observed in an inclined borehole and from other a priori information. Regarding this information, there are two modifications: a) the first concerns the case typical of many sedimentary basins when independent information on S_v , $S_3 (=S_{hmin})$ and P_p is available, and b) the second is suitable in the case when only S_v is known ($S_v=S_3$ in the reverse faulting stress regime, for example) but the azimuth of S_{Hmax} can be a priori estimated. The program may be also used to constrain the rock strength as the conditions for failure are expressed by means of the critical strength C_0 and also the breakout width may be taken into account. The in situ stress may be also computed by the *BreakoutRotation* program which is an improved version of the Barton and Zoback [1994] technique for stress magnitude measurement using observations of rotations in borehole breakout orientation in the vicinity of an active fault penetrated by the borehole.

Once the stress state is known, the *GetFailure* program computes orientations of compressive and tensile failures in an arbitrarily-oriented borehole and constrains mud weight or effective rock strength required to stabilize the wellbore. Directions of potential breakouts and tensile wall-fractures around holes of various inclinations and azimuths are shown using the "looking down the hole" convention, i.e. as if the reader is viewing the hole by looking down its axis and the breakout azimuth is displayed with respect to the bottom side of the deviated borehole (the *FailureOrientation* program gives even a more detailed look at the stress concentration around an arbitrarily oriented borehole and makes it easier to understand the "looking down the hole" convention). The *WellboreTrajectory* program also computes orientation and tendency to fail by compressive or tensile failure for the given stress field and borehole orientation but now the stress and hole orientation are functions of depth which makes possible to analyze stability along the whole borehole. Both programs are optimal to design a stable wellbore trajectory from the platform to the target under the assumption that the stress state was determined from observations in the surrounding wells.

REFERENCES

- Anderson, R. N., P. Flemings, S. Losh, J. Austin, and R. Woodhams, In situ properties of a major Gulf of Mexico growth fault: Implications for behavior as a hydrocarbon migration pathway, *Oil Gas J.*, 92(23), 97-104, 1994.
- Barton, C., and M. D. Zoback, Stress perturbations associated with active faults penetrated by boreholes: Possible evidence for near-complete stress drop and a new technique for stress magnitude measurements, *J. Geophys. Res.*, 99, 9373-9390, 1994.
- Hart, B. S., P. B. Flemings, and A. Deshpande, Porosity and pressure: Role of compaction disequilibrium in the development of geopressures in a Gulf Coast Pleistocene Basin, *Geology*, 23(1), 45-48, 1995.
- Peska, P., and M.D.Zoback, Compressive and tensile failure of inclined wellbores and direct determination of in situ stress and rock strength, *J. Geophys. Res.*, in press, 1995.
- Qian, W., and L. B. Pedersen, Inversion of borehole breakout orientation data, *J. Geophys. Res.*, 96, 20093-20107, 1991.
- Zoback, M. D., and J. H. Healy, Friction, faulting and in situ stress, *Ann. Geophys.*, 2, 689-698, 1984.
- Zoback M.D., and P. Peska, In situ stress and rock strength in the GBRN/DOE Pathfinder well, South Eugene Island, Gulf of Mexico, *J. Pet. Technol.*, July 1995.

4.3.5: Temperature Mapping (G. Guerin, LDEO)

The mapping of the present-day temperature distribution around Block 330 is now complete, and after 3D numerical modelling of the conductive regime in this area, a 5 - 10 °C anomaly following the strike of the Red Fault can be observed in the depth range of the most productive sands. This observation is interpreted as the influence of warm hydrocarbon-bearing fluids migrating up along the fault, and will be used as a constraint for the 3D numerical modelling of these circulations, under development.

4.4: Amplitude Mapping Analysis (R. Anderson, Wei He, LDEO)

This sub-task is now completed, with a patent filed and granted for geopressure mapping using seismic amplitude changes. In addition, considerable bypassed pay has been identified along the property line between Eugene Island blocks 330 and 338. New wells to test the validity of the 4-D analysis are in the planning stages by Pennzoil and Texaco for 1996, to be paid for entirely with industry funds. The A-8St continues to produce at about 1400 bbl/day, with total production now exceeding 800,000 bbl. At a royalty percentage of 18% and assuming oil prices of \$20/bbl. this entire Class I Oils study will be paid for in an additional 3 years through the royalties paid to the US Treasury on oil from just this one successful well (the A-8ST), located in no small part through the use of 4D technologies.

4.4.1 Predicting the geopressure transition zone in the Plio-Pleistocene of offshore Louisiana, Gulf of Mexico

Geopressure, or overpressure, is abnormally high pore fluid pressure. This condition occurs when the formation pressure exceeds the hydrostatic pressure. The surface that marks the first occurrence of geopressure in a sedimentary basin is termed the top-of-geopressure surface. Geopressure is common in sedimentary basins of all ages (Fertl, 1976 and Anderson et al., 1991). These abnormally high fluid pressures are an

extreme hazard to drilling, since the undercompensation for borehole pressures results in blow-outs. The top-of-geopressure is a hydrodynamic subsurface. The topography and dynamics of the geopressure surface are closely related to thermal-chemical and dynamic evolution of the basin. An accurately determined top-of-geopressure surface and a quantitatively evaluated geopressed transition zone are of great significance in studying the fluid dynamics and thermal maturation of the basin, because hydrocarbon generation and migration are usually controlled by the pressure distribution.

Geopressure can be caused by many different physical, chemical, or tectonic factors. Aquifer head (Levorsen, 1954), tectonic compression (Finch, 1969 and Hubbert et al., 1959), sediment loading, compaction, and the absence of drainage systems (Dickinson, 1953; Hubbert et al., 1959; Jones, 1969 and Harkins et al., 1969), phase changes, or diagenesis, such as the water release from the phase change of montmorillonite to illite (Powers, 1967 and Burst, 1969), smectite dehydration (Bruce, 1984), gypsum to anhydrite (Heard et al., 1966), organic material maturation (Hedberg, 1974), aquathermal expansion of water due to the temperature variations (Levorsen, 1954), osmotic membrane phenomena (Hanshaw et al., 1965), and thick shale-sand sequences with the sand to shale ratio less than 15% (Harkins et al., 1969) have all been cited as causes of geopressures.

In the offshore basins of Gulf of Mexico, geopressure is caused by continuous sediment loading at fast sedimentation rates and to a lesser extent by clay phase changes (Jones, 1969). The excessive pore fluid pressure built up in such a short geological time frame (< 2.5 ma) dissipates at an extremely slow rate due to the permeability bottle necks developed in interbedded sand and shale stratigraphic sequences (Mello et al., 1993).

The geopressure transition zone is the depth interval within which the hydrostatic pore fluid pressure gradually increases with depth to approach lithostatic pressure (Figure 5.1). The geopressure transition zone occurs at the permeability bottle neck. The bottom of the geopressed formation has not yet been reached by any wells drilled in the Gulf Coast region.

Acoustic velocity and bulk density are greatly effected geopressures. Because the excessive pore fluid pressure partially supports the weight of rock column, the effective pressure exerted on the rocks is dramatically decreased (Figure 5.1). As a result, the acoustic velocity and bulk density of geopressure formations are usually much lower than those of normally compacted formations at the same depth. For the same reason, a velocity inversion (from high to low) usually occur at the geopressure transition zone because velocity is proportional to the effective pressure (Figure 5.2). The decrease in velocity and density can be further enhanced by undercompaction of the rocks.

The original depositional porosity of sediments (often 65%) is partially preserved by undercompaction of sediments due to the geopressure. Under continuous loading at fast sedimentation rate, pore fluids of previously deposited sediments can not escape fast enough because of low vertical permeability, which effectively prevents further mechanical compaction of these sediments. With further burial, more fluids are generated from clay diagenesis and the pore fluid pressure increases (Powers, 1967 and Spencer, 1987). We believe that the remarkable decrease in compressional-wave velocity and bulk density across the geopressure transition zone in the Gulf of Mexico is due to coupling of pore fluid pressure and porosity preservation.

The geopressure transition zone is also characterized by abnormally low vertical permeability, high salinity, and high temperature gradients (Dickinson, 1953; Bredeheft et al., 1968; Burst, 1969; Jones, 1975; Hunter, 1990 and Tigert et al., 1990). In a geopressure transition zone with fixed thickness, the higher the pore fluid pressure, the lower the acoustic velocity and density. A large negative seismic amplitude is expected. On the other hand, the thicker the geopressure transition zone, the lower the frequency of the seismic reflection.

In this chapter, we present a method that uses reflection strength of real seismic data to predict the top-of-geopressure surface. We use forward seismic modeling and cross-correlation to quantitatively estimate the thickness of the geopressure transition zone. Once

validated, these methods are applied to a 2D seismic survey acquired in the South Eugene Island Area offshore Louisiana Gulf of Mexico.

The acoustic velocity transition observed in sonic logs suggests that the geopressure transition zone can be quantified in terms of two variables: pore fluid pressure gradient and the transition zone thickness. The well data also suggest that the formations below the bottom of the geopressure transition zone are highly overpressured. The well data also indicate that the velocity changes are significant only when the pressure gradient ranges from 13.6 to 18.1 MPa/Km (0.6 to 0.8 psi/ft). As the pore fluid pressure approaches the overburden pressure, no further decrease in velocity occurs. Our prediction technique is reliable only in defining the top portion of the geopressed zone.

4.4.2 Background of geopressure prediction techniques

Geophysical methods for detecting and predicting the top-of-geopressure surface can be classified into drilling methods, wireline logging methods, reflection seismic methods, and gravity or electric-magnetic potential field methods. The first two methods can only be performed when wells penetrate the top-of-geopressure surface. Seismic and potential field methods require only surface measurement. Potential field methods suffer from the limitation of being unable to distinguish overpressured formations from massive shale formations. The efficiency of reflection seismic methods are addressed in this chapter.

Many attempts to identify reflectors from the top-of-geopressure fail because the thickness of the transition zone can vary greatly over short distances (Anderson et al., 1992). Seismic interval velocity analysis (Pennebaker, 1968 and Reynolds et al., 1971) and inverted pseudo velocity or acoustic impedance analysis (Musgrave et al., 1965 and Martinez et al., 1991) attempt to detect interval velocity or impedance changes across the top-of-geopressure surface. Using velocity techniques, the top-of-geopressure surface is interpreted as the depth where the interval velocity trend departs from the velocity trend expected under normal compaction conditions. The velocity technique works well on sonic logging data, which have high resolution, but fails for lower resolution velocities determined by staking and migration. The pseudo velocity and impedance derived from seismic inversion, although have higher resolution, fails due to its lack of low frequency information (He et al., 1995). Missing the onset of geopressure can cause inconsistency in the predicted top-of-geopressure surfaces even within a single vintage of seismic data, this scenario deteriorates in areas where geopressure pressure transition zones are thick or highly variable.

Changes in seismic reflection strength (instantaneous amplitude) of reflection seismic data can be used to detect geopressures as long as a sound relationship between the velocity transition and geopressure transition can be established. Our approach is to develop techniques that can distinguish seismic amplitude anomalies caused by geopressure transition zones from other reflections. We detect reflections from acoustic transition zones. Because reflection strength measurements contain low-frequency energy contained in original seismic traces, the reflections from acoustic transition zones can be enhanced and separated from other reflections by low-pass filtering. Reflection strength estimates derived from velocity transition models are used in the design of these filters. Top-of-geopressure can be directly detected as the uppermost boundary reflector between the high and low amplitude regimes in the reflection strength cross-sections (Anderson et al., 1992 and He et al., 1992 and 1994). The geopressure transition zone can also be imaged.

4.4.3 Characteristics of seismic reflections from geopressure transition zones

4.4.3.1 The appearance of geopressure on seismic data

In the Plio-Pleistocene basin of the Gulf of Mexico, such as the South Eugene Island Area, geopressed formations produce observable features on reflection

seismogram and wireline logging records (Figure 5.3). Substantial weakening of seismic amplitude is observable in time windows between about 1,500 ms and 3,000 ms on the eastern and western footwalls of the central Eugene Island basin and between 2,800 ms and 4,000 ms on the hanging wall. This weakening is caused by strata with less internal acoustic impedance contrast than normally-pressured strata. Deepwater turbidites have reflectors of normal amplitudes, they are located beneath the weakening zones in the center of the basin. Salt diapir structures are seen beneath both footwalls. The boundaries of the weak reflection regions do not necessarily follow stratigraphic sequence boundaries (left of Figure 5.3).

4.4.3.2 Distinct features of the geopressure transition zone in seismic data

The generalized reflection coefficient of a transition zone in a laterally homogeneous acoustic medium has the form of a superposition integral (Wolf, 1937). The maximum amplitude is proportional to the ratio between the velocities at the top and bottom of the transition layer. The cut-off frequency (the highest frequency preserved) is inversely proportional to the thickness of the transition layer (Seo, 1978). An acoustic medium with a transition zone not only attenuates reflected seismic energy, but also greatly changes the phase of the reflected seismic waveforms (Bortfeld, 1960 and Gupta, 1965). We have generated two groups of seismic models to illustrate the seismic reflection effects of changing the velocity and thickness of the transition zones. Group I models have a transition zone with constant thickness and varying velocities of the underlying layer. Group II models have a transition zone that varies in thickness with a constant velocities of the top and bottom layers (Figure 5.4 (a)). The cut-off frequencies are dramatically reduced as the transition thickness increases (Figure 5.4 (b)). The reflection energy increases with the velocity contrast. Small increases of cut-off frequency are also observed for Group I models. These basic seismic characteristics of the geopressure transition zone are the main features on which our geopressure predicting technique is based.

In practice, the post-stack seismic data are usually treated as zero-offset seismic reflections. A seismic trace observed in an area with geopressured formations consists of reflections from both discrete geological events and the transitional zone. These seismic traces can be modeled as the convolution of a reflection coefficient function and a seismic source function. Using seismic data processing techniques, it is possible to separate the transitional events from the discrete events in an observed seismic trace.

4.4.4 Predicting top-of-geopressure surfaces using our seismic amplitude technique

We constructed a geological model consisting of an acoustic transition layer with varying thickness and several discrete layers with constant velocities (Figure 5.5 (a)). Using the first derivative of a 35 Hz, zero-phase, Ricker wavelet as seismic source, a synthetic seismic section was generated using a finite element seismic modeling algorithm (Teng, 1989) (Figure 5.5 (b)).

Because our prediction technique is to detect the top-of-geopressure surface in two-way traveltimes domain in which the convolution forward model is used in data processing, a synthetic model generated from a forward model other than convolution is necessary to test our prediction technique independently.

Our first step is to detect the low-frequency seismic reflections in the synthetic section. Using complex seismic trace analysis (Taner et al., 1979; also Appendix A). The algorithm treats a real seismic trace as the real part of a complex signal, with an imaginary part is equal to Hilbert transform of the real part. The reflection strength is quantified by the envelop (magnitude) of this complex function. The complex seismic trace analysis was applied to compute the reflection strength of our test model (Figure 5.6 (a)). The reflection strength section is composed only of low frequency reflections.

Thick geopressure transition zones only contribute to low frequency contents in reflection seismic data, whereas large velocity contrasts between the top and the bottom of

transition zone only contribute to large amplitudes. Therefore, our second step is to distinguish the reflections contributed by the transition layer from those contributed by discrete layers. Since the generalized reflection coefficient of typical transition zones (Figure 5.4) contains mostly low frequencies, we design a lowpass filter than enhance those frequencies. We take this filter to be simply the low-frequency part of the amplitude spectrum of the generalized reflection, up to the first zero. We then apply this filter to the reflection strength section (Figure 5.6 (b)). The bandwidth of the lowpass filter depends on the thickness of the velocity transition zone, which is unknown. We use a filter with an intermediate bandwidth (estimated from assumption), which is effective enough to enhance the majority of transition zone reflections. On the filtered reflection strength section, the top-of-geopressure surface can be interpreted as the uppermost boundary between the high (shallow) and low (deep) amplitude regimes (Figure 5.6 (b)). The top of the transition zone is interpreted as the enhanced (or unchanged) reflectors. The estimated top and bottom of the transition zone is almost identical to that of the true velocity model (compare Figures 5.5 (a) and 5.7). Our processing technique can be visualized more clearly using a single seismic trace extracted from the synthetic section (Figure 5.8).

4.4.5 Verification of the prediction technique

We apply the technique to a synthetic trace generated from sonic and bulk density logs from Eugene Island well 331_SH_1 (Figure 5.9). Both sonic and density logs show a transition from high values to low values across the geopressure transition zone.

The top of sonic velocity transition is at 2,460 ms (2,621 m), and the measured pressure gradient is 13.6 MPa/Km (equivalent to mud weight of 1,400 Kg/m³). The bottom is at 2,600 ms (2,792 m), and it corresponds to a 18.1 MPa/Km gradient (1,800 Kg/m³). Acoustic velocity at the top and bottom of the geopressure transition zone are 2,772 m/s and 2,242 m/s, respectively (a 19% decrease).

The corresponding frequency spectra of the seismic traces and reflection strength traces are shown in Figure 5.11. The reflection strength derived from the complex seismic trace analysis is lowpassed compared with data. The highest frequency preserved in both traces is less than 30 Hz. A velocity transition model with thickness of 140 ms is constructed as shown in Figure 5.12 (a). The filter is obtained (Figure 5.12 (b) and applied to the reflection strength traces (Figure 5.13). The reflections from the geopressure transition zone are clearly seen at 2,460 ms on both filtered traces.

These results suggest that our geopressure prediction technique can be used to identify the top-of-geopressure surface using seismic amplitudes. However, the nonuniqueness introduced by the low frequency cyclicity of the sedimentary sequences may sometime affect the interpretation of the top-of-geopressure. Constraints from well logs are required for two reasons: 1) A well must be used to provide *a priori* knowledge of the geopressure transition zone at one location to construct the low-pass filter; and 2) the pressure detected in the well must be used to calibrate the occurrence and depth of the top-of-geopressure surface.

4.4.6 Prediction of the top-of-geopressure surface in the Plio-Pleistocene basin in offshore Louisiana Gulf of Mexico

We use a 2D seismic survey acquired in 1983 in the Eugene Island Area of offshore Louisiana (Figure 5.14) to examine the feasibility and accuracy of our geopressure predicting technique. The survey area is about 90 Km (east-west) by 41 Km (north-south) with approximately 3.2 Km spacing between north-south “inlines” and 6.4 Km spacing between east-west “crosslines”. There are 110 seismic lines contained in this survey. The survey covers the entire Eugene Island South Addition Area Block 330 minibasin, and its vicinity (Figure 5.14). The stacked and migrated seismic data of relative seismic amplitude (“true” amplitude) have a frequency range from 6 to 60 Hz. The seismic processing parameters are listed in Table 5.1.

4.4.6.1 Regional geology

The sedimentation history of the offshore Louisiana sub-basin is well studied by numerous authors (e.g., Galloway et al., 1991). Significant sedimentation in the offshore Louisiana did not occur until the Jurassic rifting of the Gulf of Mexico and the subsequent Laramide orogeny and its uplift of the Rocky Mountains. Abundant terrigenous materials from erosion of the Rocky Mountains were delivered into the Northern Gulf of Mexico Basin, but were delayed by a lower Cretaceous barrier reef system that developed along the hinge zone of the Gulf. The Laramide erosional products finally breached the reef in the Tertiary, and the ancestral Mississippi River delta system rapidly dumped an enormous thickness of sediments into the Gulf Coast basin. The thickness of progradationally-deposited sand and shale sequences in the Cenozoic reached at least 12,000 m, and the thickness of the Pleistocene alone reached more than 3,000 m. This deposition took place in only about 5.3 ma (Galloway et al., 1991). The Pre-Tertiary sediments were buried, loaded, and heated with unusual rapidity. This rapid loading triggered the massive migration of the Louann salt toward the surface and to the south into the deepwater continental slopes. Pore pressures within the deeper sediments increased above hydrostatic, and large volumes of hydrocarbons were generated and migrated to shallow traps. These processes continue to this day (Anderson et al., 1991).

Large-scale hydrodynamic processes are coupled with the ongoing deposition of the massive sedimentary load. Convection is occurring in all three of the major hydrological regimes active in the Louisiana Gulf Coast. At shallow depths, meteoric flow, controlled by topography and directed towards the shelf, mixes with upward moving connate water and diagenetic fluids from deeper in the basin. At mid-depths, considerable dissolution of salt occurs producing an unstable layer of heavy, dense, and highly saline pore fluids.

Salinities in Pleistocene sediments are often found to be more than 4 times greater than sea water. In the deepest portion of the basin, metamorphism and hydrocarbon maturation reactions release large volumes of high-temperature, gas-charged and extremely buoyant fluids. Thermal build-up and restricted fluid flow are associated with this geopressured zone which dominates the deeper compressional system within the basin. Hydrothermal fluids migrate both laterally and vertically for considerable distances (Anderson et al., 1991).

Several minibasins were formed in the survey area by the withdrawal of a salt canopy approximately 2 ma ago. These minibasins are situated on the major shelf-margin deltaic depocenters of Plio-Pleistocene age and are bounded by regional and counter-regional growth faulting systems. Their evolution is characterized by three sedimentary phases: prodelta, proximal deltaic, and fluvial (Alexander et al., 1995). In the prodelta phase, bathymal and outer neritic shales and turbidites loaded and mobilized an underlying salt sheet. During the proximal deltaic phase, salt continued to withdraw from beneath the minibasin and lowstand shelf margin deltas deposited across a regional growth fault zone system, which grew along the northern margin of the minibasin. Sediment accumulation and fault slip rates were high as thick sequences of deltaic sands were deposited on the footwall of the fault system. During the final fluvial phase, salt withdrawal waned and the creation of accommodation space within the minibasins ceased. The Eugene Island minibasin was filled less than 500,000 years ago and the lowstand deltaic system prograded southward (Alexander et al., 1995). Many hydrocarbon reservoirs discovered in the study area were formed during the second and third phases. Continuous sediment loading at fast sedimentation rates and clay diagenesis caused geopressures to occur widely.

4.4.6.2 Velocity characteristics of geopressure transition zone

Well logs provide the starting point for understanding the behavior of acoustic velocity in the geopressure transition zone. More than 500 wells have been logged in this

area. Among them, 107 wells penetrated the top-of-geopressure surface. A 19% velocity decrease is observed in the geopressure transition, which has a pressure gradient that varies from 13.6 to 18.1 MPa/Km within a 140 ms time window. We use one well (EI-331_SH_1) to design the lowpass filter for the entire seismic survey, which is the same well used in Section 5.5 above.

The pore fluid pressure gradient measured at the bottom of the well is 19.7 MPa/Km, well above the 10.5 MPa/Km hydrostatic pressure gradient. Nevertheless, the sonic log does not show any transition at that depth, because only pressure gradients in between 13.6 MPa/Km and 18.1 MPa/Km can produce an observable velocity transition. The filter design for the velocity transition use a 30 Hz, zero-phase Ricker wavelet, (the same as in Figure 5.12 (b)). This filter is applied to all the reflection strength traces computed for the entire 2D seismic survey in the next section.

4.4.6.3 Seismic data analysis to predict the top-of-geopressure surface

The reflection strength section of Line GE-6063A (Figure 5.3) is shown in Figure 5.15, and the filtered version is shown in Figure 5.16. Well 331_SH_1 is projected onto the section, and the time where the well penetrated the top-of-geopressure surface is identified ("TOG" in Figure 5.16). The top-of-geopressure surface is then interpreted as the uppermost reflector that separates high amplitude region above from the low amplitude regions below, using the top-of-geopressure surface in 331_SH_1 well as reference. The geopressure surface is depressed in the center of the EI-330 minibasin due to the thick sediment load. The surface rises near bounding faults on both sides of the minibasin. It intersects stratigraphic and lithologic interfaces. Our results agree well with the top-of-geopressure surface detected in the another well (Figure 5.27).

Our technique allows the top-of-geopressure surface to be systematically interpreted across faults and other structural boundaries. The spatial consistency between stratigraphic horizons, faults, and the top-of-geopressure surface can be achieved. Such consistency is essential to integrate geopressure interpretations with other geological and geophysical data successfully.

By applying the same procedure to the other 109 seismic lines, we are able to predict the top-of-geopressure surface consistently with respect to faulting and stratigraphic configuration in these minibasins (Figure 5.17). The interpreted top-of-geopressure surface is then converted from two-way travel time to depth using the interval velocity derived from the corresponding stacking velocity of each seismic line. A detailed top-of-geopressure surface map is shown in Figure 5.18. The compartmentalization of the predicted geopressure surface is clearly seen, with individual pressure chambers being bounded by major growth faults.

4.4.6.4 Accuracy and reliability of the predicted top-of-geopressure surface

The accuracy and reliability of the predicted depth to top-of-geopressure surface is investigated by comparing it with that detected by well logs and mud weights. A map based on the depth to 13.6 MPa/Km pressure gradient in 107 wells is shown in Figure 5.19. Similar topographic features are observed on the both maps.

However, major discrepancies as well as some other subtle differences are present in a few places. The map based on seismic data includes faults, and thus it has much higher lateral resolution than the map based on wells. The agreement is better at the well locations themselves (Figure 5.20). The root-mean-square error is about ± 107 m. The largest errors are introduced from eighteen wells, which are located in areas with complex geological structures, such as shallow salt diapirs (Figure 5.21). If we exclude these 18 wells, the root-mean-square error is reduced to ± 46 m (Figure 5.22).

4.4.7 Quantitative evaluation of geopressure transition zone

If the geopressed formations share the same hydrodynamics, pressure differential between the top and bottom of the transition zone should be the same everywhere, regardless of the thickness of the transition zone. Quantitatively estimates of the geopressure transition zones can be obtained through the correlation of pressure gradients and acoustic velocities. Some logs from wells in our study area are shown in Figure 5.23. The thickness of the geopressure transition zones in these wells are not constant, but the measured pressure gradients tends to linearly correlate with velocity contrasts across the geopressure transition zones. This correlation is used to define an empirical, linear relationship between pressure gradient and velocity.

We develop a suite of velocity transition models with fixed velocity contrast (22.7%) and varying thickness of the velocity transition. Thirty models were generated with thickness increments of 8 ms, up to a maximum thickness of 240 ms (Figure 5.24 (a)). Using a 30 Hz, zero-phase Ricker wavelet as the source function, synthetic seismograms were computed for each of the thirty velocity models. Reflection strength traces were then computed.

Using the previously interpreted top-of-geopressure surface, we can compute cross-correlation functions between the modeled and observed reflection strength functions. The velocity model corresponding to the maximum correlation among the thirty cross-correlation functions is then chosen as the best velocity transition model for that trace. The time lag of the maximum cross-correlation function is used to precisely locate the final, predicted top-of-geopressure surface. This technique produced an improved top-of-geopressure surface, an estimate of the thickness, as well an estimate of the thickness of the velocity transition and associated geopressure transition zone.

The precisely-located top-of-geopressure surface, the previously-predicted top-of-geopressure surface, and the predicted bottom-of-geopressure transition zone are shown in Figure 5.25. Minor time shifts are observed between the newly obtained and previously predicted top-of-geopressure surfaces. The topographic variations of the predicted bottom of geopressure transition zone are different from those of the top-of-geopressure surface. The largest deviations are observed near the large growth fault systems.

Using the interval velocity derived from the stacking seismic velocity (Figure 5.26), the final, predicted top-of-geopressure surface and the bottom-of-geopressure surface are converted from time to depth (Figure 5.27). The shading represents the actual pore fluid pressure which is computed from the predicted pressure gradients in the geopressure transition zone. The pore fluid pressures above the top-of-geopressure surface are at hydrostatic pressures. Pore fluid pressures below the bottom of geopressure transition zone are not estimated, because the pressure gradients are greater than 18.1 MPa/Km in the study area and can not produce enough velocity contrast to be observable by our analysis. Two wells penetrating the top-of-geopressure surface are also projected onto the quantitatively predicted geopressure transition zone. The agreement between wells and prediction is good.

4.4.8 Geological significance of the predicted geopressure transition zone

The geopressures were developed in the early Cenozoic, when large amounts of clastic sediments were rapidly deposited. Subsequently, they have evolved along with the structural, stratigraphic, and thermal conditions. Large amounts of heat are trapped within the geopressed formations because no advective heat transport occur across the top-of-geopressure. The effects of heat insulation on thermal evolution are two fold. On one hand, the heat transport to the hydrostatic zone is reduced, causing much lower formation temperatures in the hydrostatic zone than average temperatures observed in Tertiary basins without geopressing. On the other hand, the trapped heat may have significant impact on the maturation of the deep Cenozoic organic source rocks. Strong thermal anomalies in the hydrostatic zone are observed along the red fault in the study area. They are caused by heat carried by transient fluids expelled from the overpressured formations along these faults

(Anderson et al., 1991). These thermal anomalies indicate that many of the regional growth faults in the study area are still active at the present time. When pore fluid pressures within the geopressed formation continuously built up to exceed the minimum horizontal stress, periodic reopening of these faults occurs usually parallel to the regional faults. Consequently, the reopening releases tremendous amounts of fluid from the overpressured formations into the reservoirs in the hydrostatic zone.

The periodic reopening of growth faults every two thousand years is the mechanism for present-day fluid migration. The pressurized fluid mixtures with high temperatures migrate from the geopressed formations to fill reservoirs in the hydrostatic zone and balance the pressure and temperature differences. Overproduction of some shallow reservoirs (Anderson, 1993) may be associated with this active fluid flow. To prove and quantify such a fluid recharging process, much work is still left to be done.

There is a good correlation between the locations of some large oil fields and areas with large horizontal pressure gradients (Figure 5.28). The horizontal pressures are highest near the top-of-geopressure surface, in regions where the topography of the surface is steep. The oil fields tend to occur in these areas. Since steep topographic gradients are probably associated with faults, we propose that the correlation is due to oil being forced up from greater depths along these faults by geopressure.

4.4.9 Conclusion

Geopressure transition zones are characterized by monotonically decreasing acoustic velocities in our study area. In our method, reflection strength is successfully used to extract the low-frequency content of seismic reflections needed to define acoustic transition zones. The top-of-geopressure surface, associated thickness and gradients of geopressure transition zones are obtained deterministically. Good agreement between the predicted results and measured results in wells is observed. Our prediction method is robust and effective. The accuracy of the seismically-predicted regional geopressure surface is within ± 46 m, using only one well as control, which is more accurate than the results obtained from other seismic methods.

The cross-correlation technique has several advantages over the seismic inversion technique. Accurate phase information is not required, because the technique uses phase-free reflection strength information. The implementation of our technique does not suffer from numerical instability. The cross-correlation technique is a deterministic method, of which all possible models are already generated from the well logs, the results obtained can be directly used to other geological analysis.

Missing the onset of the geopressure is avoided in our geopressure prediction method even in areas with highly variable geopressure topography. The predicted and characterized geopressure transition zones are reliable and accurate. We have successfully tested our method in other basins besides the Gulf of Mexico, as well.

References

- Alexander, L., and P.B. Flemings, 1995, Geologic evolution of a Plio-Pleistocene salt-withdrawal minibasin: Eugene Island Block 330, Offshore Louisiana: American Association of Petroleum Geologists Bulletin, v. 79, p. 1737-1756.
- Anderson, R.N., 1993, Recovering dynamic Gulf of Mexico reserves and the US. energy future: Oil & Gas Journal, week of April 26, PennWell Publication.
- Anderson, R.N., W. He, M.A. Hobart, C.R. Wilkinson, H.R. Nelson, 1991, Active fluid flow in the Eugene Island area, offshore Louisiana: The Leading Edge of Geophysics, v. 10, p. 12-17.
- Anderson, R.N., and W. He, 1992, Method and apparatus for petroleum and gas exploration: US. Patent No. 5,311,484.
- Bracewell, R., 1965, The Fourier transform and its applications: McGraw-Hill Book Co.

- Bredehoeft, J.D., and B.B. Hanshaw, 1968, On the maintenance of anomalous fluid pressures. I. Thick sedimentary sequences: Geological Society of America Bulletin, v. 79, p. 1087-1106.
- Bortfeld, R., 1960, Seismic waves in transition layers: Geophysical Prospecting, v. 8, p. 178-217.
- Bruce, C.H., 1984, Smectite dehydration-Its relation to structural development and hydrocarbon accumulation in Northern Gulf of Mexico Basin: American Association of Petroleum Geologists Bulletin, v. 68, p.673-683.
- Burst, J.F., 1969, Diagenesis of Gulf Coast clayey sediments and its possible relation to petroleum migration: American Association of Petroleum Geologists Bulletin, v. 53, p. 73-93.
- Claerbout, J.F., 1985, Fundamentals of geophysical data processing with applications to petroleum prospecting: McGraw-Hill Book Co.
- Dickinson, G., 1953, Reservoir pressures in Gulf Coast Louisiana: American Association of Petroleum Geologists Bulletin, v. 37, p. 410-432.
- Fertl, W.H., 1976, Abnormal formation pressures-Implications to exploration, drilling, and production of oil and gas resources: Elsevier Scientific Publishing Company, Amsterdam-Oxford-New York, p.
- Finch, W.C., 1969, Abnormal pressure in the Antelope field, North Dakota: Journal of Petroleum Technology, v. 21, p. 821-826.
- Galloway, W.E., D.G. Bebout, J.B. Fisher, J.B. Dunlap Jr., R. Cabrera-Castro, J.E. Lugo-Rivera, and T.M. Scott, 1991, Cenozoic in The Gulf of Mexico Basin: Geology of North America, A. Salvador, Editor, v. J, p. 245-324.
- Gupta, R.N., 1965, Reflection of plane waves from a linear transition layer in liquid media: Geophysics, v. 30, p. 122-132.
- Hanshaw, B.B. and E-an Zen, 1965, Osmotic equilibrium and over-thrust faulting: Geological Society of America Bulletin, v. 76, p. 1379-1386.
- Harkins, K.L. and W. Baugher III, 1969, Geological significance of abnormal formation pressures: Journal of Petroleum Technology, August, p. 961-966.
- He, W. and R.N. Anderson, 1992, A seismic amplitude analysis approach for mapping the top-of-geopressure surface in the Pleistocene, Offshore Louisiana: EOS Transactions, American Geophysical Union, v. 73, p. 304.
- He, W., 1994, Mapping the top-of-geopressure surface in the Pleistocene, offshore Louisiana, Gulf of Mexico: M. Phil. thesis, Columbia University.
- He, W., R.N. Anderson, and Y.-C. Teng, 1995, Application of seismic inversion to quantitative mapping geopressure transition zones in the Pleistocene, offshore Louisiana, Gulf of Mexico: The 2nd International Conference on Theoretical and Computational Acoustics, Honolulu, Hawaii.
- Hedberg, H.D., 1974, Relation of methane generation to undercompacted shales, shale diapirs, and mud volcanoes: American Association of Petroleum Geologists Bulletin, v. 58, p. 661-673.
- Heard, H.C., and W.W. Rubey, 1966, Tectonic implications of gypsum dehydration: American Association of Petroleum Geologists Bulletin, v. 77, p. 741-760.
- Hubbert, M.K., 1940, The theory of ground-water motion: Geology, v. 48, Part 1, p. 785-944.
- Hubbert, M.K., and W.W. Rubey, 1959, Role of fluid pressure in mechanics of overthrust faulting, I. Mechanics of fluid-filled porous solids and its application to overthrust faulting: Geological Society of America Bulletin, v. 70, p. 115-166.
- Hunt, J.M., 1990, Generation and migration of petroleum from abnormally pressured fluid compartments, American Association of Petroleum Geologists Bulletin, v. 74, p.1-12.
- Jones, P.H., 1969, Hydrodynamics of geopressure in the northern Gulf of Mexico Basin: Journal of Petroleum Technology, July, p. 803-810.
- Levorsen, A.I., 1954, Geology of Petroleum: W.H. Freeman, San Francisco, 703 p.

Martinez, R.D., J.D. Schroeder, and G.A. King, 1991, Formation pressure prediction with seismic data from the Gulf of Mexico: Society of Petroleum Engineers, Formation Evaluation, no. 3, p. 27-32.

Mello, U.T., G.D. Karner, and R.N. Anderson, 1994, A physical explanation for the positioning of the top of overpressure in shale-dominated sequences in the Gulf Coast Basin: Journal of Geophysical Research, v. 99, p. 2775-2789.

Musgrave, A.W., and W.G. Hicks, 1965, Outlining shale masses by geophysical methods: American Association of Petroleum Geologists Bulletin, Memoir no. 8, p. 112-136.

Pennebaker, E.S., 1968, Seismic data indicate depth, magnitude of abnormal pressures: World Oil, v. 166, p. 73-78.

Powers, M.C., 1967, Fluid-release mechanisms in compacting marine mudrocks and their importance in oil exploration: American Association of Petroleum Geologists Bulletin, v. 51, p. 1240-1254.

Reynolds, E.B., J.E. May, and A. Klaveness, 1971, The geophysical aspects of abnormal fluid pressures: Abnormal subsurface pressure, Houston Geological Society Study Group Report, p. 31-47.

Seo, J.H., 1978, Detection of abnormal geopressure using seismic reflectivity: M.A. thesis, University of Texas at Austin.

Spencer, C.W., 1987, Hydrocarbon generation as the mechanism for overpressuring in the Rocky Mountain region: American Association of Petroleum Geologists Bulletin, v. 77, p. 2006-2010.

Taner, M.T., F. Koehler, and R.E. Sheriff, 1979, Complex seismic trace analysis: Geophysics, v. 44, p. 1041-1063.

Tigert, V., and Z. Al-Shaieb, 1990, Pressure seals: their diagenetic banding patterns: Earth Science Reviews, v. 29, p. 227-240.

Teng, Yu-Chiung, 1989, Three-dimensional finite element analysis of waves in an acoustic medium with inclusion: Journal of Acoustic Society of America, v. 86, p. 414-422.

Wolf, A., 1937, The reflection of elastic waves from transition layers of variable velocity: Geophysics, v. 2, p. 357-363.

Wyllie, M.R.J., A.R. Gregory, and G.H.F. Gardner, 1958, An experimental investigation of factors affecting elastic wave velocities in porous media: Geophysics, v. 23, p. 459-493.

FIELD DATA	
SURVEY SYSTEM	ARGO
DATA TYPE	REFLECTION
RECORDING SYSTEM	DFS V
RECOEDING FORMAT	SEG B GAPPED
RECORDING DENSITY	1600 BPI
SAMPLE PERIOD	4 MSEC
RECORD LENGTH	7 SEC
GAIN CONSTANT	36 DB
RECORDING FILTER	HIGH CUT - 90 HZ. AT 72 DB/OCT. LOW CUT - 5.3 HZ. AT 18 DB/OCT.
SEISMIC SOURCE	AIRGUN (4075 CU. IN. AT 2000 PSI)
AVERAGE SOURCE DEPTH	9 M (29.52 FT)
CABLE LENGTH	3000 M (9842.4 FT)
AVERAGE CABLE DEPTH	10 M (32.8 FT)
NUMBER OF GROUPS	120
GROUP INTERVAL	25 M (82.02 FT)
SHOT INTERVAL	25 M (82.02 FT)
MULTIPLICITY	60 FOLD
AVERAGE OFFSET	265 M (869.41 FT)
PROCESSING PARAMETERS	
POLARITY	POLARITY RECORDED IN FIELD MAINTAINED IN PROCESSING
SYSTEM DELAY	51.2 MSEC. ARI GUN DELAY CORRECTION
TRUE AMPLITUDE RECOVERY	EXPONENTIAL SCALAR OF 6 DB/SEC WATER BOTTOM TO 4 SECONDS SPHERICAL DIVERGENCE CORRERCTION
MUTE	
VELOCITY FILTERING	PASS BAND +16 TO -5 MSEC/TR
WAVELET PROCESSING	DESIGNITURE ALL 120 TRACES IN SHOT DOMAIN USED IN WAVELET ESTIMATE, OFFSET DEPENDENT VELSCAN EVERY 2 KM. TO PICK STAKING FUNCTION
VELOCITY ANALYSIS	TRACE EQUALIZATION
SCALING	
NORMAL MOVEOUT CORRECTIONS	
FIRST BREAK SUPPRESSION	SEE TAPER ON
COMMON DEPTH POINT STACK	60 FOLD
DECONVOLUTION	NUMBER OF OPERATORS : 1 OPERATOR LENGTH : 120 MSEC. GAP : 40 MSEC. GATE : -50 TO 6900 MSEC REFERENCE : WATER BOTTOM
2 ON 1 TRACE MIX	
MIGRATION VELOCITIES	SEE SECTION HEADING
MIGRATION	DIP CONTROLLED MIGRATION
TIME VARIANT FILTER	FILTER (HZ) TIME (MSEC.) 10 - 55 0 10 - 45 1500 8 - 30 4500
TIME VARIANT SCALING	LOG FIT SCALING SCALING GATES = 250 MSEC. DATUM = W.B. - 30 MSEC.

Table 5.1. The field aquisition and processing parameters of the 2D seismic dataset used in our geopressure prediction.

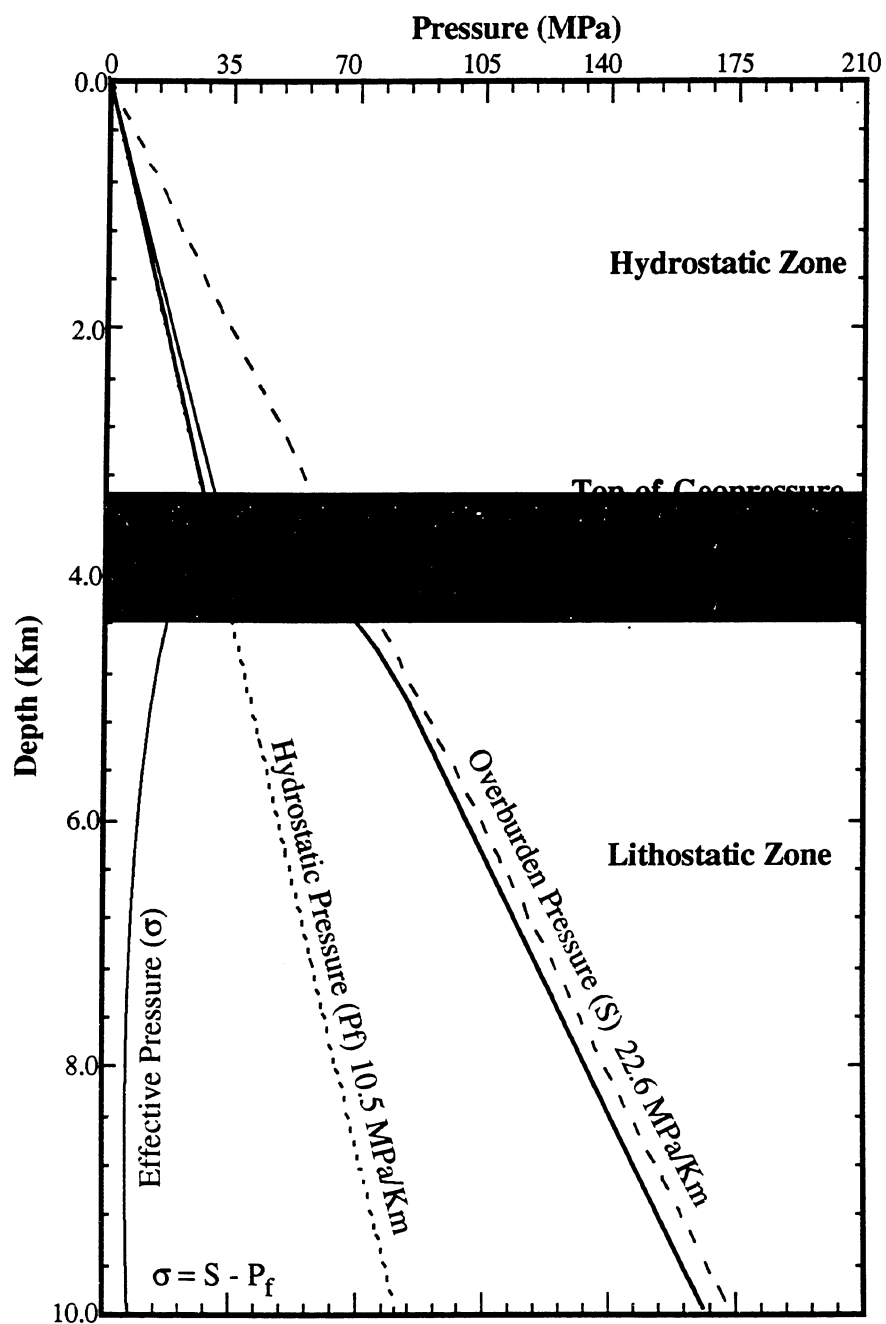


Figure 5.1. The typical pore fluid pressure profile is illustrated as a function of depth in a geopressed basin. The thick line between the hydrostatic and overburden pressure curves is the actual pore fluid pressure curve. Hydrostatic, geopressure transition, and lithostatic zones are also shown. Effective pressure is the difference between the overburden pressure and pore fluid pressure.

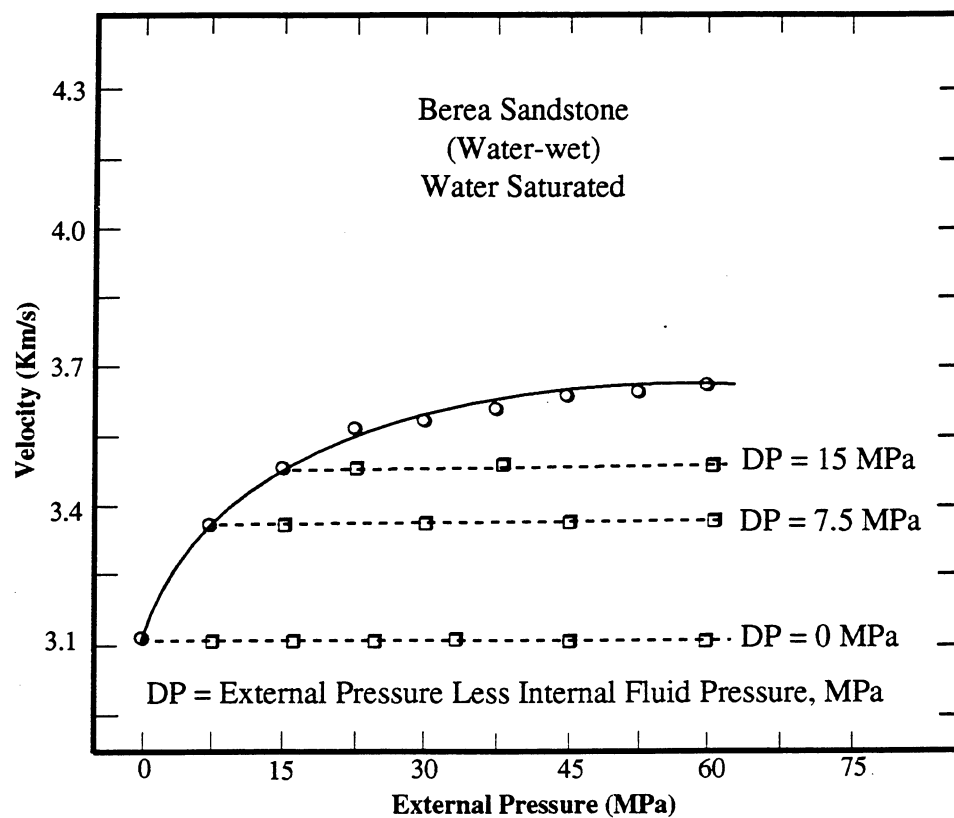


Figure 5.2. The compressional-wave velocity is shown as the function of pressures (adapted from Wyllie et al., 1958).

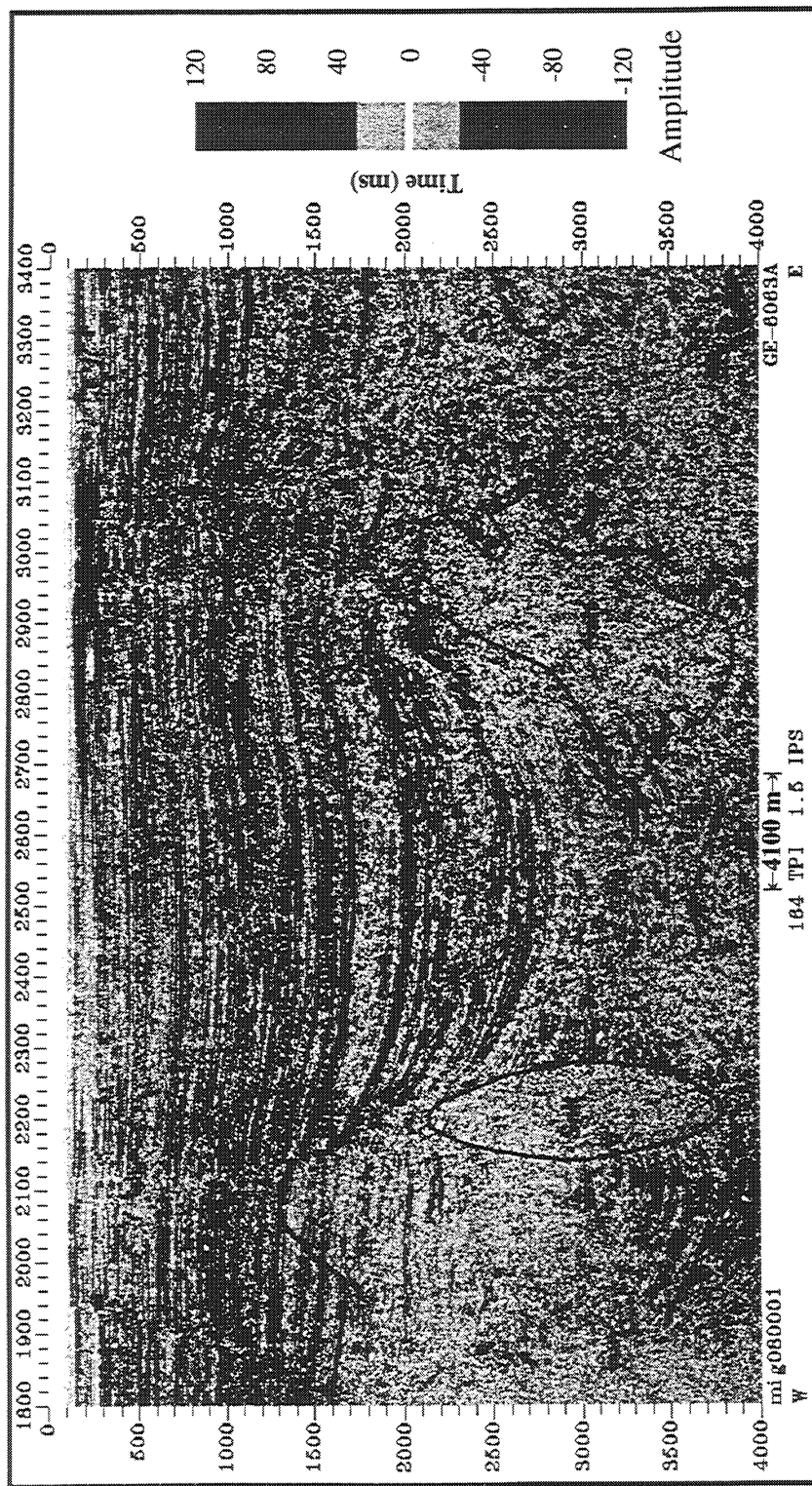


Figure 5.3. A 2D seismic line (GE-6063A) is displayed in variable density. Seismic amplitudes are dramatically weakened in several time windows. The weaker reflections are caused by geopressures, which are widely developed in the offshore Louisiana Gulf of Mexico. This seismic line is also used as the example to demonstrate our geopressure predicting technique later in the chapter.

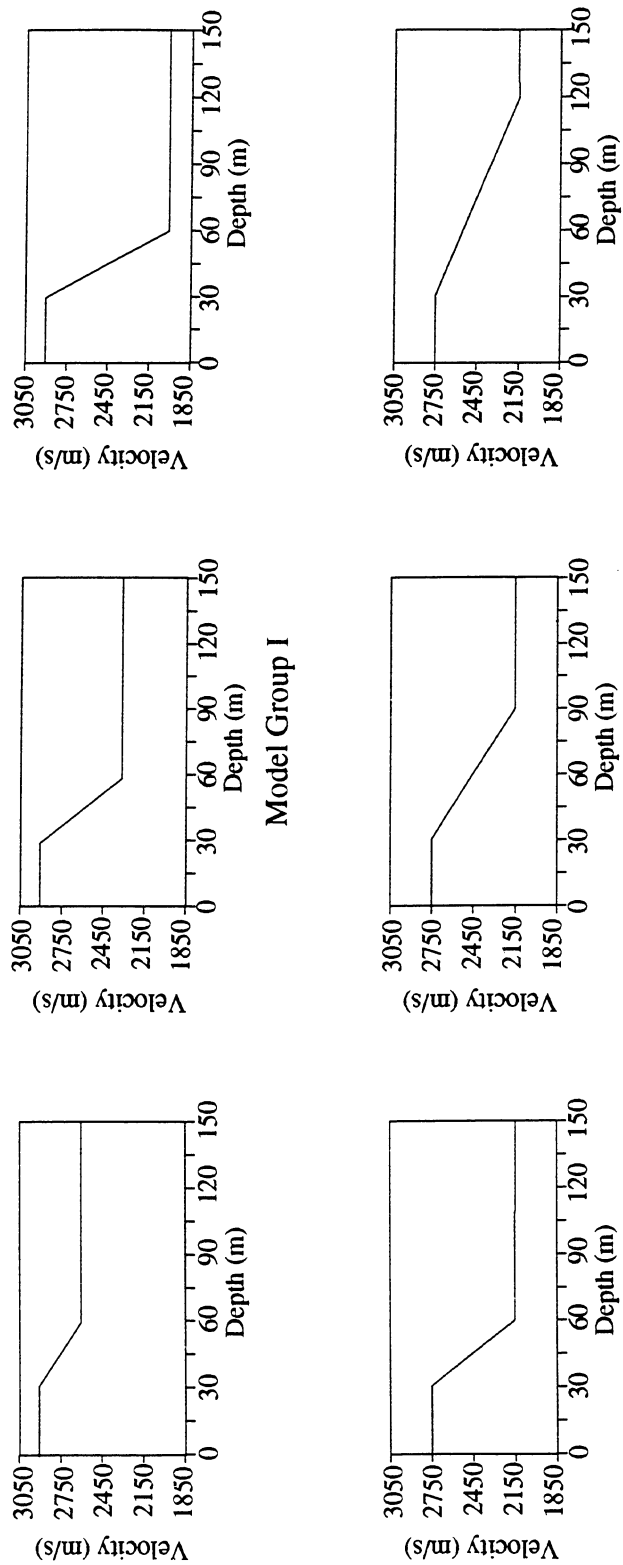


Figure 5.4 (a). Two groups of velocity transition models are developed to investigate the seismic reflection characteristics of geopressure velocity transition zone. Model group I consists of three transition models with increasing velocity contrast (top), and the model group II consists of three transition models with increasing thickness and constant velocity contrast (below).

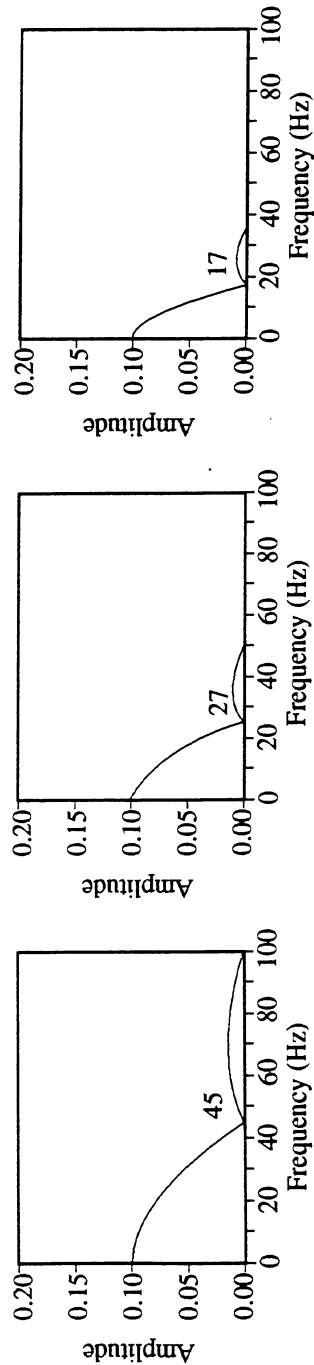
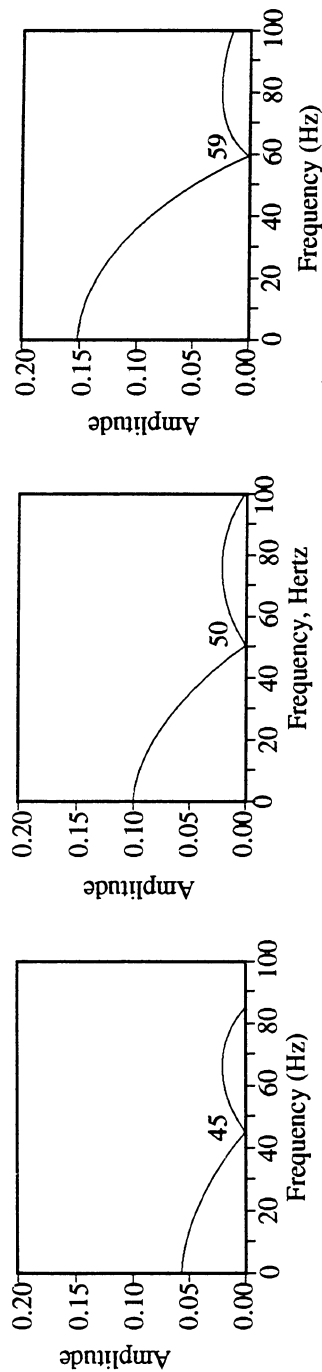
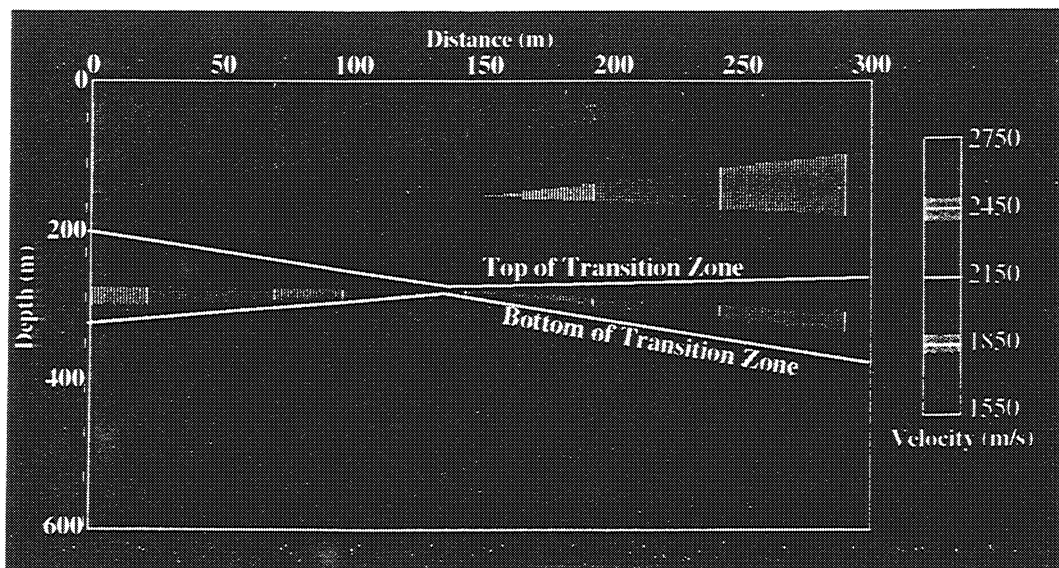
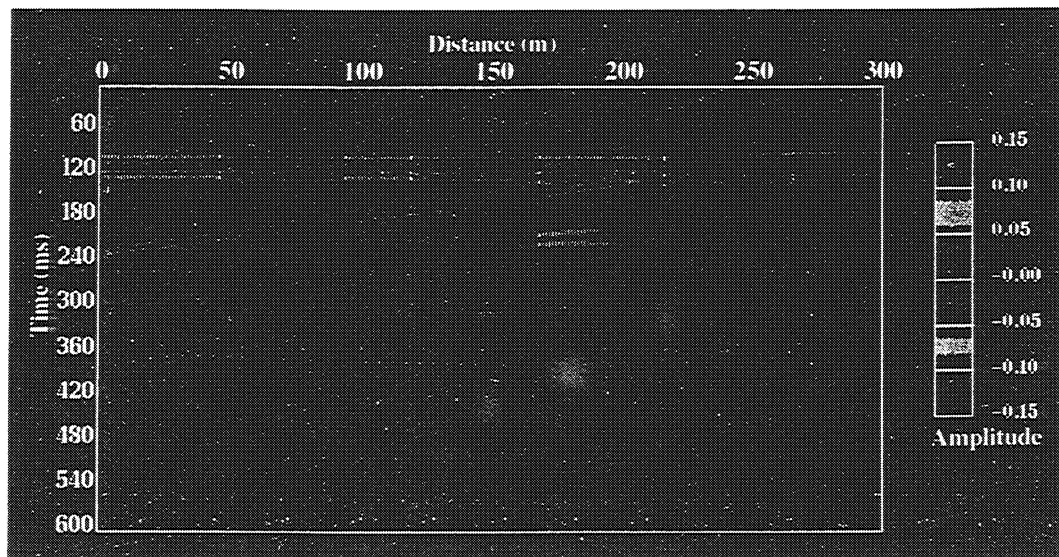


Figure 5.4 (b). The amplitude spectra of the two model groups shown in Figure 5.4 (a). For model group I (top), the increasing velocity contrasts increases the amplitude of all frequency components. The cut-off frequencies are also increased slightly. For model group II (below), the increasing thickness of geopressure transitions dramatically reduces the cut-off frequency, while the maximum amplitude on the frequency spectra is constant.

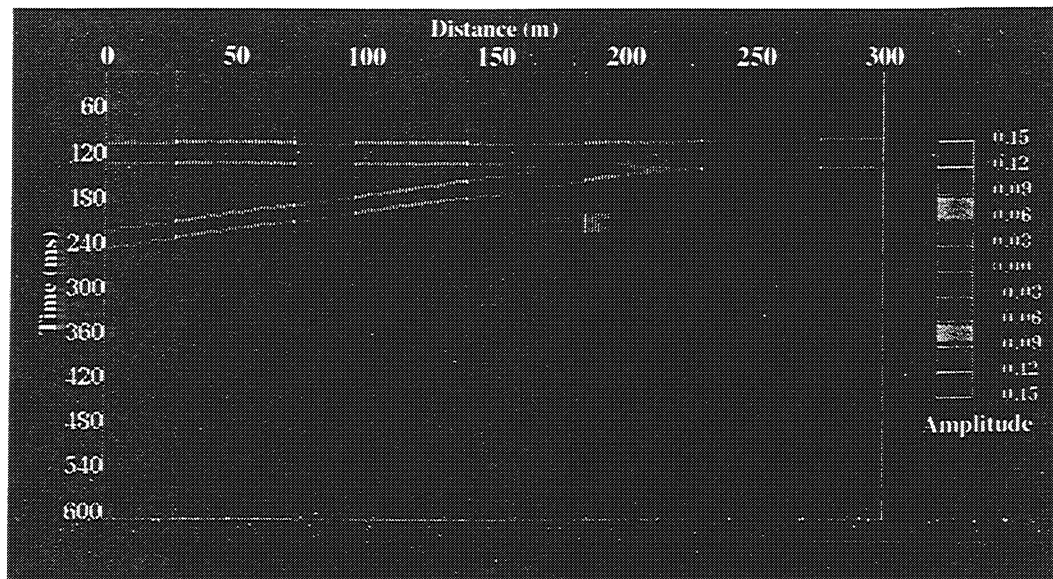


(a)

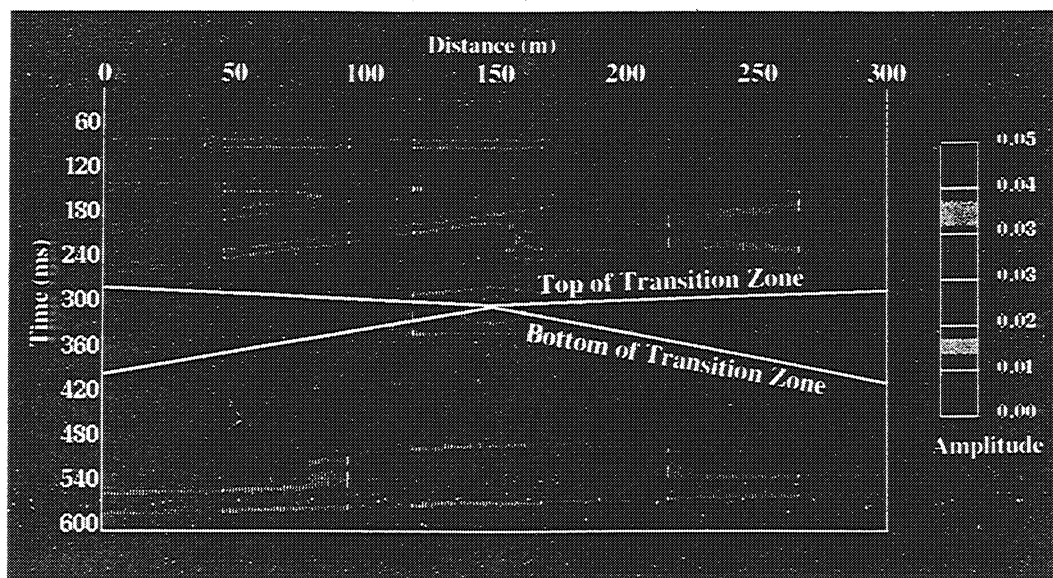


(b)

Figure 5.5. A synthetic 2D velocity model consisting of constant and transition velocity layers is shown in (a), and the modeled seismic section of (a) is shown in (b). The geopressure transition zone is annotated in the middle of the model. The transition zone has a constant velocity contrast from 2750 m/s to 2150 m/s. The thickness of the transition gradually decreases from 150 m (left) to 15 m (center), and then gradually increases to 150 m (right). The tuning effects are clearly seen at the edges of pinch-outs. The top of and bottom of the geopressure transition are barely observable in locations where the transition thickness is large.



(a)



(b)

Figure 5.6. The reflection strength section of the seismic model (Figure 5.5 (b)) is shown in (a). The filtered reflection strength using a lowpass filter is shown in (b). The filter is designed according to the reflection strength characteristics of a velocity transition zone with moderate thickness (50 m). On the resultant reflection strength section, the top and bottom of the geopressure transition zone can be interpreted directly. Compared to the velocity model in time Figure 5.7, the geopressure transition zone is well imaged.

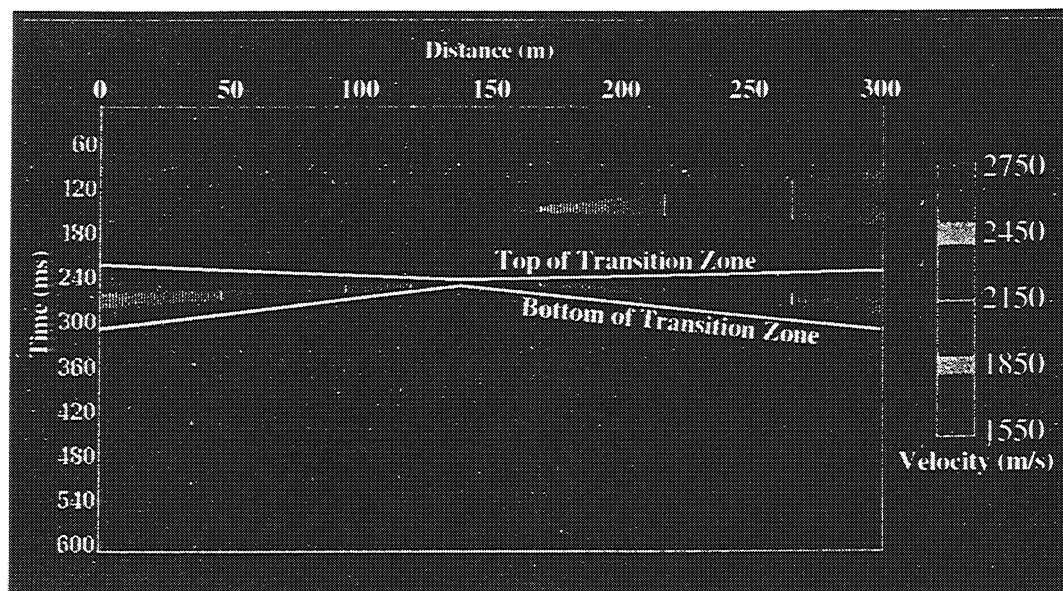


Figure 5.7. The velocity depth model is converted to two-way travel time. The top and bottom of the geopressure transition zone are annotated accordingly. The interpreted geopressure transition zone from Figure 5.6 (b) is almost identical to the velocity model.

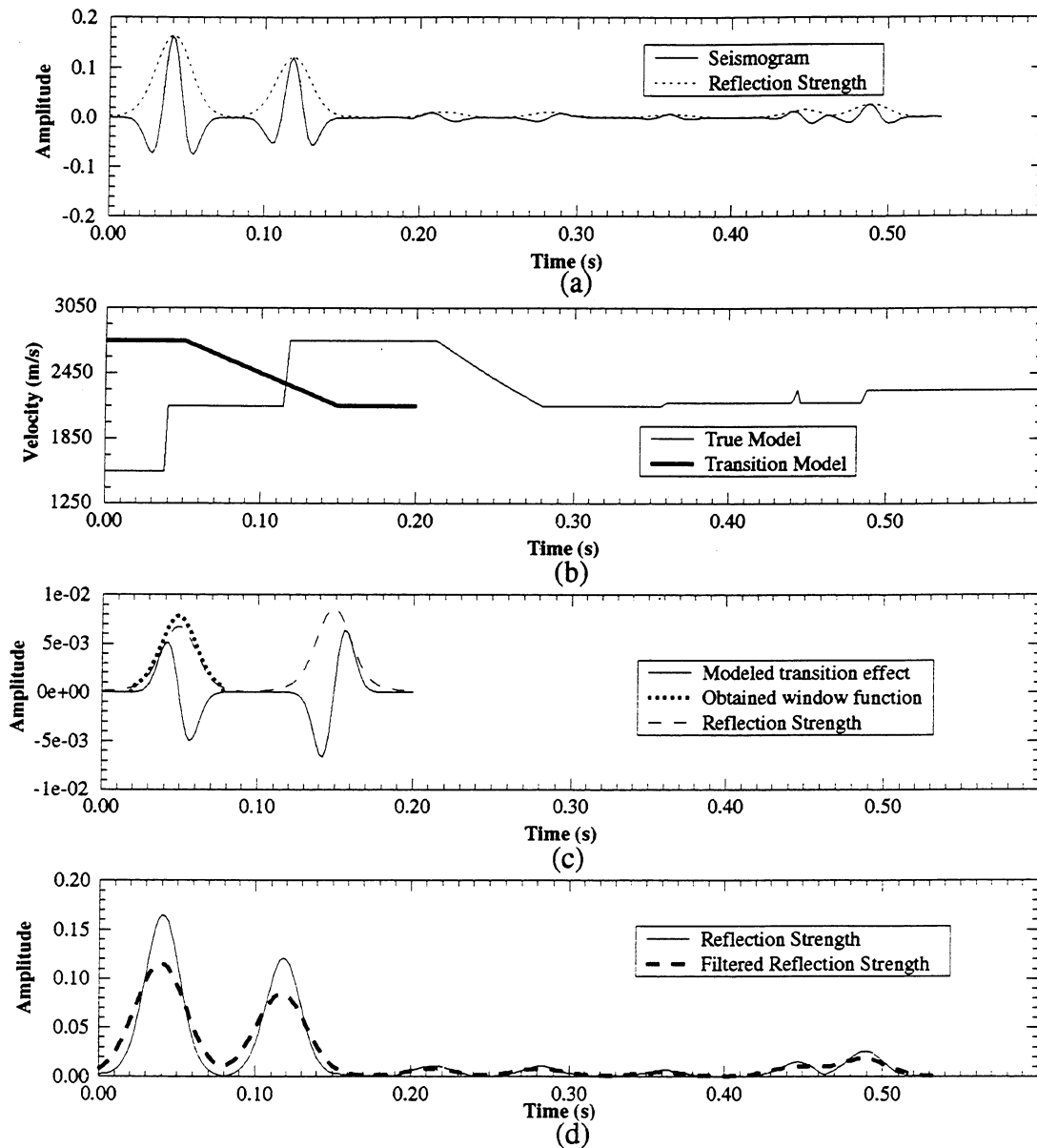


Figure 5.8. A modeled seismic trace is extracted to show the designed lowpass filter which can be used to reduce amplitude of frequency contents higher than the cut-off frequency. The modeled seismic trace and its reflection strength are shown in (a). The true velocity model and a guessed velocity transition model used to design the low-pass filter (dotted line in (c)) are shown in (b). The seismic response and the reflection strength of the transition model are shown in (c). The lowpass filter is taken as the first half of the reflection strength function shown in (c). The reflection strength of the frequencies close to the cut-off frequency is enhanced (d).

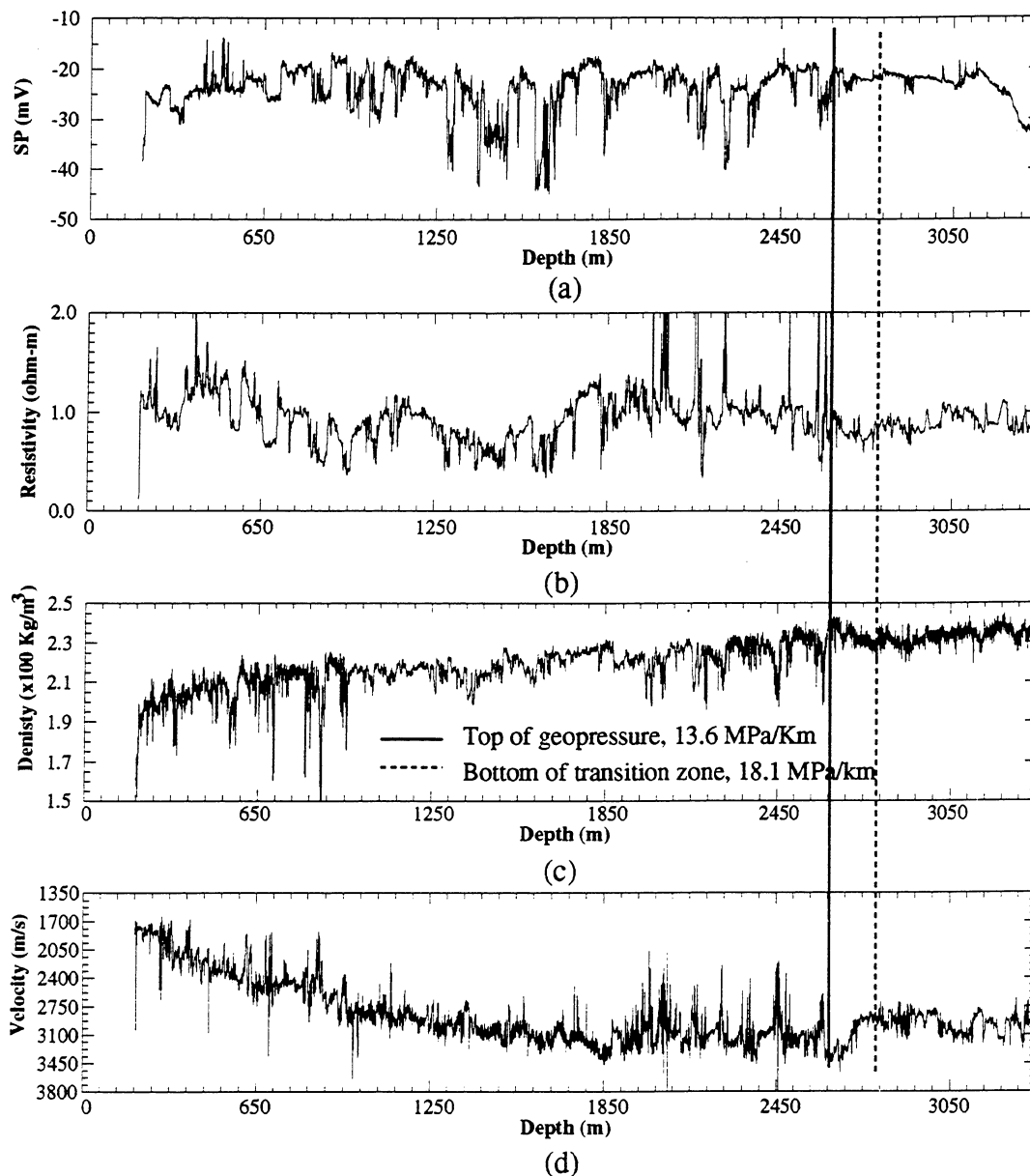


Figure 5.9. The geopressure transition zone is interpreted using well logs of EI well 331_SH_1. The SP log is used as an lithology indicator (a). The Resistivity log is shown in (b). The bulk density and sonic logs are shown in (c) and (d), respectively. The geopressure gradients of 13.6 to 18.1 MPa/Km are well correlated to the top of and bottom of the geopressure transition zone (solid and dashed lines, respectively). The velocity decreases by an amount of 23% across the geopressure transition zone (d). The density log also shows a decreasing pattern across the transition zone (c). The transition thickness is at least 177 m.

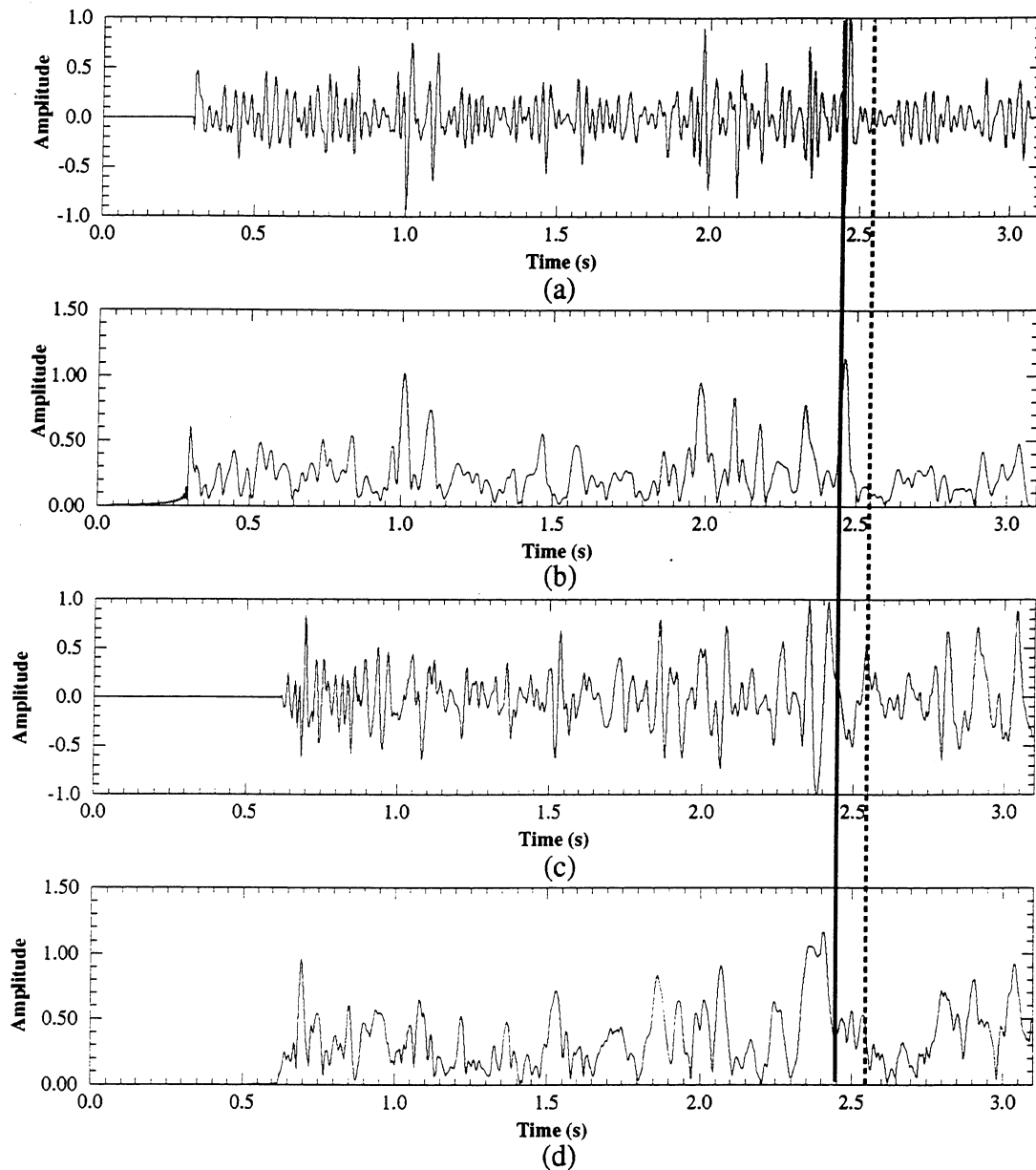


Figure 5.10. The synthetic seismogram generated from Eugene Island well 330_SH_1 is shown in (a). The seismic trace extracted from a 3D seismic survey at the same location is shown in (c). The reflection strength of the two seismic traces are shown in (b) and (d), respectively. Top and bottom of the geopressure transition zone are shown in solid and dashed vertical lines respectively.

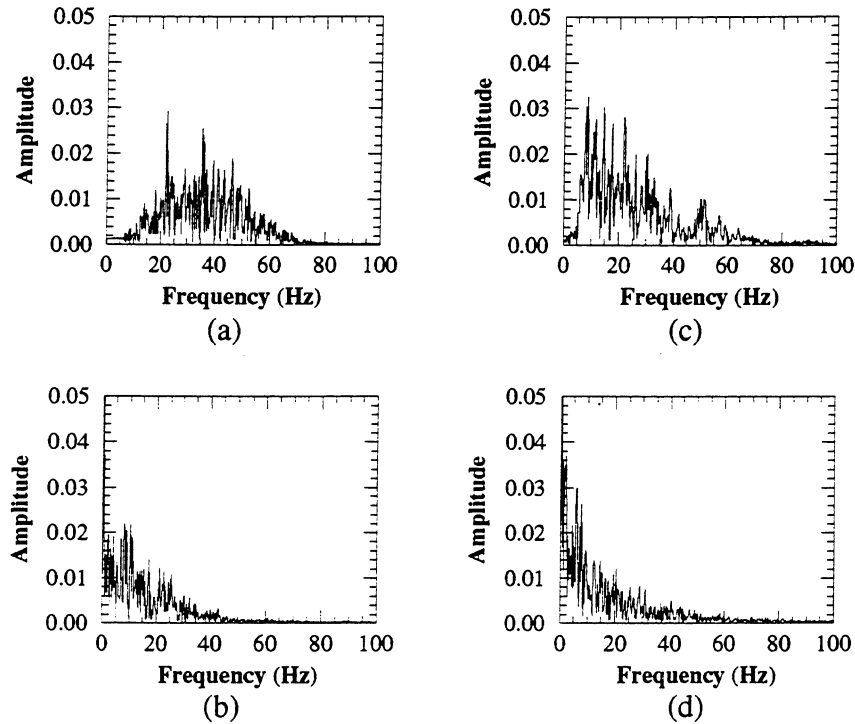


Figure 5.11. The amplitude spectra of the synthetic and real seismic traces (Figure 5.10 (a) and (c)) are shown in (a) and (c), respectively. The amplitude spectra of the reflection strength of the synthetic and real seismic traces (Figure 5.10 (b) and (d)) are shown in (b) and (d), respectively. The reflection strength derived from the complex seismic trace analysis (Taner et al., 1979) is the envelop amplitude that contains only low frequency reflections.

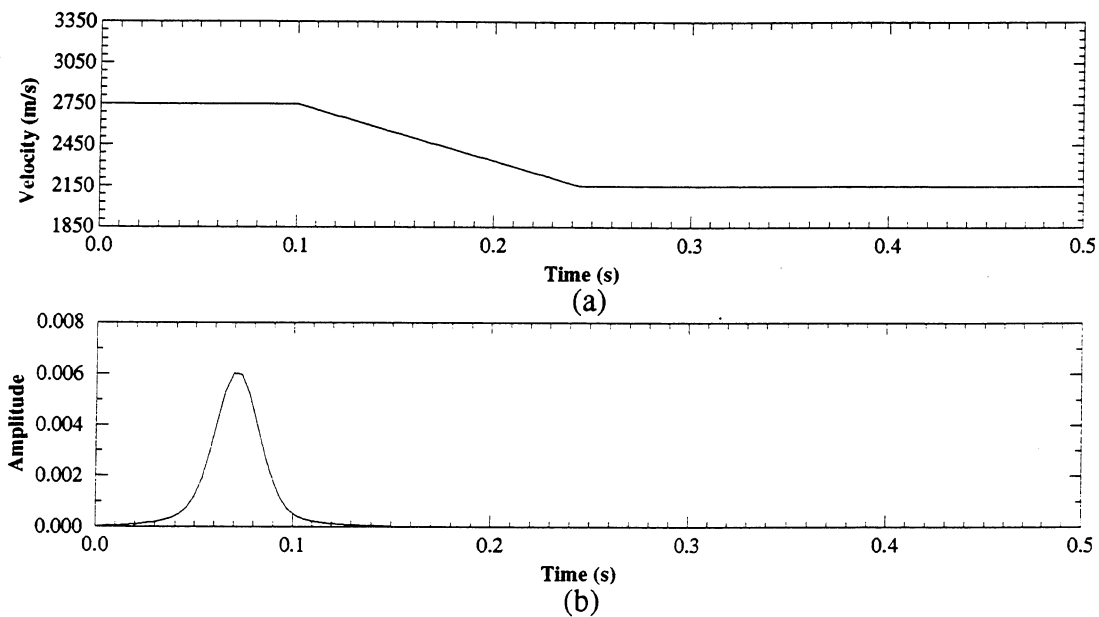


Figure 5.12. The linear velocity transition model constructed based on the sonic log of well 331_SH_1 is shown in (a). At the well, a velocity decreases of 23% across the geopressure transition zone is detected. The lowpass filter designed based on the reflection strength of the velocity transition model is shown in (b).

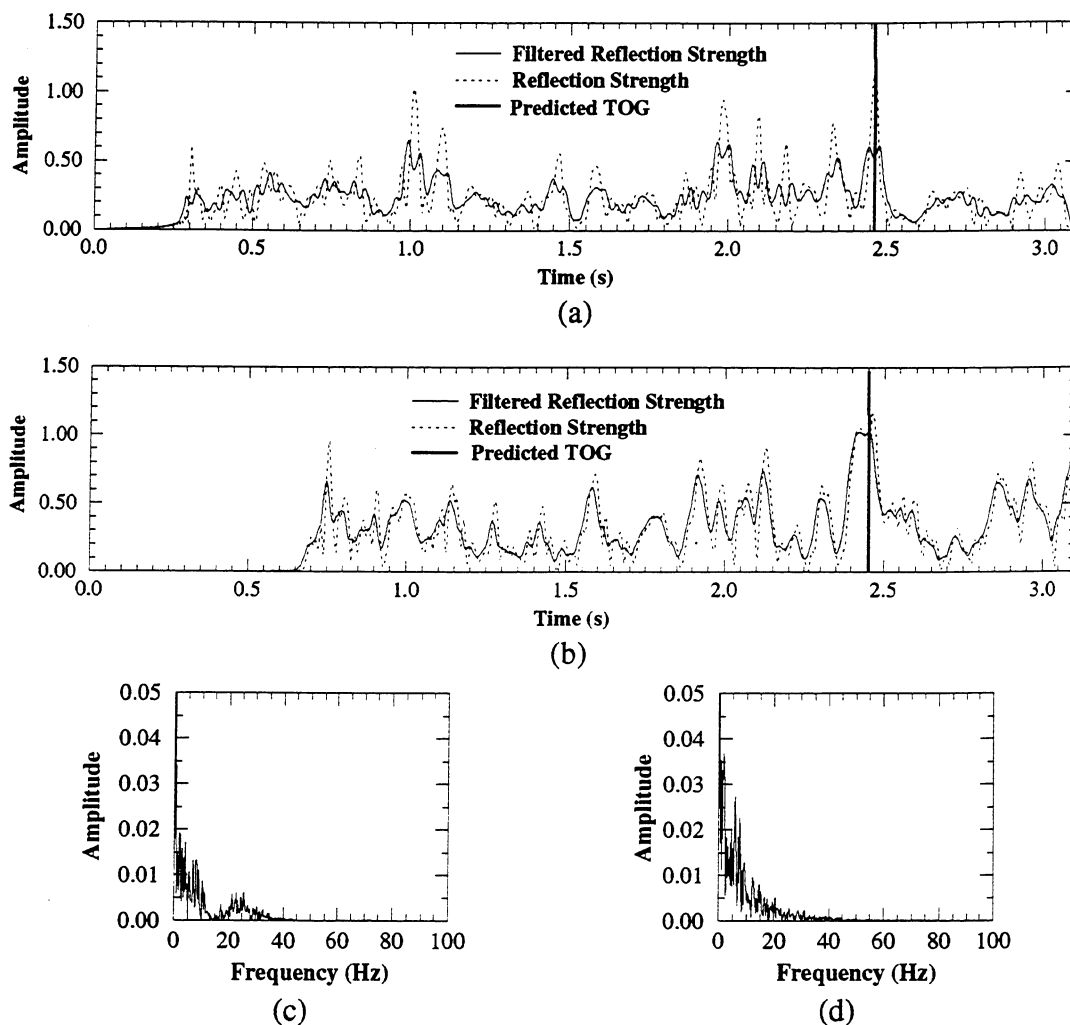
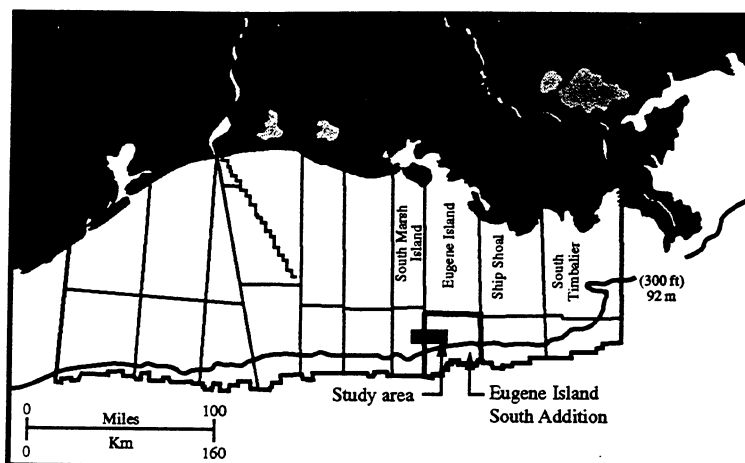
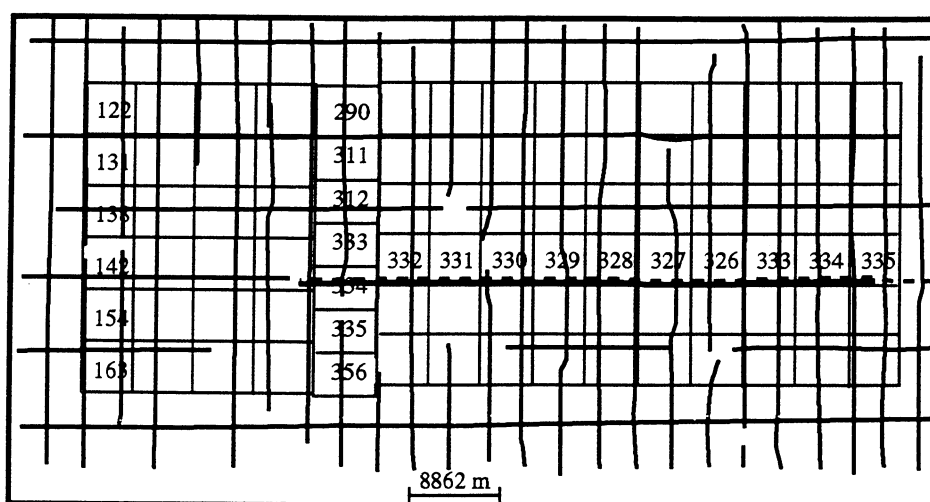


Figure 5.13. The reflection strength of the synthetic and real seismic traces are filtered using the lowpass filter shown in Figure 5.12 (b). The filtered reflection strength of the two traces are shown in (a) (synthetic seismic trace) and (b) (real seismic trace), respectively. The corresponding amplitude spectra of the synthetic and real seismic data are shown in (c) and (d). The top-of-geopressure is interpreted as the boundary between the high and low reflection strengths on the filtered reflection strength traces. The amplitude of the top-of-geopressure event is either unchanged or reduced less than other reflection events.



(a)



(b)

Figure 5.14. The geographic location of the 2D seismic survey in the South Eugene Island and South Marsh Island Areas is shown in (a). The seismic line grid of the 2D survey is shown in (b). Line GE-6063A is used to demonstrate our geopressure predicting technique (shown as dashed heavy line in the center of the survey).

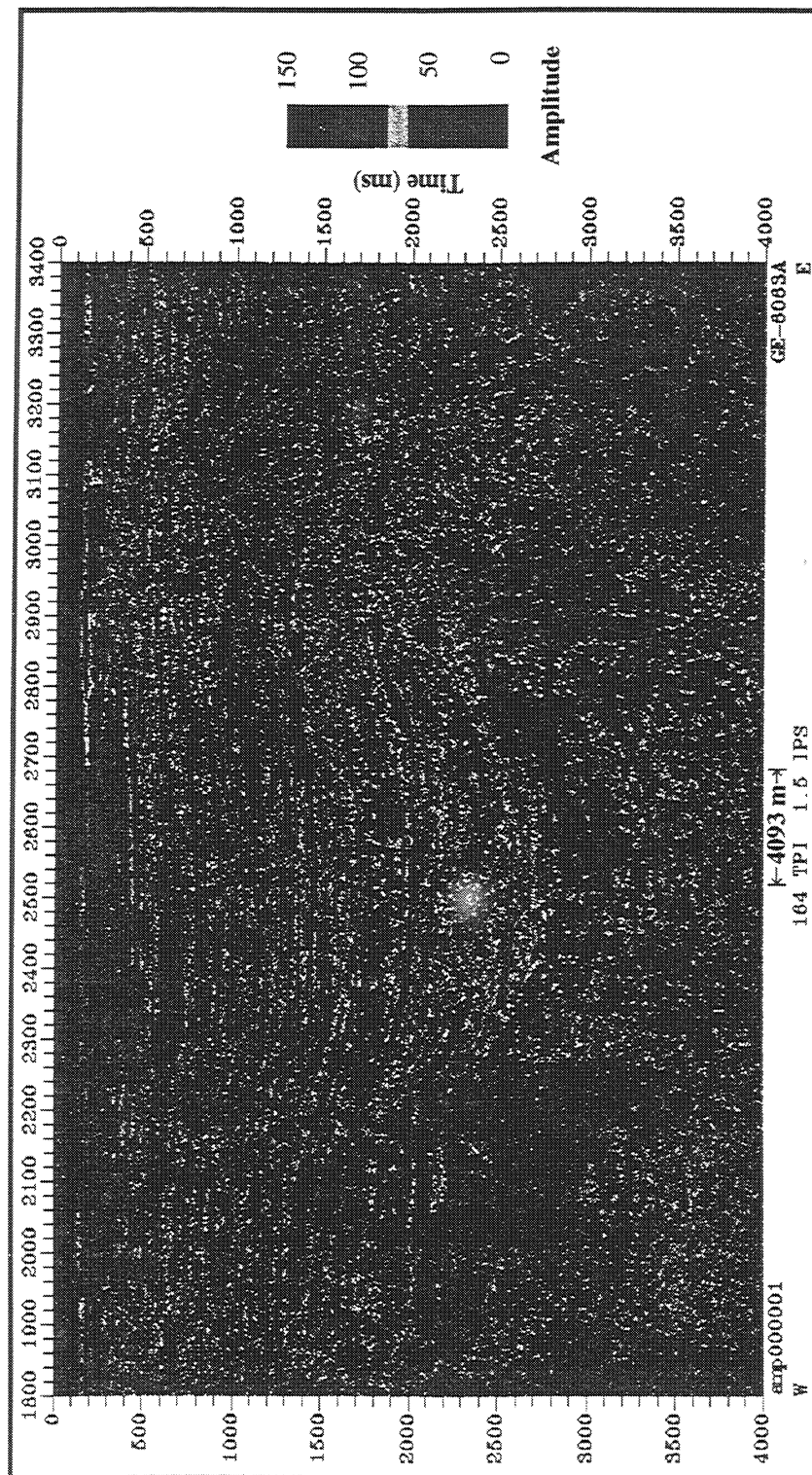


Figure 5.15. The reflection strength section of seismic line GE-6063A is computed using the complex trace analysis technique of Taner et al. (1979). The low-frequencies are preserved on such a section. Pink and red are high reflection strength and blue and green are low reflection strength. There is a distinct boundary seen in the lower one third of the section.

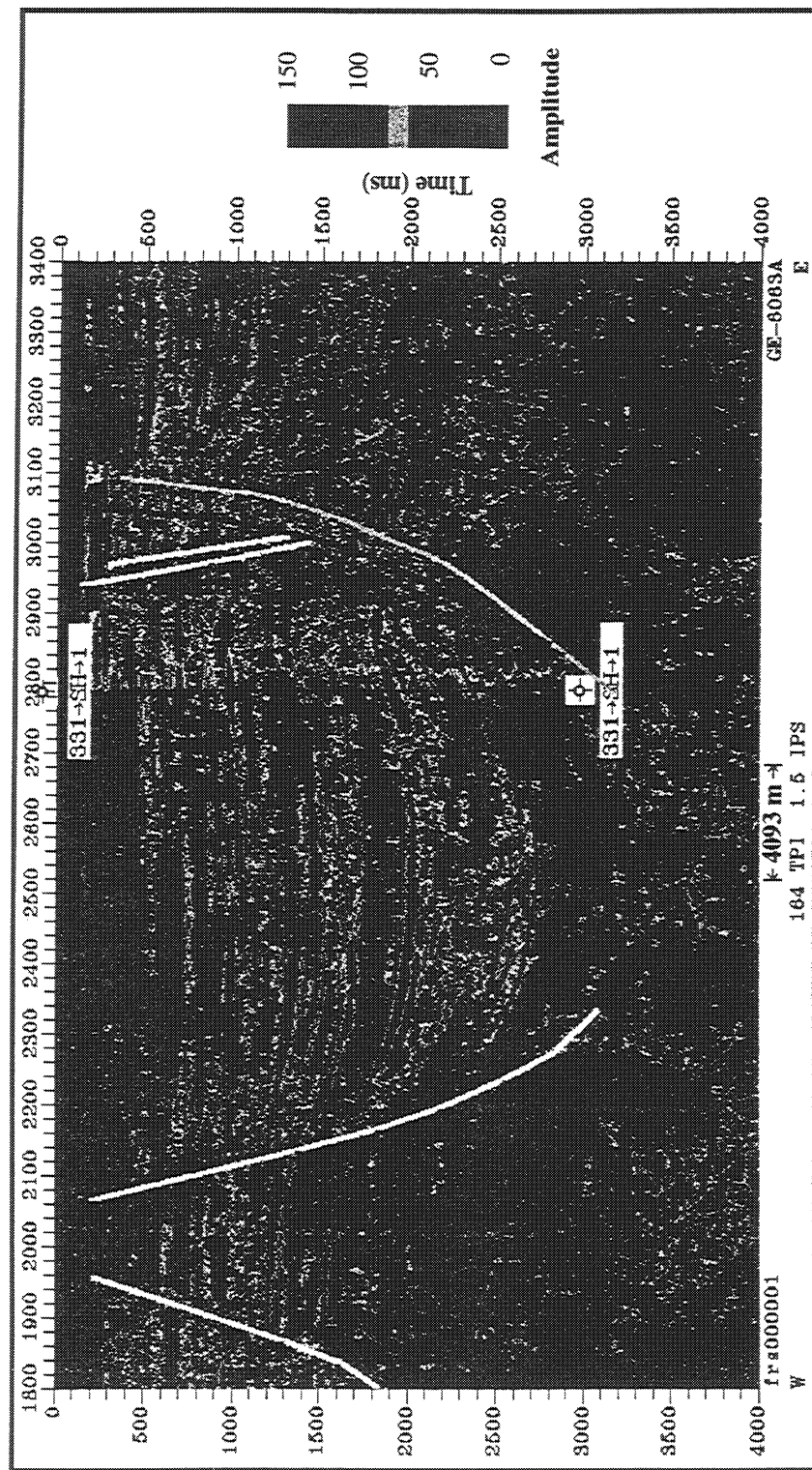


Figure 5.16. The reflection strength section of seismic line GE-6063A is filtered using only one lowpass filter designed according to the velocity across the geopressure transition zone in Eugene Island well 331_SH_1. The top-of-geopressure (TOG) is interpreted by correlating the upper most boundary between the high and low amplitude regimes using the top-of-geopressure pick in only one well as reference.

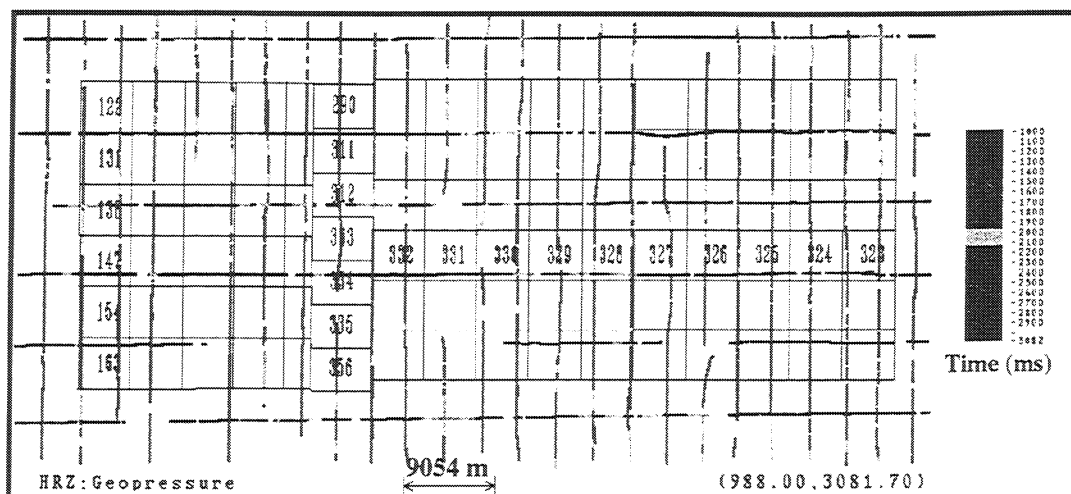


Figure 5.17. The predicted top-of-geopressure surface of the entire 2D seismic survey is display in two-way traveltime.

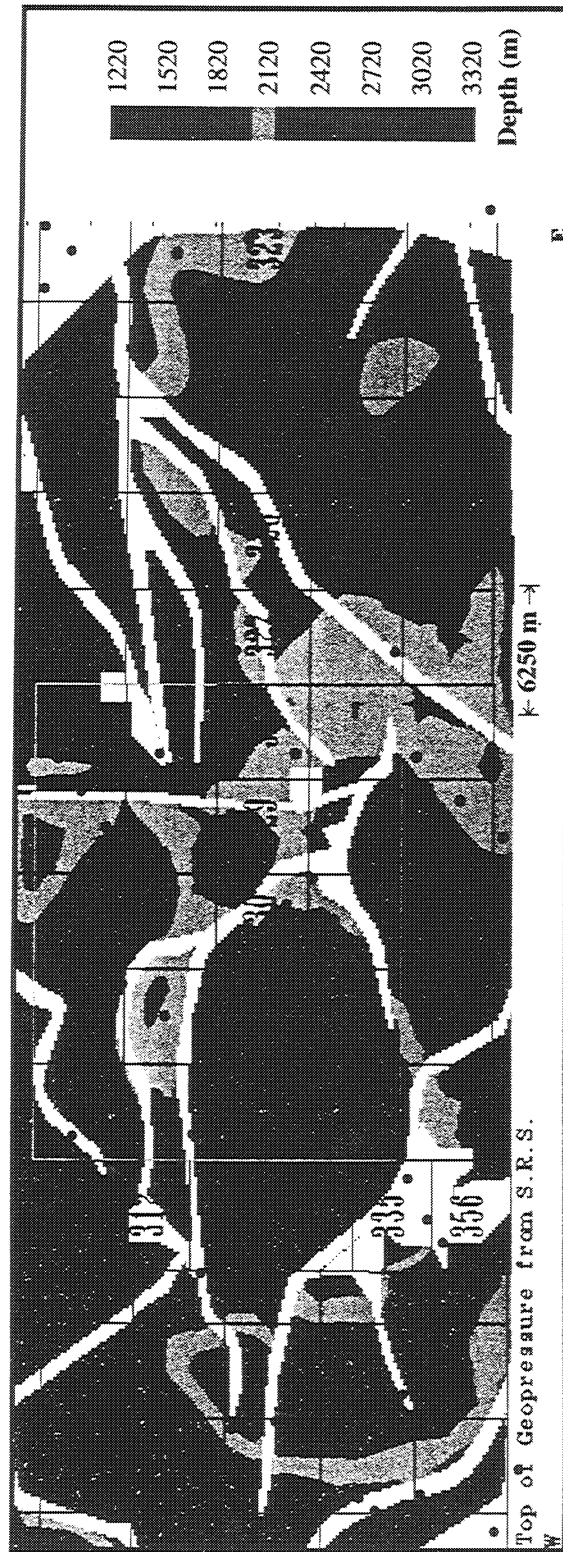


Figure 5.18. The predicted top-of-geopressure surface is converted into depth and then gridded into 150 m by 150 m grid in the study area. The velocity grid was generated from the stacking velocity used in seismic data processing. Red represents where the top-of-geopressure surface is deep. Dark green represents the uplift of the top-of-geopressure surface. Note the compartmentalization of the geopressure surface by faults (white polygons). 107 wells used to validate the interpretation are annotated as black circles.

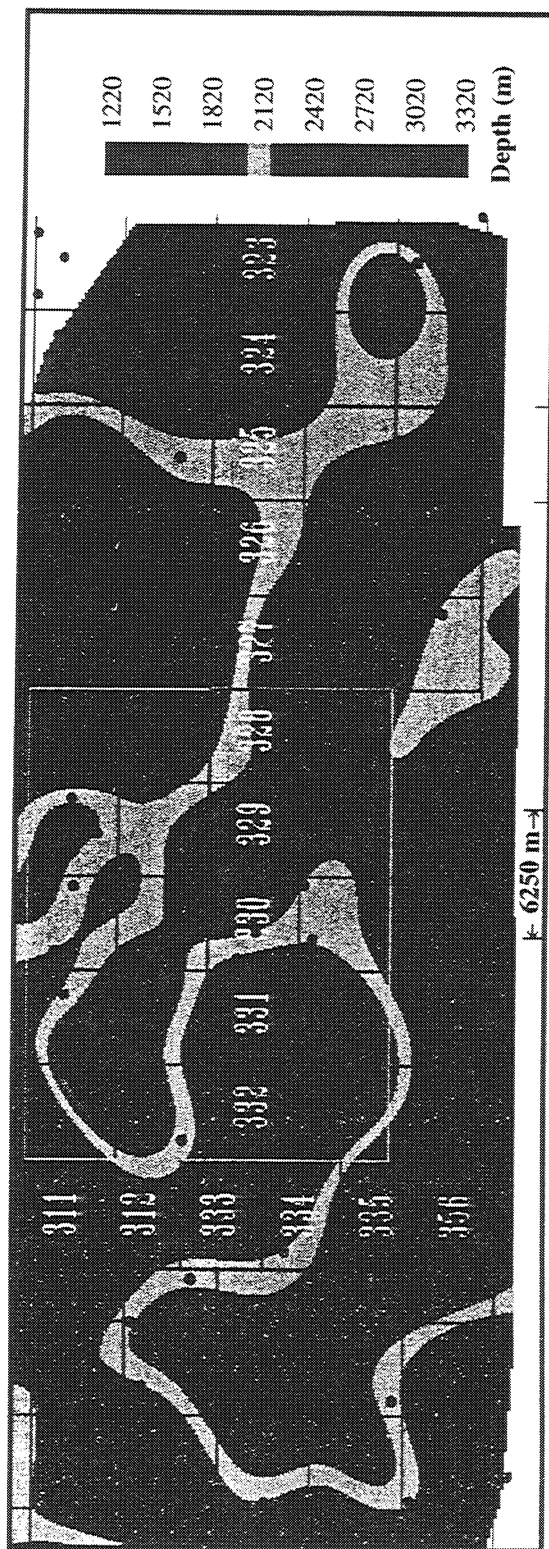


Figure 5.19. The 13.6 MPa/Km top-of-geopressure surface gridded from 107 well tops in the study area. The gridding interval is 150 m horizontally. The wells are located by black circles. Red represents where the top-of-geopressure surface is depressed , and blue represents where the top-of-geopressure surface is shallow. Faults were not integrated into the gridding.

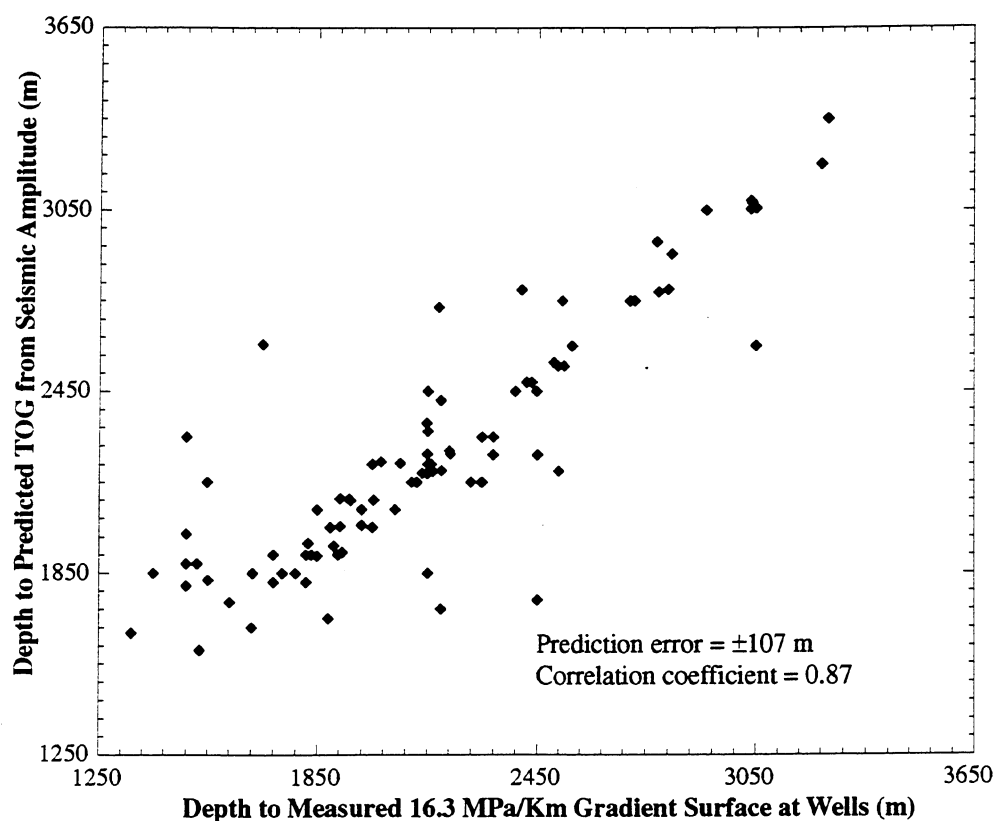


Figure 5.20. The predicted top of geopressure at well location is plotted against the measured 13.6 MPa/Km geopressure gradient surface determined at wells. The outliers are due to presence of complex geological structures (such as faults or salt diapirs). The relative error is less than 10% of the depth to top-of-geopressure.

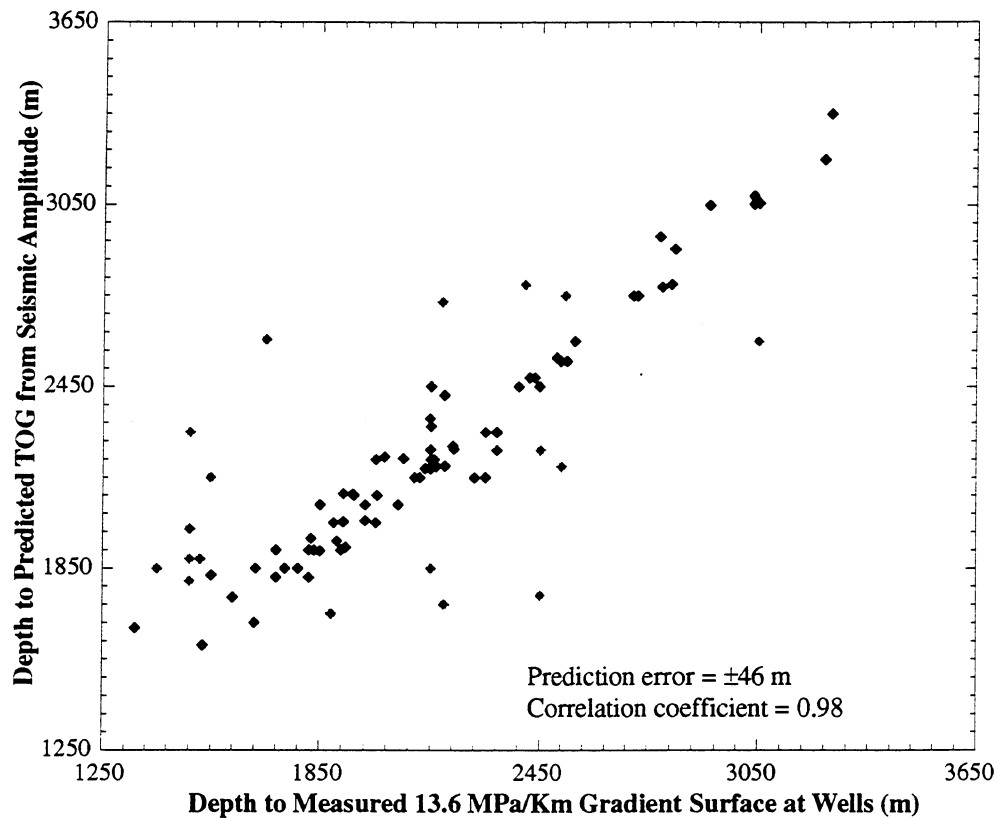
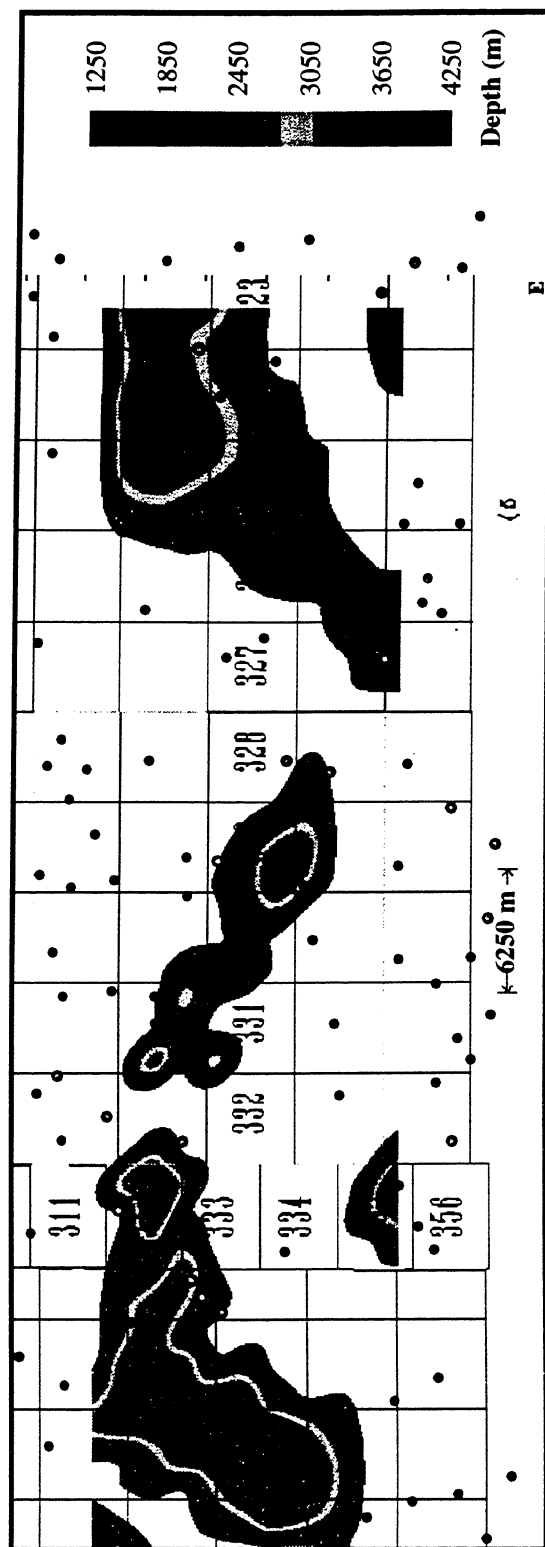


Figure 5.21. If we exclude the wells in the areas with complex geological structures, the predicted top-of-geopressure surface is in good correlation with the geopressure measured at the other well locations. The outliers are marked by light grey.



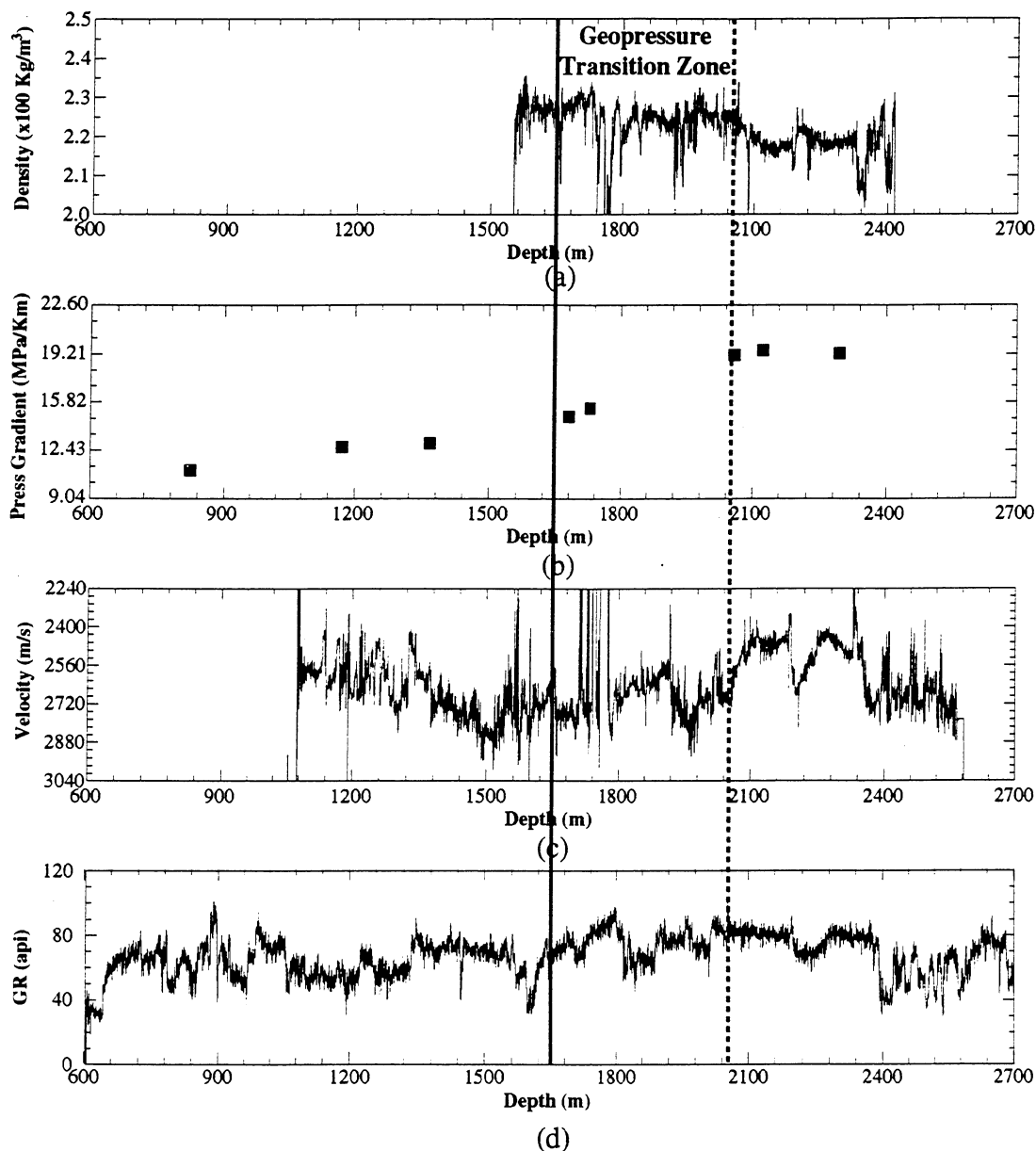


Figure 5.23 (a). The density, pressure gradient, velocity, and GR logs measured in well 316_PZ_A-2 are displayed in (a), (b), (c), and (d), respectively. Velocity decreases from 2583 to 2207 m/s (c), corresponding to the pore fluid pressure gradient increasing from 13.6 to 18.1 MPa/Km. A 17% velocity decrease is accounted by the pore fluid pressure gradient change across the geopressur transition zone. The thickness of the transition zone is 396 m. No obvious density transition is observed.

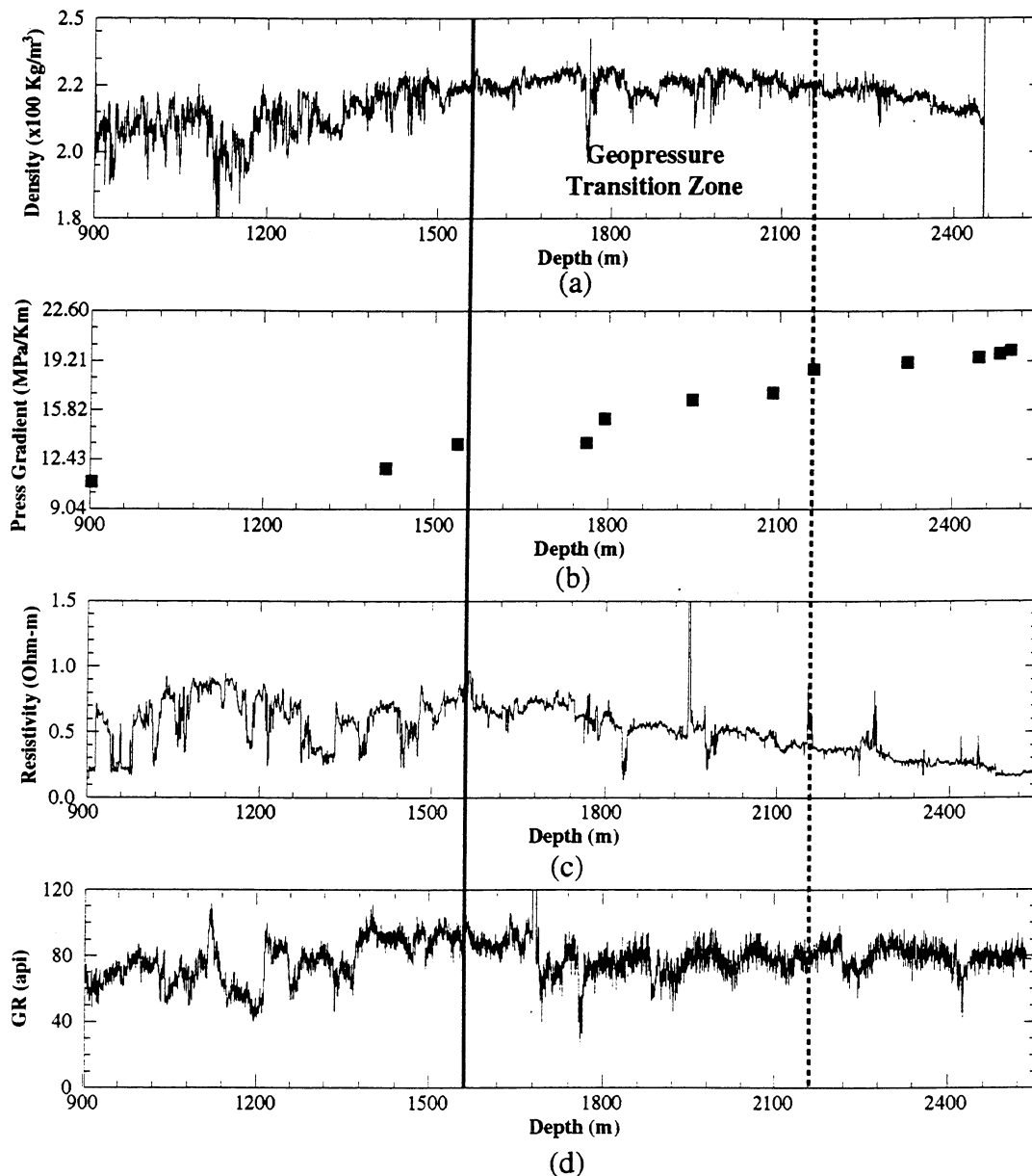


Figure 5.23 (b). The density, pressure gradient, resistivity, and GR logs measured in well 316_PZ_A-3 are displayed in (a), (b), (c), and (d), respectively. Since resistivity is closely related to sonic velocity in the study area (see Chapter 2), the resistivity decreases from 0.8 to 0.4 ohm-m (c), corresponds to the pore fluid pressure gradient increase from 13.6 to 18.1 MPa/Km. The sonic velocity is expected to decrease proportionally. The thickness of the transition zone is 610 m. The density log shows a decreasing pattern similar to that of the resistivity log.

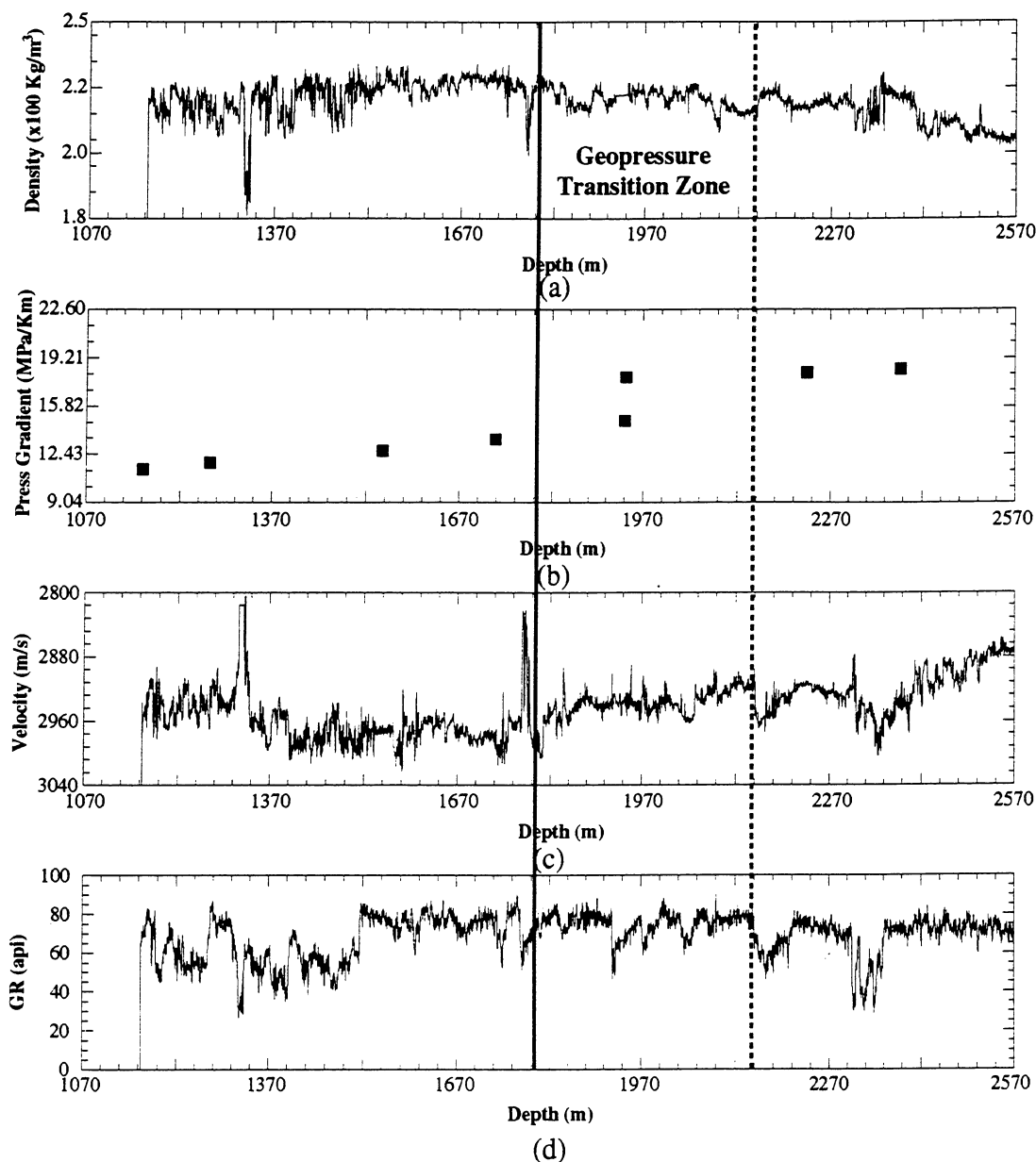


Figure 5.23 (c). The density, pressure gradient, velocity, and GR logs measured in well 316_PZ_A-6 are displayed in (a), (b), (c), and (d), respectively. Velocity decreases from 2583 to 2258 m/s (c), corresponds to the pore fluid pressure gradient increases from 13.6 to 18.1 MPa/Km. A 15% velocity decrease is accounted by the pore fluid pressure gradient increase across the geopressure transition zone. The thickness of the transition zone is 363 m. A density transition is also observed.

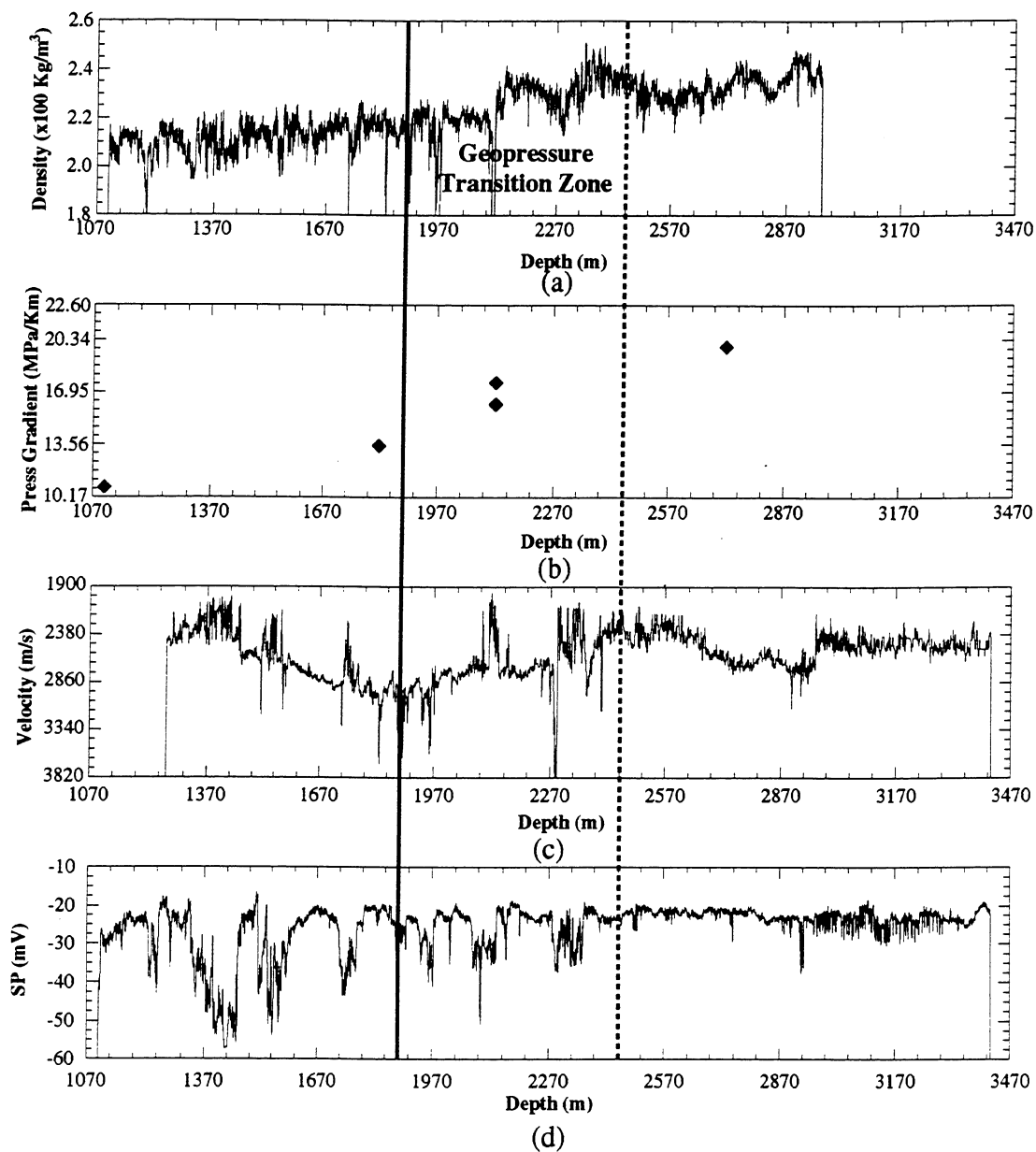


Figure 5.23 (d). The density, pressure gradient, velocity and SP logs measured in well 330_PZ_B-13 are displayed in (a), (b), (c), and (d), respectively. Velocity decreases from 2628 to 2102 m/s (c), corresponds to the pore fluid pressure gradient increase from 13.6 to 18.1 MPa/Km. A 25% velocity decrease is accounted for the pore fluid pressure gradient increase across the geopressure transition zone. The thickness of the transition zone is 579 m. The density transition is not as obvious as that of the sonic velocity.

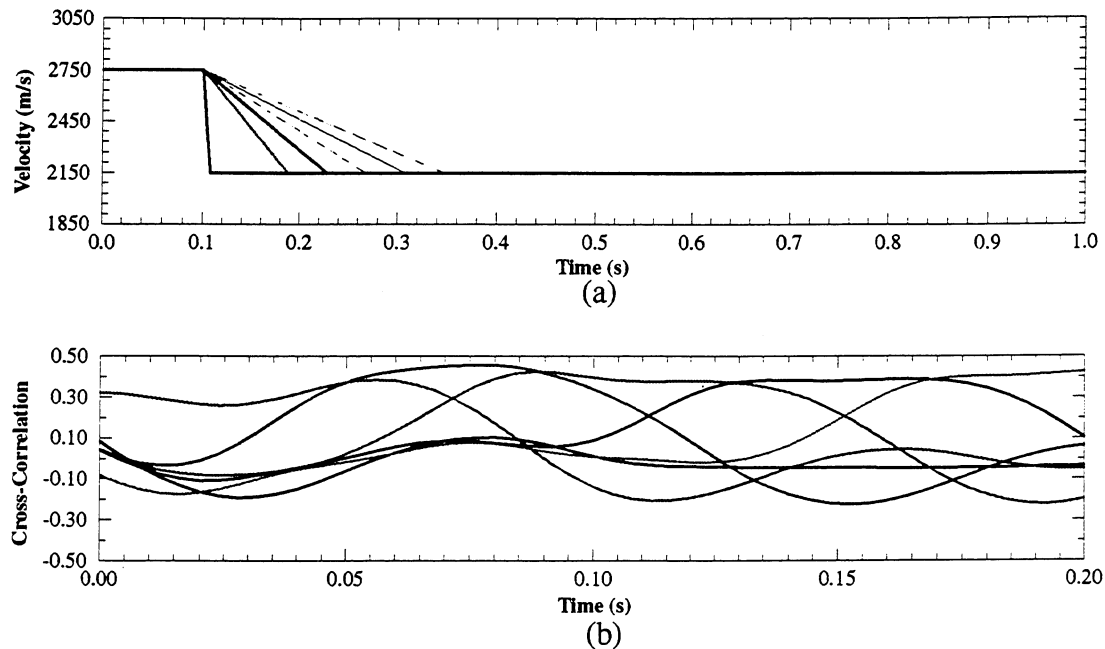


Figure 5.24. Our quantitative geopressure prediction method involves constructing velocity transition models (a), generating synthetic seismograms and their reflection traces, and computing the cross-correlation between the modeled and real reflection strength (b). The transition model whose reflection strength has the maximum correlation coefficient is chosen as the best transition model caused by the geopressure transition zones. Then a low-pass filter is constructed from the reflection strength function of the the chosen velocity model. The filter is then applied to the reflection strength trace of the seismic data to enhance the amplitude of top of the geopressure transition zone. This process is then performed on each seismic trace of Line GE-6063A (see Figure 5.25).

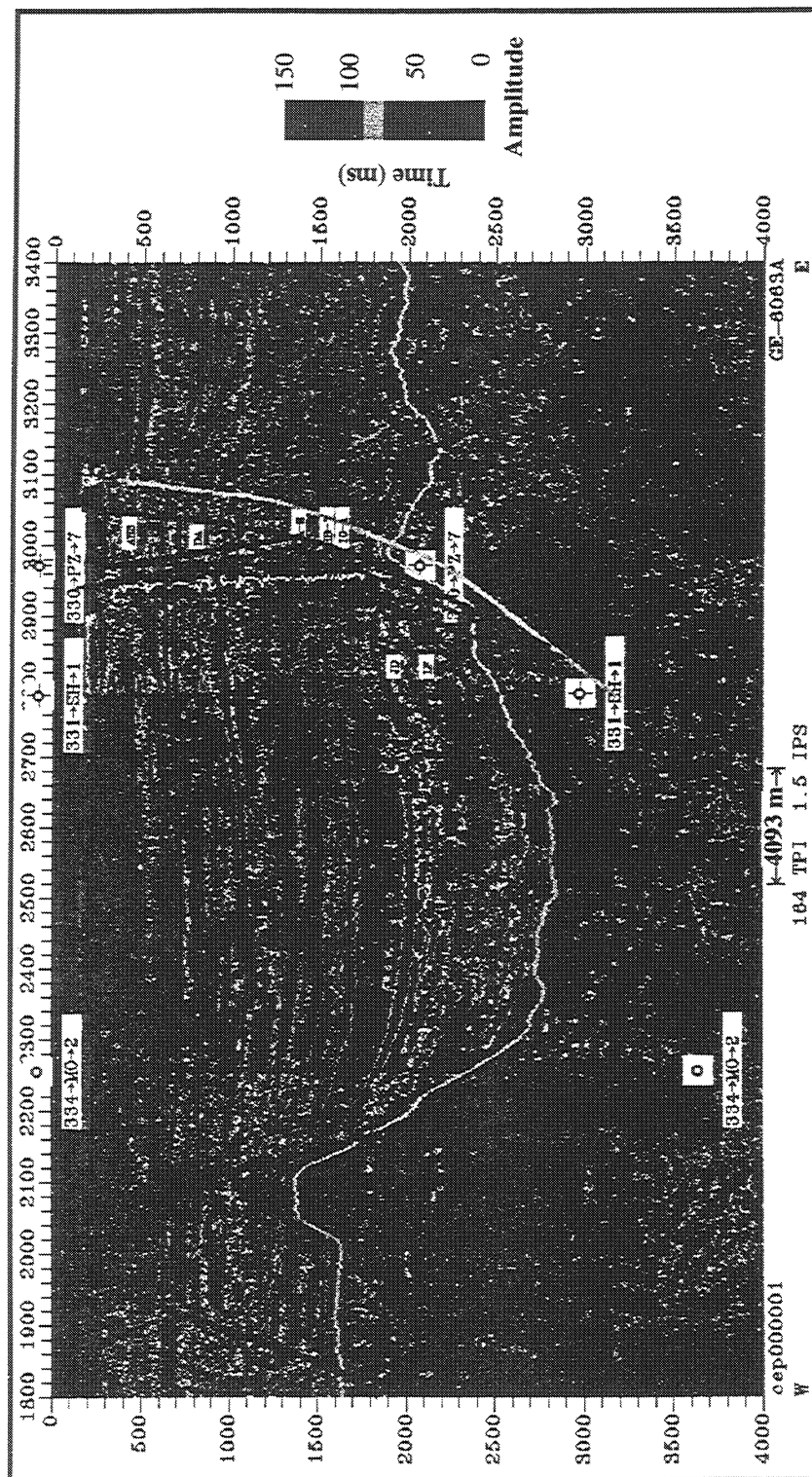


Figure 5.25. Flooding surfaces, the previously predicted top-of-geopressure (dark pink), and the final, predicted top and bottom of geopressure transition zone are superimposed on the filtered reflection strength. Three wells are also projected (< 300 m) onto the section. Note the predicted top-of-geopressure surface is in good agreement with those detected in the wells.

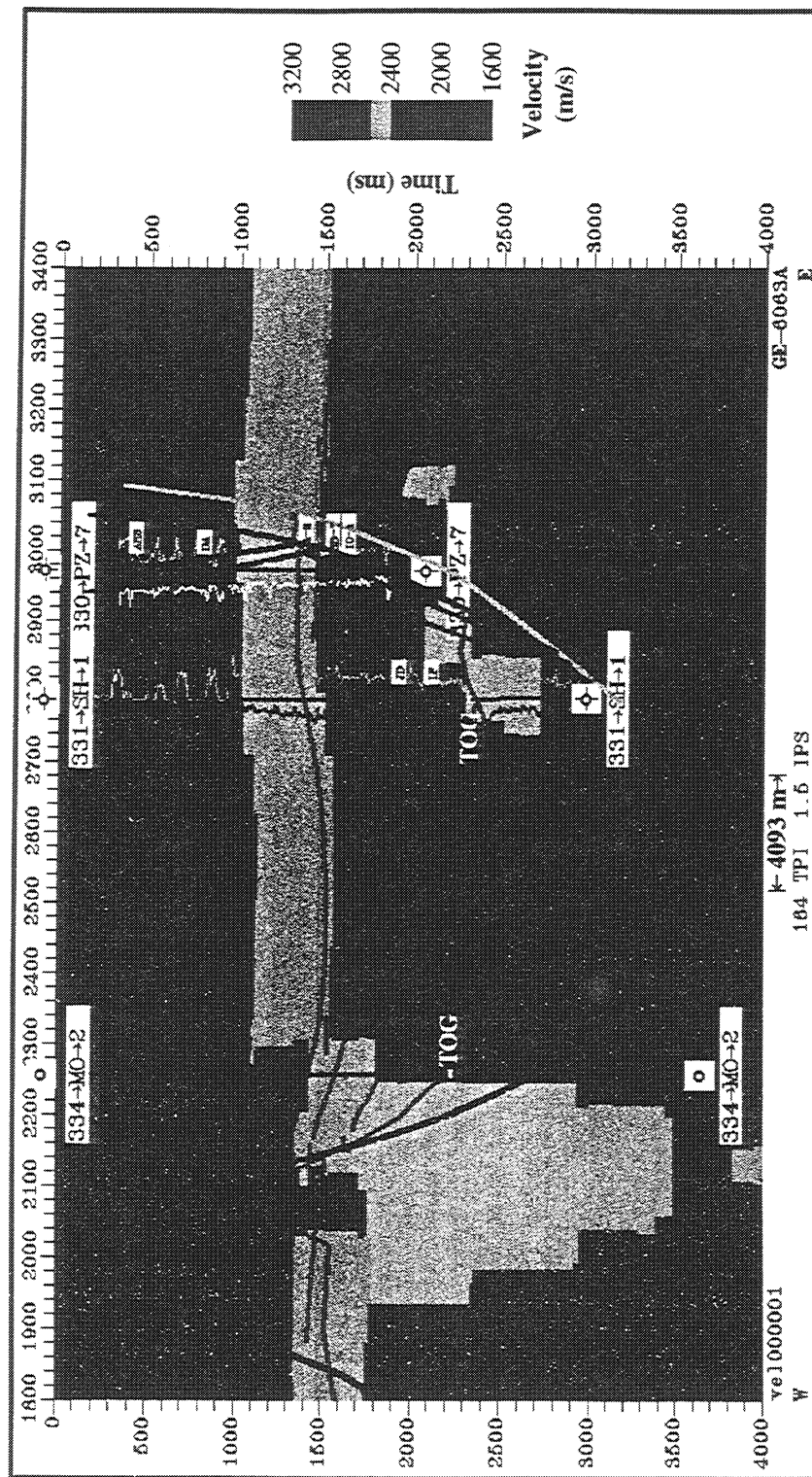


Figure 5.26. Several major flooding surfaces and the predicted top-of-geopressure surface (the deepest horizon) are displayed along the interval velocity section derived from stacking velocity of line GE-6063A. This velocity section is used to convert geopressure prediction results from two-way traveltime to depth.

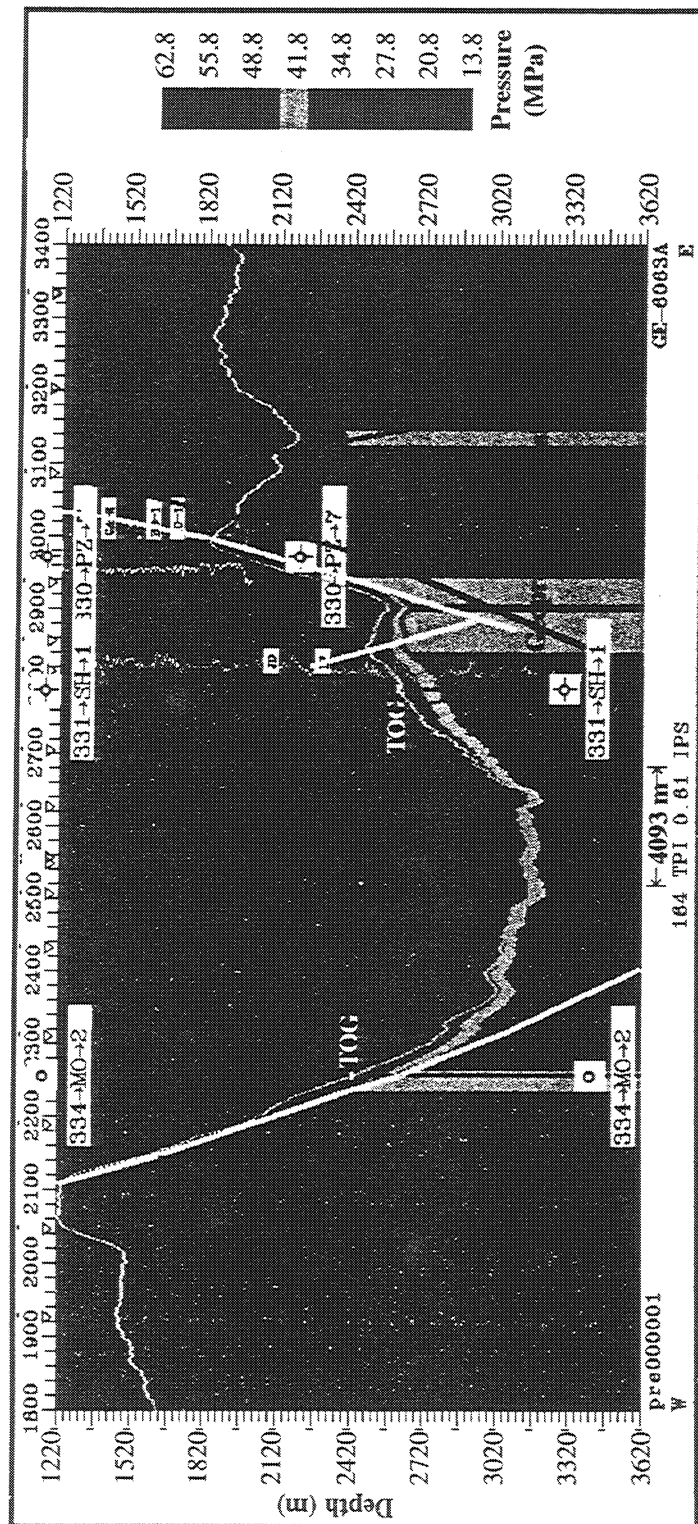


Figure 5.27. The predicted top-of-geopressure surface, the bottom of geopressure transition zone, and the pore fluid pressure predicted using our quantitative predicting method. The two predicted surfaces (iso-gradient surfaces) are converted to depth, and the pore fluid pressures in geopressure transition zone are computed using the interpolated pressure gradients.

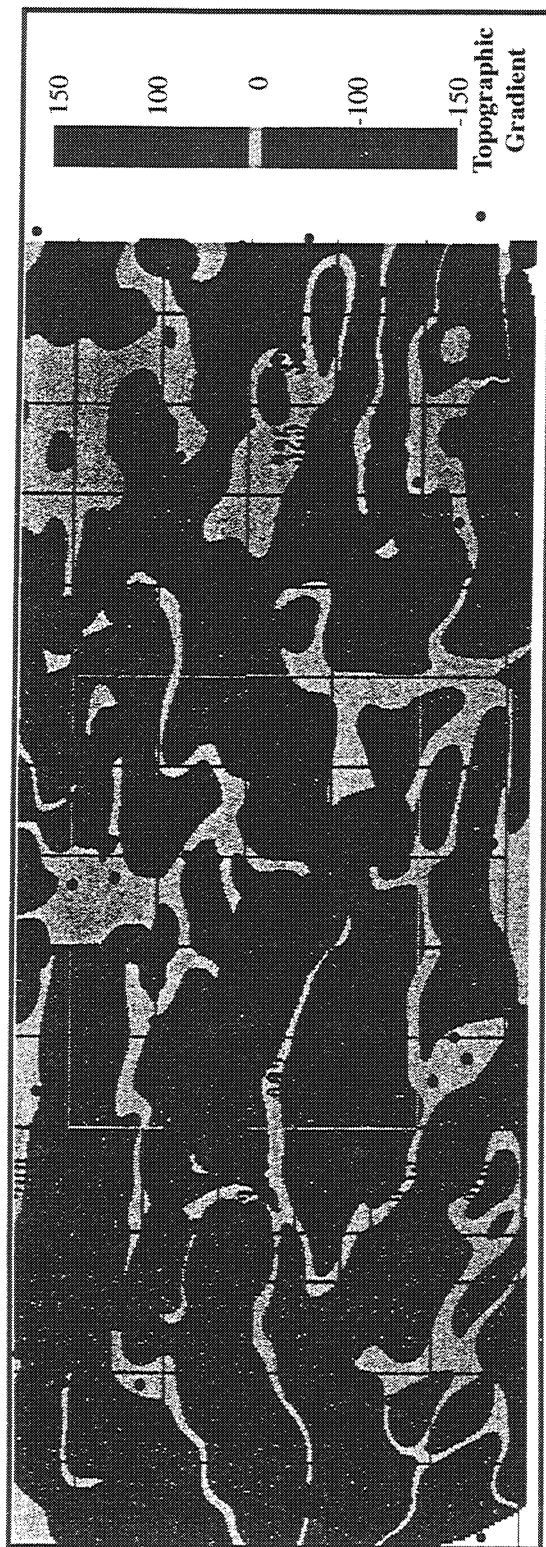


Figure 5.28. The north-south horizontal topographic gradient of depth to the predicted top-of-geopressure surface is displayed with the oil (solid green) and gas (solid red) fields discovered in previous years. The Eugene Island Block 330 Field is one of the most prolific oil fields in the US offshore Gulf of Mexico.

Task Five - Modeling

Larry Cathles - Task Manager

OBJECTIVE:

The objectives of the modeling task as set forth in the DOE proposal were to address:

- the cause of pressure, temperature, fluid chemical, and porosity anomalies near the Red Fault,
- the possible sources of oil and gas moving up the fault, and
- the causes of organic and inorganic chemical alteration near the fault.

This was to be done realistically and with the aim of facilitating the interpretation of data collected in the study area. Particular attention was to be focused on: (1) porosity and excess pressure development in the RVE, (2) hydrocarbon maturation in the RVE, (3) detailed fluid flow near the fault focusing on the detailed distribution of high permeability sands, (4) the effects of salt diapirism on subsurface temperatures, (5) the effects of fault movement on fault permeability and fluid venting out of the fault, (6) the effects of gas venting on oil migration, (7) the transport of oil as a separate phase up the fault, and (8) the effects of fluid flow (water, gas, and oil) on rock chemistry and mineralogy. The modeling was to be carried out in 3D as well as 2D.

No computer software existed that was adequate to these tasks. To even attempt to interpret specific geologic data, the models needed to couple disparate phenomena such as faulting, salt diapirism, sealing and overpressure development, temperature and fluid flow, and needed to do so realistically- specifically for the configuration of faults and salt domes in the South Eugene Island Block 330 area and in three dimensions. To fill these needs we have, in collaboration with a finite element modeling company, the Computational Mechanics Corp. of Knoxville, Tennessee, developed a basin modeling system capable of investigating the highly coupled phenomena associated with hydrocarbon migration up the Red Fault of the South Eugene Island Minibasin, and applied that modeling system to the geologic data collected under other tasks of the DOE project.

The AKCESS.BASIN Modeling System we developed and applied to the SEI Block 330 region is described in full in this final report. Because there is a great deal of material to report, the report is organized hierarchically: Section II gives an executive summary of the principle accomplishments of Modeling Task 5. Section III reviews the plans and performance in each sub-task. References are given there to the detailed reports given in the various subsections of Sections IV. In this way it is hoped that an interested reader can both rapidly obtain an overview of what has been done and also rapidly find parts of the work of specific interest.

It is probably natural that not all of the work proposed has been accomplished in exactly the fashion proposed three years ago. Preparation of the geologic data in a fashion that takes account of diapirism, overpressuring, and faulting in three dimensions, proved far more difficult and time consuming than we had anticipated. Substantial effort was also devoted to developing algorithms that accurately describe critical parameters such as thermal

conductivity and permeability in the data cube. However some areas proceeded far better than originally envisioned, and many new results have been obtained. All the important principal subtasks will be fully accomplished by the time the students involved in this project complete their Ph.D. theses. Furthermore, a powerful modeling capability has been created that is supported by a private company and a growing group of academics spread over five separate institutions. This is certain to impact basin studies for years to come.

SUMMARY:

The principal accomplishments to date under this proposal and the matching projects it encompasses are:

1. Development of a 3D finite element basin modeling system with sound and fully articulated fundamentals (Section I) and accurate algorithms for thermal conductivity and sand permeability, that provides for easy input of highly detailed three dimensional geologic data with options to infer salt diapirism from the surface pattern of sedimentation and sea level (Section II), takes into account all major physical and chemical phenomena (e.g., isostasy, salt diapirism, faulting, overpressuring, seals, hydrocarbon maturation, fluid flow driven by haline or thermal convection, water table topography, or overpressuring, salt dissolution and transport, etc.), solves the coupled equations with an easy to use but versatile and controllable finite element solver which can execute rapidly on parallel machines (Section III), and has convenient and easy to use visualization tools at all stages (Section II, III, V).
2. Distribution of that modeling system across 5 institutions (Cornell, LSU, Michigan Tech., and Bowling Green) with appropriate training of professionals and students at each.
3. Extensive benchmarking demonstrate the validity of various aspects of the modeling system (Section IV).
4. Application of the Modeling System to eight ~100 km long 2D seismic lines centered on the South Eugene Island Block 330 area of the Gulf of Mexico and one 1200 km interpreted N-S section. The modeling shows that the flexural rigidity of the Gulf lithosphere is less than about 10^{23} M-m. The history of salt movement over the last 20 Ma inferred directly from sedimentation shows evolution from a salt sheet to multiple minibasins and domes. The domes have a major impact on subsurface temperature ($\pm 70^\circ\text{C}$ temperature anomalies above and below the salt domes). (Section II and V.)
5. Construction of highly detailed 3D data cube in the SEI 330 area resolving all principal sands and their displacement across four NE-SW faults over the last 3.4 Ma. The salt movement inferred from the pattern of sedimentation shows the burial of a local salt sill and its remobilization into the South Eugene Island Block 330 Minibasin with the Red Fault at its northern margin.
6. Detailed analysis of bottom hole temperature data shows a positive temperature anomaly of about 5°C below the Pennzoil oil and gas fields roughly along the Red Fault and a negative (-5°C) temperature anomaly above the oil reservoirs. Modeling shows that temperature anomalies of this magnitude or greater will be produced by the insulating hydrocarbon-filled sand reservoirs. Fluid flow could produce the positive anomaly below the reservoirs along the Red Fault, but not the negative anomaly above the reservoirs. This suggests that the present day temperature field in the South Eugene Island Block 330 minibasin is due to thermal conductivity anomalies associated with hydrocarbon reservoirs and not rapid fluid flow (Section V).

7. Fluid flow modeling shows that pulses of overpressured fluid through the Red Fault can expel large quantities of water (and hydrocarbons), and produce significant temperature anomalies provided the permeability of the overpressured zone is on average more than ~0.05 md. Sand units below, in, and above the transition from hard overpressure to hydrostatic fluid pressures were found to be very important in controlling fluid flow and temperature anomalies associated with rapid venting. Clear vitrinite reflectance and isotopic anomalies in the A6 sidetrack (but not in the Pathfinder well 1000 ft away) suggest pulses of fluid have been expelled up the Red Fault, but that the flow channels are highly localized. (Section V).

8. Under a matching grant from the Gas Research Institute a new concept for sealing in which the flow of water (and other phases) is inhibited where there are multiple sand-shale (coarse-fine) interfaces and a non-aqueous (especially gas) phase present was conceived, tested in the laboratory, and shown to be applicable to the pressure transition drilled and cored by the Pathfinder well. (Section I).

9. The discovery that the part of the Red Fault penetrated by the Pathfinder well had a Poisson's ratio very close to that of a fluid led to the conception and quantification of a new hypothesis that significant fluid (water and hydrocarbons) migration may take place through propagating fractures. (Section V.)

